ACTIVE CONTROL OF NOISE THROUGH OPEN WINDOWS

LAM BHAN

School of Electrical & Electronic Engineering

A thesis submitted to the Nanyang Technological University
in partial fulfilment of the requirement for the degree of
Doctor of Philosophy

2019

Statement of Originality

I hereby certify that the work embodied in this thesis is the result of original research, is free of plagiarised materials, and has not been submitted for a higher degree to any other University or Institution.

19 Mar 2019

....

Date Lam Bhan

Supervisor Declaration Statement

I have reviewed the content and presentation style of this thesis and declare it is free of plagiarism and of sufficient grammatical clarity to be examined. To the best of my knowledge, the research and writing are those of the candidate except as acknowledged in the Author Attribution Statement. I confirm that the investigations were conducted in accord with the ethics policies and integrity standards of Nanyang Technological University and that the research data are presented honestly and without prejudice.

19 Mar 2019

....

Date Professor Gan Woon Seng

Authorship Attribution Statement

This thesis contains material from 14 paper(s) published in the following peer-reviewed journals / from papers accepted at conferences in which I am listed as an author.

Chapter 2 is published as Lam, B., and Gan, W.-S. (2016). "Active Acoustic Windows: Towards a Quieter Home," IEEE Potentials, 35, 11–18. doi:10.1109/MPOT.2014.2310776 and Lam, B., Shi, C., and Gan, W. (2017). "Active Noise Control Systems for Open Windows: Current Updates and Future Perspectives," Proc. 24th Int. Congr. Sound Vib., London, UK, 1–7.

The contributions of the co-authors are as follows:

- Prof. Gan provided the initial direction and edited the manuscript drafts
- I prepared the manuscript drafts. The manuscript was revised by Prof. Gan and Dr. Shi.
- I conducted the literature survey and drew all the graphics.

Chapter 3 is published as Lam, B., Elliott, S. J., Cheer, J., and Gan, W.-S. (2015). "Regularisation of the equivalent source method for robust numerical modelling of acoustic scattering," INTER-NOISE NOISE-CON Congr. Conf. Proceedings, InterNoise15, Institute of Noise Control Engineering, San Francisco, CA, USA, 976–987.

The contributions of the co-authors are as follows:

- Prof. Elliott provided the initial direction and edited the manuscript drafts
- I prepared the manuscript drafts. The manuscript was revised by Prof. Gan and Dr. Cheer.
- I co-designed the study with Prof. Elliott and Dr. Cheer and conducted all the numerical experiments and analysed all the data.
- Prof. Elliott and Dr. Cheer provided advice in the mathematical formulation and guidance in the interpretation of the results.

Chapter 4 is published as Lam, B., Elliott, S. J., Cheer, J., and Gan, W.-S. (2015). "The Physical Limits of Active Noise Control of Open Windows," In K. M. Lim (Ed.), Proc. 12th West. Pacific Acoust. Conf., Singapore, 184–189. and Lam, B., Elliott, S., Cheer, J., and Gan, W.-S. (2018). "Physical limits on the performance of active noise control through open windows," Appl. Acoust., 137, 9–17. doi:10.1016/j.apacoust.2018.02.024

The contributions of the co-authors are as follows:

- Prof. Elliott provided the initial direction and edited the manuscript drafts.
- I prepared the manuscript drafts. The manuscript was revised by Prof. Gan, Prof. Elliott and Dr. Cheer.
- I co-designed the study with Prof. Elliott and Dr. Cheer and conducted all the numerical experiments and analysed all the data.
- I also performed the numerical derivations for the verification of the FEM model accuracy under the guidance of Prof. Elliott.
- Prof. Elliott and Dr. Cheer provided advice in the presentation of the mathematical formulation and guidance in the interpretation of the results.

The main contributions in Chapter 4 are supported by two separate studies published as Elliott, S., Cheer, J., Lam, B., Shi, C., and Gan, W. (2017). "Controlling Incident Sound Fields With Source Arrays in Free Space and Through Apertures," In B. M. Gibbs (Ed.), Proc. 24th Int. Congr. Sound Vib., London, UK, 1–7. and Elliott, S. J., Cheer, J., Lam, B., Shi, C., and Gan, W. (2018). "A wavenumber approach to analysing the active control of plane waves with arrays of secondary sources," J. Sound Vib., 419, 405–419. doi:10.1016/j.jsv.2018.01.028

The contributions of the co-authors are as follows:

- Prof. Elliott provided the initial direction and edited the manuscript drafts.
- Prof. Elliott prepared the manuscript drafts. The manuscript was revised by Dr. Cheer, Dr. Shi, Prof. Gan and myself.
- I co-designed the FEM numerical study with Prof. Elliott and Dr. Cheer and conducted all the FEM simulations.
- Prof. Elliott and Dr. Cheer performed the theoretical derivations and performed the analytical numerical simulations.

Part of Chapter 4 is also presented as Lam, B., and Gan, W.-S. (2017). “Effects of acoustic scattering on the active control of noise through apertures,” COMSOL Conf. 2017, Singapore.

The contributions of the co-authors are as follows:

- Prof. Gan provided the initial direction and edited the poster contents.
- I prepared the contents of the poster.
- I co-designed the numerical experiments with Prof. Gan and conducted all the FEM simulations and analysed the results.

Part of Chapter 4 and 5 is published as Lam, B., Shi, C., Shi, D., and Gan, W.-S. (2018). “Active control of sound through full-sized open windows,” Build. Environ., 141, 16–27. doi:10.1016/j.buildenv.2018.05.042

The contributions of the co-authors are as follows:

- Prof. Gan provided the initial direction and edited the manuscript drafts.
- I prepared the manuscript drafts. The manuscript was revised by Prof. Gan and Dr. Shi, C.
- I co-designed the study with Prof. Gan and Dr. Shi, C. and conducted all the numerical experiments and analysed all the data.
- Dr. Shi, C and Mr. Shi, D assisted with the collection and provided guidance in the interpretation of the experimental data.
- Dr. Shi, C and Mr. Shi, D also assisted in the setup of the test chamber and provided guidance in the design of the active control system in the School of Electrical & Electronic Engineering.

Experiments in Chapter 5 are guided by findings presented as Fasciani, S., He, J., Lam, B., Murao, T., and Gan, W.-S. (2015). “Comparative study of cone-shaped versus flat-panel speakers for active noise control of multi-tonal signals in open windows,” INTER-NOISE NOISE-CON Congr. Conf. Proc., San Francisco, CA, USA, 1109–1120.
The contributions of the co-authors are as follows:

- Prof. Gan provided the initial direction and edited the manuscript drafts.
- Dr. Fasciani prepared the manuscript drafts. The manuscript was revised Dr. He and myself.
- I co-designed the study with Dr. Fasciani, Dr. He and Prof. Gan
- Dr. Murao and Dr. Fasciani set up and conducted the experiments.
- Dr. Murao also processed the data and provided guidance on the presentation of the analysis.

Chapter 6 is published as Lam, B., He, J., Murao, T., Shi, C., Gan, W.-S., and Elliott, S. J. (2016). “Feasibility of the full-rank fixed-filter approach in the active control of noise through open windows,” INTER-NOISE NOISE-CON Congr. Conf. Proceedings, InterNoise16, Hamburg, Germany, 3548–3555.

The contributions of the co-authors are as follows:

- Prof. Gan provided the initial direction and edited the manuscript drafts.
- I prepared the manuscript drafts. The manuscript was revised by Dr. He and Dr. Shi.
- I co-designed the study with Prof. Gan and Dr. He and conducted all the numerical experiments and analysed all the data.
- Dr. Shi, C and Dr. Murao provided guidance in the interpretation of the numerical experiments.
- Prof. Elliott provided guidance in the representation of the mathematical formulation.

Chapter 6 is also published as Lam, B., Gan, W., and Elliott, S. (2018). “Hybrid source arrangement for active control of noise through apertures at oblique incidences: A preliminary investigation,” Proc. 25th Int. Congr. Sound Vib. ICSV25, Hiroshima, Japan, 1–8.

The contributions of the co-authors are as follows:

- Prof. Gan provided the initial direction and edited the manuscript drafts.
- I prepared the manuscript drafts. The manuscript was revised by Prof. Elliott.
- I co-designed the study with Prof. Gan and Prof. Elliott and conducted all the numerical experiments and analysed all the data.

Suggestions in Chapter 7 is guided by preliminary work presented as He, J., Lam, B., Murao, T., Ranjan, R., and Gan, W.-S. (2016). "Symmetric design of multiple-channel active noise control systems for open windows," INTER-NOISE NOISE-CON Congr. Conf. Proceedings, InterNoise16, Institute of Noise Control Engineering, Hamburg, Germany, 613–622.

The contributions of the co-authors are as follows:

- Prof. Gan provided the initial direction and edited the manuscript drafts.
- Dr. He and I prepared the manuscript drafts. The manuscript was revised by Dr. Murao and Dr. Ranjan.
- I co-designed the study with Prof. Gan and Dr. He and some of the numerical experiments and analysed some of the data.

Suggestions in Chapter 7 is also guided by preliminary work presented as Ranjan, R., He, J., Murao, T., Lam, B., and Gan, W.-S. (2016). "Selective Active Noise Control System for Open Windows using Sound Classification," INTER-NOISE NOISE-CON Congr. Conf. Proceedings, InterNoise16, Hamburg, Germany, 482–492.

The contributions of the co-authors are as follows:

- Prof. Gan provided the initial direction and edited the manuscript drafts.
- Dr. Ranjan prepared the manuscript drafts. The manuscript was revised by Dr. Murao and Dr. He and myself.
- Dr. Ranjan co-designed the study with Prof. Gan and Dr. and performed the simulations and analysis.

19 Mar 2019 

....

Date Lam Bhan

Acknowledgements

I would like to express an immense gratitude to my supervisor, Professor Gan Woon Seng, for believing in me and providing a plethora of opportunities and advice throughout my PhD. His patience and enthusiasm have cultivated a vibrant and conducive research environment. On Professor Gan's recommendation, equalled by Professor Steve Elliott's alacritous acceptance, I had a fortuitous opportunity to conduct part of my PhD research at the Institute of Sound and Vibration Research (ISVR) in Southampton under Professor Elliott's guidance. Professor Elliott has provided significant technical input to the work presented in notable parts of this thesis. I would like to express my heartfelt gratitude to him.

Numerous people have helped me throughout the pursuit of my PhD, and I would like to recognize their contributions and thank them as follows:

- Dr Shi Chuang for his guidance and help in the conduct of experiments in the test chamber.
- Dr Jordan Cheer for his advice and guidance during my time at ISVR.
- Dr He Jianjun for his help in the initial setup of the test chamber and the experiments.
- Mr Shi Dongyuan for his help in the realization of the FPGA platform and the subsequent improvements in the PXI platforms.
- Mr Yeo Sung Kheng for his administrative assistance, and companionship in numerous leisure runs around the campus.
- All members and alumni of the lab that have been a significant part of PhD life, in no particular order – Joseph (Dr), Rishabh (Dr), Kaushik (Dr), Mu Hao (Dr), Ko ko, Ted, Duy Hai, Santi, Aproov, Stefano (Dr), Tatsuya (Dr), Yi Yang, Valiatsin, Zhen Ting, Joo Young (Dr), Rishabh, Aayush, Ashok (Dr), Tho, Cao Yi, and Rina.

- Friends at ISVR for their hospitality and discussions – Nikhil, Fábio, Falk-Martin, Jamie, Pina, Marcos (RS), Alice, Marcos (SG), Stefano, Alicia, Arthur, and Zhenbin.

- Members of the administrative staff at the University

Last but not least, I would like to thank my wife, Viki, and my family for their encouragement and support throughout.

Table of Contents

Summary

Active noise control (ANC) is a noise abatement technique that preserves an abode's natural ventilation when applied on domestic windows. ANC systems for open windows mitigates noise at the receivers' end, which augments solutions that are less effective for urban noise in high-rise cities. The target of the ANC system is to reduce noise that propagates through an open aperture, such as a window, into the interior of a room. This thesis presents a systematic approach to the open window ANC system design to address the complex practical implementation challenges.

Firstly, the fundamental limits of the ANC system in controlling noise through an open aperture are determined by numerical simulations. The investigation into the performance of different physical arrangements reveals that the upper limit frequency limit of control is determined by the separation distance between the sources of the planar array, distributed evenly in the aperture. As a result, the minimum number of sources needed for good control is generalized for a rectangular aperture and the dominant noise incidence angles. Based on the design guidelines for the open aperture, a further numerical study was conducted to investigate the influence of passive elements (i.e. glass panel) in the aperture on the active control performance. Moreover, it was shown that the arrangement of control sources in a partially glazed aperture (~75%) based on the established design guidelines could provide more attenuation than a fully-glazed aperture without active control.

Next, an experimental setup with a full-sized domestic window is designed and installed on a room model placed in a recording studio. The active control units were custom designed and secured within the aperture via the security grille. A total of 24 control sources of the multiple-input-multiple-output (MIMO) ANC system are

implemented on a fully-opened two-panel sliding window. The active control attenuation performance was predicted to be 10 dB at the error microphones through offline simulations with measured transfer functions.

Due to the high computational complexity, the real-time active control system was implemented on an FPGA platform, which operated at 25 kHz sampling rate. The active control performance was determined by an array of 18 microphones distributed within the interior of the test chamber, of which 12 microphones monitored the noise directly in front of the aperture in a plane array, and the rest were distributed according to the ISO standard to measure the energy-averaged sound pressure level of the room interior. The active control performance was compared to the passive insulation provided by a fully-closed window. In both tonal and broadband noise scenarios, the active control system was comparable to the passive insulation of a fully-glazed window in the mid-frequencies and at oblique angles of incidence for the entire frequency range of interest.

Lastly, considerations to increase the practicability of the active noise control system for domestic windows are discussed. Namely, the omission of error microphones but implementing fixed filters and the reduction of the number of control sources that are distributed in the aperture in an effort to reduce the physical and visual obstructions.

List of Figures

List of Tables

List of Abbreviations and Acronyms

1D	One-dimensional
2D	Two-dimensional
3D	Three-dimensional
ANC	Active Noise Control
BEM	Boundary Element Method
BLWN	Band-limited White Noise
END	Environmental Noise Directive
ESM	Equivalent Source Method
FEM	Finite Element Method
FPGA	Field-programmable Gate Array
FXLMS	Filtered-*x* Least-Mean-Square
HVAC	Heating, Ventilation, and Air Conditioning
LMS	Least-Mean-Square
MPA	Micro-perforated Absorbers
PML	Perfectly-matched Layer
SAR	Successive Approximation Register
SPCW	Soundproofing Casement Window
SPL	Sound Pressure Level
SPRING	Standards, Productivity and Innovation Board
VHDL	VHSIC Hardware Description Language
VHSIC	Very-High Speed Integrated Circuit
WHO	World Health Organisation

List of Symbols

A	The left boundary in the 1D duct (Chapter 3), the coefficient of the squared term in the quadratic factorization (Appendix A)
A'	The right boundary in the 1D duct (Chapter 3)
b	The coefficient of the linear term in the quadratic factorization (Appendix A)
B	Ratio of N evaluation points to M equivalent sources (Chapter 3)
c	The constant term in the quadratic factorization (Appendix A)
c_0	The speed of sound in air
C	The cost function (Chapter 4, 6)
d	The distance between the boundaries (Chapter 3)
D	Sum of all linear dimensions (Chapter 1), left boundary in the 1D duct (Chapter 3)
$\mathbf{d}$	The $(M \times 1)$ vector of complex disturbance signals (Chapter 4, 6)
E	Error criterion at all evaluation points on the boundaries (Chapter 3)
E'	Error criterion of all evaluation points in the 2λ zone (Chapter 3)
$\mathbf{e}$, $\mathbf{e}(e^{j\omega T})$	The $(M \times 1)$ vector of complex error signals (Chapter 4, 6)
$\mathbf{e}(n)$	The vector of error signals (Chapter 5)
F	The right boundary in the 1D duct (Chapter 3)
$\hat{\mathbf{g}}(n)$	The vector of secondary path impulse response
$\mathbf{G}$, $\mathbf{G}(e^{j\omega T})$	The $(M \times N)$ matrix of complex secondary plant responses, and the $(M \times K)$ matrix of complex secondary plant responses (Chapter 6)
$\mathbf{G}(z)$	The matrix of secondary path responses (Chapter 5)
$\hat{\mathbf{G}}(z)$	The matrix of estimated secondary path responses (Chapter 5)
GR	Glazing ratio (Chapter 4)
h_x	The separation distance between the double-layer sources (Chapter 6)
h_y	The distance of the pair of sources in the double-layer configuration to the wall edge (Chapter 6)
^{H}	Hermitian operator
$H_0^{(2)}$	Zeroth-order Hankel function of the 2nd kind
i	Total number of points in the left-hand $2\lambda \times 2\lambda$ area
$\mathbf{I}$	Identity matrix
J	The number of reference sensors (Chapter 5, 6)

J_0	Zeroth-order Bessel function of the first kind
k	Acoustic wavenumber
K	The number of noise incidence angles (Chapter 6)
L	The size of aperture
L_w	The width of the glass panel (Chapter 4), the number of taps in the control filter (Chapter 5)
L_g	The length of the glass panel within the aperture (Chapter 4)
L_s	The number of taps in the secondary path transfer function (Chapter 5)
M	Modal density (Chapter 1), number of equivalent sources (Chapter 3), the number of error sensors (Chapter 5, 6)
n	The discrete time index
N	The number of evaluation points on the boundary (Chapter 3), number of secondary sources (Chapter 4, 5, 6)
N_{min}	Minimum number of secondary sources
o	The index for the O observation microphones (Chapter 5)
O	The total number of observation microphones (Chapter 5)
p	Acoustic pressure
p^+	Acoustic pressure in the positive x-direction
p^-	Acoustic pressure in the negative x-direction
p_p	Acoustic pressure due to the primary source
p_s	Acoustic pressure due to the secondary source
$p_{int,m}$	Acoustic pressure due to the m-th internal equivalent source
p_{image}	Acoustic pressure calculated from the perfect image source model
$\mathbf{p}_{L_g}$	The vector of complex pressure values in the presence of a glass panel of size L_g
q	Complex source strength
q_p	Complex source strength of the primary source
q_s	Complex source strength of the secondary source
$q_{s,opt}$	Optimal complex source strength of the secondary source
q_N	Complex source strength of source number N
$q_{(x,y)}$	Source strength at cartesian coordinate (x, y)
$\mathbf{q}$	The vector of complex secondary source strengths (Chapter 4, 6)
$\mathbf{q}_0$	The vector of optimal complex secondary source strengths (Chapter 4, 6)

$\mathbf{q}_{int}$	The vector of complex source strengths of the internal equivalent sources
r	The radial distance from the acoustic source with respect to the origin of the Cartesian plane
r_l	Radial distance to the l-th position in the $2\lambda \times 2\lambda$ zone
r_p	The radial distance from the primary source
$r_{m.n}$	The radial distance from the m-th internal equivalent source to the n-th evaluation point
$r_{p.n}$	The radial distance from the primary source to the n-th evaluation point
r_s	The radial distance from the secondary source
RT_{60}	The reverberation time parameter, which represents the time taken for the space-averaged sound energy density in an enclosure to attenuate by 60 dB after the source emission has stopped.
S	Total surface area
S_{duct}	Cross-sectional surface area of the duct
SPL_{EA}	The energy-averaged sound pressure level (Chapter 5)
SPL_{PA}	The average sound pressure level across a plane array of observation microphones (Chapter 5)
$SPL_{TA,o}$	The time-averaged sound pressure level of the o-th observation microphone (Chapter 5)
$^{\mathrm{T}}$	The transpose operator
T_{30}	The reverberation time, in seconds, based on a 30 dB evaluation range as stated in ISO 3382-2:2008
TL_{GR}	Transmission loss at glazing ratio GR due to passive insulation only
$TL_{GR,ANC}$	Transmission loss at glazing ratio GR due to both passive and active control
$\mathbf{T}$	(2 × 2) Transform matrix (Chapter 3)
$\mathbf{T}_e$	($N \times M$) Transform matrix (Chapter 3)
u^+	Particle velocity in the positive x-direction
u^-	Particle velocity in the negative x-direction
u_A	Total particle velocity at the boundary A (Chapter 3)
$u_{A'}$	Total particle velocity at the boundary A' (Chapter 3)
$\mathbf{u}$	The vector of normal particle velocities due to the pair of sources in the duct (Chapter 3). The vector of complex secondary source input signals (Chapter 6).

$\mathbf{u}_p$	The vector of normal particle velocities due to the primary source on both boundaries
$\mathbf{u}_{p,2\lambda}$	The vector of normal particle velocities due to the primary source in the $2\lambda \times 2\lambda$ area
$\mathbf{u}_T$	The vector of normal particle velocities at both boundaries, i.e. $x = A$ and B; and $x = D$ and F.
$\mathbf{u}_{T,2\lambda}$	The vector of total normal particle velocities in the $2\lambda \times 2\lambda$ area
$\mathbf{u}_{\text{int}}$	The vector of particle velocities due to the internal secondary sources at all the evaluation points on the boundaries
$\mathbf{u}_{opt}$	The vector of optimal secondary source strength (Chapter 6)
$\mathbf{U}_{opt,\theta_k}$	
v	Total number of points in the right-hand $2\lambda \times 2\lambda$ area (Chapter 3), the distance between the edge of the wall to the nearest secondary source (Chapter 4)
V	Volume in m^3
w	The separation distance between acoustic sources (Chapter 3, 4)
w_{vert}	The separation distance between acoustic sources in the y-axis direction (Chapter 3)
$w_{wall,L}$	Distance from the left boundary to the left column of equivalent sources
$w_{wall,R}$	Distance from the right boundary to the right column of equivalent sources
$\mathbf{w}$	The vector of control filter coefficients
W	The acoustic power output
W_d	The acoustic power at the evaluation arc due to the primary disturbance
W_e	The acoustic power at the evaluation arc due to both the primary and secondary sources
W_p	The acoustic power output of the primary source
W_0	The minimum acoustic power output
$\mathbf{W}$	The matrix of control filter coefficients (Chapter 4, 6)
$\mathbf{W}_0$	The matrix of the optimal filter coefficients (Chapter 6)
$\mathbf{W}_{o,\theta_k}$	The matrix of the optimal filter coefficients calculated using K noise incident angles
x	The horizontal axis in the cartesian plane
$\mathbf{x}(n)$	The vector of reference signals (Chapter 5)
$\mathbf{x}(e^{j\omega T})$	The $(J \times 1)$ vector of complex reference signals (Chapter 6)
y	The vertical axis in the cartesian plane

$\mathbf{y}(n)$	The vector of output signals to the secondary sources (Chapter 5)
Y_0	The zeroth-order Bessel function of the second kind
Z_0	The real part of the acoustic impedance
Z	The complex acoustic impedance
β	The regularisation parameter
λ	Acoustic wavelength
μ	The step-size parameter (Chapter 5)
ω	Angular frequency
ψ	Damping ratio
ρ_0	Density of air
θ	The incidence angle of the primary plane wave
$\theta_{m,n}$	The angle between the m-th internal equivalent source and the n-th evaluation point
$\theta_{p,n}$	The angle between the primary source and the n-th evaluation point
ζ_L	Pressure difference index for $2\lambda \times 2\lambda$ on the left side of the boundary (Chapter 3)
ζ_R	Pressure difference index for $2\lambda \times 2\lambda$ on the right side of the boundary (Chapter 3)
$\mathbb{Z}^+$	Positive integer

Chapter 1

Introduction

Aside from the auditory health effects (i.e. hearing loss) of exposure to excessively high levels of sound, non-auditory health effects arising from chronic exposure to transportation noise should be a cause for concern. Increasing evidence showing significant proportions of the urban population being exposed to chronic levels of transportation noise highlights the urgency in deploying effective noise mitigation measures. However, widely implemented noise abatement methods (i.e. noise barriers, porous asphalt) are contradictory to sustainable development efforts such as naturally ventilated buildings and greening efforts.

Traditional noise abatement for naturally ventilated buildings tend to either obstruct daylight ingress, restrict airflow, prevent access to the façade or in any combination of the three (e.g. acoustic louvres, double-glazing, resonators). Since transportation noise is predominantly low-frequency in nature, there is potential for the implementation of active noise control (ANC) techniques. ANC is effective at low-frequencies that passive methods struggle at, and can abate noise while maintaining daylight ingress, airflow and access to the façade.

1.1. Urban Noise Environment on Health

Environmental noise is a prevalent feature of an urban soundscape. Of the numerous environmental noise sources (e.g. aircrafts, road traffic, railways, industries and construction), the World Health Organisation (WHO) has identified road traffic noise as one of the main contributors to urban noise pollution [European Environment Agency, 2017; Fritschi et al., 2011; Nugent et al., 2014].

Owing to widespread exposure and its pervasiveness, urban noise has been linked to a myriad of non-auditory health effects by an increasing number of health studies [Basner et al., 2014; Fritschi et al., 2011; Nugent et al., 2014; Stansfeld and Matheson, 2003; World Health Organization Regional Office for Europe, 2009]. Six major health effects were identified from WHO's compilation of health studies in 2011: cardiovascular disease, cognitive impairment in children, sleep disturbance, tinnitus and annoyance.

Sleep disturbance has been determined to be the most detrimental non-auditory effect due to its effect on daytime function and performance, and health. Psychological adaptations to noise do not translate to physiological adaptations as the autonomic, motor, and cortical arousals can still be invoked during sleep. Epidemiological research has indicated that prolonged activation of the physiological system due to long-term chronic exposure to noise, even at low noise levels, is associated to an increase in adverse health risks (i.e. hypertension, arteriosclerosis, and ischaemic heart disease). With relation to noise levels, meta-analyses of studies assessing the link between transportation noise exposure (i.e. road traffic and aircraft noise) and health effects (i.e. hypertension, ischaemic heart diseases, including myocardial infarction), indicates a 7% to 17% increase in risk per 10 dB increase in equivalent noise level [Basner et al., 2014].

Thus, the design goal for noise mitigation strategies can be based on the specific night noise threshold levels (in decibels) and their associated observed health effects, as summarised by WHO in Table 1 [World Health Organization Regional Office for Europe, 2009]. Even if the 55 dB A-weighted equivalent noise level is a difficult goal, a 10 dB decrease can result in a 7% to 17% reduction in health risks.

Table 1.1: Associated health effects at different night noise levels (A-weight equivalent noise levels) [Fritschi et al., 2011]

Average night noise level over a year.	**Health effects observed in the population**
Up to 30 dB	No substantial biological effects are observed (subject to individual differences).
30 to 40 dB	Several effects on sleep observed but seem modest even in the worst cases. Vulnerable groups (e.g. children, elderly) are more susceptible.
40 to 55 dB	Adverse health effects observed among the exposed population. Many people adapt their lives to cope with the noise at night. Vulnerable groups are more severely affected.
Above 55 dB	Considered increasingly dangerous for public health. Frequent occurrence of adverse health effects, with a sizeable proportion of the population highly annoyed and sleep-disturbed. There is evidence that the risk of cardiovascular disease increases.

1.2. Noise Mitigation Strategies from an Urban Sustainability Perspective

Escalating vehicular usage in densely populated areas usually result in congested road networks that may be in close proximity to current (and future) residential areas. This is a rising concern especially in densely populated Asian cities [Schwela et al., 2014]. The

resulting inadvertent exposure to unhealthy noise levels and rising complaints have prompted local authorities to explore innovative noise control measures for safeguarding public health in a sustainable manner.

Noise mitigation strategies are multi-faceted, spanning from measures at the source, through the propagation path, and to the receiver end. The focus of this section is placed on the control measures pertaining to road traffic noise owing to its pervasiveness. Based on the reported Environmental Noise Directive (END) action plan measures for road traffic noise by the European Union member states, heavy emphasis is placed on road traffic management (25%) and measures along the propagation path (25%); followed by measures at the receiver (13.89%); promotion and awareness (11.11%); measures at the source (8.33%), socio-economic measures (8.33%); and land use and urban planning (8.33%).

1.2.1. Measures at the Source

The most productive and effective noise control measures are targeted at the source [Guarinoni et al., 2012; Nilsson et al., 2014; Nugent et al., 2014]. Road traffic noise is mainly attributed to: (1) tyre-road interaction when the vehicle is travelling above 30 km/h, and (2) by propulsion sources (i.e. engine, exhaust, air intake, etc.) below this speed [Nilsson et al., 2014; Nugent et al., 2014; Science Communication Unit, 2017].

Low-noise road surfaces made of porous asphalt and low-noise tyres are effective at reducing noise levels by up to 4 dB and 3 dB respectively at present. However, porous asphalt is less durable (than dense asphalt concrete) and requires more frequent maintenance on top of higher application costs. The need for maintenance also results in obstruction to traffic and additional noise from asphalt milling machines. Further

improvement to achieve quieter tyres requires more radical design changes such as using airless tires [Science Communication Unit, 2017].

Vehicle noise emission limits are only as effective as their test methodologies. Even if the appropriate test methodology is selected, a substantial lead time is required for successful implementation in the vehicle population. Moreover, the effectiveness of these limits is thwarted by irresponsible driving (e.g. engine revving) and asocial behaviours (e.g. modification to tailpipes), which are evident from the prevalence of noise complaints. Hence, innovative methods such as a remote detection system [Agha et al., 2017] should be developed to deter such behaviours.

1.2.2. Measures Along the Propagation Path

Both road traffic management measures and mitigation strategies along the propagation path are the most emphasised methods in Europe due to the immediacy of the mitigation effects. The erection of noise barriers to obstruct direct propagation of the noise to the recipients is the most popular abatement method in Europe and perhaps across the world.

The effectiveness of the barriers is dependent on: (1) height, (2) length, (3) material (4) its position, (5) and even the soil upon which it is placed [Murphy and King, 2014]. Ideally, the barrier should be tall enough to obscure the line-of-sight between the source and the receiver. It should be long enough to cover a 160 degrees field-of-view from the perspective of the receiver. The barrier should also be solid and continuous with no gaps and be positioned as close as possible to either the source or the receiver. Lastly, the addition of soil cover over rigid berms can improve attenuation of up to 5 dB [Van Renterghem and Botteldooren, 2012].

Although noise barriers can be applied across different noise types (e.g. construction noise and train noise), the mechanism of the noise barrier is paradoxical in a high-rise scenario [Murphy and King, 2014]. Noise barriers diffract noise over its top and around its edges, limiting its effectiveness to sections of the building in its shadow zone and inadvertently increasing the noise levels for a larger portion of a tall building (i.e. upper floors). Tall barriers (usually above 3 m) require an additional foundation to maintain structural integrity, thereby increasing its already high cost, especially so for transient activities such as construction sites. Often, land-scarce cities (e.g. Hong Kong and Singapore) do not allow the barriers to be placed in their optimal positions and inevitable obstructions (e.g. large trees, telephone poles, traffic signals, etc.) result in discontinuities in the barriers, reducing its effectiveness. Moreover, on top of the barrier's poor aesthetics, it is a hindrance to the city's sustainability efforts (e.g. limits tree-planting, obstructs airflow, affects wildlife – avian collisions with transparent panels).

1.2.3. Measures at the Receiver End

Recommendations for abatement measures at the receiver end are lacking in noise directives and reports, which is evident from the preference for the erection of noise barriers [Guarinoni et al., 2012; Nugent et al., 2014; Science Communication Unit, 2017]. The measures mentioned are usually limited to building and façade insulation such as double or triple glazing of windows or implementation of winged walls to diffract noise away from the façade openings.

Despite the effectiveness of glazed windows (up to 30 dB insulation), the requirement for windows to remain closed are not suitable for tropical climates.

Moreover, natural ventilation is vital for good indoor air quality as recommended by the WHO to reduce: (1) risks of airborne communicable disease transmission, (2) build-up of, and exposure to indoor air pollutants, (3) mould and dampness, and (4) microbial build-up in air-conditioned areas [Nathalie, 2011]. Natural ventilation is also a sustainable design goal that can enhance the cooling of buildings, yielding up to 25-50% in energy savings [Fisk and Rosenfeld, 1997; Nathalie, 2011].

Noise control strategies for naturally ventilated buildings usually involve passive elements that affects the airflow and visibility of the façade openings such as the addition of louvres, or resonators. However, such methods are ineffective at the low-frequency range (<500-1000Hz), where most transportation noise falls within. Hence, there is an underexplored area where active methods, which are effective at low frequencies, can be exploited to tackle environmental noise [De Salis et al., 2002; Tang, 2017].

1.3. Active Methods for the Abatement of Noise in Naturally Ventilated Buildings

Active noise control methods have been applied successfully to ventilation ducts [Kuo and Morgan, 1996], aircraft cabins [Nelson and Elliott, 1992], automobile cabins [Samarasinghe et al., 2016], and headphones [Kajikawa et al., 2012]. However, these control environments are usually confined to small interior spaces (i.e. ventilation ducts, automobiles, and headphone cups) or tackle harmonics (i.e. car engine, propeller revolutions).

1.3.1. Active Control of Acoustic Modes in an Interior Space

In a large interior space, one strategy for effective control of noise within the entire interior is to control all the relevant acoustic modes. In general, the number of sound sources (e.g. loudspeakers) required is proportional to the desired number of modes to be controlled.

The number of modes in a room can be approximated by calculating the modal overlap $M(\omega)$, a dimensionless parameter that quantifies the number of modes that are significantly excited in the enclosure (i.e. a room with rigid walls) at any one excitation frequency, ω [Bies and Hansen, 2009; Elliott, 2001; Hansen et al., 2012]. Since a room with rigid walls can be modelled as a three-dimensional enclosure, the acoustic modal overlap can be approximated from the modal densities and is given by [Elliott, 2001]

$$M(\omega) = \frac{2\psi\omega L}{\pi c_0} + \frac{\psi\omega^2 S}{\pi c_0^2} + \frac{\psi\omega^3 V}{\pi^2 c_0^3}, \tag{1.1}$$

where L is the sum of all the linear dimensions (i.e. all edges), S is the total surface area of the room interior, V is the volume, ψ is the damping ratio, and c_0 is the speed of sound. Considering the desired range of control up to 1000 Hz (typical of transportation noise), a typical apartment room size in Singapore of $3 \times 4 \times 2.6$ m^3, and a damping ratio of 10%, (1.1) can be plotted as a function of frequency as depicted in Figure 1.1. The number of modes and hence the number of control sources required is over 2500, as shown in Figure 1.1 which is impractical.

Furthermore, the number of sensors required to obtain an accurate estimate of the sound field for effective control over the entire interior is proportional to the number of significantly excited modes.

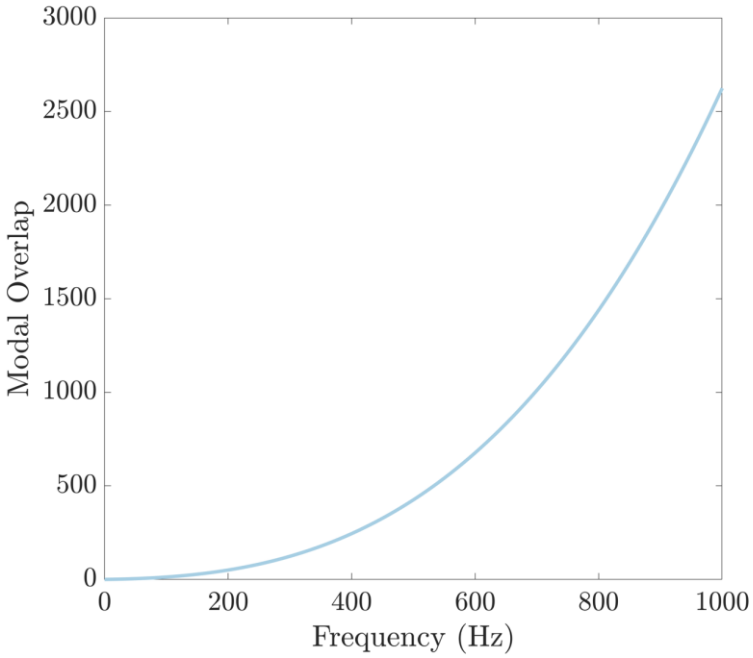

Figure 1.1: Modal overlap of a rectangular cuboid ($3 \times 4 \times 2.6$ m^3) with a damping ratio of 10% as a function of frequency.

1.3.2. Active Control of Sound Transmission Through Façade Openings

Instead of controlling all the significantly excited modes in the room interior, control can be targeted at the point of entry of the noise sources. In an apartment with thick concrete walls, it is reasonable to assume that the main point of entry for noise are the façade openings (i.e. windows).

As shown in section 0, it is important to determine the fundamental physical limitations of the environment in which active control is to be applied. For the successful practical implementation of active control, the fundamental limits of control through an aperture (i.e. the window in a wall) should be determined.

1.4. Thesis Structure and Objectives

In view of the situation, this thesis focuses on the practical implementation of an active noise mitigation method for naturally-ventilated building façade openings (i.e. open windows). Based on the review of the health impacts of chronic exposure to transportation noise, there is a pressing need to develop noise mitigation measures that can immediately and effectively alleviate low-frequency transportation noise in residential high-rise apartments. Noise control is particularly challenging in naturally ventilated buildings as there is little obstruction to the noise impinging on the building façade.

Although the use of active control methods for noise control in naturally ventilated buildings has been suggested in the past, there is a lack of research activity that seeks to fully define the fundamental limits and subsequent practical implementation of active control systems for full-sized façade openings. Therefore, the aims of this thesis are to: (1) define the fundamental limits of active control for practical façade openings, (2) develop a real-time active control system for a full-sized window in a domestic setting.

The structure of this thesis is as follows:

Chapter 1

The challenges of sustainable environmental noise control in densely-populated high-rise cities is addressed. From a meta-analysis of health studies, a reduction in noise of 10 dB could reduce noise-induced health risks by 7% to 17%. A survey of the current state of noise control measures from the source to the receiver reveal that conventional solutions are ineffective for naturally-ventilated high-rise buildings. Promising

solutions based on active noise control for façade openings of naturally-ventilated buildings, however, are still not fully understood.

Chapter 2

Building façade openings serve multiple functions in allowing daylight ingress, providing natural ventilation, insulates against noise, and allows access to the façade. Hence, this chapter surveys both the passive and active methods of noise control for apertures in the perspective of high-rise buildings in a tropical climate. The active control techniques employed, and their attenuation performance is surveyed and summarised.

Chapter 3

The complex mechanism of acoustic propagation through a rectangular aperture offers no computationally efficient analytical solution for an active control performance analysis [Rdzanek, 2018]. Based on previous active control analysis in an enclosure [Johnson et al., 1998], a numerical model based on the equivalent source method (ESM) is developed to determine the limits of active control of sound through an aperture. Owing to limitations of the regular geometry, the ESM method proved to be insufficiently accurate despite regularisation. Hence, an alternative model based on the finite element method (FEM) was developed and shown to have sufficient accuracy for the chosen parameters.

Chapter 4

Determination of the fundamental physical limitations is essential to the successful implementation of a practical active noise control system [Hansen et al., 2012; Nelson and Elliott, 1992]. Using the FEM-based numerical model, the optimal active control source arrangement within an unobstructed aperture along with the maximum achievable attenuation is determined. From the results, a relationship between the minimum number of sources required for good attenuation up to the desired frequency is derived. The simulation model is extended to include the occlusive effects of a regular glass panel to represent a typical two-panel sliding window configuration. The process is repeated to determine the minimum number of sources required for good control in relation to the size of the sliding window opening.

Chapter 5

Guided by the results of the numerical simulations, a real-time active noise control system is developed for a full-sized sliding window in a mock-up room. This chapter details the construction of the experimental test chamber and the active control units. The performance of the active control system is predicted by simulation with measure transfer responses between the active control loudspeakers and the error microphone array in the interior of the room. Subsequently, the performance of the real-time active control system is measured for a number of primary disturbance conditions by taking the space and time average sound pressure levels in the room interior.

Chapter 6

Based on the development of the active control system in Chapter 5, two important considerations for practical implementation are discussed. This chapter presents preliminary investigations into addressing the identified challenges namely: (1) omission of error microphones, and (2) the reduction of the number of control sources distributed within the aperture without a reduction in control performance.

Chapter 7

The final chapter summarises the findings presented in the preceding chapters and suggests directions for future work.

1.5. Contributions

The main contributions of this thesis are as follows:

(i) An equivalent source method approach was devised and demonstrated to be insufficiently accurate for simulating the propagation of planes waves through an aperture in a wall with finite thickness [Lam et al., 2015a]. (Chapter 3)

(ii) The physical limits of active control of noise through an unobstructed aperture was determined numerically for a number of control source configurations using the finite element method. Based on the analytical solution of a plane array of active control sources in the free-field [Elliott et al., 2018], the optimal arrangement of sources in the open aperture is determined for the complete range of noise incidences [Lam et al., 2015b, 2018a]. (Chapter 4)

(iii) Building upon the unobstructed aperture case, the optimal source arrangement and its fundamental limits of control are determined for a full-sized sliding window at a number of glazing scenarios (i.e. different stages of opening a sliding window) [Lam et al., 2018c]. (Chapter 4)

(iv) Based on the dimensions of the simulated sliding window, a full-sized sliding window and a test chamber were constructed for the real-time implementation of an active noise control system [Lam et al., 2018c]. The active control performance is measured for a number of primary source configurations using an array of microphones to obtain a space and time average sound pressure level in the room interior. (Chapter 5)

(v) A numerical experiment was conducted to determine the feasibility of using fixed-filters to achieve a practical active control system that omits the requirement of error microphones [Lam et al., 2016]. (Chapter 6)

(vi) A hybrid source configuration is proposed to improve the active control performance at oblique noise incidences and to reduce the visual obstruction in the aperture opening [Lam et al., 2018b]. (Chapter 6)

The published articles and conference proceedings that have arisen from the work in this thesis and related work produced in the same period is listed in the section of Author's Publications.

Chapter 2

Control of Noise through Apertures for Naturally Ventilated Residential Buildings

One of the main noise mitigation strategy at the receivers' end is to control the noise that propagates through a façade opening into an interior space. Targeting the main propagation path of the noise into an interior space (i.e. windows) guarantees that the noise is attenuated in the entire interior space. However, there are few noise mitigation techniques tailored for naturally-ventilated residential buildings, which have been widely adopted.

Design of noise control measures for residential façade openings should ideally not obstruct airflow, prevent daylight ingress, and restrict the access to the façade, especially in tropical climates. Although passive methods have traditionally struggled to effectively control low-frequency noise, recent developments in passive control methods for residential buildings are surveyed to assess their noise abatement limitations, and restrictions in terms of airflow, daylight ingress and façade access.

Finally, active noise control strategies are surveyed and analysed according to the layout of transducer arrangement: (1) boundary layout, where the control sources are arranged around the edges of the opening, and (2) distributed layout, where the control sources are distributed across the opening. Based on the summary of the active noise

control techniques, observations and research gaps are derived to be addressed throughout this thesis.

2.1. Passive Strategies

Silencers and acoustic treatments are traditional noise mitigation strategies for apertures, usually for heating, ventilation, and air conditioning (HVAC) systems. Although they are heavily utilised in the industrial setting, where daylight ingress and aesthetics are of minor importance, some researchers have attempted to adopt them for domestic window apertures. One prominent team proposed a silencer-type structure installed in the window aperture based on the incorporating Helmholtz resonators into sonic crystals. By tuning the resonators and adjusting the gap between the rectangular tubes, 9 dB of attenuation was achieved in the 700 to 1400 Hz band at the ears of a dummy head in an in situ setup [Lee et al., 2016, 2017; Lim et al., 2017]. Besides poor low-frequency performance, the daylight obstruction, rigidness, and poor aesthetics limit the sonic crystal window's practicality.

To strike a balance between acoustic insulation, natural ventilation, and daylight admission, recent passive techniques to mitigate noise at the window aperture are usually based on two staggered glass panels, also known as the plenum design. The plenum design is a variant of the staggered double window investigated by Ford and Kerry [Ford and Kerry, 1973], as a follow up to sliding double window recommendations from 1968 by Stephenson and Vulkan [Stephenson and Vulkan, 1968]. As opposed to recommended window treatments usually with separate mechanical ventilators [Ford and Kerry, 1973; Utley et al., 1986], the plenum design mitigates noise whilst maintaining sunlight admission and allowing natural ventilation.

Kang demonstrated an experimental staggered glass panel design lined with transparent micro-perforated absorbers (MPA), and louvres installed in between the glass sheets [Kang, 2009]. The noise attenuation performance of the proposed staggered panel system outperformed a fully closed single glazed window while maintaining sufficient ventilation. However, the attenuation performance degrades below 500 Hz, leaving room for further improvement.

Tong et al. conducted a full-scale field study to investigate the attenuation performance of the plenum window for traffic noise [Tong et al., 2015]. The acoustical shielding of the plenum window against traffic noise was determined to be 7.1 to 9.5 dB, in the test room located 3 m above the road surface. Tong et al. also noticed that the modes and resonances within the plenum window degrade the noise reduction performance of the plenum window in the low frequencies (250 to 400 Hz).

Other methods that considers acoustic insulation, daylight ingress, and natural ventilation include (1) a soundproofing casement window (SPCW) concept [Yuya, 2010; Yuya et al., 2009], (2) an air transparent soundproof window [Kim and Lee, 2014], and (3) a ventilated window with quarter-wave resonators and membrane absorbers. The SPCW consists of opaque ventilation units with staggered inlets and outlets for natural ventilation. The ventilation units are separated by transparent glass panels for daylight ingress. Without absorbent materials such as MPAs, however, significant attenuation only occurred at 800 and 1000 Hz 1/3 octave band centre frequencies.

The air transparent soundproof window proposed by Kim and Lee is based on the combination of MPA and Helmholtz resonator concepts [Kim and Lee, 2014]. The cylindrical holes in the middle of the transparent cubic cells serve as both diffraction resonators for acoustic insulation, whilst allowing airflow for natural ventilation. When the diameter of the cylindrical openings is 50 mm wide, up to 35 dB of transmission loss

was achieved between 700 to 2200 Hz. Since the acoustic attenuation performance is inversely proportional to the diameter of the cylindrical openings, the natural ventilation would be insufficient if good low-frequency performance is desired.

Building upon the quarter-wave resonator concept by Field and Fricke [Field and Fricke, 1998], Wang et. al. designed a silencer for ventilation openings based on quarter-wave resonators in combination with a winged wall that acts as a funnel to increase air flow rate [Wang et al., 2014]. In the frequency range of 500 Hz to 4 kHz, 10 to 22 dB of transmission loss was reported.

Aside from the double sliding window suggested by Stephenson and Vulkan [Stephenson and Vulkan, 1968], the passive strategies introduced have proposed fundamental changes to traditional window design. In dense, high-rise Asian cities, the function of the window goes beyond occupant comfort. Due to the lack of interior living space as well as cultural habits, drying of laundry on the building façade is a common sight. Hence, access to the façade through the windows are important factors to consider when implementing new window designs. For a clearer overview, the passive strategies can be classified according to their functions, as depicted by the Venn diagram in Figure 2.1. Unfortunately, none of the passive methods surveyed falls within the desired zone, where all four functions are met. Nevertheless, the passive methods could be used in predominantly temperate climates where the use of laundry drying machines are culturally prevalent.

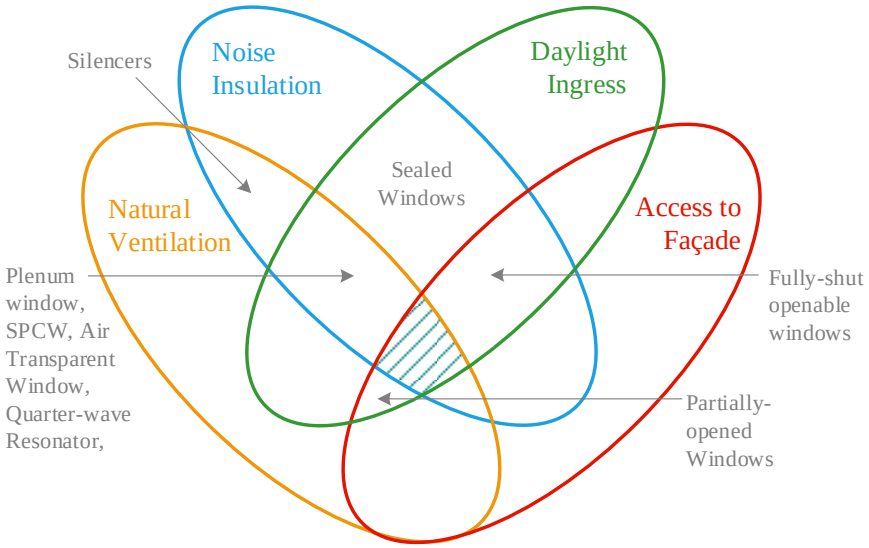

Figure 2.1: Functions of the domestic window with considerations of access to the Façade [Wang et al., 2014].

2.2. Active Strategies

The active noise control (ANC) concept is based on the wave superposition phenomenon, where the disturbance signal to be controlled is attenuated by an anti-phase wave with the same amplitude at the same point in space and time. While the concepts and theory behind active noise control are well-established, the complexities of practical implementation have limited its applications.

In the last decade, however, ANC has been increasingly deployed in mass-produced consumer automobiles to increase fuel efficiency and improve acoustic comfort [Samarasinghe et al., 2016]. More importantly, the switch to ANC in automobiles is also triggered by the more efficient low-frequency noise attenuation performance (<500 Hz) over traditional passive methods. The consumerisation of ANC technology has rekindled interest in controlling low-frequency sounds in other areas [Kajikawa et al.,

2012]. In particular, the application of ANC on domestic window apertures have gained some traction. To date, several preliminary studies of ANC for open apertures have demonstrated the feasibility of achieving good attenuation without affecting natural ventilation [Lam et al., 2018c; Lam and Gan, 2016]. Recently, Qiu presented an updated but brief overview of past and ongoing projects from around the world that have implemented ANC on apertures [Qiu, 2017]. Since there are relatively few active control implementations that are not based on duct acoustics for sealed windows [Jakob and Möser, 2003a, 2003b; Yu et al., 2007], the focus of this section will be on active control techniques implemented on open apertures for natural ventilation.

The investigation of active control methods to control noise transmission through apertures can be traced back to the proposed active sound power absorption method by Emms [Emms, 2000; Emms and Fox, 2001]. The suggested monopole-dipole absorber absorbs the incident sound power at the aperture, as opposed to the ANC technique used in the examples above, which minimises the sum-of-squared sound pressure. In the experimental system, the sound power transmitting through the 0.6 m × 0.6 m aperture was absorbed significantly in the frequency range of 200 Hz to 500 Hz. The absorption performance of active sound absorbers, however, is limited by the finite drivers of the control sources and are also highly sensitive to calibration errors. Despite the negatives, conclusions such as (1) sensitivity to deviations in control source position relative to the aperture, and (2) deciding the appropriate separation distance between sources in an array, are important considerations for scaling to larger apertures and extending the upper-frequency limit. At present, the practical realisation of the active sound absorber concept is still technically challenging [Cho et al., 2018; Nelson and Elliott, 1992].

In the past decade, the interest in the active control of sound through apertures re-emerged independently in Europe and Asia and has gained momentum until today.

Although the adaptive algorithms are similar, the techniques can be broadly classified by their physical arrangement of control sources with respect to the aperture, namely: (1) in the boundary layout, where control sources are placed around the periphery of the aperture, or (2) in a distributed layout, where control sources are usually distributed across the aperture.

2.2.1. Boundary Layout

The boundary layout is an enticing solution as the aperture will be unobstructed by the control sources. The boundary layout has been tested on different types of openings, such as unobstructed apertures, tilt windows, sliding windows, and an interesting study that is applied to an aperture of a baffled rectangular cavity.

2.2.1.1. Open Aperture

Based on Ise's boundary surface control principle [Ise, 2005], Kwon and Park proposed a feedforward approach to ANC implementation where reference sensors are introduced to detect the impinging noise [Kwon and Park, 2013]. The scaled-down model consists of 8 control sources arranged evenly around the 30 × 30 cm (900 cm^2) aperture. The main disadvantage, however, is the non-causal filter implementation that requires reference sensors to be placed a distance away from the control sources. In field implementations, the complex sound fields in front of the aperture will alter the transfer functions of the estimated reference signal. Thus, the attenuation performance will be degraded, especially for glancing incidences. Nevertheless, in the anechoic setup, reduction of up to 10 dB was achieved in the entire interior of the scaled-down model, regardless of noise incidence from 0º up to 60º.

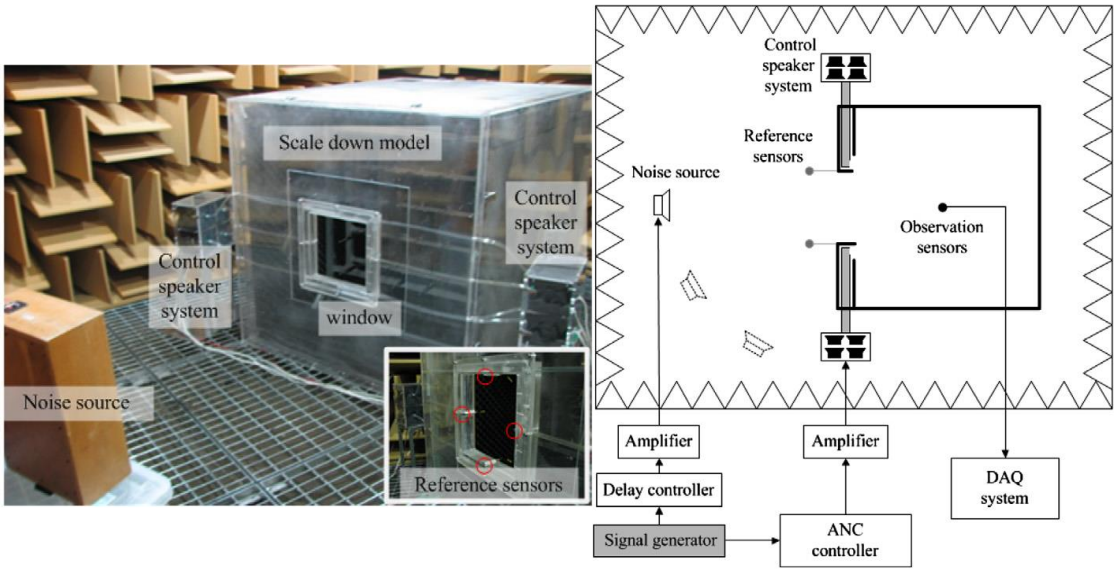

(a) (b)

Figure 2.2: (a) Image of the scaled-down model room and an open aperture with the active noise control sources embedded in the surrounding frame. (b) The block diagram and cross-sectional representation of the active control system [Kwon and Park, 2013].

2.2.1.2. **Tilt Windows**

In a field experiment, as shown in Figure 2.3(a), Pàimes et. al. implemented an active control system on a regular hopper-style (56 × 142 cm) tilt window with the goal of reducing aircraft fly-over noise. The adaptive feedforward system is depicted in Figure 2.3(b) and comprises of (1) a reference sensor, placed 15 m in front of the façade, (2) a control source, installed on the outside of the window, (3) an error microphone, placed at the opening of the tilted window, and (4) a commercial controller that drives the control source to minimise the pressure at the error microphone. Pàimes et. al. concluded that the complex geometry of the tilt window coupled with the poor coherence between the error and reference signals resulted in limited attenuation of the ANC system (3 dB IL).

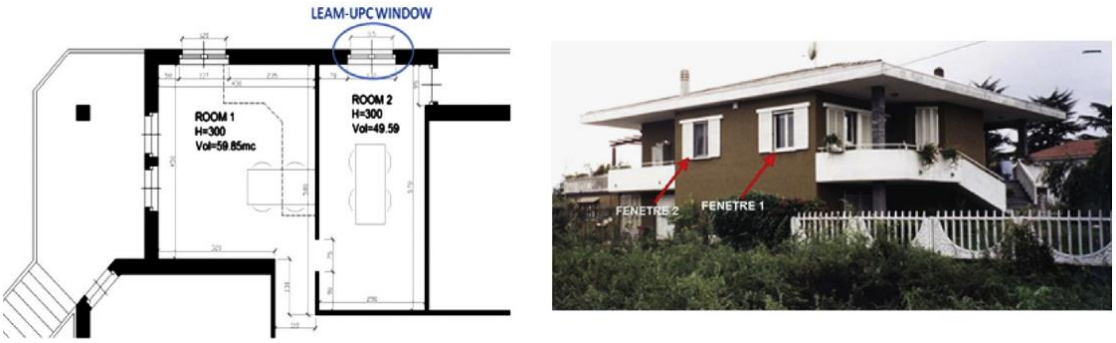

(a)

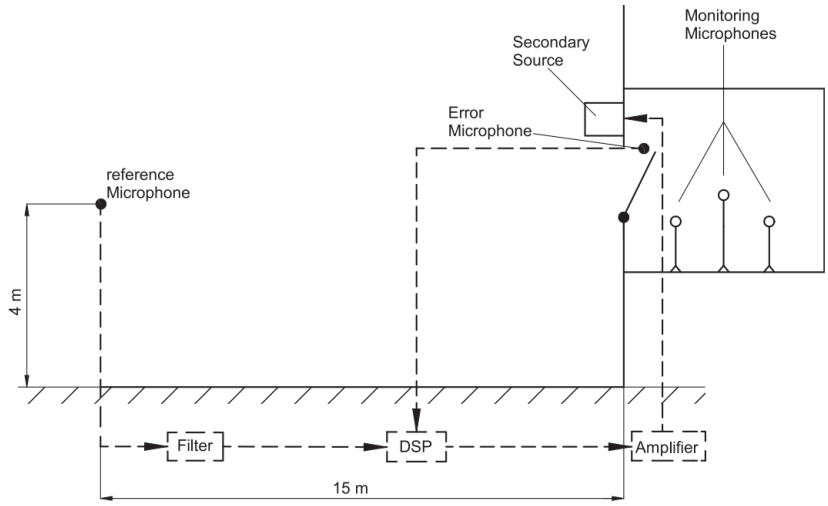

(b)

Figure 2.3: (a) Floor plan and image showing the site where the active control system is installed, and the (b) schematic of the ANC system in a cross-sectional view [Pàmies et al., 2014b].

To tackle the complex geometry of the Hopper-style tilt window, Hanselka et. al. investigated different sensor and actuator arrangements for effective control. From the myriad of sensor and actuator positions experimented, it was determined that the orientation of the speakers was less critical than the arrangement of the error sensors. Moreover, Hanselka et. al. concluded that the density of error sensors was crucial to the successful attention of high frequencies. The best performance achieved was

approximately 12 dB (100 – 1000 Hz) in the room interior when 8 control sources are placed perpendicular to the opening of the window in the room interior.

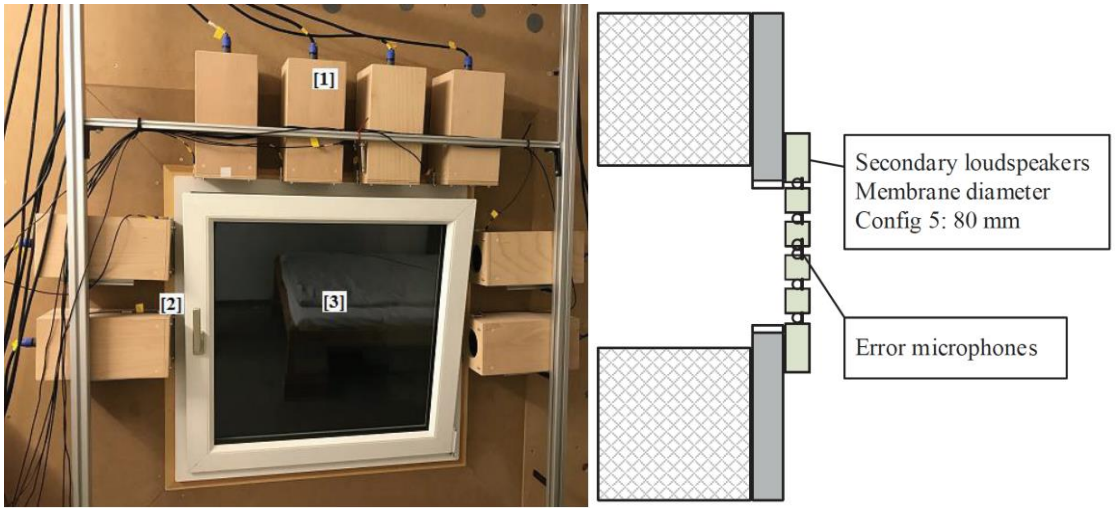

(a) (b)

Figure 2.4: (a) Image of the hopper-style tilt window installed with 8 active noise control sources [Eder et al., 2017], and (b) the cross-section representation of the ANC system [Hanselka et al., 2016].

2.2.1.3. **Sliding Windows**

The rising demand for noise mitigation solutions that maintain natural ventilation has begun to attract commercial interest. A commercial company, TechnoFirst, has developed a prototype ANC system for regular sliding windows [Carme et al., 2016a]. The column of control sources is flushed to one vertical edge of the window frame, with loudspeaker mounted perpendicularly to the opening. From the results presented, the active control system reduced 12 dB of noise in the frequency range of 100 – 300 Hz. As the window is designed for the French market, where the law mandates that the

maximum window gap is 13 cm for child safety, the maximum opening of the sliding window is 13 cm × 75 cm (975 cm^2).

(a) (b)

Figure 2.5: (a) Active control units in a sliding window configuration, and (b) a cross-sectional view of the system [Carme et al., 2016b, 2016a].

2.2.1.4. **The Aperture of the Baffled Rectangular Cavity**

In a different use case, but nevertheless important, Wang et. al. conducted a follow-up investigation to determine the performance limits of an ANC system, where control sources are distributed around the edges of the opening of a baffled rectangular cavity [Wang et al., 2017c]. In simulations, with the number of sources fixed at 36 for a 100 × 120 cm aperture, the upper limit of control for the boundary layout was limited to 300 Hz, whereas it was beyond 1000 Hz when the sources as distributed evenly over the entire aperture.

To further improve the performance of the boundary layout, Wang et. al. proposed a double layer configuration, where two layers of boundary sources are stacked in a parallel fashion relative to the plane of the opening 0.432 m × 0.670 m wide [Wang et al., 2017a, 2017b]. In an experiment investigation, the upper frequency limit of

attenuation using the double layer configuration is more than twice that of the single layer, with the number of sources kept constant. Wang et. al. also concluded that the upper frequency limit of both the single and double layer boundary layout is determined by the size of the aperture, whilst noting that increasing the number of sources has limited effect beyond a certain threshold [Wang et al., 2018]. Nevertheless, the noise reduction upper limit of the double layer boundary layout was determined to be inferior to the distributed layout, but sufficient for low frequencies.

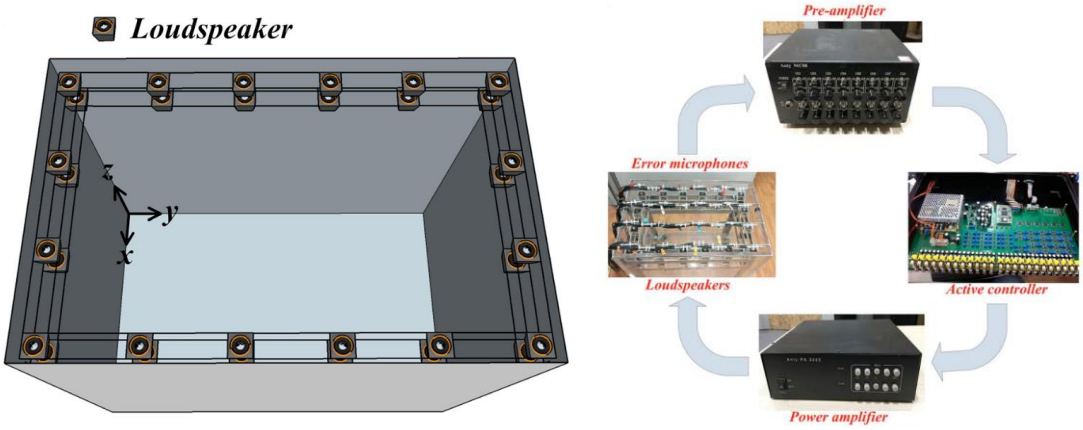

(a) (b)

Figure 2.6: (a) 3D model of the double-layered active control system layout around the boundary of the large duct with a rectangular baffle. (b) The schematic diagram showing the components in the active noise control system [Wang et al., 2017a].

2.2.2. Distributed Layout

Ise investigated the performance of 16 independent actuator-transducer (i.e. loudspeaker and error microphone) pairs distributed evenly around an open aperture [Ise, 2005], as shown in Figure 2.7. Based on the boundary surface control principle, each speaker and microphone pair are driven independently reduce the sound pressure at a single

microphone located directed in front of each control source. This “decentralised” control strategy is more computationally efficient but are less effective for moving and multiple noise sources [Murao et al., 2017]. Although an average of 10 dB of reduction was achieved at error sensors in the frequency range of 200 – 700 Hz, the reduction performance inside the room and the performance of the system in noise from different incidences were not reported.

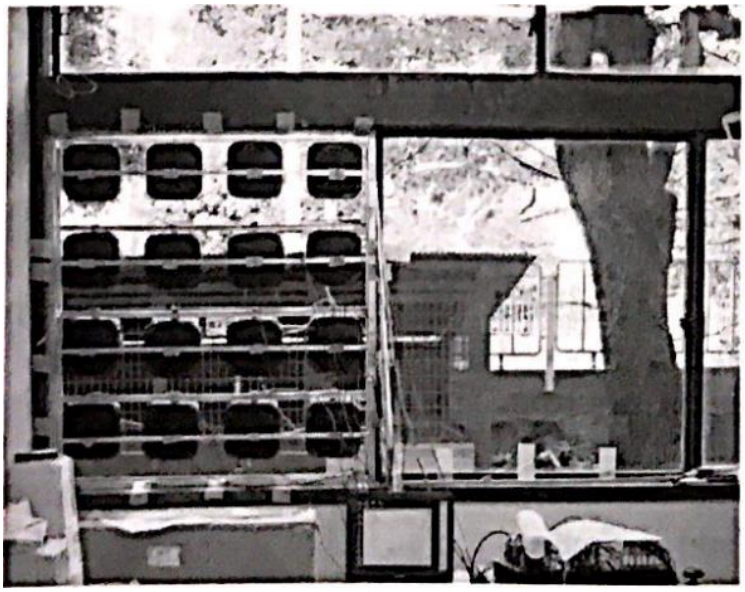

Figure 2.7: ANC window with 16 loudspeakers distributed evenly across the entire window opening [Ise, 2005].

The feasibility of attenuating noise through an aperture by an array of control sources distributed evenly in an aperture was demonstrated by Nishimura et al. in a test box, as shown in Figure 2.8 [Nishimura et al., 2008]. Based on free-field simulations, Nishimura et al. determined the wavelength of the upper-frequency limit of control to be greater than two times the separation distance between the sources, when the angle

of incidence is less than 60º. The error microphone should also be at least as far as the separation distance between the sources away from the array to achieve good control.

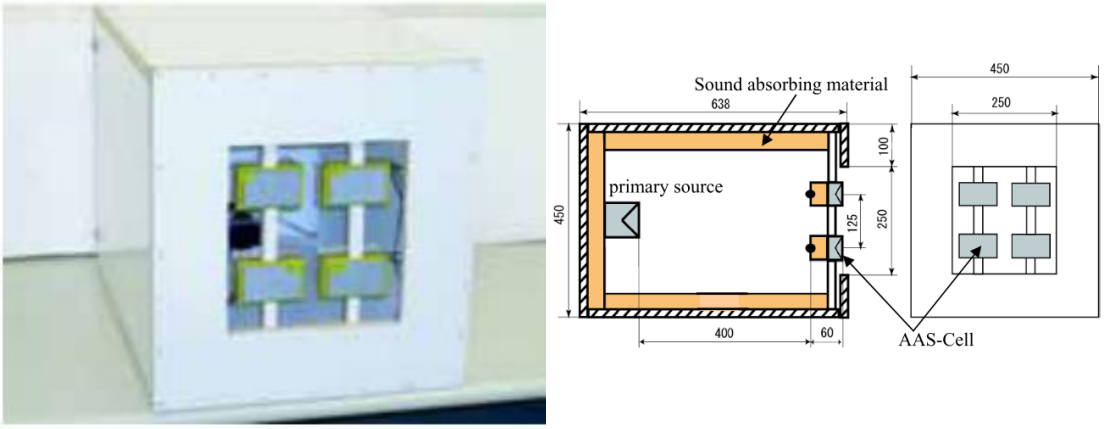

(a) (b)

Figure 2.8: (a) Image of the control units in the aperture of the test box, and (b) a schematic cross-section of the test box.

In further work, the four-channel system was implemented on an aperture with the same dimensions as the test box (i.e. 25 × 25 cm^2) but now on a wooden door fitted to the entrance of an anechoic chamber, as shown in Figure 2.9 [Murao and Nishimura, 2012]. The band-limited primary noise source (500 – 1200 Hz) was reduced by 10 – 15 dB when the noise incidence angle is 0º. Using the same filter trained with the band-limited white noise (BLWN) at 0º, a similar reduction was achieved in the range of 500 – 1500 Hz when the noise is at 30º. Although the noise incidence angle plays an important role in deciding the upper limit of control, no formal relationship was established.

Since the lower limit of control is determined by the control source characteristics, flat speakers used by Murao and Nishimura may not be suitable candidates for low-frequency noise reduction [Fasciani et al., 2015]. In the proposed system, the distance

between the reference sensor and the control source was carefully balanced as it determines both the causality and noise reduction performance of oblique incidences. A shorter distance improves the oblique incidence performances but worsens the causality problem of the ANC system.

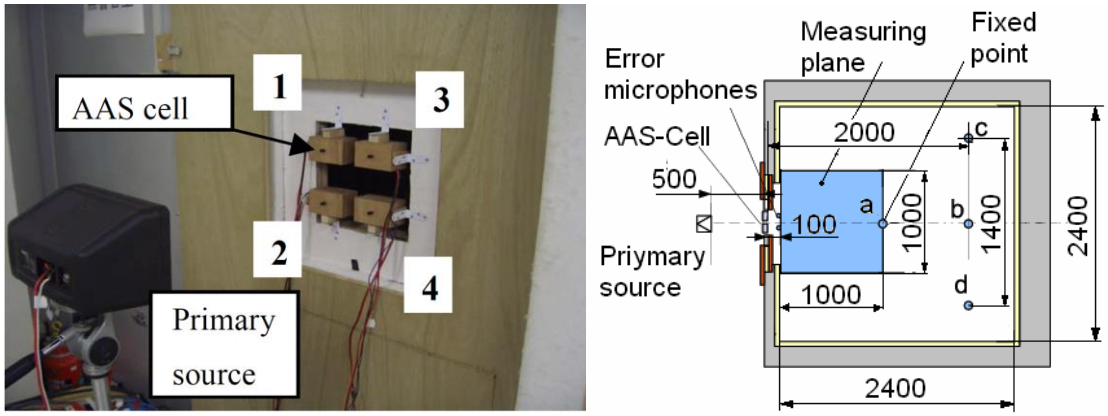

(a) (b)

Figure 2.9: (a) Image of the four control units installed in an open aperture on the door to an anechoic chamber, and (b) the cross-sectional schematic of the active control system [Murao and Nishimura, 2012].

Recent developments on the distributed layout originated from a different use case, as highlighted in the previous sub-section 2.2.1.4. Wang et al. and Tao et al. investigated the noise attenuation performance of the proposed planar virtual sound barrier at the aperture of a baffled rectangular cavity, as shown in Figure 2.10 [Tao et al., 2016; Wang et al., 2015, 2017c]. Although it has been shown that with a fixed aperture size, increasing the number of sources improves the upper-frequency limit of control, no formal relationship has been established between a number of sources (separation distance) and the wavelength of the disturbance to be cancelled. Since Wang et. el. has

conducted a number of experiments, the most relevant ones have been summarised in Table 2.1, along with all the prior work introduced in this section.

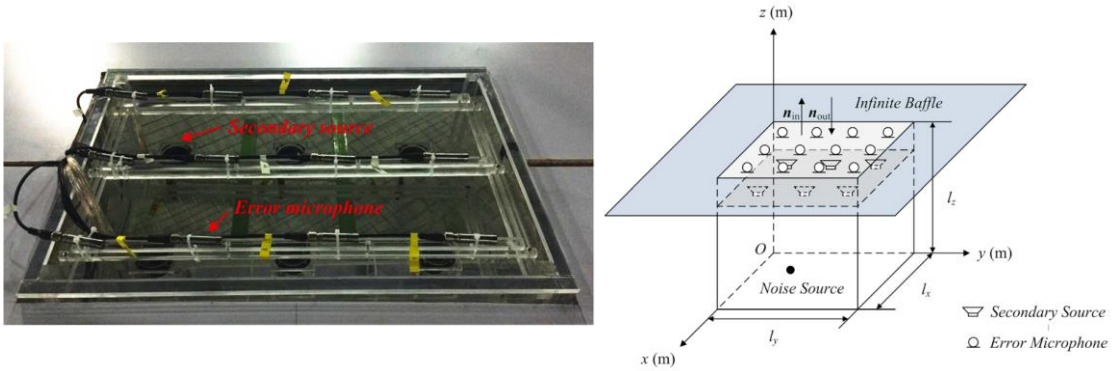

(a) (b)

Figure 2.10: (a) Image of the planar virtual barrier system, and (b) its 3D schematic [Wang et al., 2015].

2.2.3. Observations and Research Gaps

Of all the studies presented, unfortunately, none has determined the fundamental limits of active control with respect to attenuating noise through an aperture into the interior of a room. However, important observations should be analysed and taken into consideration when designing a practical ANC system for apertures. These observations have been summarised in Table 2.2, and classified into two dominant domains of an ANC system, the physical domain and the electronic domain.

Based on the summary of important observations in Table 2.1, and from the performance of the different control source layouts in Table 2.2, one can deduce that the distributed layout has higher scalability and noise control performance than the boundary layout.

Table 2.1: Summary of experimental investigations of active noise control for apertures.

Author	Layout	Type	Window Dimensions (W×H cm)	Opening Size	No. of Control Sources	Type of Noise	Reduction (Global/ Local)
Window							
Ise 2005	Boundary	Open Aperture	Not Stated	Not Stated	16	0.2 to 0.7 kHz	10 dB (Error Microphone)
Murao 2012 [Murao and Nishimura, 2012]	Distributed	Open Aperture	25 x 25	25 x 25	4	BLWN (0.5 to 2kHz)	10-15 dB (Global)
Kwon 2013 [Kwon and Park, 2013]	Boundary	Open Aperture	30 x 30	30 x 30	8	BLWN (0.4 to 1 kHz)	Up to 10 dB (Global)
Paimes 2014 [Pàmies et al., 2014b]	Boundary	Tilt Window (Hopper)	56 x 142	5cm Gap 2° Tilt	Not stated	Real aircraft pass-by (0.2 to 0.16 kHz)	3 dB (Global)
Carme 2016 [Carme et al., 2016b]	Boundary	Sliding Window	75 x 75	13 x 75	5	Traffic Noise (<300 Hz)	15.5 dB (Not Stated)
Hanselka 2016 [Eder et al., 2017; Hanselka et al., 2016]	Boundary	Tilt Window (Hopper)	91 x 91	Not stated	8	BLWN (0.1 to 1 kHz)	13 dB (Local)
The opening of the baffled rectangular cavity							
Wang 2015, 2016 [Tao et al., 2016; Wang et al., 2015]	Distributed	Open Aperture	-	43 x 67	6	BLWN (<0.5 kHz)	~15 dB (Global)
Wang 2017 [Wang et al., 2017a]	Boundary	Open Aperture	-	43 x 67	8	BLWN (<1 kHz)	10 dB (Local, 0.2 m around error points)
Wang 2017 [Wang et al., 2017a]	Boundary	Open Aperture	-	43 x 67	32	Tonal (<1 kHz)	~20dB (Global)
Wang 2017 [Wang et al., 2017a]	Distributed	Open Aperture	-	43 x 67	32	Tonal (<1 kHz)	~20dB (Global)

Table 2.2: Summary of important observations in designing a practical ANC system for apertures

Physical Domain	Electronic Domain
• Attenuation performance is sensitive to the deviations in positions relative to the aperture [Emms, 2000]	• Good coherence between the error and reference signals improves attenuation performance [Pàmies et al., 2014b]
• The acoustic effect of big loudspeakers blocking the sound propagation path needs to be taken into account [Hanselka et al., 2016]	• Sufficient error microphones are crucial to increasing the upper limit of control performance [Hanselka et al., 2016]
• The upper-frequency limit of control for the boundary layout is determined by the aperture size rather than the number of sources [Wang et al., 2017b]	• The lower frequency limit of control is determined by the response of the actuators [Murao and Nishimura, 2012]
• The separation distance between the control sources in the distributed layout determines the upper-frequency limit of control [Murao and Nishimura, 2012; Nishimura et al., 2008]	• A shorter distance between the reference sensor and the control source improves attenuation performance for oblique incidences but may result in causality issues [Murao and Nishimura, 2012]

Since understanding the physical geometries are extremely important to achieve good control [Warnaka, 1982], and it should be the first step in practical ANC system design [Elliott, 2001; Hansen et al., 2012], this thesis will address the gaps in the physical limits of active control for apertures, with a focus on distributed layout, as follows:

- Does diffraction through the aperture affect active control performance?
- What is the quantified effect of separation distance and angle of noise incidence on active control performance?
- How does the active control system compare with the performance of a fully-glazed window?
- What is the feasibility of implementing the active control system on a partially opened aperture (i.e. sliding window), as compared to full-glazing?

Chapter 3

Numerical Modelling of Sound Fields through Open Apertures for Active Control

Since every control problem has its unique set of challenges, it is imperative to develop simple analytical models of the physical active control system to assess the proposed control strategies in terms of its fundamental physical limitations [Elliott, 2001]. Although analytical solutions have been developed for characterising active control strategies for an aperture with an infinite rectangular baffle, there are still no established solutions developed for apertures in a wall with finite thickness due to the complex nature of the sound field at higher frequencies [Rdzanek, 2018; Sieck, 2013].

In light of the situation, a numerical approach based on the equivalent source method (ESM) is proposed. Firstly, a 1D ESM model is demonstrated in an infinite duct before the extension to a 2D scenario to model a rigid wall with finite thickness. Despite previous work demonstrating the accuracy of ESM and the employment of regularisation methods in the proposed model, the ESM method did not achieve sufficient accuracy for the geometrical requirements of this study.

Hence, a simulation model based on the finite element method was developed. The parameters and perfectly matched layer (PML) used in the FEM method was firstly

validated with analytical solutions in a free field condition. Subsequently, the size of the computation plane was investigated to achieve an optimal size for time efficiency.

3.1. The Physical Basis for Active Control

In every active noise control application, there are numerous design decisions involved. Since each successful application of active noise control is characterised by its own unique set of optimum decisions, Hansen et. al. proposed a systematic, hierarchical approach to the optimisation process, as shown in Figure 3.1 [Hansen et al., 2012]. As illustrated, the maximum noise reduction in an ideal scenario is determined by the physical arrangements of the controls sources, which indirectly accounts for acoustical effects due to the geometries of the control zone. This is congruent with the first stage of active control system design suggested by Elliott, where the physical system should be analysed with analytical models of simplified arrangements [Elliott, 2001].

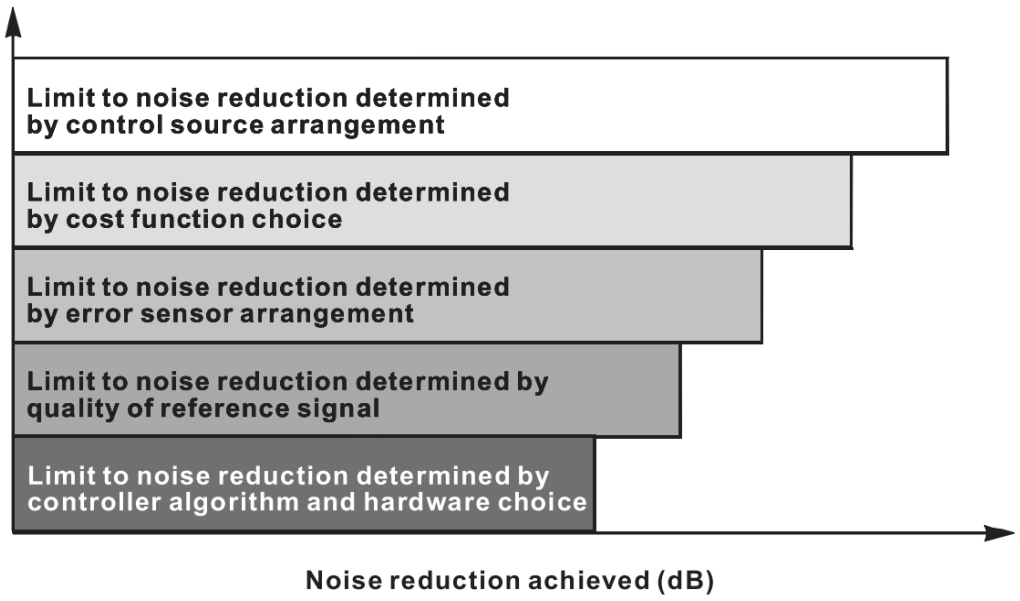

Figure 3.1: The hierarchy of a practical active noise control system design by Hansen et. al. [Hansen et al., 2012].

Unfortunately, active noise control strategies developed to mitigate noise propagating into the interior through open apertures have not taken such physical factors into consideration. Moreover, the analytical model developed for a baffled rectangular cavity has been derived based on duct acoustics and does not directly apply to this scenario [Wang et al., 2015].

It is common practice to represent a window with a simplified geometry to analyse its acoustic field. The most common geometries adopted to investigate active control of sound transmission through apertures are: (1) square apertures in a rigid, infinitesimally thin wall [Emms, 2000; Magnusson et al., 2014], and (2) rectangular apertures in a thin wall [Pàmies et al., 2011, 2014b] and a wall with finite thickness [Sieck, 2013], backed by a cavity. However, the analytical solutions developed are still limited by their uncertainties at low frequencies [Magnusson et al., 2014], validated only for low frequencies [Sieck, 2013], and concerned with the modal effects of the attached cavity [Pàmies et al., 2011, 2014a; Sieck, 2013].

To avoid uncertainties at low frequencies, and to obtain a fairly accurate solution that spans a wide frequency range for arbitrary incidences, Emms relied on numerical methods based on the boundary element method (BEM) [Emms, 2000]. However, care must be taken when implementing BEM for higher frequencies as the non-uniqueness problem arises [Crocker, 2007; Emms, 2000]. Furthermore, the error in the sound field increases as the sampling points get nearer to the surface, impeding the analysis of diffraction through observation of the normal velocities near the wall edges.

This chapter will first discuss various simulation methods proposed by past studies and in other active control problems, before arriving at a method used in this thesis.

3.2. Equivalent Source Method

Numerical modelling techniques have been widely used to solve radiation and scattering problems and are able to provide a visual analysis of a complex sound field. These techniques such as the finite element (FE) method, boundary element method (BEM), and increasingly, the wave superposition or equivalent source method (ESM), each have their own merits depending on the type of boundary conditions specified.

Since BEM has an inherent singularity problem when solving boundary integral equations on the surface, and non-uniqueness in the solutions at certain wavenumbers [Emms, 2000; Fairweather et al., 2003; Johnson et al., 1998; Leblanc et al., 2010; Lee, 2017], alternative solutions such as the equivalent source method (ESM) has been proposed.

The ESM has been widely adopted by engineers to model complex sound fields of large arbitrarily shaped objects (e.g. aircraft bodies and engines) in significantly less time than BEM. The faster computation time is attributed to the meshless nature of ESM and requirement of fairly few sources to reconstruct a scattered field to satisfactory accuracy.

Originally called the wave superposition method [Fahnline and Koopmann, 1991; Koopmann et al., 1989; Leblanc et al., 2010; Song et al., 1991] by Koopmann et al, ESM possesses unique merits over BEM. Key advantages include: (1) increased computational efficiency over BEM and FEM [Johnson et al., 1998], (2) Non-uniqueness and singularities are avoided as equivalent sources are placed a distance away from the boundary instead of on the boundary in BEM.

The principles of the wave superposition method has also been studied in literature as the method of fundamental solutions [Fairweather et al., 2003], and more commonly,

the equivalent source method (ESM) [Bai et al., 2011; Bi et al., 2008; Bi and Stuart Bolton, 2012; Gounot et al., 2005; Gounot and Musafir, 2007, 2011; Holste, 1997; Johnson et al., 1998; Lee et al., 2011; Lee, 2017; Lee et al., 2010; Piscoya et al., 2008; Valdivia and Williams, 2006]. Applications of the ESM has expanded to areas in near-field acoustic holography [Bai et al., 2011; Bi et al., 2008; Valdivia and Williams, 2006], aeroacoustics [Holste, 1997; Lee et al., 2010, 2011], and acoustic scattering in general [Fairweather et al., 2003; Gounot et al., 2005; Gounot and Musafir, 2007, 2011; Johnson et al., 1998].

ESM replaces the radiator with an array of virtual point sources (within the radiator) that emulate the normal particle velocity distribution on the boundary according to the required radiation conditions. Similarly, acoustic scattering is simulated by replacing a scattering object with an array of point sources. Equivalent sources are excited relative to the incident field at the boundary to achieve the desired condition (e.g. rigid wall).

3.3. Equivalent Source Method in 1D Infinite Duct

In the one-dimensional perspective, the equivalent source method (ESM) can be developed from the classical plane monopole/dipole combination for unidirectional radiation in an infinite duct [Nelson and Elliott, 1992]. A harmonic plane monopole source q (at $x = 0$) in an infinite duct, produces an upstream pressure (p^+) and associated particle velocity (u^+) fields in the positive x-direction. Simultaneously, q generates downstream pressure (p^-) and particle velocity (u^-) fields in the negative x-direction. Both upstream and downstream fields are illustrated in Figure 3.2. Downstream fields are formulated in terms of the negative x-direction and are given by

$$p^-(x) = \rho_0 c_0 u(x) e^{jkx}, \quad x < 0, \tag{3.1}$$

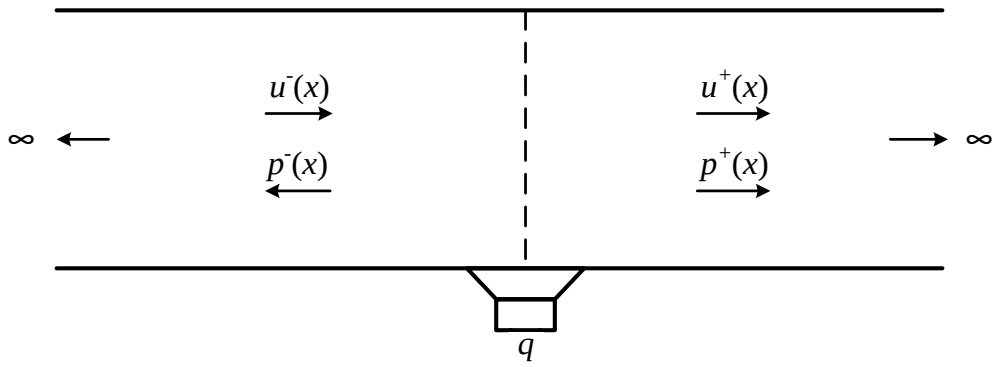

Figure 3.2: Upstream and downstream representations of particle velocity and pressure of a plane monopole harmonic source in an infinite duct.

$$u^{-}(x) = -u(x)e^{jkx}, \quad x < 0, \tag{3.2}$$

where ρ_0 is the density (1.204 kg/m^3 in air at 20°C) and c_0 is the speed of sound (343.3 m/s in dry air at 20°C). Similarly, the upstream pressure and particle velocity fields in the positive *x*-direction are given by

$$p^{+}(x) = \rho_0 c_0 u(x)e^{-jkx}, \quad x < 0, \tag{3.3}$$

$$u^{+}(x) = u(x)e^{-jkx}, \quad x < 0. \tag{3.4}$$

To simulate acoustic reflection off a rigid surface (normal particle velocity = zero), the upstream pressure at the boundary should be higher (~twice) than the incident pressure and there should be zero downstream pressure. The rigid boundary effect proposed, is essentially similar to the unidirectional radiation case by Nelson and Elliott, in the reversed direction [Nelson and Elliott, 1992]. Building from the single monopole, a pair of monopoles q_1 and q_2 are placed in an infinite duct, a distance d apart in an incident field generated by q_p, as shown in Figure 3.3. Assuming that the phase of the incident wave is normalised with the position of q_1, we can examine the conditions of

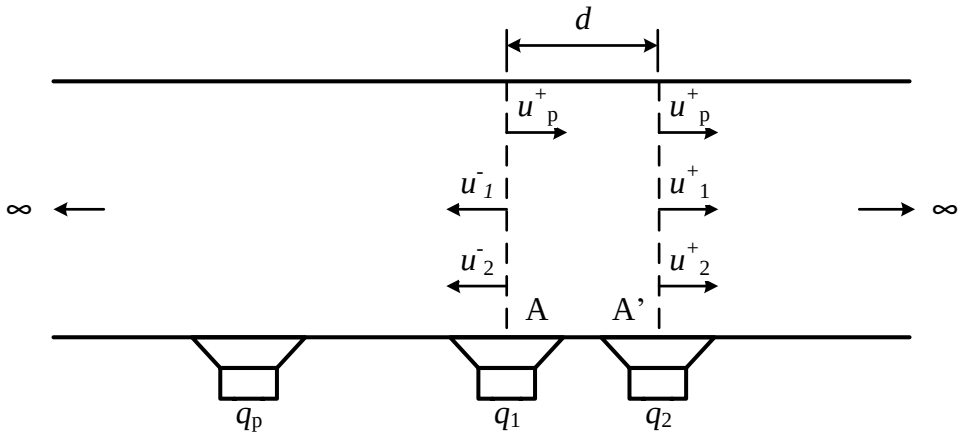

Figure 3.3: Three harmonic plane monopole sources: (1) primary source, q_p, (2) pair of sources, q_1 and q_2, located at boundary A and A', and separated by distance d in an infinite duct.

distance d with a rigid boundary condition. The particle velocity field at the boundary A, can be expressed as

$$u_A(x) = u_p(x) - u_1(x) - u_2(x)e^{-jkd}, \tag{3.5}$$

and the particle velocity field at the boundary A' can be expressed as

$$u_B(x) = u_p(x)e^{-jkd} + u_1(x)e^{-jkd} + u_2(x). \tag{3.6}$$

Equations (3.5) and (3.6) can be represented in the matrix form as

$$\begin{bmatrix} u_A \\ u_{A'} \end{bmatrix} = \begin{bmatrix} 1 \\ e^{-jkd} \end{bmatrix} u_p + \begin{bmatrix} -1 & -e^{-jkd} \\ e^{-jkd} & 1 \end{bmatrix} \begin{bmatrix} u_1 \\ u_2 \end{bmatrix}, \tag{3.7}$$

and further simplified to

$$\mathbf{u}_T = \mathbf{u}_p + \mathbf{T}\mathbf{u}. \tag{3.8}$$

Under rigid boundary conditions, $\mathbf{u}_T = 0$, yielding the expression

$$\mathbf{u} = -\mathbf{T}^{-1}\mathbf{u}_p. \tag{3.9}$$

Evaluating (3.9) gives

$$u_1 = -\frac{1+e^{-jkd}}{1-e^{-jkd}}u_p = -\frac{j\cos(kd)}{\sin(kd)}u_p, \tag{3.10}$$

$$u_2 = \frac{2e^{-jkd}}{1-e^{-jkd}}u_p = \frac{j}{\sin(kd)}u_p. \tag{3.11}$$

If d is small compared to the wavelength, or $kd \ll 1$, the dipole condition (anti-symmetric radiation) is achieved, as shown below

$$\frac{u_1}{u_p} = -\frac{j}{kd}, \quad \frac{u_2}{u_p} = \frac{j}{kd} \Rightarrow u_1 = -u_2, \quad kd \ll 1, \tag{3.12}$$

3.3.1. Dipole Equivalent Sources Within an Arbitrarily Placed Boundary in a 1D Infinite Duct

Since the principle of the equivalent source method is to replace a rigid body with a small set of equivalent sources, sources are usually located within the body and not on the boundaries. With the example of a dipole located in an incident field of an infinite duct, within two boundaries as shown in Figure 3.4, the ESM is first verified in this 1D scenario.

The boundary conditions are expressed in terms of particle velocity contributions from the incident field and the dipoles and are given by

$$u_D = u_p^+(D) + u_1^-(D) + u_2^-(D), \quad x = D, \tag{3.13}$$

$$u_F = u_p^+(F) + u_1^+(F) + u_2^+(F), \quad x = F, \tag{3.14}$$

And expressed in similar matrix form to (3.7) as

$$\begin{bmatrix} u_D \\ u_F \end{bmatrix} = \frac{1}{2S_{duct}} \begin{bmatrix} e^{-jkD} \\ e^{-jkF} \end{bmatrix} q_p + \frac{1}{2S_{duct}} \begin{bmatrix} -e^{jk(D-x_{q_1})} & -e^{jk(D-x_{q_2})} \\ e^{-jk(F-x_{q_1})} & e^{-jk(F-x_{q_2})} \end{bmatrix} \begin{bmatrix} q_1 \\ q_2 \end{bmatrix}, \quad (3.15)$$

where u_D is the total particle velocity at the boundary D, u_F is the total particle velocity at boundary *F*, and S_{duct} is the cross-sectional area of the duct. If $u_D = 0$ and $u_F = 0,$ (3.15) can be expressed in similar form to (3.9) as

$$\begin{bmatrix} q_1 \\ q_2 \end{bmatrix} = -\begin{bmatrix} -e^{jk(D-x_{q_1})} & -e^{jk(D-x_{q_2})} \\ e^{-jk(F-x_{q_1})} & e^{-jk(F-x_{q_2})} \end{bmatrix} \begin{bmatrix} e^{-jkD} \\ e^{-jkF} \end{bmatrix} q_p. \quad (3.16)$$

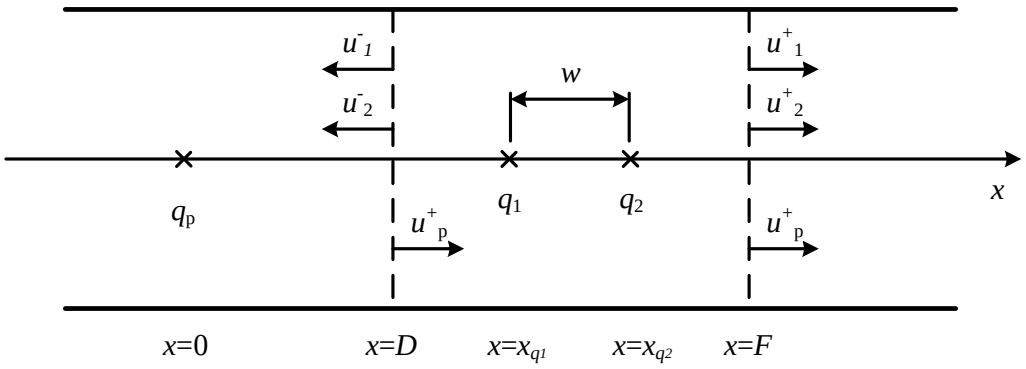

Figure 3.4: Dipole equivalent sources at q_1 and q_2 in an incident field generated by q_p, bounded by rigid boundaries at D and F in an infinite duct.

3.3.2. Numerical Simulations of 1D Case

A primary point source is located at $x = 0$ with $|A|$ fixed at 90 dB (ref $20\,\mu$Pa). The boundary D is set at 1 m and F is set at 1.09 m. The dipole separation distance w is fixed at 0.03 m with $x_{q_2} = x_{q_1} + w = 1.06\,\text{m}.$

Based on (3.16), the dipole source strengths and the total pressure distribution from the primary and dipole sources for were calculated for increasing wavelength. For the

test cases of 1 kHz, 500 Hz and 300 Hz, the downstream pressures were reduced to zero and the upstream pressure was approximated twice the amplitude of the primary wave. The total pressure and normalised velocity distributions; and the primary source pressure are shown in Figure 3.5, Figure 3.6 and Figure 3.7 for the 1 kHz, 500 Hz, and 300 Hz test cases, respectively.

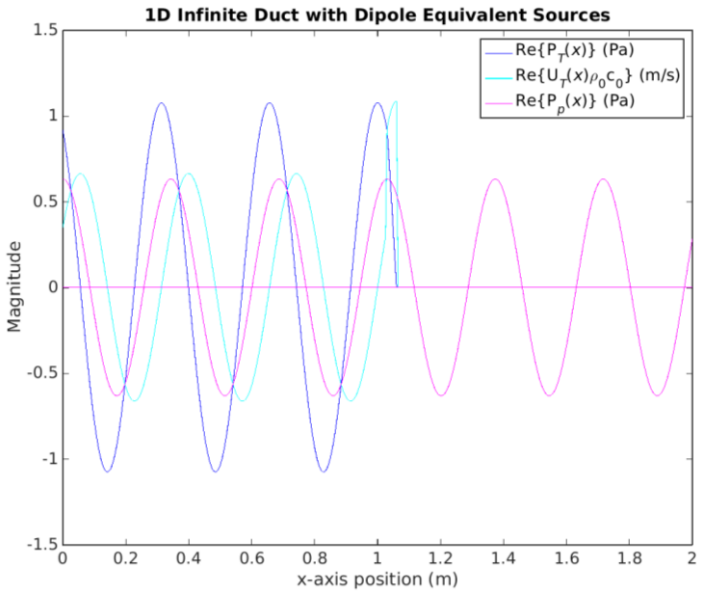

Figure 3.5: Total pressure and normalised velocity due to dipoles and primary source, $p_T(x)$ and $u_T(x)$; and pressure due to primary source only, $p_p(x)$, at 1 kHz.

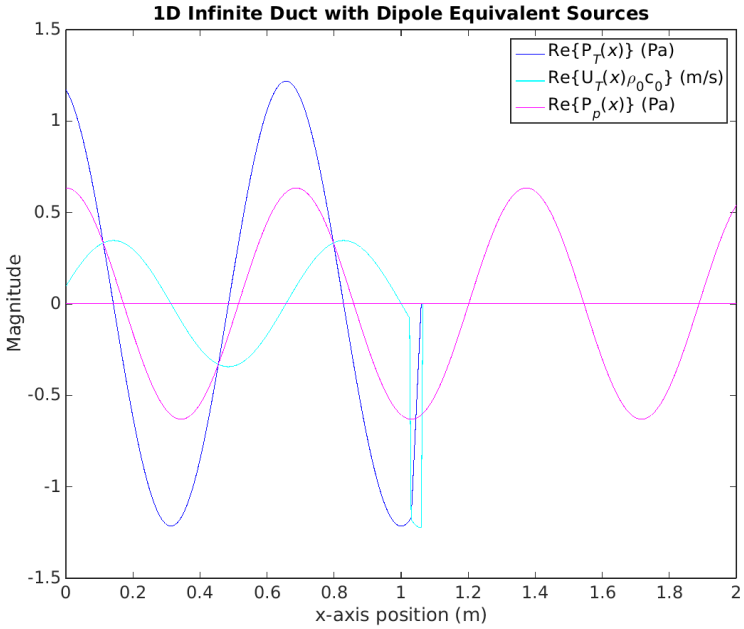

Figure 3.6: Total pressure and normalised velocity due to dipoles and primary source, $p_T(x)$ and $u_T(x)$; and pressure due to primary source only, $p_p(x)$, at 500 Hz.

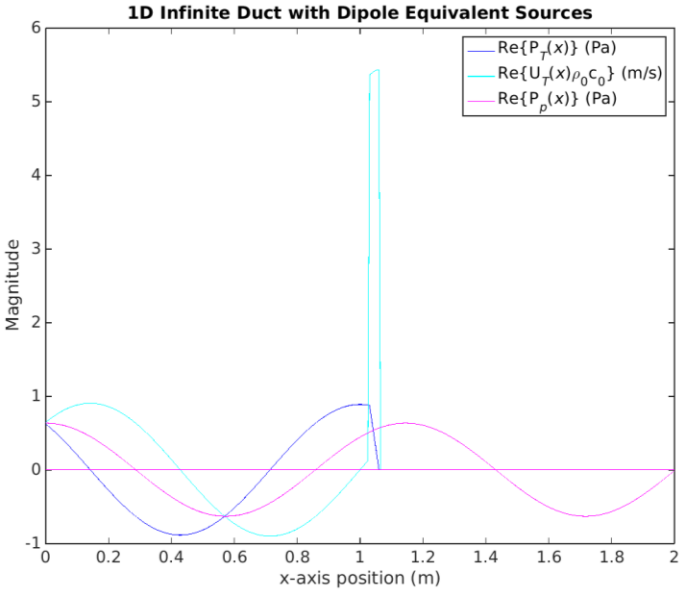

Figure 3.7: Total pressure and normalised velocity due to dipoles and primary source, $p_T(x)$ and $u_T(x)$; and pressure due to primary source only, $p_p(x)$, at 300 Hz.

3.4. Equivalent Source Method in 2D Infinite Wall

Modelling of the acoustic scattering through an aperture in a wall with finite thickness can be built upon a model of a perfectly reflecting rigid wall that is infinitely long with a finite thickness. The infinite rigid wall is formulated through the extension of the dipole sources in the 1D case to form a array of dipole sources.

3.4.1. Theory

The 1D equivalent source formulation is extended to model a 2D rigid wall based on free-field acoustic equations. The 2D formulation is regularised to prevent ill-conditioning during matrix inversion and evaluation criterion is devised to analyse the performance of the equivalent source method.

3.4.1.1. Free-field Acoustic Equations

The complex free-field pressure equation for a diverging spherical wave is given by [Nelson and Elliott, 1992]

$$p(r) = \frac{Ae^{-jkr}}{r}, \tag{3.17}$$

where A is proportional to the source strength, and its corresponding complex velocity equation as

$$u(r) = \frac{A}{j\omega\rho_0}\left(\frac{jk}{r} + \frac{1}{r^2}\right)e^{-jkr}, \tag{3.18}$$

where r is the distance from the source to the location at which it is evaluated.

A point source can also be expressed with respect to its volume velocity for complex pressure as

$$p(r) = \frac{j\omega\rho_0 q e^{-jkr}}{4\pi r}, \tag{3.19}$$

and complex velocity as

$$u(r) = \frac{q}{4\pi}\left(\frac{jk}{r} + \frac{1}{r^2}\right)e^{-jkr}, \tag{3.20}$$

where q is the complex volume velocity and $A = j\omega\rho_0 q/4\pi$.

3.4.1.2. **Matrix Formulation of Equivalent Source Method for a 2D Wall**

The complex normal velocity field $\mathbf{u}_T$ on a boundary, can be evaluated by summing the contributions of the primary disturbance and the internal equivalent sources at evaluations points on the boundary, depicted in Figure 3.8. $\mathbf{u}_T$ is a complex vector that can be expressed in matrix form as

$$\mathbf{u}_T = \mathbf{u}_p + \mathbf{u}_{int}, \tag{3.21}$$

where $\mathbf{u}_p$ is an $N \times 1$ complex vector of boundary velocities due to a primary source of amplitude A is given by

$$\mathbf{u}_p = \left[\frac{A}{j\omega\rho_0}\left(\frac{jk}{r_{p,1}} + \frac{1}{r_{p,1}^2}\right)e^{-jkr_{p,1}}cos\theta_{p,1} \cdots \frac{A}{j\omega\rho_0}\left(\frac{jk}{r_{p,N}} + \frac{1}{r_{p,N}^2}\right)e^{-jkr_{p,N}}cos\theta_{p,N}\right]^{\mathrm{T}}, \tag{3.22}$$

where $r_{p,n}$ represents the distance from the primary source location to the n-th evaluation point of which there are N and $\theta_{p,n}$ is the angle formed between the primary source and the n-th evaluation point, as illustrated in Figure 3.8. The normal velocity

contribution from the M internal equivalent sources at the evaluation points $\mathbf{u}_{int}$, is expressed with a $N \times M$ transform matrix, $\mathbf{T}_e$, as

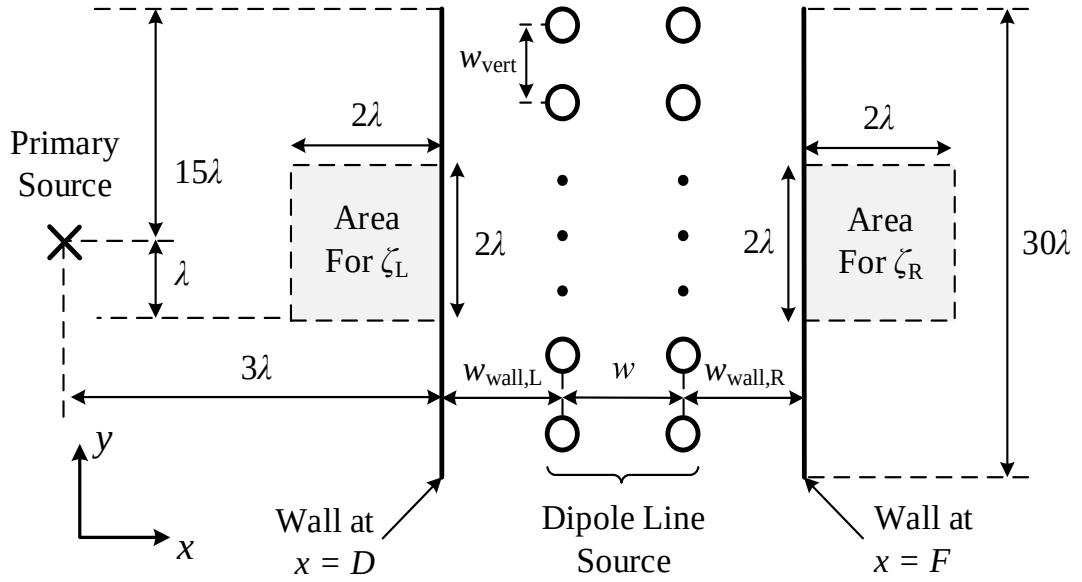

Figure 3.8: The cross section of a 30λ m long wall with a thickness of $(w_{wall,L} + w + w_{wall,R})$ m; with the left and right boundaries at $x = D$ m and $x = F$ m, respectively; and its rigid conditions at the boundaries driven by the internal equivalent dipole line sources. The primary source is 3λ m away from boundary at $x = D$. The $2\lambda \times 2\lambda$ m^2 evaluation zones for the calculation of ζ_L and ζ_R are demarcated by the shaded grey regions. [Lam et al., 2015a].

$$\mathbf{u}_{int} = \mathbf{T}_e \mathbf{q}_{int} \tag{3.23}$$

where $\mathbf{q}_{int} = [q_1 \ldots q_M]^{\mathrm{T}}$ is an $M \times 1$ complex vector of internal volume velocities. The transform matrix $\mathbf{T}_e$ takes into account the reverse direction (normal primary velocity on the boundary) to emulate a rigid wall $(\mathbf{u}_T = 0)$ condition for perfect reflection of the wave at $x = D$ for a primary source located at $(0, 0)$, and is expressed as

$$\mathbf{T}_e = \frac{1}{4\pi}\begin{bmatrix} -\left(\frac{jk}{r_{1,1}}+\frac{1}{r_{1,1}^2}\right)e^{-jkr_{1,1}}\cos\theta_{1,1} & \cdots & -\left(\frac{jk}{r_{M,1}}+\frac{1}{r_{M,1}^2}\right)e^{-jkr_{M,1}}\cos\theta_{M,1} \\ \vdots & \ddots & \vdots \\ -\left(\frac{jk}{r_{1,\frac{N}{2}}}+\frac{1}{r_{1,\frac{N}{2}}^2}\right)e^{-jkr_{1,\frac{N}{2}}}\cos\theta_{1,\frac{N}{2}} & \cdots & -\left(\frac{jk}{r_{M,\frac{N}{2}}}+\frac{1}{r_{M,\frac{N}{2}}^2}\right)e^{-jkr_{M,\frac{N}{2}}}\cos\theta_{M,\frac{N}{2}} \\ \left(\frac{jk}{r_{1,\frac{N}{2}+1}}+\frac{1}{r_{1,\frac{N}{2}+1}^2}\right)e^{-jkr_{1,\frac{N}{2}+1}}\cos\theta_{1,\frac{N}{2}+1} & \cdots & \left(\frac{jk}{r_{M,\frac{N}{2}+1}}+\frac{1}{r_{M,\frac{N}{2}+1}^2}\right)e^{-jkr_{M,\frac{N}{2}+1}}\cos\theta_{M,\frac{N}{2}+1} \\ \vdots & \ddots & \vdots \\ \left(\frac{jk}{r_{1,N}}+\frac{1}{r_{1,N}^2}\right)e^{-jkr_{1,N}}\cos\theta_{1,N} & \cdots & \left(\frac{jk}{r_{M,N}}+\frac{1}{r_{M,N}^2}\right)e^{-jkr_{M,N}}\cos\theta_{M,N} \end{bmatrix}. \quad (3.24)$$

Similar to (3.22), $r_{m,n}$ represents the distance between the m-th internal equivalent source and the n-th evaluation point on the boundary. $\theta_{m,n}$ is the angle between the m-th equivalent source and the n-th evaluation point. For values in $\mathbf{T}_e$ from 1 to $N/2$ (top half), an additional negative sign is added to indicate an inversion in direction of normal velocity on the boundary at $x = D$.

3.4.1.3. **Regularisation**

With a rigid boundary condition, and incorporating (3.23) into (3.21), the volume velocities can be evaluated by

$$\mathbf{q}_{int} = -\left(\mathbf{T}_e\right)^{-1}\mathbf{u}_p. \quad (3.25)$$

Taking into account that $\mathbf{T}_e$ is not a square matrix, a Moore-Penrose pseudoinverse form is adopted as

$$\mathbf{q}_{int} = -\left(\mathbf{T}_e^{\mathrm{H}}\mathbf{T}_e + \beta\mathbf{I}\right)^{-1}\mathbf{T}_e^{\mathrm{H}}\mathbf{u}_p, \quad (3.26)$$

where $\mathbf{I}$ is an $N \times N$ identity matrix and β is a regularisation parameter that is added to regularise [Elliott, 2001] the $\mathbf{T}_e^{\mathrm{H}}\mathbf{T}_e$ matrix to prevent it from being ill-conditioned during inversion. $^{\mathrm{H}}$ is defined as the conjugate transpose.

3.4.1.4. **Velocity Error Criterion**

A normalised velocity error criterion, E, at all evaluation points on the boundaries, is minimised based on (3.26) and is evaluated by

$$E = 10\log_{10}\left(\frac{\mathbf{u}_T^{\mathrm{H}}\mathbf{u}_T}{\mathbf{u}_p^{\mathrm{H}}\mathbf{u}_p}\right). \tag{3.27}$$

To discount the effects of inaccuracies expected at the end of the wall, another velocity error criterion, E' is defined as

$$E' = 10\log_{10}\left(\frac{\mathbf{u}_{T,2\lambda}^{\mathrm{H}}\mathbf{u}_{T,2\lambda}}{\mathbf{u}_{p,2\lambda}^{\mathrm{H}}\mathbf{u}_{p,2\lambda}}\right), \tag{3.28}$$

where $\mathbf{u}_{T,2\lambda}$ and $\mathbf{u}_{p,2\lambda}$ represent, in order, the total and primary normal velocities on the wall boundary at $x = D$ and $x = F$, bounded by the 2λ zone shown in Figure 3.8.

3.4.2. The Accuracy of the Equivalent Source Method

The accuracy of the ESM 2D simulation model is examined by comparison with the complex pressure values of an analytical solution. To determine the suitability of the ESM in the frequency range of interest, the effect of the regularisation parameter, the number of evaluation points, and the number of equivalent sources is quantified.

3.4.2.1. **Method of Evaluation**

The pressure in the $\mathbf{u}_{p,2\lambda}$ computation plane is the real part of the total pressure due to the sum of primary and equivalent sources, $p(r)$, multiplied by $e^{j\omega t}$ when t = 0, and is expressed as

$$p(r) = p_p(r) + \sum_{m=1}^{M} p_{int,m}(r), \tag{3.29}$$

where $p_p(r)$ is the pressure at radial distance r due to the primary source and $p_{int,m}(r) = j\omega q_{int,m} e^{-jkr} / 4\pi r$ is the complex pressure fluctuation at r from the m-th internal equivalent source ($m \in \mathbb{Z}^+$ from 1 to M).

3.4.2.2. **Pressure Difference Performance Criteria**

The accuracy of the equivalent source method can be evaluated by comparing the difference between the reflection pattern in an area near the rigid boundary with that calculated analytically using the image of the primary sound source. A combined sound field of the primary source and its image (located at 6λ or 2D in the positive x-direction) is set up as shown in Figure 3.9.

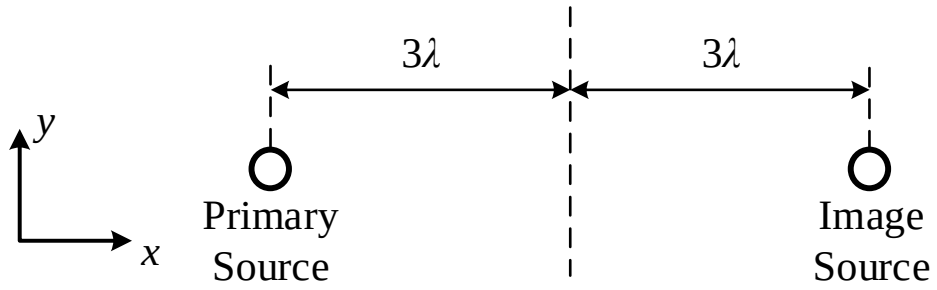

Figure 3.9: Primary source and its image.

The difference between the desired sound field due to the primary and its image source (perfect reflection) and the sound field produced by the equivalent sources method is expressed by a pressure difference index, ζ_L, over the left-hand 2λ × 2λ region shown in Figure 3.8 as

$$\zeta_L = 10\log_{10}\left(\frac{\sum_{l=1}^{i}\left|p_{image}(r_l) - p(r_l)\right|^2}{\sum_{l=1}^{i}\left|p_{image}(r_l)\right|^2}\right), \tag{3.30}$$

where *i* is the total number of points in the area as defined by the left-hand 2λ × 2λ area in Figure 3.8; r_l is the radial distance to the l-th position in the 2λ × 2λ evaluation area; $p_{image}(r_l)$ is the complex pressure calculated using the image source model at r_l; and $p(r_l)$ is the pressure due to the equivalent source model at r_l.

To evaluate the attenuation 'behind' the wall, another pressure difference index, ζ_R, is defined in relation to the sum-square pressures due to $p_{image}(r_l)$ of the left-hand 2λ × 2λ evaluation area as

$$\zeta_R = 10\log_{10}\left(\frac{\sum_{l=1}^{v}\left|p(r_l)\right|^2}{\sum_{l=1}^{i}\left|p_{image}(r_l)\right|^2}\right), \tag{3.31}$$

where *i* and *v* is the total number of points in the left-hand and the right-hand 2λ × 2λ area in Figure 3.8, respectively.

3.4.2.3. **Effect of the Number of Source and Evaluation points**

The number of equivalent sources has been known to play an important role to achieve a low boundary error [Johnson et al., 1998]. At a constant ratio of evaluation points to equivalent sources, $B = N/M = 16$, boundary error E decreases with increasing M, as shown in Figure 3.10. Although a similar trend in E is observed when N is fixed at 15938, the error becomes constant when $M \geq 600$. The difference index ζ_L, however, is not affected by the number of internal equivalent sources as depicted in Figure 3.10. Thus, a low boundary error has no indication of an accurate sound field reproduction near the boundary surface.

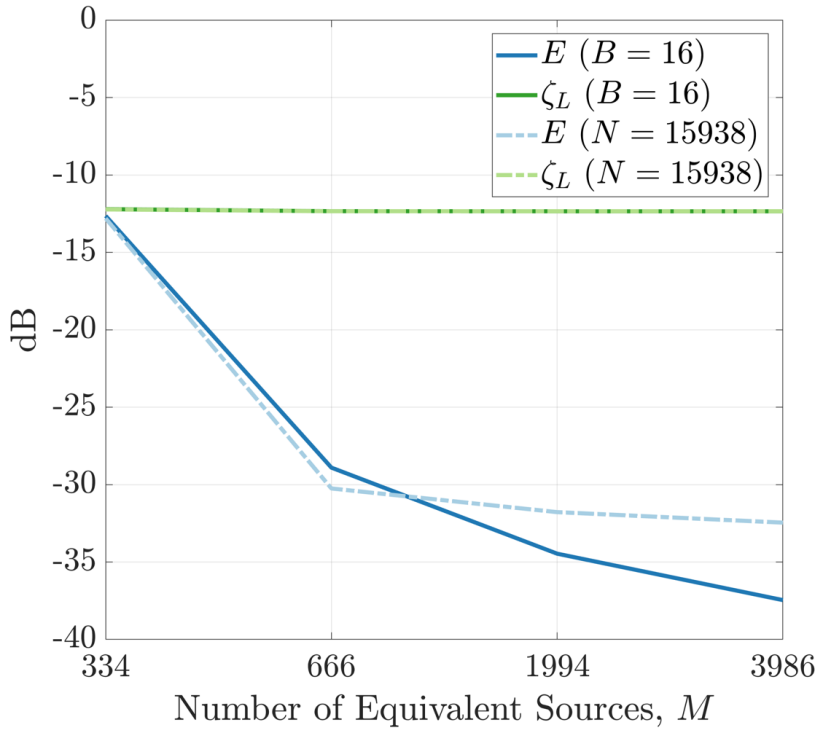

Figure 3.10: The velocity error, E, and the pressure difference, ζ_L, as a function of the number of equivalent sources, M, when the ratio of evaluation points to equivalent sources, B, is 16, and when the number of evaluation points, N, is fixed at 15938.

3.4.2.4. **Effect of the Wall Width**

In the 1D case, for a dipole source to radiate in only one direction, the separation distance, *d*, has to be small compared to the wavelength [Nelson and Elliott, 1992]. As a general guideline $w < \lambda/10$ can yield close to zero downstream radiation. Thus, *w* is fixed at $\lambda/10$ in the simulation below.

The total number of equivalent sources is determined by the total height of the wall at 30λ and the separation between the sources, $w = w_{vert} = \lambda/10$. The ratio, *B*, of *N* evaluation points on the boundary to *M* equivalent sources is fixed at 16 to ensure an accurate reconstruction of the velocity at the boundary.

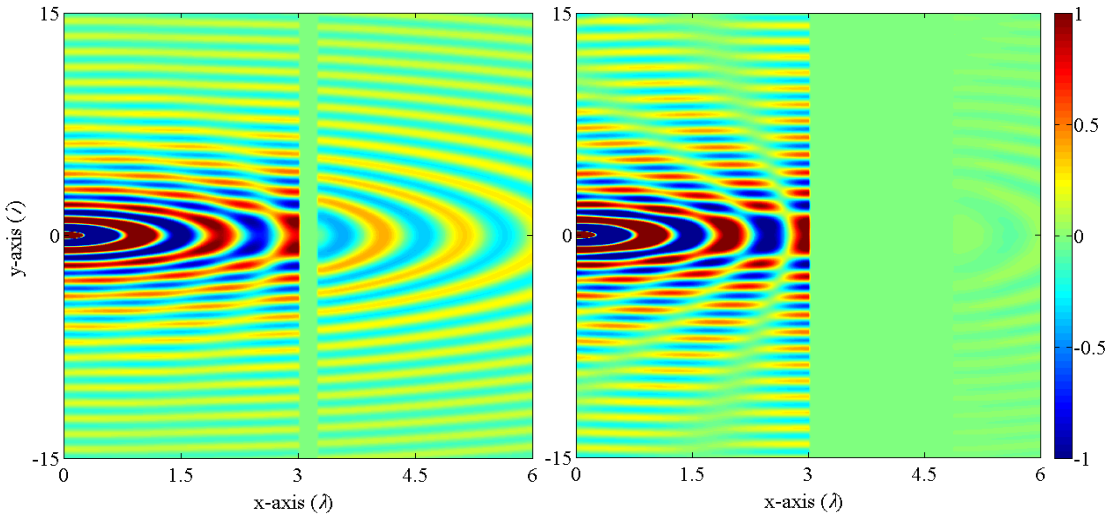

Figure 3.11: Sound pressure distribution of an 'infinite' wall with rigid boundaries generated with the equivalent source method for (a) $kw = 0.03$ and (b) $kw = 0.22$, without regularisation.

The stability of the equivalent source method (ESM) solution is particularly sensitive to the distance between the boundary and the equivalent sources [Jeans and

Mathews, 1992]. By varying the width of the wall, $d = w_{wall,L} + w + w_{wall,R}$, the ability of the regularisation parameter, β, to yield stable ESM solutions can be evaluated.

The pressure field of a perfect reflection produced by the analytical image source model is shown in Figure 3.12. Visual comparison of the pressure field using the ESM for $kw = 0.03$ in Figure 3.11(a) with the analytical solution in Figure 3.12, illustrates the inability of ESM to reproduce an accurate pressure field for low *kw*. For higher *kw*, ESM is able to reproduce a visually similar pressure distribution to the analytical solution, as seen by comparing Figure 3.12 and Figure 3.11(b).

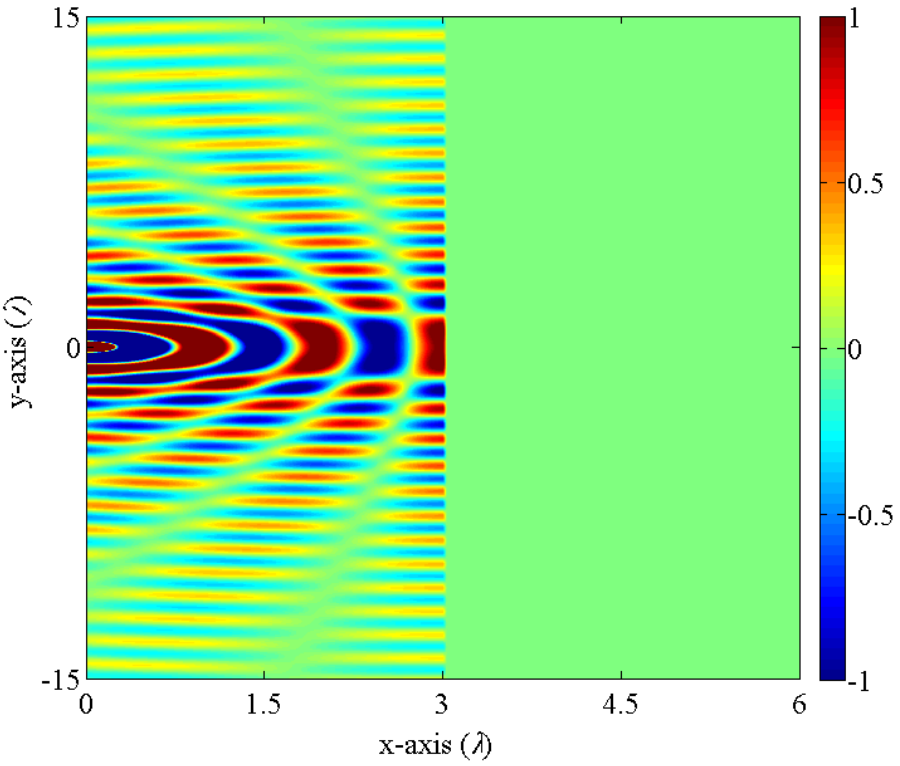

Figure 3.12: Sound pressure distribution of an acoustic reflection from a point source at $(0,0)$ off an 'infinite' wall 3λ m away generated using an analytical image source method.

3.4.2.5. Effect of β on Boundary Velocity Error E

In order to prevent β from overcompensating, resulting in inaccuracies, the value of β should be carefully chosen. A wide of range of β values were tested to illustrate the effects of overcompensation when the magnitude of β is too large, as shown in Figure 3.13(a).

As kw increases, the velocity reconstruction at the boundary improves, yielding low boundary error values. At higher values of kw, however, ill-conditioning during matrix inversion results in poor reconstruction, shown by the high boundary error values when $\beta = 0$.

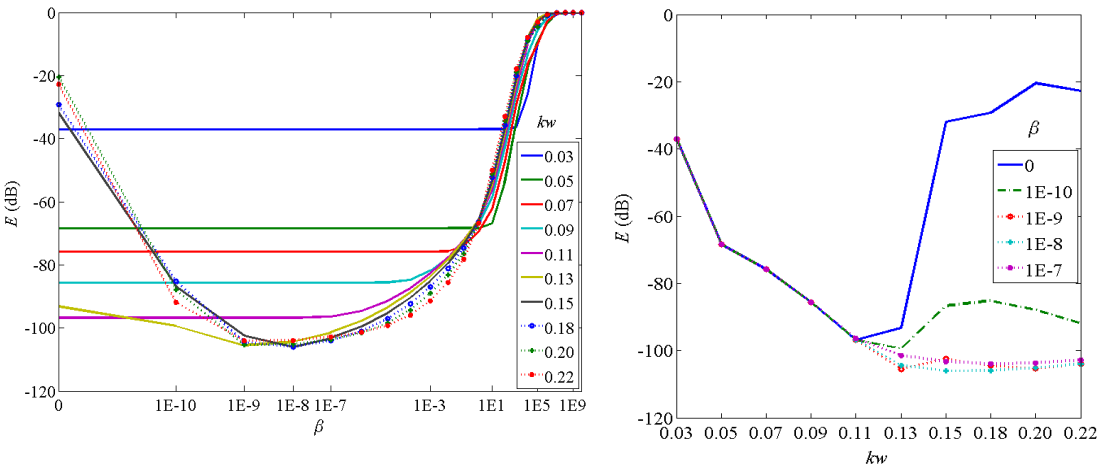

(a) (b)

Figure 3.13: (a) Boundary error, E, over the entire wall as a function of β at different kw. (b) Effect of β on boundary error E as a function of kw.

Introduction of small values of β significantly reduces the boundary error for $kw > 0.11$ as shown in Figure 3.13(b). For the values of kw tested, β values in the range from 10^{-9} to 10^{-5} provide a substantial improvement for the ill-conditioned

cases ($kw > 0.11$) without affecting the performance of well-conditioned ($kw > 0.13$) cases.

Evaluating the boundary error, E', within the 2λ zone depicted in Figure 3.8, a similar increase in error due to ill-conditioning occurs for $kw > 0.11$, as shown in Figure 3.14(a). The improvement in E', due to the introduction of β values in the range from 10^{-9} to 10^{-5}, is still evident as highlighted in Figure 3.14(b). The similar improvements in the boundary error for both E and E' show that ill-conditioning results in inaccuracies across the entire length of the boundaries.

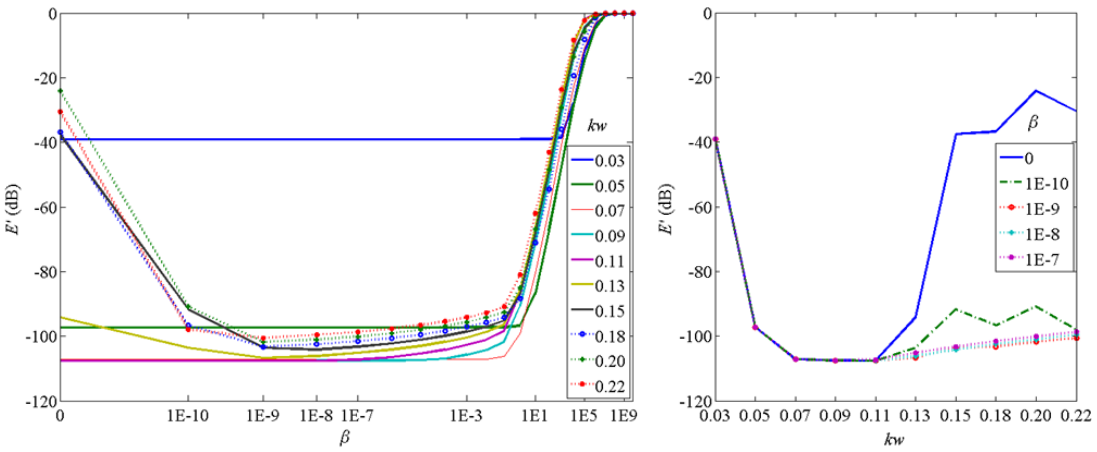

Figure 3.14: Boundary error within the 2λ zone, E', as a function of β at different kw. (b) Effect of β on boundary error E', as a function of kw.

3.4.2.6. Effect of β on the Pressure Difference Indices, ζ_L and ζ_R

For the equivalent source method (ESM) to radiate/scatter accurately, it should also produce pressure fields that are also the same as the analytical solution. The normalised difference in sum-of-the-squared pressures between the analytical solution (e.g. perfect

reflection) and the ESM is defined in (3.30) as ζ_L. Since lower values (in dB) of ζ_L indicate less difference between ESM and the analytical solution, it can be seen from Figure 3.15(a) that as kw increases, ζ_L decreases.

The normalised sum-of-the-squared pressures in the 2λ × 2λ zone after the wall, where no wave propagation is expected, is defined in (3.31) as ζ_R. The trend is consistent, with ζ_L as ζ_R both being inversely proportional to kw according to Figure 3.15(b), but not increasing for large kw, as the velocity error did.

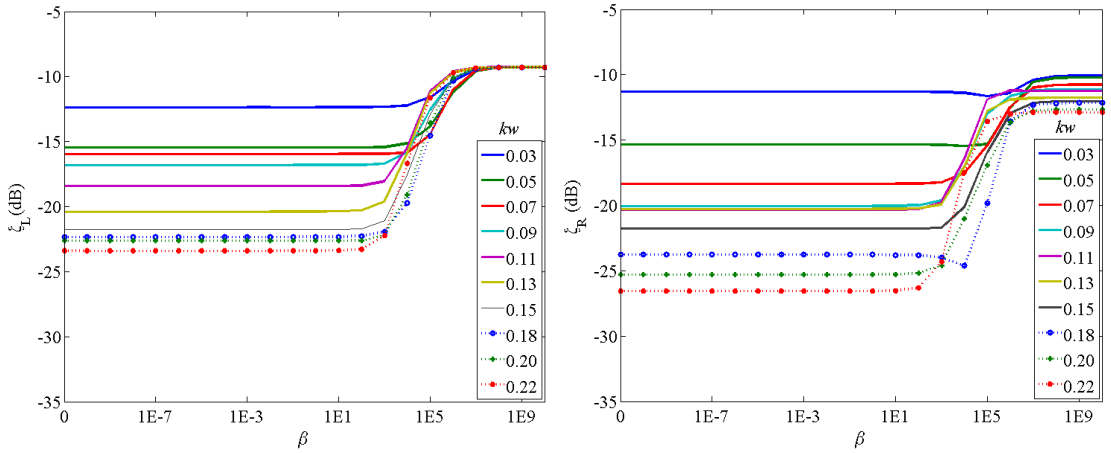

(a) (b)

Figure 3.15: (a) Pressure difference index ζ_L in the left-hand zone as a function of β. (b) Pressure difference index ζ_R in the right-hand zone as a function of β.

Figure 3.15 shows that the introduction of β has no impact on the radiation pattern of ESM provided that the value of β is less than about 10, which is higher than the value for which the boundary error is not increased in Figure 3.14. Even though high boundary velocity errors, due to ill-conditioning, did not appear to translate into spurious radiation in the studied zone, spurious radiation has been observed near the edges of the 'infinite'

wall. Therefore, ill-conditioning will cause inaccuracies in radiation/scattering under certain scenarios.

3.4.2.7. **Effect of Frequency**

With a fixed dipole separation distance w at $\lambda/10$, a ratio of evaluation points to equivalent sources B at 16, and a fixed ratio of wall width to w, the error at the boundary E and pressure difference index ζ_L is similar for different values of λ, as shown in Figure 3.16.

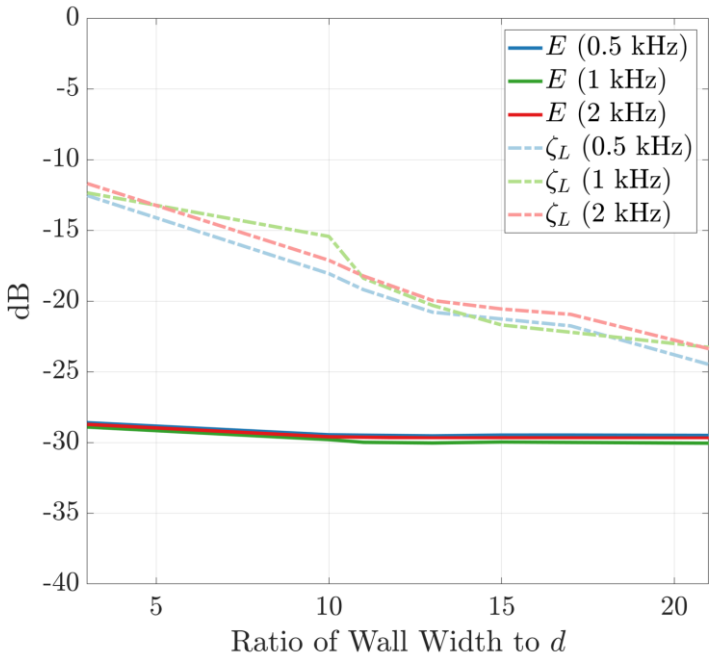

Figure 3.16: Boundary error E and pressure difference index ζ_L as a function of wall width, d m, for a constant equivalent source separation distance of $w = \lambda/10$, and $B = 16$.

Hence, the accuracy of the ESM method appears highly dependent on the frequency-dependent retreat distance of the equivalent sources.

3.4.3. A Summary on the Equivalent Source Method

In the example of a perfect reflection off a rigid wall, results have revealed that after regularizing the ill-conditioned matrices, an inherent problem of the ESM [Lee, 2017], large errors in the reconstructed sound field still persists. Ultimately, the accuracy of the reconstructed sound field is dependent on both the condition of the matrices, but more affected by the retreat distances of the equivalent sources within the reflecting body (i.e. wall) [Bai et al., 2011; Lam et al., 2015a]. This sensitivity to the frequency-dependent retreat distance of the equivalent sources limits the effective range of the active control analysis for a fixed wall thickness.

3.5. Finite Element Method Formulation

Although the most computationally demanding out of the methods mentioned, the finite element method (FEM) provides more flexibility and accuracy for a wide frequency range. In addition, materials such as glass can be easily integrated into the simulation model for greater insight into the behaviour of the sound field in a realistic scenario.

Due to its widespread utility, FEM is available through several commercial software packages and have been optimised to run fairly efficiently on modern machines. The FEM simulations in this thesis were performed using the commercial software package COMSOL [COMSOL Multiphysics, 2015] on a high-performance workstation with a XEON E5-2699 processor (18 cores, 2.3 GHz) and 128 GB of memory.

Before employing the FEM method to analyse the physical limits of active control, it is important to determine the appropriate parameters for sufficient accuracy. The free-field characteristics of the FEM simulation model are firstly tested for a large

computation plane. Subsequently, the computation plane is reduced to a minimum size while maintaining accuracy.

3.5.1. Suitability of two-dimensional FEM models

Owing to the huge meshes required to model realistic dimensions, studies that investigate the physical properties of sound propagation through windows [Yu et al., 2017] and active noise control in general [Huang et al., 2015] have relied on 2D instead of 3D simulations. To determine whether a 2D simulation can provide sufficiently accurate insight into the physical limits of active control through an aperture, the propagating modes of an infinite plane array of control sources in free-field is investigated.

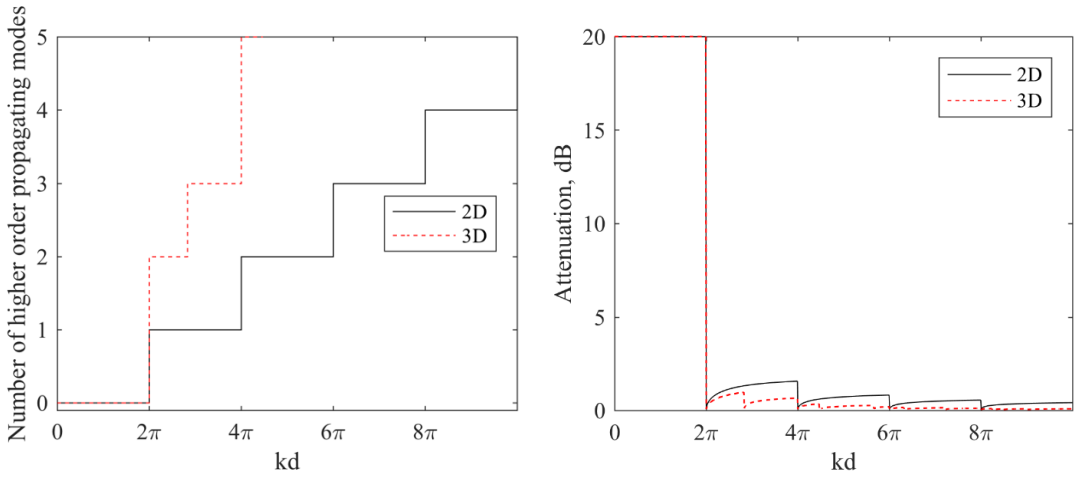

(a) (b)

Figure 3.17: (a) High order propagating modes, and (b) active control attenuation as a function of normalised frequency for 2D and 3D formulations [Elliott et al., 2017].

At high frequencies where the wavelength is small compared to the size of the aperture, the control problem approximates to a free-field condition [Elliott et al., 2017].

The analytical solution to the free-field problem can be derived from an analogous active control problem in ducts, to represent a normally incident plane wave being controlled by an infinite plane array of monopole sources [Elliott et al., 2017].

The degree to which 2D simulations will differ from 3D ones will depend on differences in the propagating modes because the pressure in the far-field is determined by contributions from propagating modes [Elliott, 2001]. This deviation in propagating modes only occurs at normalised frequencies (wavenumber multiplied by the separation distance between control sources) greater than 2π, as shown in Figure 3.17(a). Since attenuation becomes poor above normalised frequencies ($kd = 2\pi$) where the deviation between 2D and 3D free-field formulations occur, as shown in Figure 3.17(b), it is reasonable to derive guidelines just from 2D simulations.

3.5.2. Free-field Accuracy of the 2D FEM Model

Knowledge of the total acoustic power output of the control sources, as well as the primary noise, enables the quantification of the global effectiveness of active control (i.e. control of noise in an entire 3D space). In practice, this is usually achieved by far-field estimation through the sum-of-the-squared pressures at all locations in the far-field.

Although a free-field condition can be created in a FEM model, it is usually achieved by surrounding the entire computation field with a perfectly matched layer (PML). The effectiveness of the PML's damping mechanism is dependent on the wavelength and incidence angle of the impinging waves. Hence, it is necessary to determine the free-field accuracy of the FEM model and the respective parameters at the lowest frequency of interest. The quantification of the FEM model's free-field accuracy also allows the computation space to be shrunk to a minimum for increased computational efficiency.

The free-field accuracy of a FEM simulation model can thus be determined by quantifying the difference in the maximum achievable reduction in total sound power an analytical solution with that derived from the sum-of-the-squared pressures at the far-field in the FEM simulation model.

3.5.2.1. Minimum Power Output of Two Monopole Point Sources

Since the point sources in a 2D FEM model are defined as incoherent line sources producing cylindrical waves [COMSOL Multiphysics, 2015], an analytical solution can be reformulated from that of the monopole point source in a free-field. The power output of a harmonic monopole point source is given by [Nelson and Elliott, 1992]

$$W = \frac{1}{2}\mathrm{Re}\left\{p^* q\right\} = \frac{1}{2} Z_0 \left|q\right|^2, \tag{3.32}$$

where * represents complex conjugate operator, $Z_0 = \omega^2\rho_0/4\pi c_0$, and q is the complex source strength. An example of a pair of monopole sources, separated by a distance w, is depicted in Figure 3.18. q_p and q_s are the complex source strengths of a primary disturbance and secondary source, respectively. Hence, the combined source power output of both the primary and secondary monopole sources can be written as

$$W = \frac{1}{2}\mathrm{Re}\left\{\left[p_p\left(r_p\right) + p_s\left(r_p\right)\right]^* \cdot q_p\right\} + \frac{1}{2}\mathrm{Re}\left\{\left[p_p\left(r_s\right) + p_s\left(r_s\right)\right]^* \cdot q_s\right\}, \tag{3.33}$$

where q_p is the complex strength of the primary source; and $p_p(r_p)$ and $p_s(r_p)$ respectively represent the contributions of the primary and secondary sources to the pressure at the primary source point [Nelson et al., 1987]; it follows that $p_p(r_s)$ and $p_s(r_s)$ respectively represent the pressure contributions of the primary and secondary sources at the secondary source location.

After expansion by substituting (3.19) into (3.33), (3.33) can be reduced to a quadratic form given by [Nelson and Elliott, 1992]

$$W = A\left|q_s\right|^2 + q_s^* b + b^* q_s + c, \tag{3.34}$$

where $A = (1/2)Z_0$, $b = -(1/2)Z_0 \mathrm{sinc}(kw)q_p$, and $c = (1/2)Z_0\left|q_p\right|^2$. The last term is equals to the power output due to the primary source alone and shall be denoted by W_p, for ease of reference. The quadratic function has a unique minimum given by an optimum secondary source strength

$$q_{s,opt} = -q_p \,\mathrm{sinc}\,(kw), \tag{3.35}$$

and a unique minimum power output is given by

$$W_0 = W_p\left[1 - \mathrm{sinc}^2(kw)\right]. \tag{3.36}$$

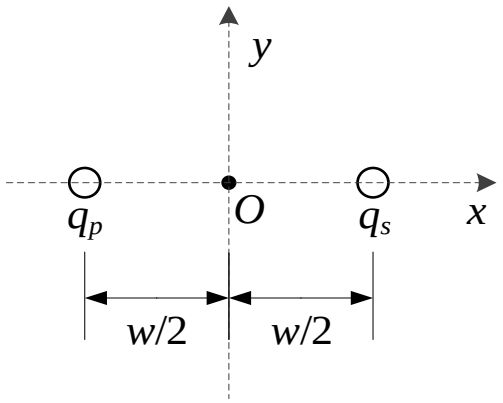

Figure 3.18: A primary and secondary monopole point source with complex source strength q_p and q_s respectively. Both sources are separated by a distance *w* [Nelson and Elliott, 1992].

3.5.2.2. **Minimum Power Output of Two Incoherent Line Sources**

The optimal secondary source strength and minimum power output of two monopole points sources in (3.35) and (3.36) are adapted for two incoherent point sources as detailed in Appendix A to give

$$q_{s,opt} = -q_p J_0(kw), \tag{3.37}$$

$$W_0 = W_p \left[1 - J_0^2(kw)\right], \tag{3.38}$$

where J_0 is the zeroth-order Bessel function. The maximum attainable attenuation is thus evaluated by

$$\text{Attenuation} = -10\log_{10}\left(\frac{W_0}{W_p}\right), \tag{3.39}$$

where W_0 refers to the minimum power output defined in (3.38), and $W_p = (1/2) Z_0 \left|q_p\right|^2$ power output from the primary source alone.

3.5.2.3. **Comparing FEM Model to Analytical Solution**

Firstly, a large simulation space in the form of a 2D square spanning 50 m by 50 m, bounded by a perfectly matched layer (PML) of 0.5 m thickness, is created in the FEM software as shown in Figure 3.19. At the lowest frequency of interest of 100 Hz, the simulation space measures approximately 14.5 by 14.5 wavelengths.

To determine the total sound power output in the far-field, the sum-of-the-squared pressures are calculated at the evaluation circle with a radius of 6λ of 100 Hz, as shown in Figure 3.19. The resolution of the mesh is fixed at 6 elements per wavelength. At the fixed frequency of 100 Hz, and the separation distance *w* is varied for three instances to

achieve: (1) $kw = 0.2\pi$, (2) $kw = 0.4\pi$, and (3) $kw = \pi$, where k is the acoustic wavenumber.

With a fixed value of q_p, the optimal secondary source strengths are determined for three cases of kw. The power attenuation from the FEM simulation model is calculated by

$$\text{Attenuation} = -10\log_{10}\frac{\mathbf{e}^{\mathrm{H}}\mathbf{e}}{\mathbf{d}^{\mathrm{H}}\mathbf{d}}, \tag{3.40}$$

where **e** is the vector of complex pressure values at the evaluation arc from the contributions of both the primary and secondary sources, **d** is the vector of complex pressure values due to the primary source only, and $^{\mathrm{H}}$ is the Hermitian operator. Hence, $\mathbf{e}^{\mathrm{H}}\mathbf{e}$ is the far-field estimation of W_o, and $\mathbf{d}^{\mathrm{H}}\mathbf{d}$ is the far-field estimation of W_p.

The attenuation results of the three instances of kw (0.2π, 0.4π, and π) are plotted as a function of kw, indicated by orange circles in Figure 3.20. The maximum attainable attenuation of the analytical solution calculated with the same value of q_p is similarly plotted as a function of kw in Figure 3.20. At the far-field evaluation distance of 6λ, the analytical solution matches the estimated power from the FEM model up to an accuracy of 6 decimals places.

To reduce the computation time, the evaluation circle is gradually reduced to within an error margin of 0.5 dB to ensure an accurate far-field approximation. The radius of the evaluation circle approaches ~1.5λ and rounded to an absolute value of 5 m for ease of implementation.

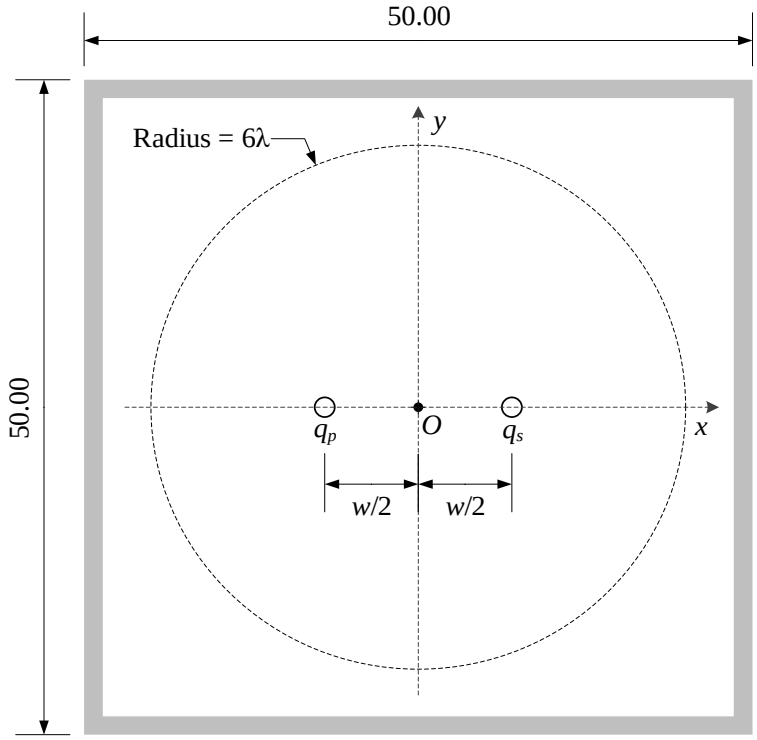

Figure 3.19: Dimensions of the FEM simulation model where the primary source q_p and secondary source q_s are placed half a wavelength apart and centred symmetrically around the origin *O*. The evaluation circle has a radius of six wavelengths and all elements are enclosed in a 50 m by 50 m square with a 0.5 m thick perfectly matched layer along its boundary.

3.5.3. 2D FEM model of an open aperture in a rigid wall

The 2D FEM simulation model of an unobstructed aperture in a rigid wall is constructed with maximum element size set to one-sixth the wavelength at 4 kHz. To emulate a free-field condition in the sound field on both sides of the aperture, the entire structure is bounded by a perfectly matched layer (PML), as shown in Figure 3.21. This encapsulation allows the effect of diffraction around the wall edges on the active control

performance to be quantified, without interference from the reflections in the room interior.

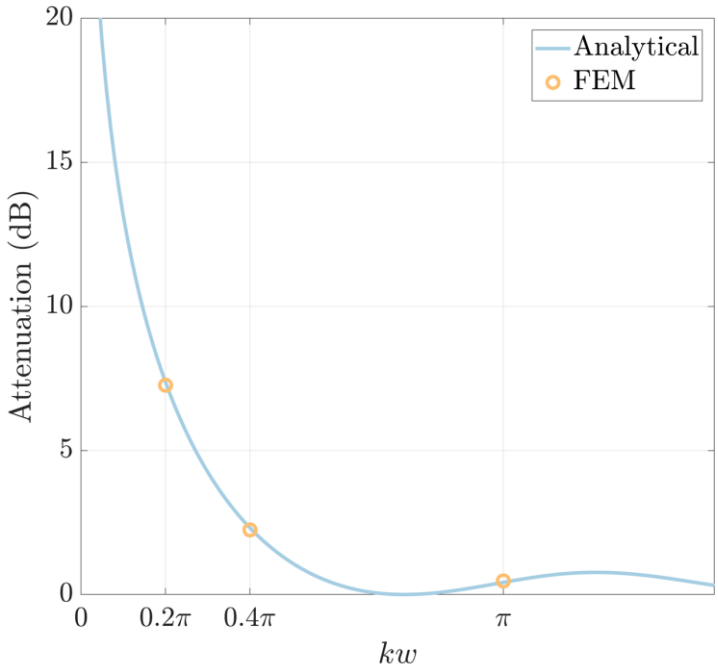

Figure 3.20: Power attenuation (in dB) of the analytical solution (blue line) and the solution derived from the FEM software (orange circles) as a function of the wavelength λ multiplied by the separation distance *w*.

The rigid walls have a fixed thickness of 0.1 m to represent a realistic depth. One should note that the thickness of the depth does not affect transmission loss of the aperture except at very low frequencies [Sieck, 2013]. The aperture is fixed at a size of L = 2 m, and an evaluation arc with a radius of 5 m (i.e. $\sim 1.5\lambda$ of 100 Hz), consisting of 1100 discrete points, encompasses the entire aperture. The acoustic power of the sound propagating through the aperture can be calculated with the far-field approximation method (i.e. sum-of-the-squared pressure values at all the discrete points on the evaluation arc).

As a reference for variations in geometrical arrangements, the origin of the cartesian coordinates is in the centre of the wall depth and aperture opening. The plane wave is excited in the left section of the simulation plane and travels in the positive x direction through the aperture.

For computational efficiency, the size of the computation plane is reduced from 50 m by 50 m in Figure 3.19 to 12 m by 12 m, with a minimal reduction in accuracy. The 2D model has around 1 million elements, which is reasonably quick to run for different geometric variations. For reference, the corresponding 3D model will require at least 120 million elements and impractical to run all the cases to provide physical insight and practical guidelines for the active control system.

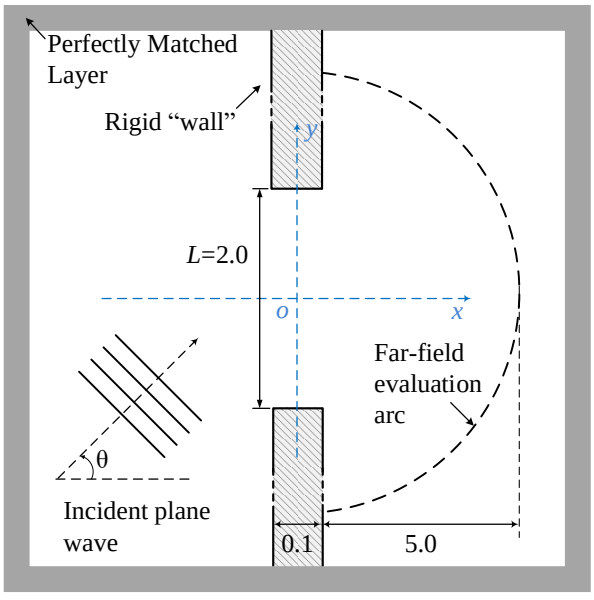

Figure 3.21: 2D FEM model of a 0.1 m wide rigid wall with an open aperture to emulate noise propagating through the aperture in a free-field condition (in m).

3.6. Summary

The equivalent source method (ESM) can be used to study acoustic scattering by driving an array of equivalent sources to match the desired boundary condition of the scattering/radiating object. ESM can be solved either by the least-squares or full-field equation approach with the former yielding higher accuracy in the low-frequency region. Low frequencies are an area of interest for ANC applications as they operate most effectively at such frequencies.

The matrix formulation of the least-squares method gives rise to an inherent conditioning problem, due to matrix inversion. Introduction of a regularisation parameter, β, has been shown to significantly mitigate the errors introduced by ill-conditioning without affecting cases where the problem is well-conditioned.

Regularisation of ESM has demonstrated improvements in reducing boundary reconstruction error of the surface velocity. However, the sound field radiation accuracy is ultimately dependent on the frequency-dependent distance between the boundary and the embedded equivalent sources and appears to be less affected by the ill-conditioning. Thus, the equivalent source method is unsuitable for the acoustic wavelengths of interest in this study.

In light of the limitations of the ESM, the fundamental limits of active control are proposed to be investigated via the finite element method (FEM). Before the FEM model can be developed for numerical analysis of active control, the sound power accuracy based on the far-field sound pressure estimation accuracy is analysed and optimised for computational efficiency. Based on comparison with an analytical formulation, it was determined that an evaluation circle with a radius of minimally ~1.5 times the wavelength under test is sufficiently accurate to determine the sound power radiating from both the primary and secondary sources.

Chapter 4

Fundamental Limits of Control through Fully and Partially Open Apertures

This chapter focuses on the physical limitations of active control in simplified arrangements of sources in an aperture with the FEM simulation model defined in section 3.5. Based on the findings from the literature survey in Chapter 2, the investigation will firstly focus on the distributed-layout strategy using a plane array of sources distributed across a fully open aperture to determine: (1) the effect of placing the peripheral sources of the planar array on the boundary of the aperture, (2) the effect of translating the array towards and away from the noise source, (3) the limit of control as a function of angle of incidence, and (4) the fundamental limits of a sliding window application scenario.

After the fundamental limitations have been determined for an open aperture, the physical limits of active control are further characterised for a more realistic window scenario. The open aperture is occluded with a glass panel forming a simplified model of a sliding window in a FEM simulation model. As a benchmark for active control performance, the passive insulation provided by the glass panel is characterised by the state of glazing (i.e. how wide the window is opened). The physical limits of control are subsequently defined in conjunction with the passive insulation properties of the glass panel to determine the minimum configuration required for adequate attenuation of noise. Experimentation based on the same physical dimensions of the FEM model is described in Chapter 5.

4.1. Global Active Control Formulation

The proposed active control concept achieves global attenuation in the room interior by treating the window as the sole point of entry for noise [Kwon and Park, 2013; Lam et al., 2015b]. Thus, global control is achieved through the minimisation of the sum of squared pressures on the far-field arc that envelopes the entire window opening, as shown in Figure 4.1. The corresponding vector of complex pressures at the discrete points on the evaluation arc is expressed as

$$\mathbf{e} = \mathbf{d} + \mathbf{G}\mathbf{q}, \tag{4.1}$$

where $\mathbf{d}$ is the vector of complex pressures at the evaluation positions due to the scattered incident plane waves through the window, $\mathbf{q} = \begin{bmatrix} q_1 & q_2 & \dots & q_N \end{bmatrix}^{\mathrm{T}}$ is the vector of complex source strengths of N secondary sources, and $\mathbf{G}$ is the matrix of

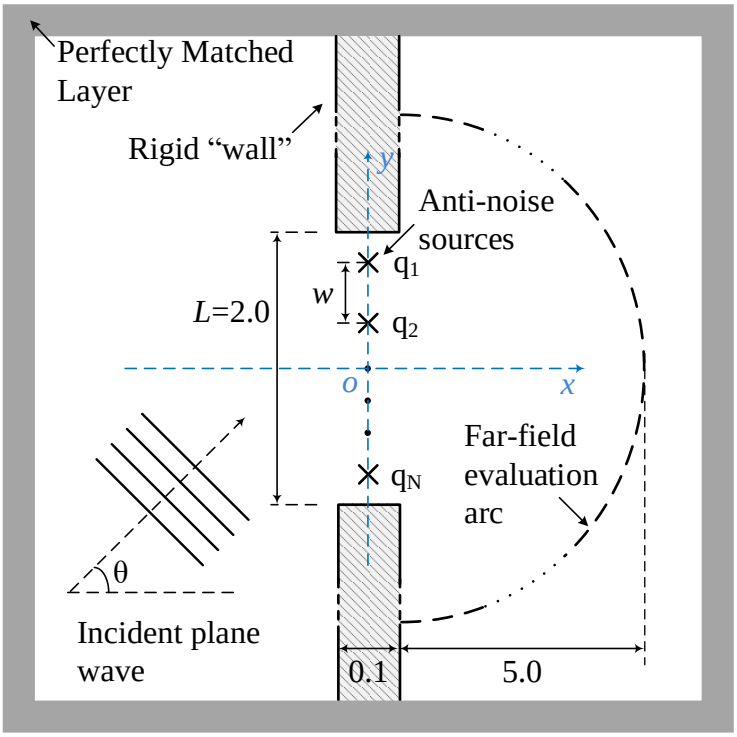

Figure 4.1: 2D FEM model of a 0.1 m wide rigid wall with an open aperture to investigate the active control of noise propagating through an aperture (in m).

complex plant responses between the secondary sources and the evaluation positions on the far-field arc. Both $\mathbf{d}$ and $\mathbf{G}$ were obtained through the FEM simulation. The sum of squared pressures at the evaluation positions is minimised using the exact least-squares method with the cost function given by

$$C = \mathbf{e}^{\mathrm{H}}\mathbf{e} = \mathbf{q}^{\mathrm{H}}\mathbf{A}\mathbf{q} + \mathbf{q}^{\mathrm{H}}\mathbf{b} + \mathbf{b}^{\mathrm{H}}\mathbf{q} + \mathbf{d}^{\mathrm{H}}\mathbf{d}, \tag{4.2}$$

where $\mathbf{A} = \mathbf{G}^{\mathrm{H}}\mathbf{G}$ and $\mathbf{b} = \mathbf{G}^{\mathrm{H}}\mathbf{d}$.

By setting the derivative of the cost function in (4.2) with respect to the real and imaginary components of $\mathbf{q}$ to zero [Elliott, 2001], a set of optimised secondary source strengths is obtained, given by

$$\mathbf{q}_0 = -\left(\mathbf{G}^{\mathrm{H}}\mathbf{G} + \beta\mathbf{I}\right)^{-1}\mathbf{G}^{\mathrm{H}}\mathbf{d}, \tag{4.3}$$

where β is a parameter that regularises the matrix in order to compensate for the ill-conditioning that arises from the overdetermined problem [Elliott, 2001], $\mathbf{I}$ is an identity matrix, the superscript $^{\mathrm{H}}$ is the Hermitian operator. The regularisation parameter was set to the minimum value necessary to obtain a well-conditioned inverse of the matrix in brackets in (4.3).

4.1.1. Evaluation Parameters

The acoustic power radiated through the window from the primary noise source can be determined by the sum of squared pressures evaluated in the far-field on an enclosing surface [Nelson and Elliott, 1992], which can be written as

$$W_d = \frac{|\mathbf{d}|^2}{2\rho_0 c_0}\pi r, \tag{4.4}$$

where ρ_0 is the density of air, c_0 is the speed of sound in air, and r is the radius of the evaluation arc. The acoustic power after ANC is calculated similarly, based on contributions from both the noise and secondary sources as

$$W_e = \frac{|\mathbf{e}|^2}{2\rho_0 c_0}\pi r, \tag{4.5}$$

The attenuation performance of the active acoustic window system is then defined by normalising (4.4) with (4.5), which is represented as

$$Attenuation = -10\log_{10}\frac{W_e}{W_d}. \tag{4.6}$$

4.2. Active Control of Sound Through Fully Open Apertures

An open aperture in a wall with a finite thickness is the simplified representation of an actual window system in residential buildings. The complex sound field propagating through the aperture and its interaction with the sound fields generated by the secondary sources, is modelled numerically to optimise secondary source arrangements. By studying the impact on active control performance, the secondary source arrangements are optimised in terms of: (1) their separation distances and distance of the peripheral sources to the wall edges; (2) the position along the depth of the aperture, i.e. x-axis direction. Based on the trends observed as a function of frequency and angle of noise incidence, guidelines are deduced to determine the minimum number of sources required to attain good control up to a desired frequency and angle of noise incidence.

4.2.1. Secondary Source Positioning

Based on Huygens principle, Murao and Nishimura [Murao and Nishimura, 2012] identified that the separation distance between the secondary sources was as an important factor affecting the attenuation performance of the active acoustic window system in the free-field. When the effects of scattering around the edges of the window are considered, however, the design of the ANC system based on this separation distance alone is insufficient. Additional factors that can potentially affect the performance of the ANC system including the placement of the secondary sources relative to the depth of the wall, and the proximity of the sources to the edges of the window. Due to the lack of an established analytical solution to the window problem, (1) the effect of source separation (*y*-axis) and hence, the number of sources required, and (2) the source placement relative to the depth of the wall (*x*-axis), are systematically evaluated using the finite element models.

4.2.1.1. Secondary Source Separation

In a finite aperture, the number of sources is dictated by the separation distance between the sources, w, and the distance of the peripheral sources away from the edges of the walls, v, as shown in Figure 4.2. This separation distance w determines the upper-frequency limit of control as shown in the free-field investigation of an infinite plane array of control sources [Elliott et al., 2017, 2018]. Although it is intuitive that sources should be evenly distributed across the aperture for normal incidence plane wave, the separation distance between the sources w can span from $L/(N+1)$ to $L/(N-1)$ m, depending on how close the peripheral sources of the array are to the edge of the wall, i.e. the size of v. It can be hypothesized that for optimal control of diffraction, sources

should be placed at the edges (i.e. $w = L/(N-1)$), such that the normal velocities at the edges can be controlled by the edge sources.

The effect of source separation, w, on the attenuation performance is explored for increasing number of sources N. Only frequencies up to 4 kHz are considered, which corresponds to the upper limit of the traffic noise spectrum [Jagniatinskis and Fiks, 2014] in conjunction with the upper limit of practical ANC performance. In the FEM simulations, the plane wave noise source is incident at $\theta = 0°$, and secondary sources are fixed at $x = 0$ m. The sources are distributed symmetrically about the x-axis and separated by a distance of w m, as exemplified in Figure 4.2(a) and (b) for $N = 2$ and $N = 3$ respectively.

The distance from the wall edge to the peripheral source, v, as shown in Figure 3, is given by

$$v = \frac{L - w(N-1)}{2}. \tag{4.7}$$

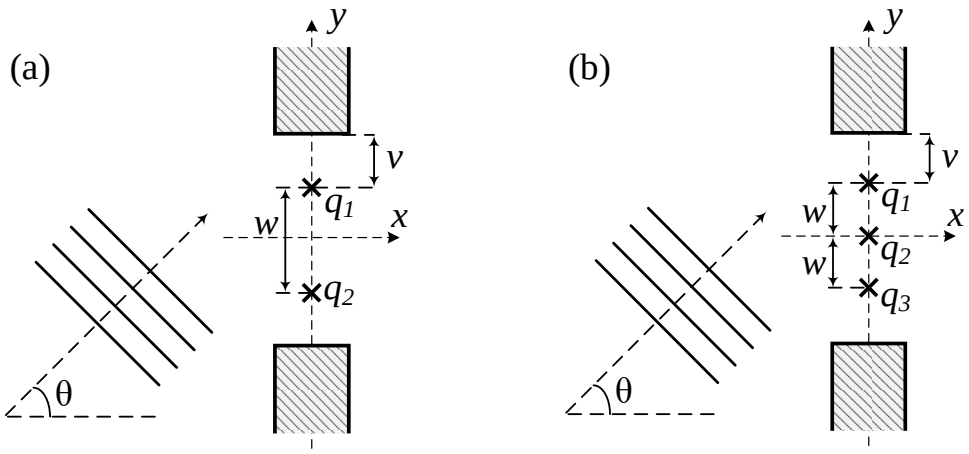

Figure 4.2: Secondary sources q_1 to q_N at $x = 0$ m and symmetric about the x-axis, with separation distance (a) $0.01 \le w < 2$ m for $N = 2$ sources, and (b) $0.01 \le w < 1$ m for $N = 3$ sources [Lam et al., 2018a].

Hence, v equals zero if $w = L/(N-1)$, and v approaches w as w approaches $L/(N+1)$ m.

Based on the global control formulation defined in 4.1, the attenuation is analysed as a function of v for $N \in \{3, 5, 9, 13\}$. The general trend observed across all cases of N in Figure 4.3 shows that the attenuation performance degrades sharply as v approaches w, when $\pi < kw < 2\pi$. k is the acoustic wavenumber, which is equal to 2π divided by the wavelength.

As N increases, the attenuation performance peaks at $v = w/2$ regardless of kw, as seen in Figure 4.3(b) to (d), for the frequency range $\pi < kw < 2\pi$. Hence, it is evident that sources should not be positioned at the edge even for large N (small w), as may have been expected from the literature on the active control of sound diffracted over barriers [Fan et al., 2013; Hart and Lau, 2012]. Based on an evaluation of the results for $N \geq 5$, a uniform and symmetric distribution of sources is suggested, where $v = w/2$ and w is given by

$$w = \frac{L}{N}. \tag{4.8}$$

4.2.1.2. **Location of Secondary Sources Along the Depth of the Aperture**

The effect of scattering is prominent when the wavelength of the primary source is large compared to the size of the aperture ($\lambda > L$) [Elliott et al., 2017, 2018; Emms, 2000]. To evaluate the effect of the translational movement of the array relative to the depth of the aperture, i.e. along the x-axis in Figure 4.1, on the attenuation performance, simulations were conducted with $N = 5$, 7, 9, and 13 sources. The separation distance

w is selected using the guideline in (4.8) so that $w = 0.4$ m, 0.2857 m, and so forth, for corresponding values of N.

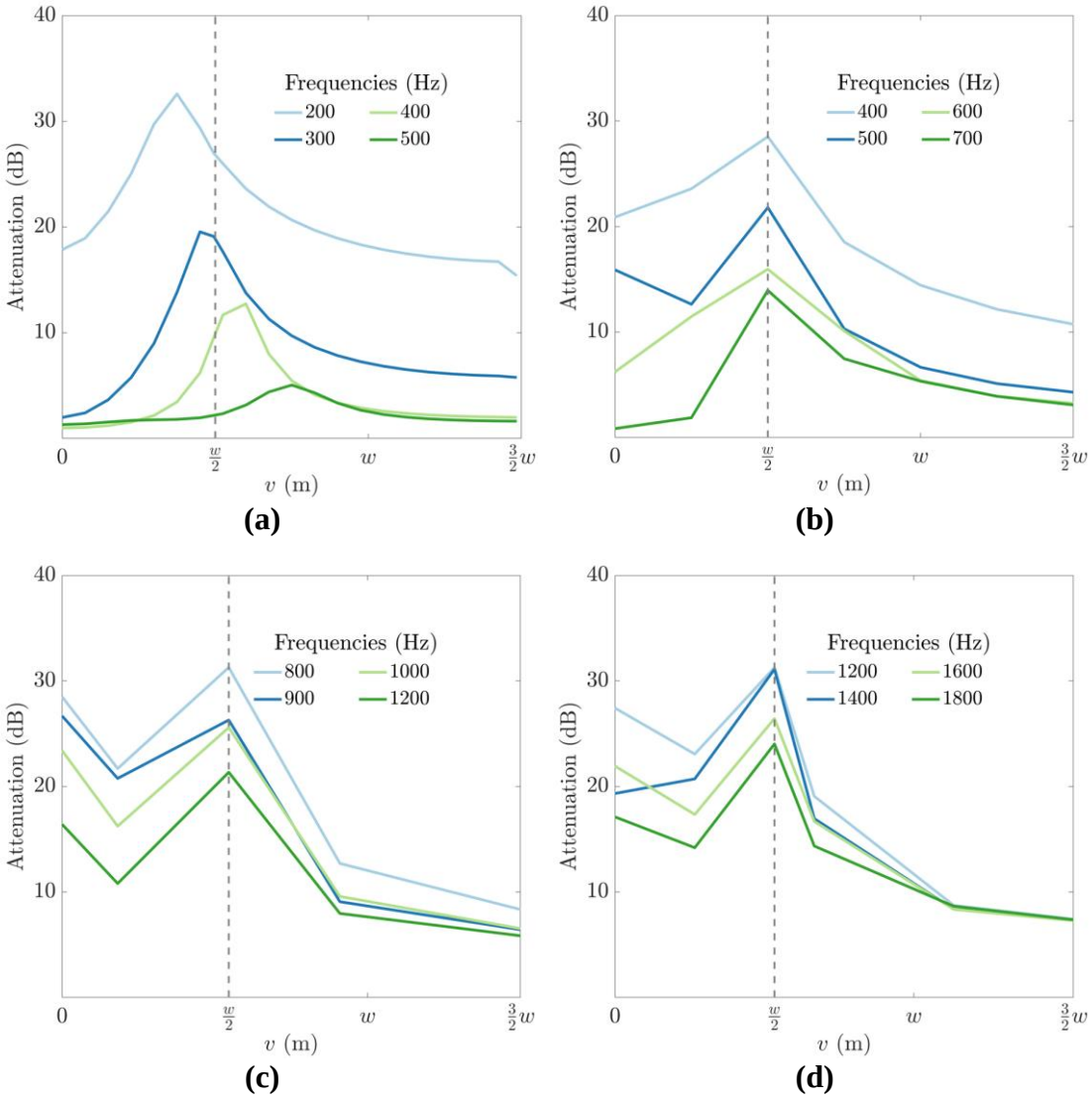

Figure 4.3. Attenuation performance as a function of increasing distance between the peripheral sources and the wall edge, v m, in terms of the source separation distance w m when (a) $N = 3$, (b) $N = 5$, (c) $N = 9$, and (d) $N = 13$ sources. The dashed line indicates when $v = w/2$ m [Lam et al., 2018a].

The results for $N = 5$ are shown in Figure 4.4(a), from which it can be seen that the x-axis position has no significant effect on the performance of the ANC system for frequencies at which the attenuation is at least 10 dB.

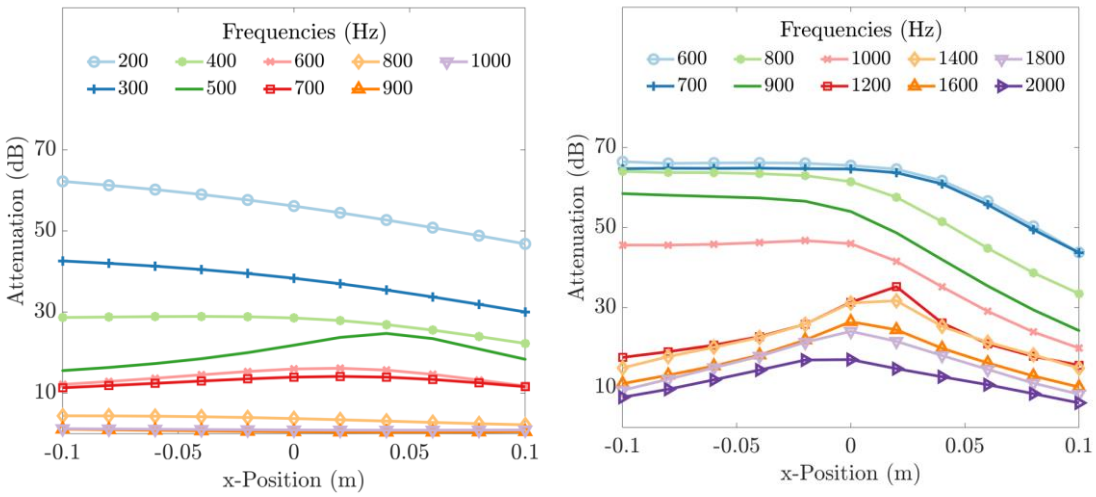

(a) (b)

Figure 4.4: Attenuation performance as a function of the x-axis position of the secondary sources where (a) $N = 5$ sources uniformly distributed between $-0.8 \le y \le 0.8$ m at intervals of $w = 0.4$ m, and (b) $N = 13$ sources uniformly distributed between $-0.9231 \le y \le 0.9231$ m at intervals of $w = 0.1538$ m. The plane primary wave is incident at $\theta = 0°$, for a number of frequencies [Lam et al., 2018a].

The results for $N = 13$ is shown in Figure 4.4(b), in which the control performance degrades rapidly when secondary source positions are situated beyond $x = 0.02$ m, for the frequencies plotted. Control performance at lower frequencies (i.e. $kw < \pi$) is rather constant with x locations farther from the control zone ($x < 0$ m), but start to degrade by as much 30 dB when $x > 0$ m. This observation suggests that the array of secondary sources struggle to generate anti-noise waves that can match and attenuate the scattered

primary noise waves, as the array is situated farther away from the primary source (aperture).

For frequencies in the range of $\pi < kw < 2\pi$, however, control performance degrades as the sources are situated both farther into ($x > 0$ m), and away ($x < 0$ m) from the control zone. Maximum control is attained when secondary sources are located along x positions between 0 and 0.02 m. At frequencies approaching the spatial aliasing limit, the resolution of the reconstructed anti-noise plane waves becomes increasingly poor.

Overall, placing the plane of the secondary sources at $x = 0$ m, i.e. in the centre of the wall with respect to its depth, gave the best average performance, so this position was used in the further simulations below.

4.2.2. Performance as A Function of Frequency and Angle of Incidence

For a finite aperture, the minimum number of sources required is based on the frequency upper bound and dominant angle of incidence for global control. Firstly, the upper-frequency limit of control for different source configurations is determined for impinging plane waves at normal incidence. Secondly, the maximum separation distance for good control and its respective cut-off frequency is generalised as a function of normalised frequencies for different source configurations, also for normal incident plane waves. Lastly, the generalisation is extended to include oblique incidence angles.

4.2.2.1. As a Function of Frequency at Normal Incidence

A cut-off frequency, above which the performance is poor, is clearly illustrated in Figure 4.5(a) for cases when N is equals to 3, 5, 7, 11 and 15 sources, which is consistent with that identified in [Elliott et al., 2017, 2018], for the 2D and 3D free field case. By plotting the attenuation as a function of N for selected frequencies, the minimum number of sources required for good global control (>20 dB) can be deduced, as shown in Figure 4.5(b). For instance, at least 9 sources are required to obtain good global control up to 1 kHz, for this aperture of width $L = 2$ m.

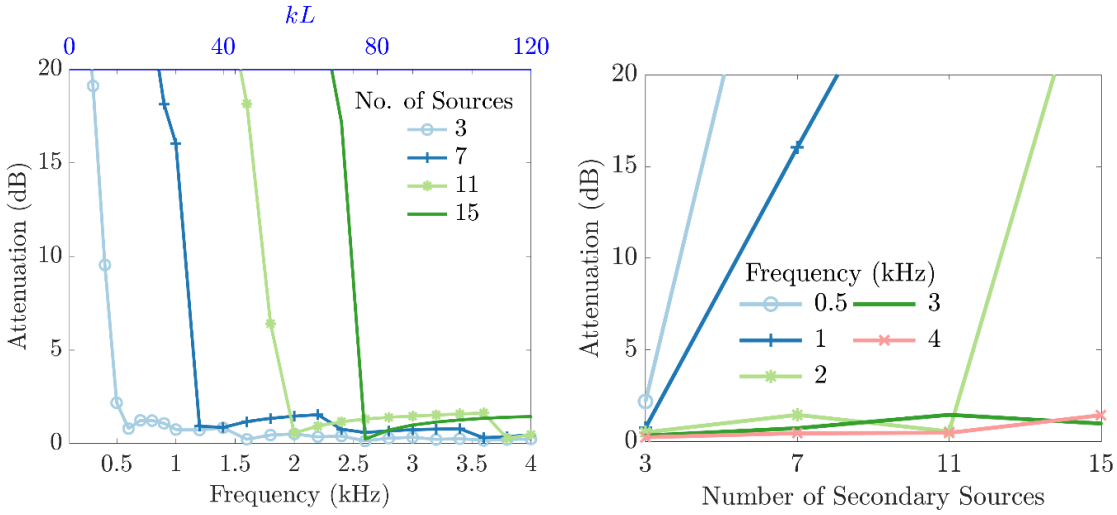

Figure 4.5: Attenuation performance (a) as a function of frequency, and (b) as a function of the number of secondary sources, when the primary noise is incident at $\theta = 0°$, and all sources located at $x = 0$ m [Lam et al., 2018a].

Figure 4.6 shows the sound pressure level (SPL) distribution plots of selected frequencies for different number of secondary sources, N. In cases where good control is achieved, such as when $N = 7$ at 500 Hz, complex residual sidelobes are present in

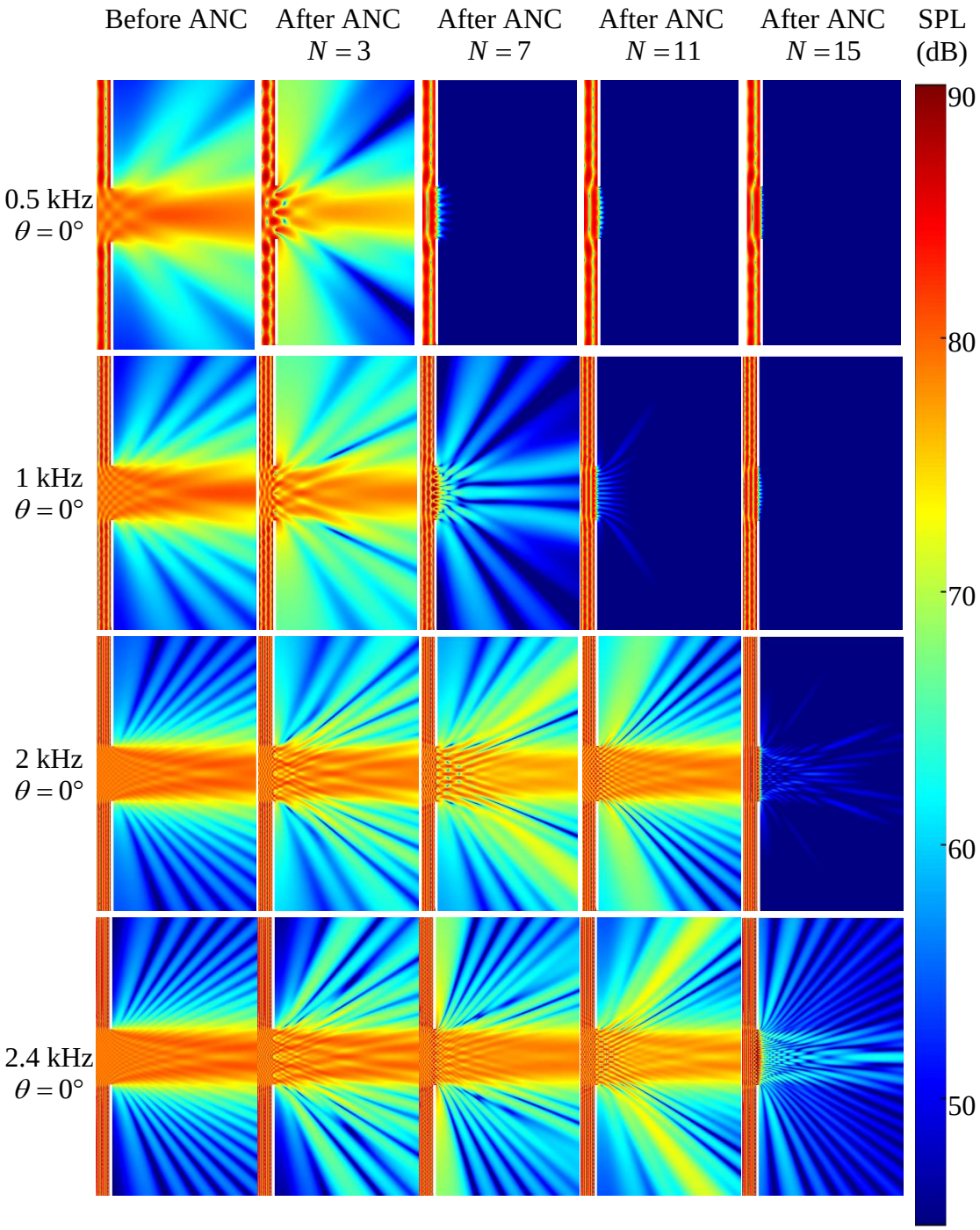

Figure 4.6: Sound pressure level distribution plots for four frequencies at when primary noise is incident at $\theta = 0°$ and secondary source array is at $x = 0$ m for $N = 3$, $N = 7$, $N = 11$, and $N = 15$ sources [Lam et al., 2018a].

the near field. This suggests that in practical applications of active control, the error microphones should be placed at a sufficient distance away. Based on the free-field

analytical analysis of an infinite plane array of sources, the error microphones should be placed at least half the separation distance away for frequencies at which w is less than half a wavelength [Elliott et al., 2018]. From observation of other instances of good control in Figure 4.7 and as suggested by Elliott et al. [Elliott et al., 2018], the error microphones should be greater than half the source separation distance away at higher frequencies due to more complex and intense near-field sound pressures.

In cases beyond the cut-off frequencies in Figure 4.5(a), such as at 2 kHz with $N = 7$, there is an undesired increase of sound pressure at other areas outside the noise main lobes, as depicted in the corresponding plots of Figure 4.6. Hence the frequency range of the controller should be limited to avoid such high-frequency enhancements.

4.2.2.2. Number of Sources Required for Good Control

To determine the maximum separation distance, and hence the total number of sources required to achieve global reduction for an aperture of variable size, the attenuation performance is plotted as a function of kw. The results for six different separation distances, w, are shown in Figure 4.7, namely, with N equals to 2, 3, 5, 7, 9, and 13, and w set using (4.8). The array of sources is situated at $x = 0$ m, and a primary plane wave impinging at $\theta = 0°$ incidence. The results of $N = 1$ are included in Figure 4.7, for reference, with w set to 1.

When $kw < \pi$, the attenuation performance was at least 20 dB for $N > 2$ sources, where the separation distance w is less than half the acoustic wavelength. Attenuation performance terminates at frequencies $kw \geq 2\pi$, in line with the free-field cases [Elliott et al., 2017] and as shown evidently in Figure 4.7. It is also worth noting that as N increases, the minimum separation distance approaches λ instead of $\lambda / 2$. While using

this guideline, one must keep in mind that these results are the theoretical limits of the ANC system and must consider the loss in fidelity when electronic systems are implemented.

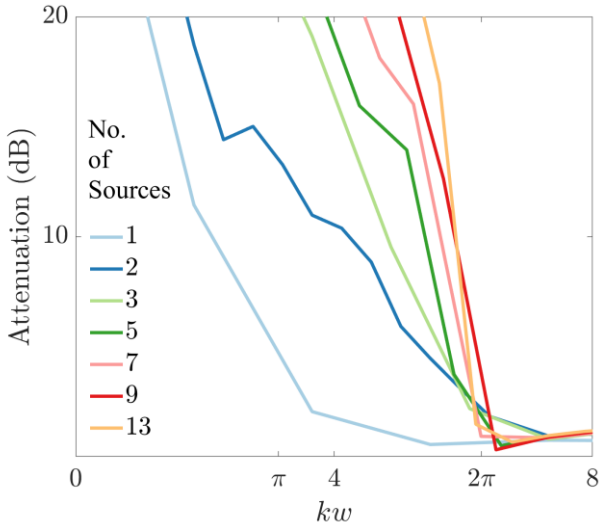

Figure 4.7: Attenuation performance as a function of frequency and separation distance, kw, when primary noise is incident at $\theta = 0°$, for a number of control sources arrangements located at $x = 0$ m [Lam et al., 2018a].

As the acoustic window is required to attenuate noise from different dominant incidence angles (e.g. control of traffic noise at the upper floors of high-rise buildings), the active control performance is investigated in the following sub-section for different noise source incidence angles.

4.2.2.3. Performance at Oblique Angles of Incidence

Oblique noise incidences are cases analogous to noise impinging on windows at different levels of a high-rise building. For instance, an incidence angle of $60°$

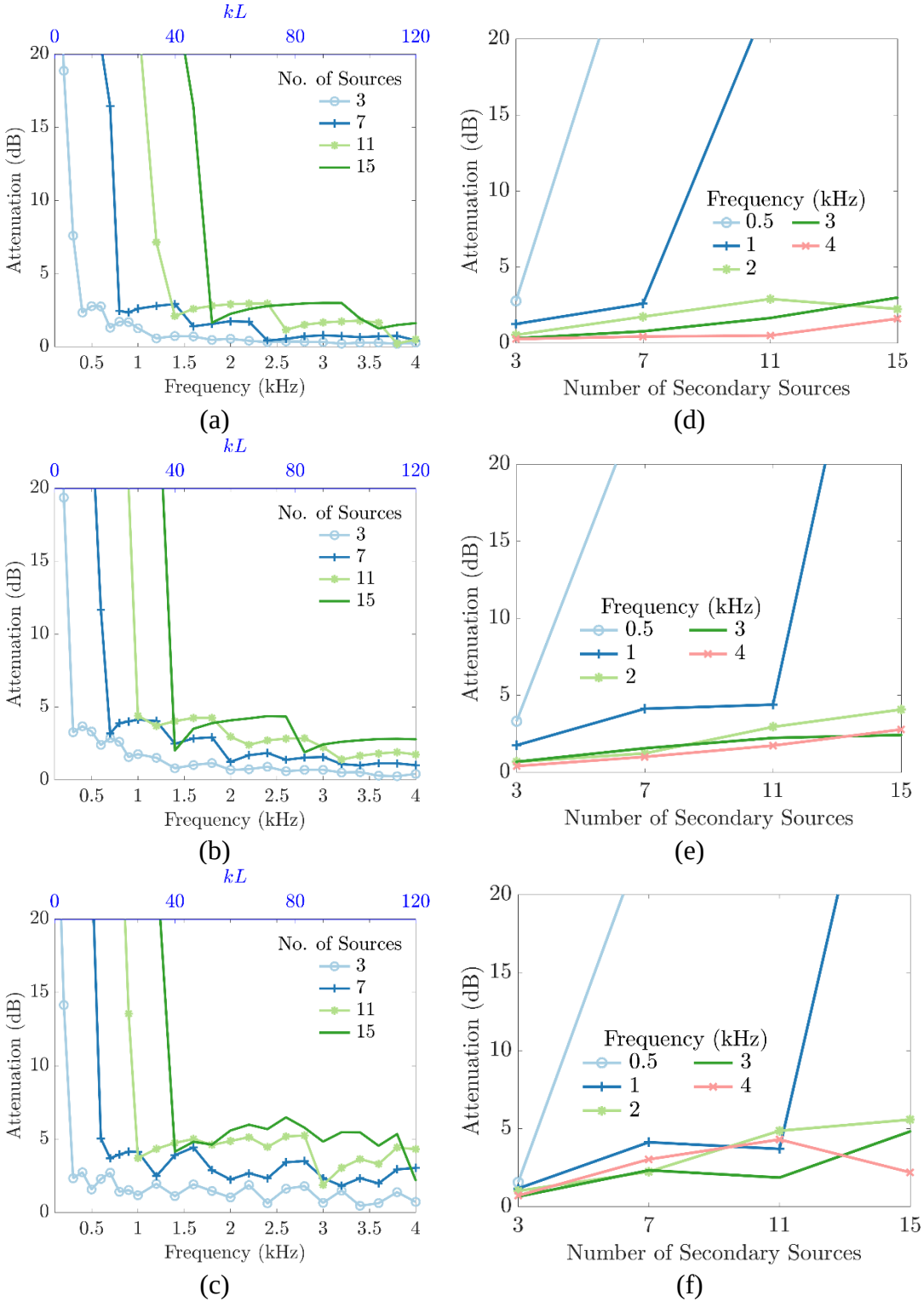

Figure 4.8: Attenuation performance as a function of frequency when the primary noise is incident at (a) 30° , (b) 60° , and (c) 90° ; and as a function of the number of secondary sources when the primary noise is incident at (d) 30° , (e) 60° , and (f) 90° [Lam et al., 2018a].

corresponds to an approximate position at the tenth storey of the building (for a road at surface level, 100 m away from the building).

As the angle of incidence increase, the cut-off frequencies decreases as shown in Figure 4.8 for incidence angles θ at (a) $30°$, (b) $60°$, and (c) $90°$. The corresponding minimum number of sources to achieve 20 dB of attenuation at 1 kHz increased from $N = 9$, for the normal incidence case in section 0, to $N = 11$ for $\theta = 30°$, and $N = 13$ for $\theta = 60°$ and $90°$, as shown in Figure 4.8 (d), (e), and (f), respectively.

To illustrate the effect of oblique incidences on the minimum source separation distance w for good global control, the attenuation is plotted as a function of kw for different values of θ, when $N = 15$, as shown in Figure 4.9. The cut-off frequencies in Figure 4.9 show that for frequencies up to $90°$, the separation distance has to be less than half the wavelength ($kw < \pi$). These results are in line with the guideline determined from the free field analysis [Elliott et al., 2017, 2018], such that $w < \lambda/(1+\sin\theta)$.

The findings can be further generalised by taking the window size, L, into consideration. Since $w = L/N$, N can be decided based on $w < \lambda/(1+\sin\theta)$ to give

$$N > \left\lceil \frac{L(1+\sin\theta)}{\lambda} \right\rceil, \text{ for all } \theta \le 90°, N \in \mathbb{Z}^+ \tag{4.9}$$

where N is a positive integer $\mathbb{Z}^+$, and $\lceil L(1+\sin\theta)/\lambda \rceil$ is the ceiling function that yields the smallest integer greater or equals to $L(1+\sin\theta)/\lambda$. As seen in Figure 4.8(e) and from (4.9), more than 11 sources are needed if $\theta = 60°$ for frequencies up to 1 kHz.

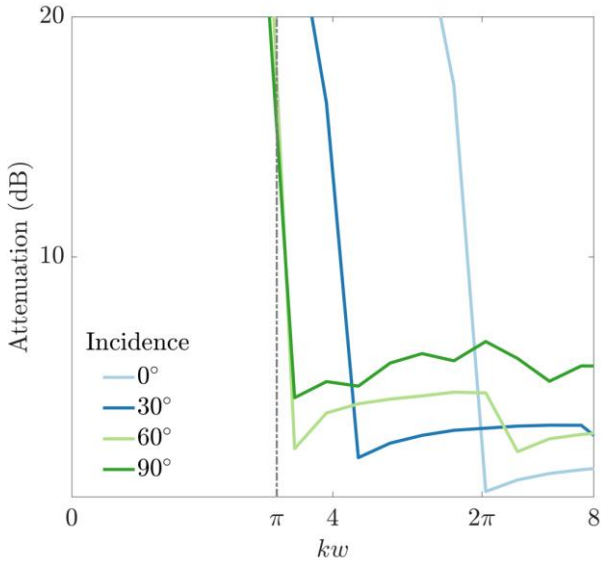

Figure 4.9: Attenuation performance as a function of kw when $N = 15$ at primary noise incidence angles from $\theta = 0°$ up to $90°$, [Lam et al., 2018a].

4.3. Active Control of Sound through Partially Blocked Apertures

The distributed layout ANC studies introduced in section 2.2.2 are focused on the control of noise through unobstructed apertures. With the fundamental limits of control established for the open aperture in the previous subsection, the application to a viable scenario is explored next. Since sliding windows are common fixtures around the world and are especially prevalent in Singapore, the effect of sliding window panels on ANC performance is introduced and investigated through numerical studies and to be validated with experiments in Chapter 5.

4.3.1. Passive Insulation of Single-glazed Windows

Sound insulation provided by a tightly-sealed, 6 mm thick, single-glazed window is a reasonable benchmark to grade the attenuation performance of open window active control systems. The 2D finite element method (FEM) simulation is set up to determine

the transmission loss of a fully glazed window, as shown in Figure 4.10(a). The noise source is initiated as a background plane wave that is travelling in the x-axis direction when the incidence angle θ is $0°$. For consistency and accuracy, the minimum element size is fixed at one-sixth the wavelength of 4000 Hz.

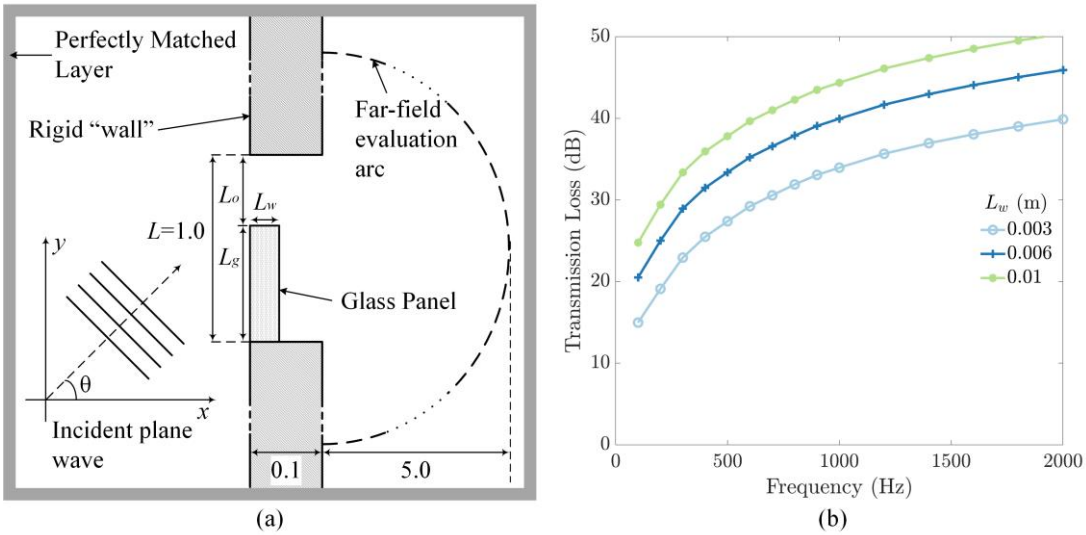

Figure 4.10: (a) FEM simulation model to determine passive insulation of a fully-glazed aperture with glass thickness of L_w m. (b) The corresponding transmission loss $TL_{GR=1}$ of glass panels with different thickness, L_w m, at 0° noise incidence [Lam et al., 2018c].

The transmission loss is calculated by evaluating the sum-of-the-squared pressures on a far-field arc, written as

$$TL_{GR} = 10\log_{10}\frac{\mathbf{p}_{L_g}^{\mathrm{H}}\mathbf{p}_{L_g}}{\mathbf{d}^{\mathrm{H}}\mathbf{d}}, \tag{4.10}$$

where $\mathbf{d}$ is a vector of complex pressure values at the arc without the glass panel, $\mathbf{p}_{L_g}$ is the vector of complex pressure values at the arc when the glass is L_g m, and $GR = L_g / L$ is the glazing ratio.

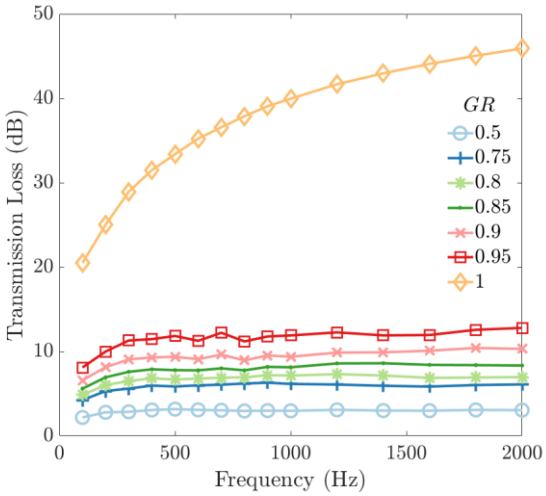

Figure 4.11: Transmission loss TL_{GR} for different GR, with glass thickness L_w at 6 mm, at $0°$ noise incidence [Lam et al., 2018c].

Transmission loss due to the passive insulation of a sealed window is emulated with a glass panel spanning the entire aperture and a thickness of L_w m, as shown in Figure 4.10(b). From the simulation with a plane wave at $0°$ incidence, the full glazing performance $TL_{GR=1}$ increases uniformly across all frequencies as thickness L_w increases. Performance decreases rapidly with increasing wavelength, when the wavelength is larger than the size of the aperture, L m. Results from the FEM simulation for $L_w = 0.003$ m agrees with the measured data from past experiments using the reverberation chamber method as described in ISO 10140 [Quirt, 1982; Tadeu et al., 2007; Tadeu and Mateus, 2001; Yu et al., 2017]. To form a basis of comparison to the full-scale model, the size of the aperture is fixed at $L = 1.0$ m for all FEM simulations in this study. The thickness L_w is fixed at 0.006 m (6 mm) from this point forth, as the thickness of 6 mm is commonly used in single panel windows in Singapore and Hong Kong [Tong et al., 2015].

The transmission loss TL_{GR} due to the glass panel degrades drastically once the glazing ratio is less than 100%, and degrades gradually as the glazing ratio decreases, as shown in Figure 4.11. It is worth noting that passive attenuation is still notable (more than 5 dB) and uniform across all frequencies for glazing ratio is between 75% and 95%. The reduced attenuation of the window panel at frequencies 300 Hz and below also presents a complementary role for an ANC system to provide increased attenuation, as demonstrated by Carme et al [Carme et al., 2016a].

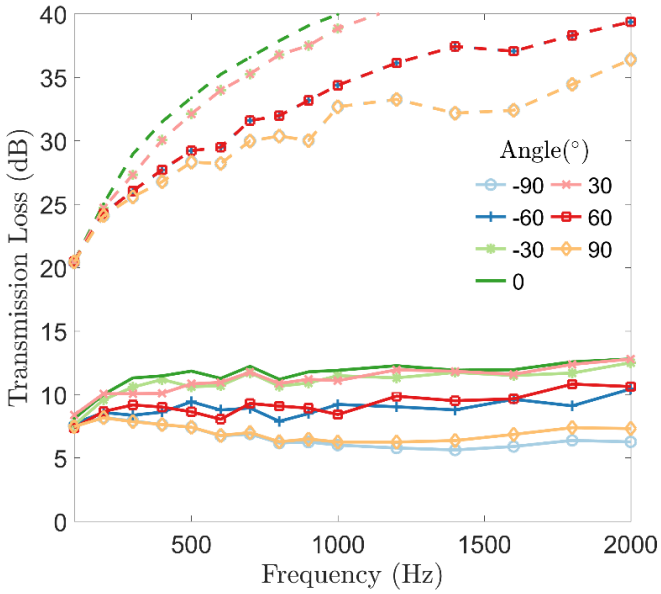

Figure 4.12: Transmission loss as a function of frequency at full glazing $TL_{GR=1}$ (dashed line), and 95% glazing, $TL_{GR=0.95}$ (solid line), for noise incidence angles from –90° to 90° in 30° intervals [Lam et al., 2018c].

When the plane wave incidence angle is varied from –90° to 90°, the attenuation performance degrades noticeably as shown in Figure 4.12. There is also no notable difference between the symmetric (with respect to the x-axis) noise incidence angles (negative), as shown in Figure 4.12.

4.3.2. Active Control Formulation

The active control system is evaluated using a combination of the simulation setup shown in Figure 4.10(a) and Figure 4.1. In the distributed control system, the control sources are symmetrically distributed across the entire opening, where sources are spaced $w = L/N$ m apart with peripheral sources $w/2$ m away from the wall, as determined by (4.8) and depicted in Figure 4.13. The minimum number of sources required in the aperture can be guided by (4.9).

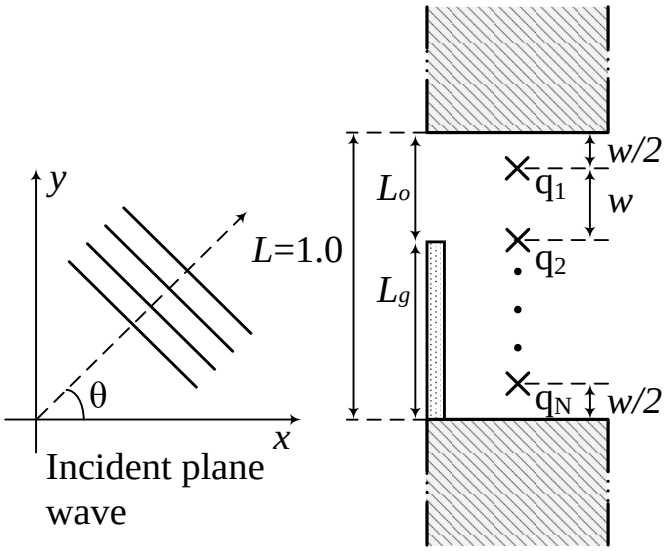

Figure 4.13: Relative position of a L_g m wide glass panel with secondary sources distributed within the $L = 1$ m wide aperture. [Lam et al., 2018c].

Similar to the transmission loss defined in (4.10), the transmission loss of the active control system can be written as

$$TL_{GR,ANC} = -10\log_{10}\frac{\mathbf{e}^{\mathrm{H}}\mathbf{e}}{\mathbf{d}^{\mathrm{H}}\mathbf{d}}, \tag{4.11}$$

where GR is the glazing ratio, **e** is the vector of complex pressure values after active control, and **d** is the vector of complex pressure values of the fully open aperture ($L_g = 0$ m), with the latter two defined in (4.1).

4.3.3. Active Control of Noise with a Single Array of Control Sources

Although another active control system was proposed to control noise through the partial opening of a sliding window in France, the design was limited by the maximum opening size of 0.13 m as mandated by the local government for child safety reasons [Carme et al., 2016a]. However, it is still useful to determine the physical limits of the single-sided boundary layout used in the French study, in comparison to a distributed layout to achieve global reduction of noise in the room interior.

The single-sided boundary layout, and a proposed single array distributed system is evaluated numerically in 2D as depicted in Figure 4.14(a), where $q_{(x,y)}$ represents the source locations in their respective cartesian coordinates. Based on the general rule from (4.8), $w/2$ is 0.0625 m if the aperture is 1 m wide. Besides the comparison between single boundary and distributed control strategies, the attenuation contributed only by passive structures is also included in Figure 4.14(b) and (c), for a normally incident plane wave noise.

The 2D numerical simulation is analogous to a top-view cross-section of a sliding window system. When L_g is set to 0.5 m, it depicts the scenario of a fully-open two-panel sliding window system that is typically installed in Singaporean homes. As expected, both the single source systems struggle to yield noticeable attenuation beyond 100 Hz, as shown in Figure 4.14 (b). At 90% glazing ($L_g = 0.9$ m), however, an increase

in attenuation by as much as 8 dB is observed when the source is located $w/2$ m away from the wall for frequencies less than 800 Hz, as illustrated in Figure 4.14(c).

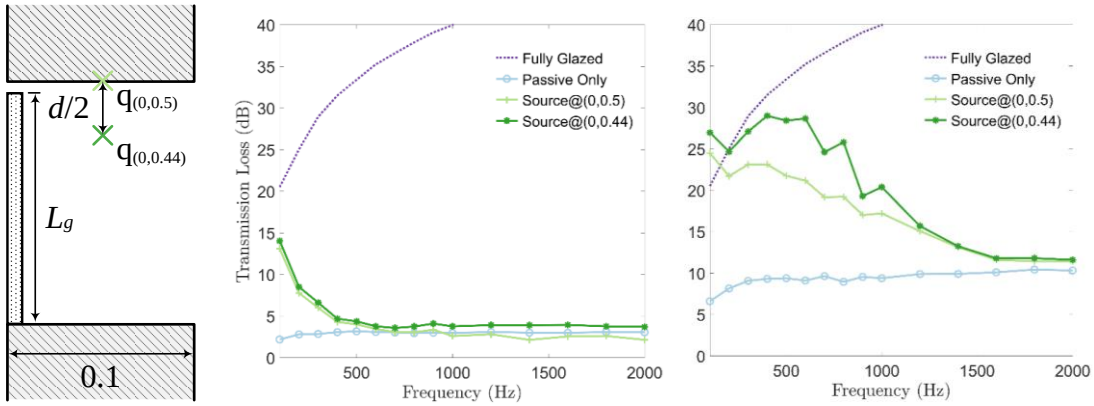

(a) (b) (c)

Figure 4.14: Transmission loss (TL) of two single source ANC systems at source positions (0, 0.5) m (—●—) and (0, 0.44) m (—+—), as a function of frequency in comparison to passive performance of the glass panel (—○—) and when fully-glazed (''''). The TL when $L_g = 0.5$ m and $L_g = 0.9$ m is shown in (b) and (c) respectively, with the relative positions of the sources depicted in the cross-sectional view in (a) [Lam et al., 2018c].

As the angle of noise incidence increases, the improvement in performance by placing the single line source $w/2$ m away from the wall edge is similar to the normally incident case. The attenuation performance of both single line sources at $\theta = 30°$ and $\theta = 90°,$ is depicted in Figure 4.15(a) and (b) respectively. Hence, it is evident that the attenuation performance of an open window ANC system is significantly limited when sources are placed at the boundary, especially at higher frequencies of interest and steeper angles of incidences.

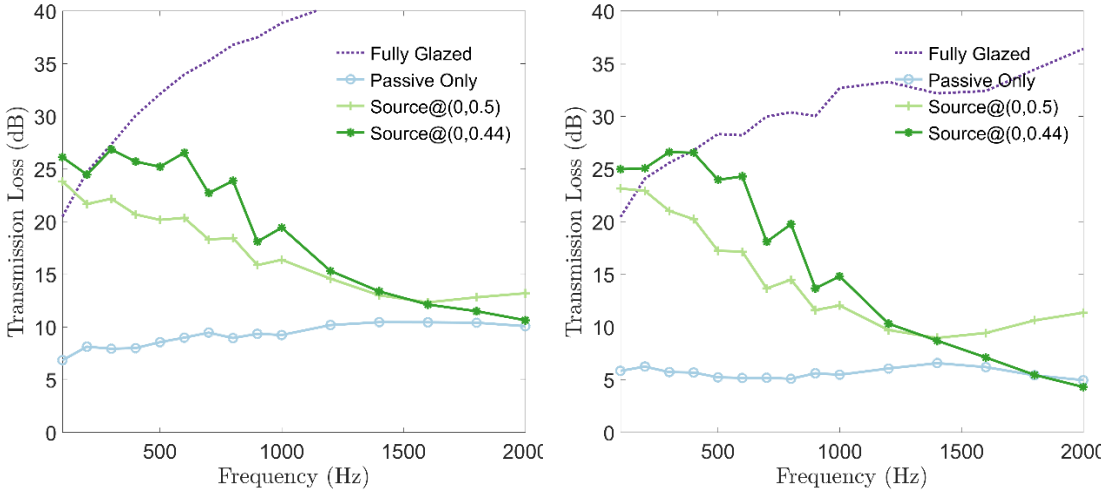

(a) (b)

Figure 4.15: Transmission loss as a function of frequency, $TL_{GR,ANC}$, of two single source ANC systems with $L_g = 0.9$ m at source positions (0, 0.5) m (—●—) and (0, 0.44) m (—+—), when the primary noise is incident at (a) $30°$, and (b) $90°$. For comparison, the passive attenuation provided by the glass panel (—○—), $TL_{0.9}$, and when fully-glazed (····), TL_1, is included. [Lam et al., 2018c].

4.3.4. Distributed Layout Active Control System at Normal Incidence

By investigating the physical limits of different distributed-layout configurations, the minimum source configuration can be determined for a specific glazing ratio and vice versa. The attenuation performance of different configurations with noise at $\theta = 0°$ incidence, is illustrated in Figure 4.16 for glazing ratio of (a) 90%, (b) 80%, (c) 75%, and (d) 50%.

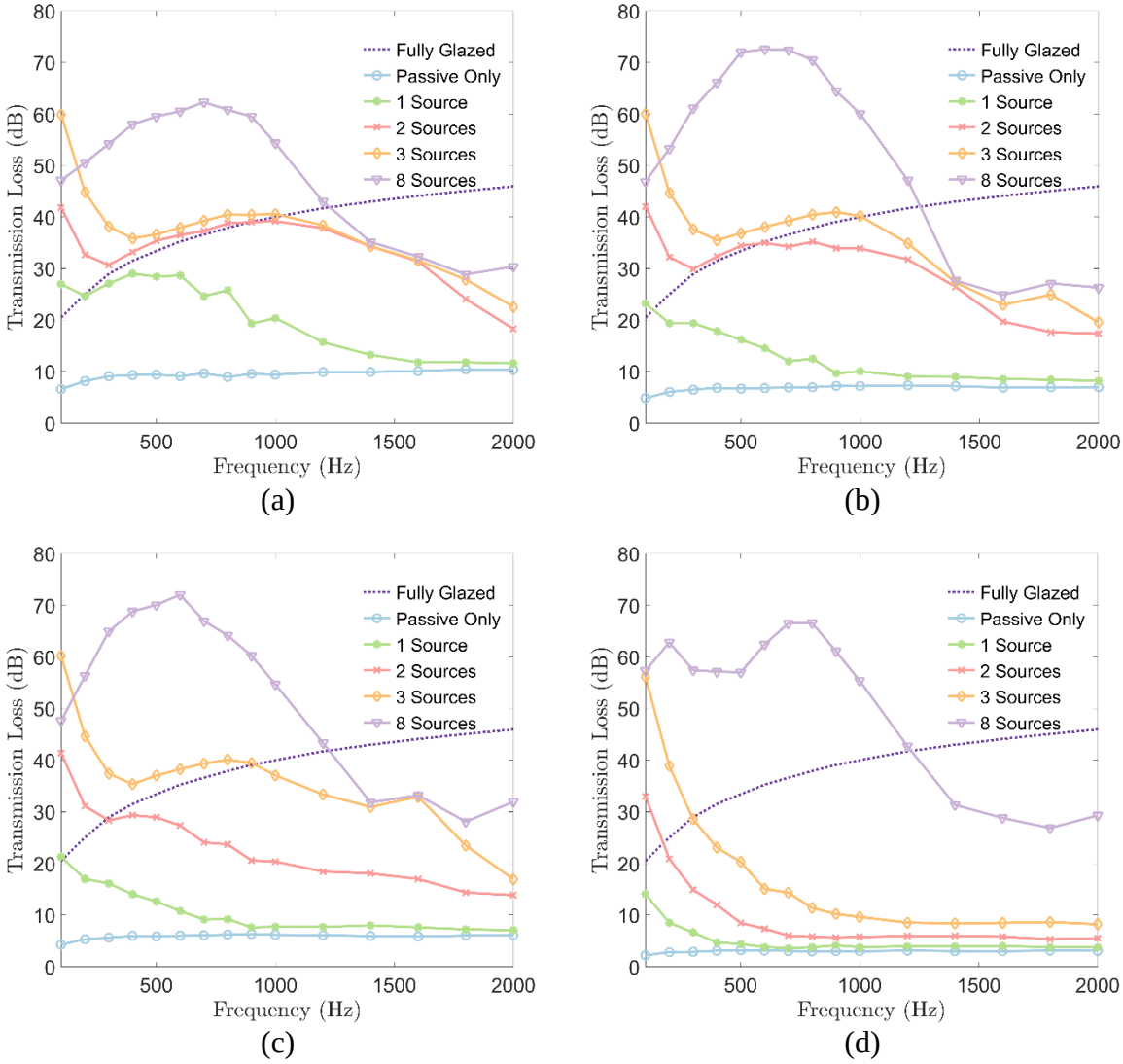

Figure 4.16: Transmission loss (TL) with 1 (), 2 (), 3 (), and 8 () control sources with (a) 90%, (b) 80%, (c) 75%, and (d) 50% glazing, at $0°$ noise incidence angle [Lam et al., 2018c].

For the numerical simulations of the distributed layout, the position of the N incoherent line sources corresponds to the subscript numbering of sources q_N as shown in Figure 4.13. For instance, one source corresponds to q_1, and three sources are located at positions q_1, q_2, and q_3. The results when N is 1, 2, 3, or 8 are highlighted and

compared to the transmission loss of a fully glazed window, and the contributions due to partial glazing without control, as shown in Figure 4.16.

When there are control sources symmetrically distributed across the entire aperture (i.e. $N = 8$), the transmission loss of the ANC system $TL_{GR,ANC}$ exceeds that of a fully glazed aperture without control TL_1 (''''), up till 1200 Hz for GR greater than 50%. Although active control with sufficient sources across the entire aperture could ideally yield greater attenuation performance than a fully glazed aperture, it is still worthwhile to determine the minimum configuration that can yield sufficient attenuation for sustainability and practicality.

To achieve similar attenuation as the fully glazed aperture, a minimum of two sources are required when the glazing ratio is 80% or less, for frequencies less than 1000 Hz, as shown in Figure 4.16(a) and (b). If the benchmark is lowered to 20 dB, a minimum of 2 sources is required for 75% glazing as shown in Figure 4.16(c). The minimum number of sources with respect to the opening size L_o, can be further generalised to $N_{min} = L_o / w$, where w is predetermined based on the general rule shown in (4.8). At a separation of $w = 0.125$ m, the ANC system would be effective up to 2500 Hz at $0°$ incidence and up to half that frequency at $90°$, which would be sufficient to tackle traffic noise at the window [Jagniatinskis and Fiks, 2014].

4.3.5. Performance at Different Angles of Incidence

In the 2D simulation model shown in Figure 4.13, the angle of incidence refers to the azimuthal angles, for instance, from a moving noise source in the horizontal plane. This is analogous to a top-view cross-section of a domestic sliding window. Since the glass

panel in the aperture is asymmetric, the angles of incidence are simulated from $\theta = -90°$ to $90°$.

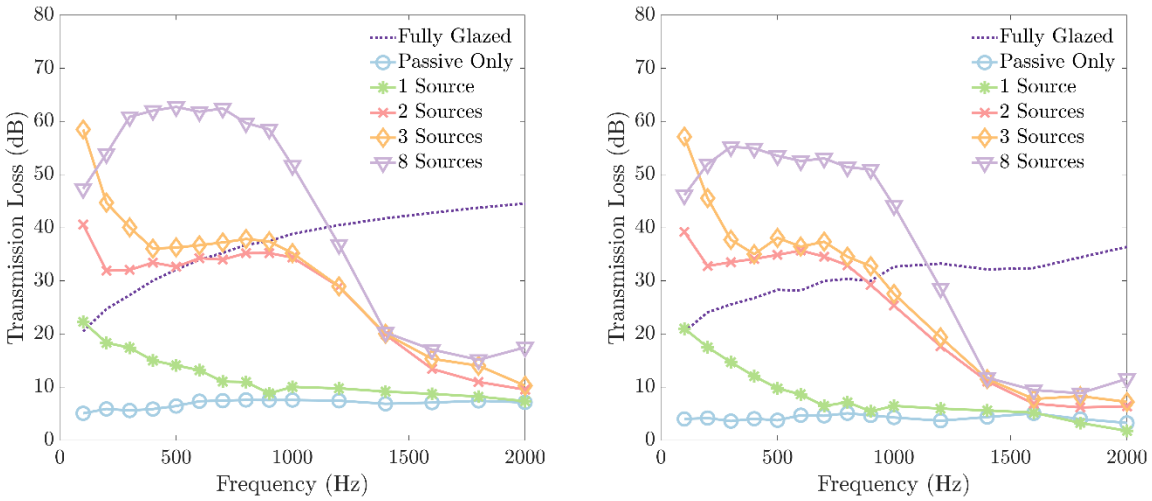

Figure 4.17: $TL_{GR,ANC}$ of $N = 1, 2, 3,$ and 8 source configurations at 80% glazing for noise incidence angles at (a) $30°$, and (b) $90°$ [Lam et al., 2018c].

When the noise is normally incident, the performance of both two and three source configurations at a glazing ratio of 80%, sufficiently satisfy the benchmark of the fully glazed system, as shown in Figure 4.16. At glazing ratio of 80%, the $TL_{0.8,ANC}$ of the two and three source configurations also satisfy the benchmark as shown in Figure 4.17 for incidence angles of (a) $30°$ and (b) $90°$. The attenuation performance of the corresponding negative noise incidence angles are similar to the positive ones. Since the performance of the two-source system closely matches that of the three sources, it suggests that two sources at 80% glazing can sufficiently attenuate noise at least as well as full glazing at all incidences θ.

4.4. Summary

The fundamental limits of control were firstly determined for an unobstructed open aperture via 2D FEM simulations. From the effect of source arrangement on attenuation performance of the secondary source array, it was found that the peripheral sources of the array should not be placed on the edge of the walls. The gap between the peripheral sources and the wall edge was determined empirically to be half the separation distance between the sources in the array. The underlying factors behind this observation can be explained by the failure of the single source at the edge in controlling the large magnitude normal particle velocities due to diffraction at the edges, which will be discussed in further detail in Chapter 6. Aligning the array in the centre of the wall depth yielded the best average performance for the frequency range of interest (100 Hz to 4 kHz). Finally, a design guideline was derived to suggest the minimum number of sources required for good control in terms of the desired upper frequency and noise incidence angle limit.

Based on the findings from the open aperture investigation, the fundamental limits of control were determined for an aperture fitted with a glass panel to emulate a sliding window system. The passive insulation at different states of glazing of a 6 mm thick single glass panel is firstly characterised to form a benchmark for active control. For an 80% glazing scenario, three sources arranged based on the open aperture guidelines in the opening can provide better attenuation than that of the passive insulation of a fully-closed window, up to 1 kHz at 90°. An experimental setup based on the dimensions of the simulations emulating the sliding window system is described in Chapter 5.

Chapter 5

Real-time Active Control of Noise through a Full-sized Sliding Window

After determining the physical limits of active control for numerical model of the system under study (a regular sliding window configuration) in Chapter 3, the cost function choice, error sensor arrangement, the quality of the reference signal and the controller algorithm and hardware choice must be optimized in sequence to approach the physical limits [Hansen et al., 2012].

Hence, this chapter firstly describes the test chamber with full-sized windows and its interior acoustic characteristics. Secondly, the construct of the control sources and sensors, and their placements based on the guidelines obtained in Chapter 4 is detailed. Thirdly, the active control performance is predicted with an offline simulation using measured secondary path transfer responses. Lastly, the real-time active control performance is evaluated with monitoring microphones distributed across the interior of the test chamber to evaluate the reduction energy-average and planar-average sound pressure levels.

5.1. Test Chamber

To realise the distributed layout active control system on a full-sized sliding window, a test chamber was designed and constructed to mimic a small room in a regular apartment. The frequency response of the chamber was measured to determine the extent of modal effects in the chamber after acoustic treatment. An acoustic camera used to analyse the sound pressure distribution of the primary noise source propagating through the window aperture to understand the limitations during the interpretation of the experimental results as a result of space constraints in the test environment.

5.1.1. Physical Characteristics of Test Chamber

A $2\times2\times2$ m^3 wooden chamber was constructed and placed in a recording studio, as depicted in Figure 5.1 and Figure 5.2(a). The wooden chamber consists of five 30 mm and one 36 mm thick plywood panels, with the thickest panel housing the window structure that faces the noise source.

A 1×1 m^2 sliding window is installed in the aperture, accompanied by a security grille. The window and grille conform to the standards for domestic windows set by the Singapore standards body, SPRING Singapore [SPRING (Standards Productivity and Innovation Board) Singapore, 2007]. After discounting the frames of the window and grilles, the effective open area of the two-panel sliding window is $(0.93/2)\times0.93$ m^2, where the shorter dimension represents the width and the larger dimension representing the height.

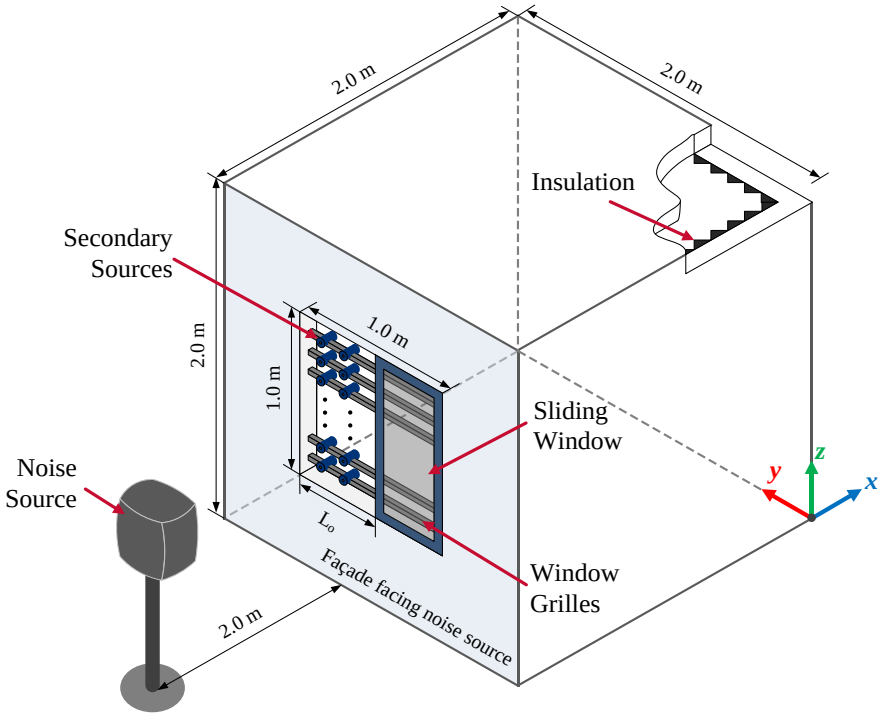

Figure 5.1: A sketch of the experimental setup with dimensions in m [Lam et al., 2018c].

(a) (b)

Figure 5.2: Image of the test chamber from the (a) exterior, and (b) interior.

To minimise the interference at the error microphones due to reverberation, the inside surface of the entire chamber has been lined with acoustic foam, as shown in Figure 5.2(b). The opening size is depicted by L_o m and the noise source is located 2 m away from the middle of the opening, as depicted in Figure 5.1.

5.1.2. Acoustic Characteristics of the Test Chamber

Although the interior of the test chamber has been lined with acoustic foam to reduce reverberations, it is still necessary to determine the lowest frequency where the active and passive control performances are not affected by acoustic modes. To evaluate the diffuseness of the sound field within the chamber, the frequency response of the test chamber and its reverberation time is evaluated. The equipment and software used to evaluate the frequency response and reverberation time is detailed in the appendix B.1.

The frequency response of the chamber is measured with the windows fully closed, as the modes are released when the window is opened. The sound pressure level is plotted as a function of frequency, as shown in Figure 5.3(a). The first six modes of the room can be distinguished from the sharp crests and troughs and are annotated in Figure 5.3(a). It is evident from the frequency response that frequencies above 700 Hz will not be affected by the room effects.

For further insight into how the low frequencies may affect the active control performance, the reverberation time and its corresponding correlation factor is evaluated. The reverberation time RT_{60} is estimated using the T_{30} method in accordance to ISO 3382-2:2008 [International Organization for Standardization, 2008], using a logarithmic sine sweep from 50 Hz to 20 kHz. The RT_{60} is presented as a function of one-third

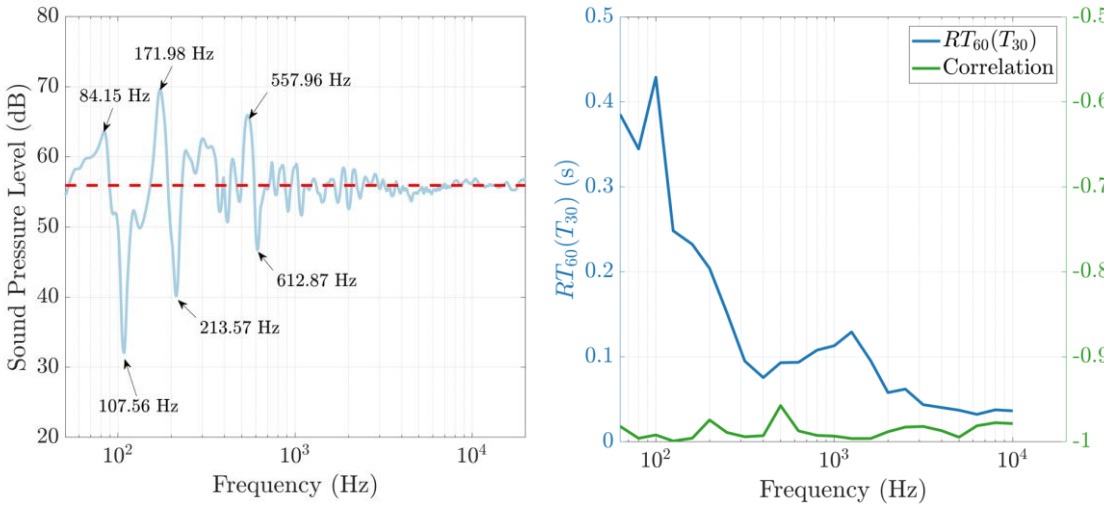

(a) (b)

Figure 5.3: (a) Frequency response of the test chamber and the (b) RT_{60} reverberation time measurement calculated with the T_{30} method and its corresponding correlations.

octave frequencies from 50 Hz to 10 kHz, as shown in Figure 5.3(b). The RT_{60} is less than 0.15 s when frequencies are 315 Hz and above, as depicted in Figure 5.3(b) by the left-hand y-axis. The corresponding correlation factors (measurement reliability of RT_{60}) are close to -1 (< -0.98) at all frequencies, with the exception at 200 Hz and 500 Hz, which correspond to modes as shown in Figure 5.3(a). Hence, based on the RT_{60} and correlation factor, frequencies 300 Hz and above are sufficiently damped in the test chamber.

5.1.3. Primary Source Characteristics

The primary noise source is emitted from a large loudspeaker (8351A, Genelec, Finland) that generates a large wave front to mimic plane waves arriving at the aperture of the window. To determine the limitations due to limited space in the recording studio that houses the test chamber, a 30-channel sliced wheel array acoustic camera (Type 9712-

Figure 5.4: Image of the acoustic camera placed 1 m from the window in the interior of the test chamber (Image has been enhanced for clarity).

W-FEN, Brüel & Kjær, Denmark) is employed to analyse the sound pressure distribution of the impinging primary noise at the sliding window aperture. The equipment and software used are listed in the appendix B.2.

The acoustic camera was placed 1 m away from the window aperture inside the test chamber and tuned to the beamforming mode to evaluate higher frequencies (1 kHz to 12 kHz), as shown in Figure 5.4. The sound pressure distribution is depicted by coloured contours at 1 dB intervals, as shown in Figure 5.5. The sound pressure distribution across the window of a 1 kHz sine tone shows that at least half of the active control units are within a 3 dB difference, as shown in Figure 5.5(a). When a bandlimited white noise signal (400 Hz to 1300 Hz) was emitting from the primary noise source, at least two-thirds of the units are within a 3 dB difference, as shown by the sound pressure level contours in Figure 5.5(b).

Although the primary noise source is not fully planar, the sound pressure distribution across the entire aperture is within 6 dB difference (note: primary noise speaker is placed in the centre of the opening; the off-centre view is a due to parallax error from the limited space in the chamber).

(a) (b)

Figure 5.5: Sound pressure distribution as detected by the acoustic camera when the primary noise is emitting a (a) 1 kHz tone, and (2) 400 Hz to 1.3 kHz bandlimited white noise.

5.2. Real-time Active Noise Control System

A real-time active noise control system is an electro-acoustical system consisting of numerous components. This section discusses the physical components and algorithms in the proposed multichannel ANC system for a full-sized sliding window. For ease of reference and clarity, the multichannel system is described based on a reference to a single-channel implementation. The design of the active control units comprising of a loudspeaker and microphone combination is described in detail. Finally, the active controller and the control algorithm is detailed.

5.2.1. Components of a Single-Channel Feedforward Active Noise Control System

A generalised practical active noise control system can be categorised into three distinct domains, as depicted in Figure 5.6: (1) the acoustic region, where the acoustic waveforms interact; (2) the analogue electronics region, where the acoustic waves are sampled and digitized for analysis and reconstructed for actuation; and (3) the digital domain, where the sampled waves are continuously analysed to generate a digital filter that seeks to minimise the acoustic pressure at the error microphone location.

The ANC system, as illustrated in Figure 5.6, is a typical single-channel feedforward configuration that consists of a pair of transducers (reference and error microphones) and a single actuator (loudspeaker). A reference microphone is placed along the propagation path of the noise to detect the oncoming noise signal. The reference signal, $x(n)$, is sampled and digitised by the analogue-to-digital converter (ADC) and input into the digital processor in the digital domain. The secondary source produces the acoustic anti-noise signal that is generated by the digital processor via the digital-to-analogue converter (DAC). At the error microphone position, the anti-noise signal from the secondary source combines with the noise source, which results in sound pressure reduction if the anti-noise signal is of equal amplitude and opposite phase with the noise. The error microphone signal, $e(n)$, is also sampled and digitised through an ADC to provide a feedback loop to the digital processor for a real-time adaptation to changes in the noise signal detected by the reference microphone and converge to a steady-state.

The blocks in the digital domain portray the commonly implemented filtered-x implementation of the least-mean-squares (LMS) algorithm [Elliott, 2001; Kajikawa et al., 2012; Kuo and Morgan, 1996], which is detailed in section 5.2.5. Adaptive filter

$W(z)$ is updated by the LMS algorithm, which aims to minimise the residual error signal $e(n)$. Since the output of $W(z)$ is calculated from $x(n)$ and $e(n)$, and combine acoustically with the noise signal at the error microphone location, there is a need to compensate the effects of the secondary-path transfer function. The secondary-path transfer function $G(z)$ from $y(n)$ to $e(n)$, includes the electronic components in between, as shown in Figure 5.6. This compensation for $G(z)$ is achieved by filtering the reference signal $x(n)$ with an estimate of the secondary path $\hat{G}(z)$, and hence the name filtered-x LMS (FXLMS).

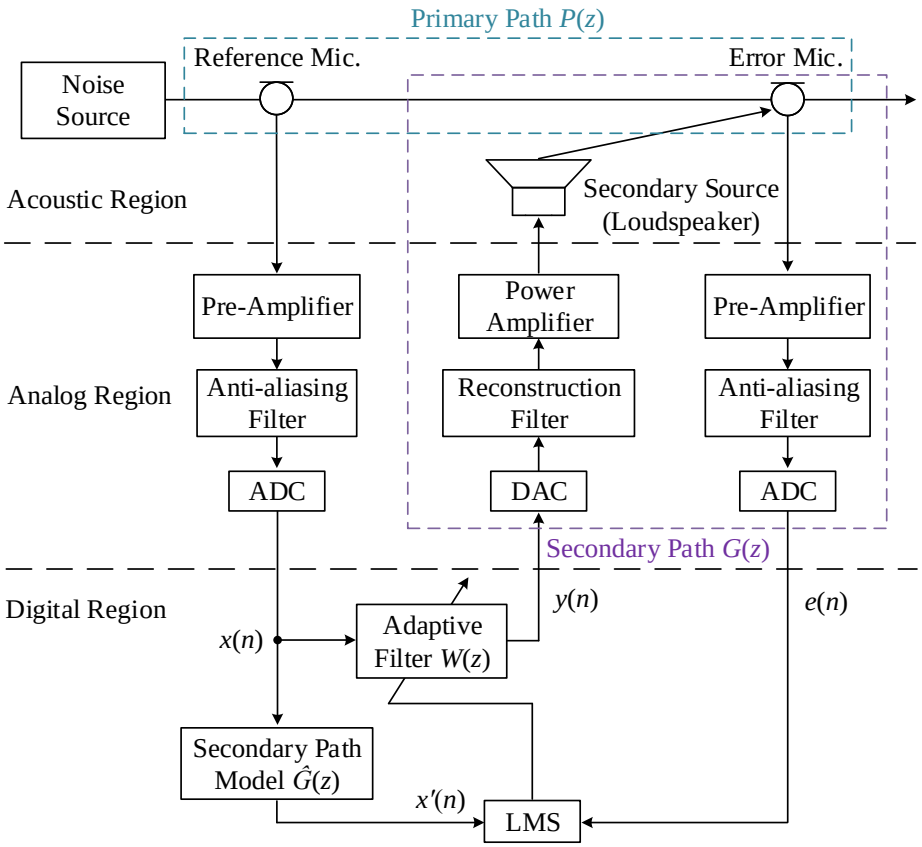

Figure 5.6: Block diagram of a single-channel FXLMS broadband feedforward ANC system segregated into three domains for clarity [Kajikawa et al., 2012]

The primary path $P(z)$ is the transfer function from the reference sensor to the error sensor, which includes the acoustic plant and the sensor transfer function (including electronic components, such as the pre-amplifier, anti-aliasing filter, and ADC). Hence, if $W(z)$ is a good estimate of $P(z)$, good attenuation of broadband stochastic disturbances can be achieved, which is the goal of the ANC system for open windows. However, this assumes that there is sufficient time for the system to compute and generate the anti-noise signal before the noise signal passes beyond error sensor location, also known as the causality constraint.

5.2.2. Multi-channel Feedforward Active Control System

The single-channel system, which was introduced in Section 5.2.1, can be scaled to a multichannel system as depicted in Figure 5.7. A fully-coupled FXLMS implementation is usually denoted as the $J \times K \times M$ FXLMS system, where there are J reference inputs, K secondary sources, and M error sensors. Since each secondary source is controlled by its own control filter, there are K control filters to be updated in each time step. Moreover, there are $K \times M$ secondary paths and M primary paths.

However, the computational complexity of the fully-coupled FXLMS system increases dramatically with large K and M. Since the reference microphones are designed to be near the secondary sources, the collocated FXLMS algorithm [Murao and Nishimura, 2012] is adopted to reduce the computational complexity by K times, as shown in Table 5.1.

Hence, in the interest of investigating the real-time feasibility of an active control system with 24-channels distributed across the opening of a full-sized window, other variants of the FXLMS algorithm such as the leaky-FXLMS or normalised FXLMS

algorithms were not implemented. It is well documented that more robust variants of FXLMS carry additional computational overhead and have slower convergence rates.

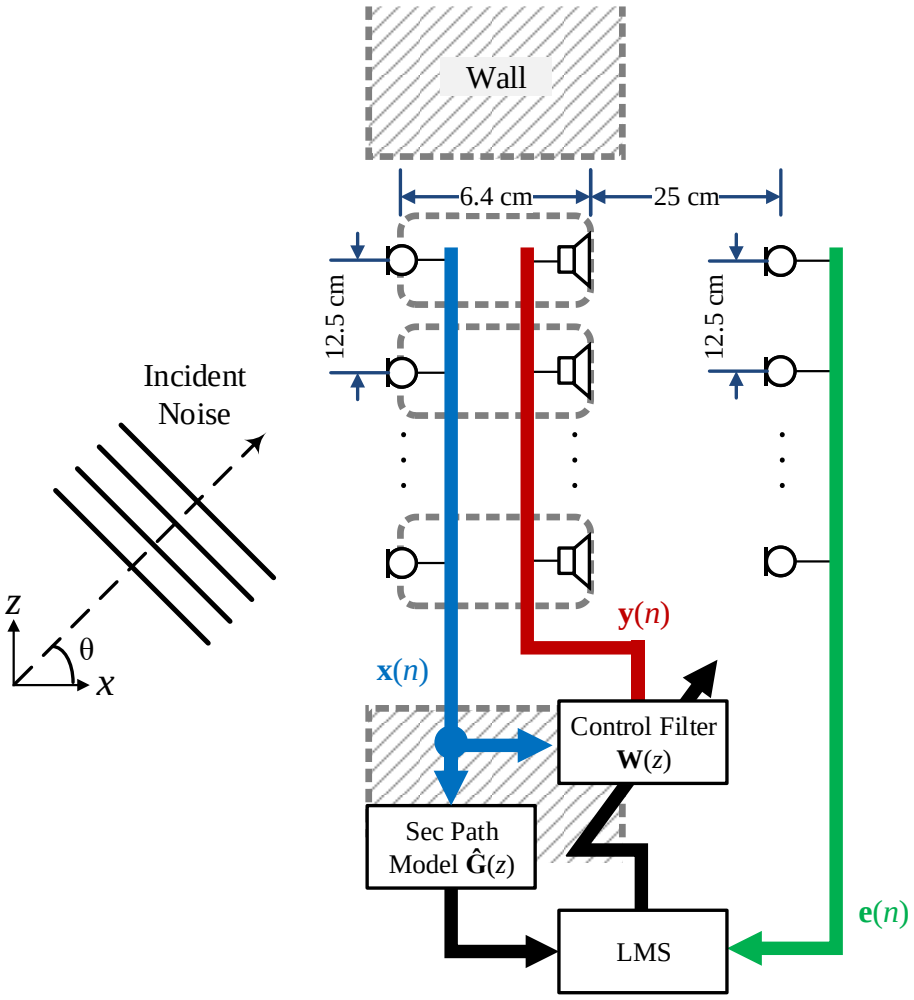

Figure 5.7: Block diagram depicts the side-view cross-section of the multichannel active control system in the window aperture showing the reference $\mathbf{x}(n)$, control $\mathbf{y}(n)$ and error $\mathbf{e}(n)$ signal vectors. The control filter $\mathbf{W}(z)$ is updated by the FXLMS algorithm. [Lam et al., 2018c]

Table 5.1: Comparative computational complexities of the fully-coupled and the collocated FXLMS algorithms with J reference sensors, K secondary sources, and M error sensors. L_w and L_s represent the filter tap lengths of the control filters and secondary paths respectively [Murao et al., 2017].

	Generating $\mathbf{y}(n)$	Filtering $\mathbf{x}(n)$	Updating $\mathbf{W}(z)$	Total Cost
Fully-coupled $J \times K \times M$	JKL_w	$JKML_s$	$JKM(L_w+1)$	$JK\left[M(L_s+1)+(M+1)L_w\right]$
Collocated $J(1\times1)\times M$	JML_s	JML_s	$JM(L_w+1)$	$J\left[M(L_s+1)+(M+1)L_w\right]$

5.2.3. Active Noise Control Units

The design of the active control units of the proposed system is adopted from previous designs by Murao et. al. [Murao et al., 2014; Murao and Nishimura, 2012]. Ideally the microphone and speaker should be collocated for optimal control performance; however, their proximity is highly dependent on the selection of transducers and the associated trade-offs. Since microphones have a significantly smaller physical footprint than loudspeakers, the selection of loudspeakers is an important factor affecting both the active control performance and visual obstruction in the window aperture.

To meet the low frequency attenuation requirements, electrodynamic speakers were chosen over the flat panel speakers used by Murao et al., based on results of a prior investigation [Fasciani et al., 2015]. Based on manufacturer reported specifications and preliminary testing, the Visaton BF 45 exhibited an acceptable low-frequency performance for speakers that are less than 5 cm in diameter, albeit at the expense of SPL output (79 dB mean SPL with 1W input measured at 1m). The detailed specification

of the Visaton BF 45 is appended in B.5.1. As the loudspeakers are not custom designed, the loudspeaker choice is limited by commercial availability and shaped by market demands. The surface area of the Visaton BF 45 aluminum diaphragm electrodynamic speakers ($\pi \times 0.045^2 = 0.002$ m^2) is approximately 2.5 times smaller than the flat panel speakers ($0.091 \times 0.055 = 0.005$ m^2) used by Murao and Nishimura, which translates to 2.5 times smaller visual footprint within the aperture.

Since the ANC system is adaptive in nature, a low-cost electret microphone breakout board can provide a reference signal of sufficient quality when coupled with anti-aliasing filters or oversampled by high resolution ADCs. The characteristics of the microphone module and its preamplifier is detailed in B.5.2 and B.5.3 respectively.

The enclosure is similarly lined with rockwool (100 kg/m^3) to reduce the acoustic feedback to the microphone and to increases the apparent volume of the speaker enclosure for more stable frequency response at low frequencies (< 500 Hz) [Beranek and Mellow, 2012a]. A detailed list of components used to construct the active control unit and their respective datasheets are shown in B.3.1 and B.5 respectively.

Each unit comprises of two separate housings for a speaker driver and a microphone, as depicted in the top and bottom 3D renderings of Figure 5.8(a) respectively. All the housings were 3D printed using polylactic acid (PLA) thermoplastic (1.25 g/cm^3) with the hexagon infill pattern at 80% infill density. Both sections of the housings are secured together by nylon screws and the air gaps are sealed with silicone. Each unit is mounted onto the horizontal bars of the window grille with nylon screws and damped with rubber mats to minimise the structural coupling when the speakers are operating. The attached units are shown from the interior and exterior perspectives in Figure 5.8(b) and (c) respectively.

(a) (b) (c)

Figure 5.8: (a) 3D diagram of the active control unit, (b) image of the active control units from the interior, and (c) exterior of the chamber.

The dimensions of the speaker housing are detailed in Figure 5.9, where the narrower and wider side-view cross-section dimensions are depicted in Figure 5.9(a) and (b) respectively. The front-view perspective of the speaker housing is shown in Figure 5.9(c). For a clearer representation, a darker shade represents depth and the shaded area indicates a solid fill. The dimensions of the microphone housing are detailed in Figure 5.10, where the inside-view and side view cross-section of the housing are shown in Figure 5.10(a) and (b) respectively.

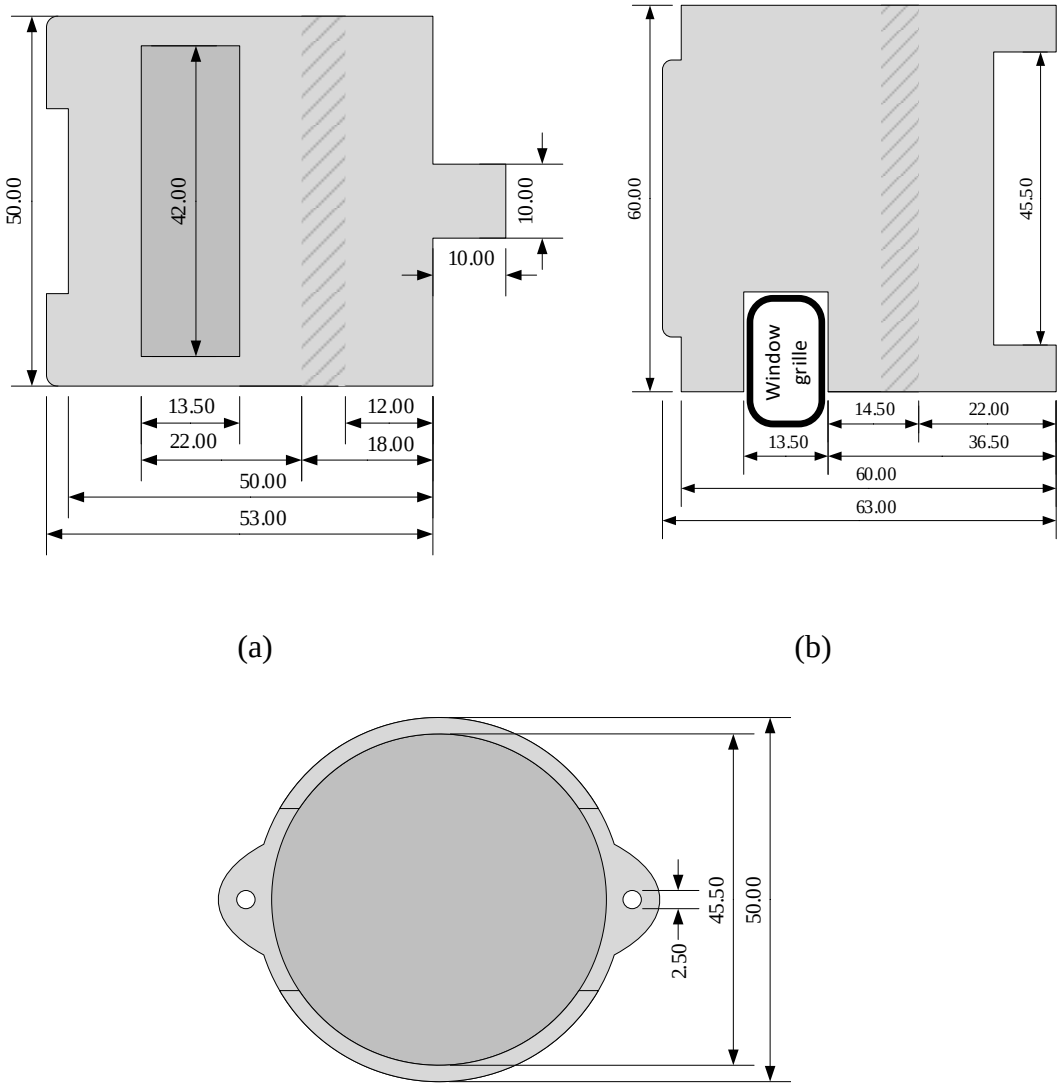

Figure 5.9: Cross-section of the (a) shorter and (b) wider sides of the speaker housing, which details the cut-out for attaching to the window grilles, and the (c) front view showing where the speaker driver is housed. The shaded area represents the solid sections and the darker shades indicates depth.

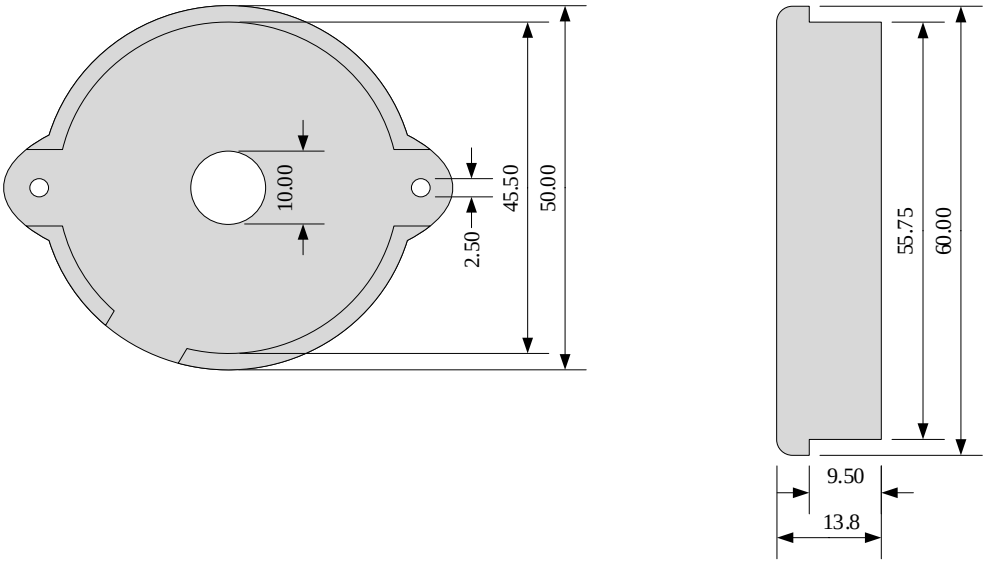

(a) (b)

Figure 5.10: (a) The inside view and the (b) side view cross-section of the of the microphone housing.

The placement of these active control units within the window aperture is guided by the conclusions from Chapter 4. A total of 24 active control units are evenly distributed in the open aperture of a full-opened 1 m by 1 m sliding window. As shown in Figure 5.7, the separation distance between the sources is 12.5 cm. This separation distance is equivalent to a cut-off frequency of 2747.2 Hz and 1373.6 Hz at $0°$ and $90°$ angles of incidence, respectively, as given by the relationship of $w < \lambda/(1+\sin\theta)$ in Chapter 4.2.2.3. The peripheral sources are placed approximately 6.5 cm away from the window frame. This configuration also corresponds to the 3 source representation in Chapter 4.3, which reflects at least 10 dB of insertion loss up till 1200 Hz at 50% glazing.

5.2.4. Active Controller

The adaptive FXLMS algorithm is programmed onto the configurable field-programmable gate array (FPGA) on the embedded controller (NI cRIO-9039) via National Instruments LabVIEW software and custom VHDL (VHSIC Hardware Description Language) code. The cRIO-9039 embedded controller is a modular 8-slot chassis that comprises of three NI-9220 16-channel input modules and two NI-9264 16-channel output module, as listed in B.3.2.

The 16-channel NI-9220 input module utilises individually isolated 16-bit resolution successive approximation register (SAR) ADCs, which have the lowest latency and settling time amongst the most common ADC topologies (e.g. pipeline and delta-sigma). Of the 48 channels available, 24 are connected to the reference microphones and the remainder connected to the 24 error microphones, as shown in Figure 5.11.

Each NI-9264 output module consists of 16 isolated channels of 16-bit resolution string DACs. Although the string DAC architecture is not built for high-speed applications, it has similar settling times as compared to resistor ladder (R/2R) DACs (~10 μs) and are considerably faster than delta-sigma DACs (> 1000 μs). A total 24 of the 32 available channels are connected to class AB amplifiers, which drives the loudspeakers in the active control units described in the previous section. Although class AB amplifiers are not energy efficient, their energy-efficient class D counterparts usually implement FIR filters that add significant delays (usually in tens to hundreds of ms).

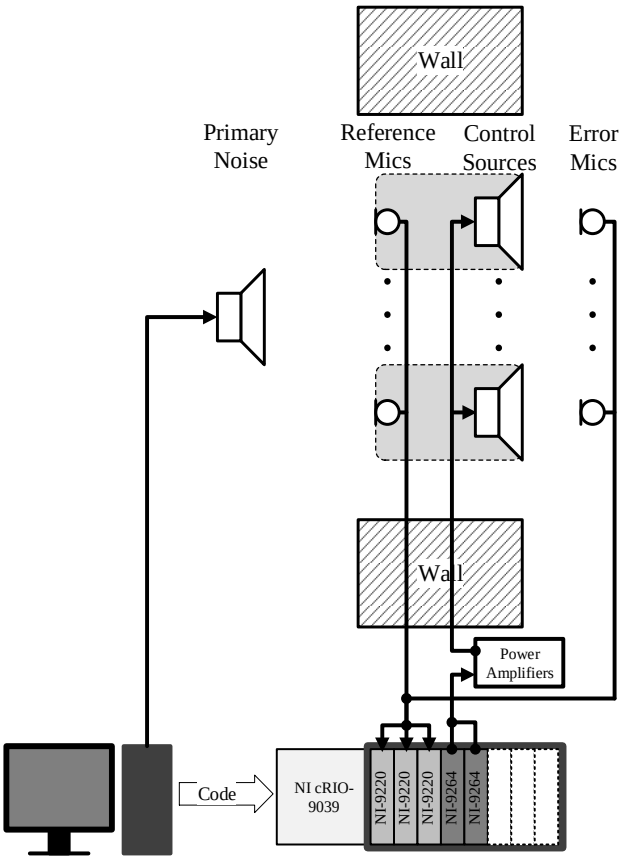

Figure 5.11: Block diagram of the components in the real-time active control system

5.2.5. Collocated Filtered-x Least Mean Square Algorithm

The non-causal optimal filters used in the FEM simulations in Section 4.1 can be decomposed from (4.3) to include the reference signal given by

$$\mathbf{q}_{opt} = \mathbf{W}_{opt}\mathbf{x}, \tag{5.1}$$

where $\mathbf{W}_{opt}$ is the optimal control filter and $\mathbf{x}$ is the reference signal picked up by acoustic transducers. In the interest of implementation, instead of calculating the coefficients of the optimal causal FIR control filter in (5.1), an adaptive approach is preferred as it is not strictly bounded by the assumption of stationarity and hindered by the potential instabilities during the inversion of potentially large matrices. Moreover,

adaptive algorithms usually consist of finite length FIR filters that can converge to the optimal Wiener filter coefficients under stationary conditions and are also capable of tracking changes in statistical properties of non-stationary signals.

The most widely implemented adaptive algorithm, the least-mean-squares (LMS) algorithm based on the concept of stochastic descent, adjusts the filter coefficients at each sample time n based on the instantaneous estimate of the error gradient [Kuo and Morgan, 1996] to give

$$\mathbf{w}(n+1) = \mathbf{w}(n) + \mu \mathbf{x}(n)\mathbf{e}(n), \tag{5.2}$$

where μ is the step size that determines the convergence rate and stability. Since the physical secondary path $\mathbf{G}(z)$ 'delays' the reference signal, it must be compensated in the adaptive algorithm to ensure convergence. Hence, the reference signal $\mathbf{x}(n)$ is filtered with an estimate of the secondary path $\hat{\mathbf{G}}(z)$ to time-align the reference and control signals at the error microphone position. The resultant FXLMS algorithm is a modified form of (5.2) [Kuo and Morgan, 1996] given by

$$\mathbf{w}(n+1) = \mathbf{w}(n) + \mu \mathbf{X}'(n)\mathbf{e}(n), \tag{5.3}$$

where $\mathbf{X}'(n) \equiv \hat{\mathbf{G}}^{\mathrm{T}}(n) \otimes \mathbf{x}(n)$ is the $JKL_s \times M$ matrix of filtered reference signals, and $\otimes$ denotes the Kronecker product convolution. The specific components of (5.3) can be written as

$$w_{kj}(n+1) = w_{kj}(n) + \mu \sum_{m=1}^{M} \mathbf{x}'_{jkm}(n) e_m(n), \tag{5.4}$$

where j, k and m are the indices of the respective J, K and M components. The vector

$$\mathbf{x}'_{jkm}(n) \equiv \hat{\mathbf{g}}_{mk}(n) * \mathbf{x}_j(n), \tag{5.5}$$

represents the components of the filtered reference signal $\mathbf{X}'(n)$. The vector $\hat{\mathbf{g}}_{mk}(n)$ denotes the impulse response of the estimated secondary path from the k-th secondary source to the m-th error microphone, and $*$ is the linear convolution operator.

The motivation behind the design of the active control units in chapter 5.2.3 is the adoption of the collocated FXLMS algorithm. As can be observed, there are equal number of reference sensors and secondary sources ($J = K$), and each reference microphone and secondary loudspeaker pair forms one collocated channel. Essentially, the collocated channels simplifies the output of the k-th secondary source from

$$y_k(n) = \sum_{j=1}^{J} y_{kj}(n), \tag{5.6}$$

where

$$y_{kj}(n) = \mathbf{w}_{kj}^{\mathrm{T}}(n)\mathbf{x}(n), \tag{5.7}$$

to

$$y_j(n) = \mathbf{w}_{jj}^{\mathrm{T}}(n)\mathbf{x}_j(n), \tag{5.8}$$

based on the input only from its microphone pair (i.e. $j = k$) [Murao et al., 2017]. This collocated is henceforth adopted in the real-time implementation of the active control system.

5.3. Predicted Performance of the Control System

The expected performance of an active noise control system can be predicted via an off-line simulation of the 24-channel active control system with the measured secondary path responses. The bandlimited reference signal $x(n)$ is a random signal band passed with a FIR filter as specified in Table 5.2. The magnitude response and pole-zero plot of the bandpass filter is depicted in Figure 5.12(a) and (b) respectively.

Table 5.2: Bandpass FIR filter specifications for primary random signal $x(n)$

Specification	Value
Filter structure	Chebyshev Type II
First stop band	100 Hz
Second stop band	2000 Hz
Filter order	50
Stopband attenuation	60 dB
Sampling rate	12000 Hz

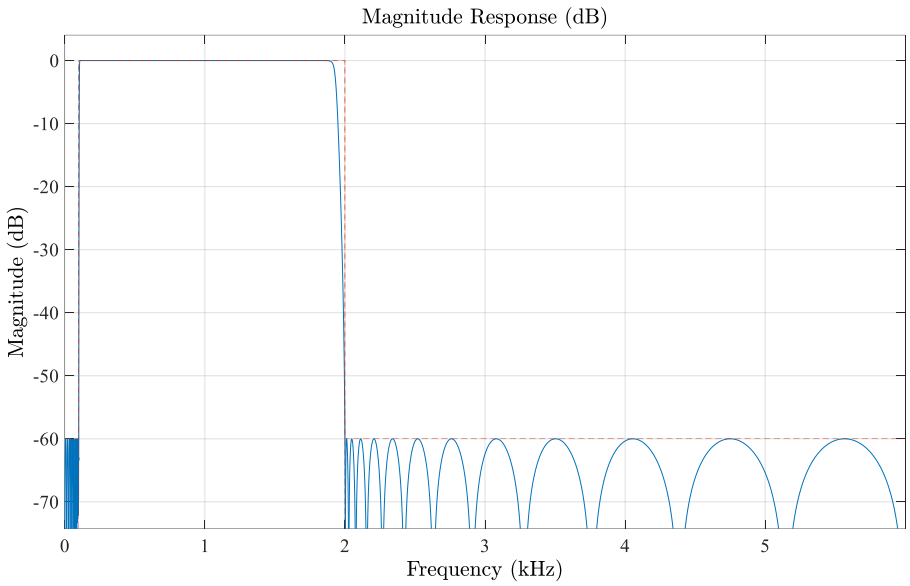

(a)

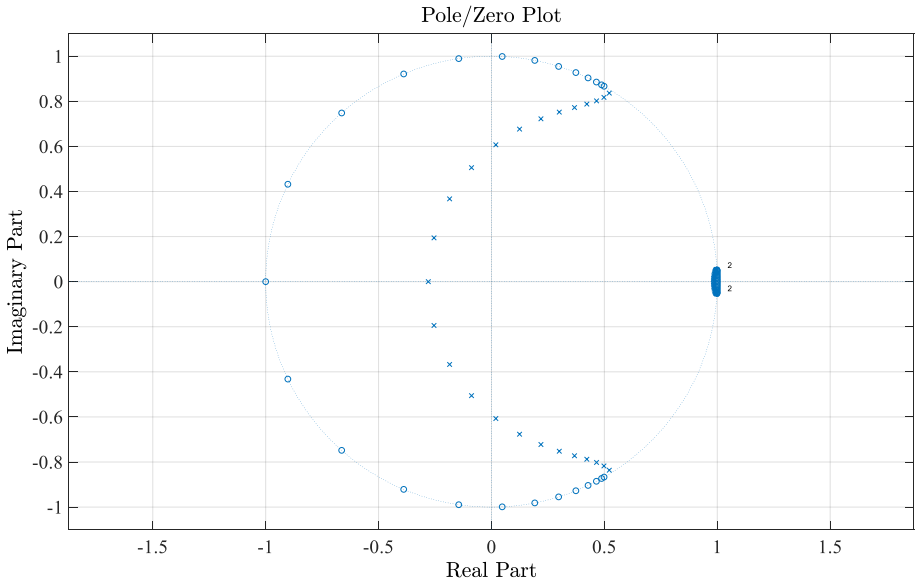

(b)

Figure 5.12: (a) Magnitude response and (b) pole-zero plot of the bandpass filter used to generate a bandlimited white noise signal.

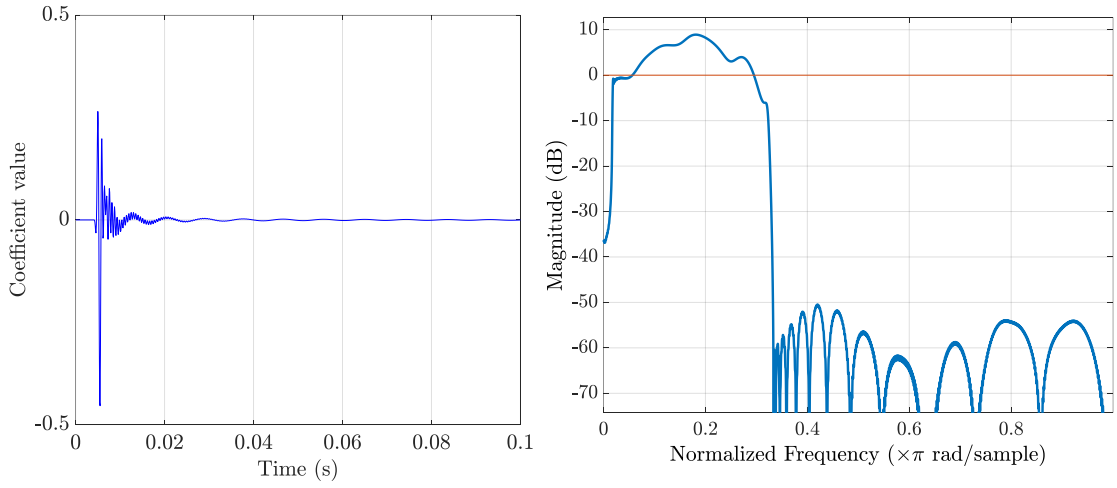

(a) (b)

Figure 5.13: (a) The impulse response and (b) frequency response of the desired signal $d(n)$ during one iteration.

The primary path is modelled as an ideal 50 sample delay at the sampling rate of 12 kHz. The resultant impulse and frequency response of the desired signal $d(n)$ (convolution of $x(n)$ and $P(n)$) is illustrated in Figure 5.13 for one iteration.

Table 5.3: Simulation parameters of the 24-channel FXLMS algorithm

Parameter	Value
Iterations	40
Step size	5×10^{-5}
Sampling rate	12 kHz
Adaptive filter length	350 Taps
Secondary path transfer function length	200 Taps
Primary path transfer function length	1200 Taps

A fully-coupled 24-channel FXLMS algorithm is implemented with the simulation parameters detailed in Table 5.3 and executed in MATLAB 2017b (The MathWorks Inc., USA). The predicted active control performance is averaged over 40 iterations as shown in Figure 5.14, where the sound power before and after ANC are indicated by the blue and green lines respectively. An average of 10 dB reduction is achieved across all frequencies from 100 Hz to 2 kHz. The time histories of the sum-of-the-squared errors averaged over all 40 iterations reveal a slow convergence of the 24-channel system, as shown in Figure 5.14(b). Hence, the feasibility of the 24-channel system is demonstrated, and its convergence shows that the causality constraint is not violated.

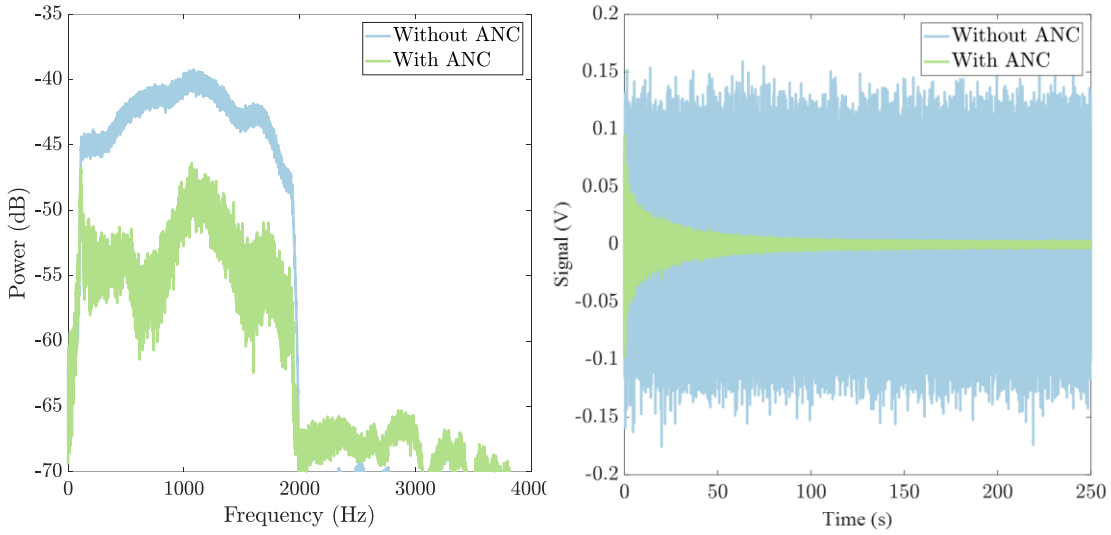

(a) (b)

Figure 5.14: (a) Predicted attenuation performance of the 24-channel ANC system in frequency domain, and the (b) corresponding time histories of the sum of squared error signals of all 24 microphones.

5.3.1.1. **Coherence and causality**

For the multichannel ANC system to achieve control, and as mentioned in Table 2.2, the reference signals have to be correlated to the error signals. Since the collocated implementation is adopted, the individual coherence between the reference sensors and error sensors should be measured instead of multiple coherence as in a car cabin application Cheer and Elliott [2015].

The physical positions of the reference and error microphones are labelled in an exploded view as shown in Figure 5.15. The coherence is measured when a bandlimited white noise signal from 200 to 2000 Hz is generated by the primary speaker positioned normal to the window aperture (i.e. $0°$ incidence).

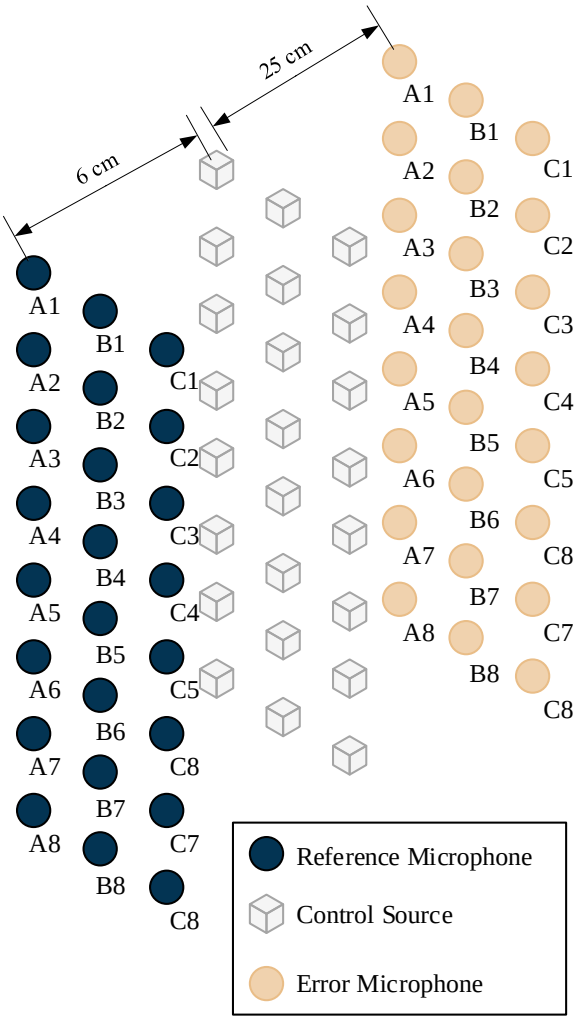

Figure 5.15: Exploded view of the array of 24 reference and 24 error microphones and their positions relative to the 24 control sources.

Overall, the coherence is high (>0.98) between all the reference and error microphones. For clarity, only the coherence of the microphones located in the corner of the 24 channel array are discussed in detail. Figure 5.16(a) shows the coherence between the reference microphone at the A1 position to error microphones at the A1, C1, A8, and C8 microphones. Although the coherence at error microphones that are further away (A8 and C8) should be lower than those where the error microphones are closer to the reference microphone positions (A1 and C1), the calculated coherence values are expected attenuation are similar, as shown in Table 5.4. A similar observation

can be made when examining the coherence from reference microphone positions at C1, A8 and C8 to the same four error microphone positions, as shown in Figure 5.16(b), (c) and (d) respectively.

This shows that the array is effective at attenuating planewaves and the microphones at the extreme positions detect most of the noise between 200 to 2000 Hz. However, it is worth noting that there is a drop in coherence at the low frequency region where there are modes forming.

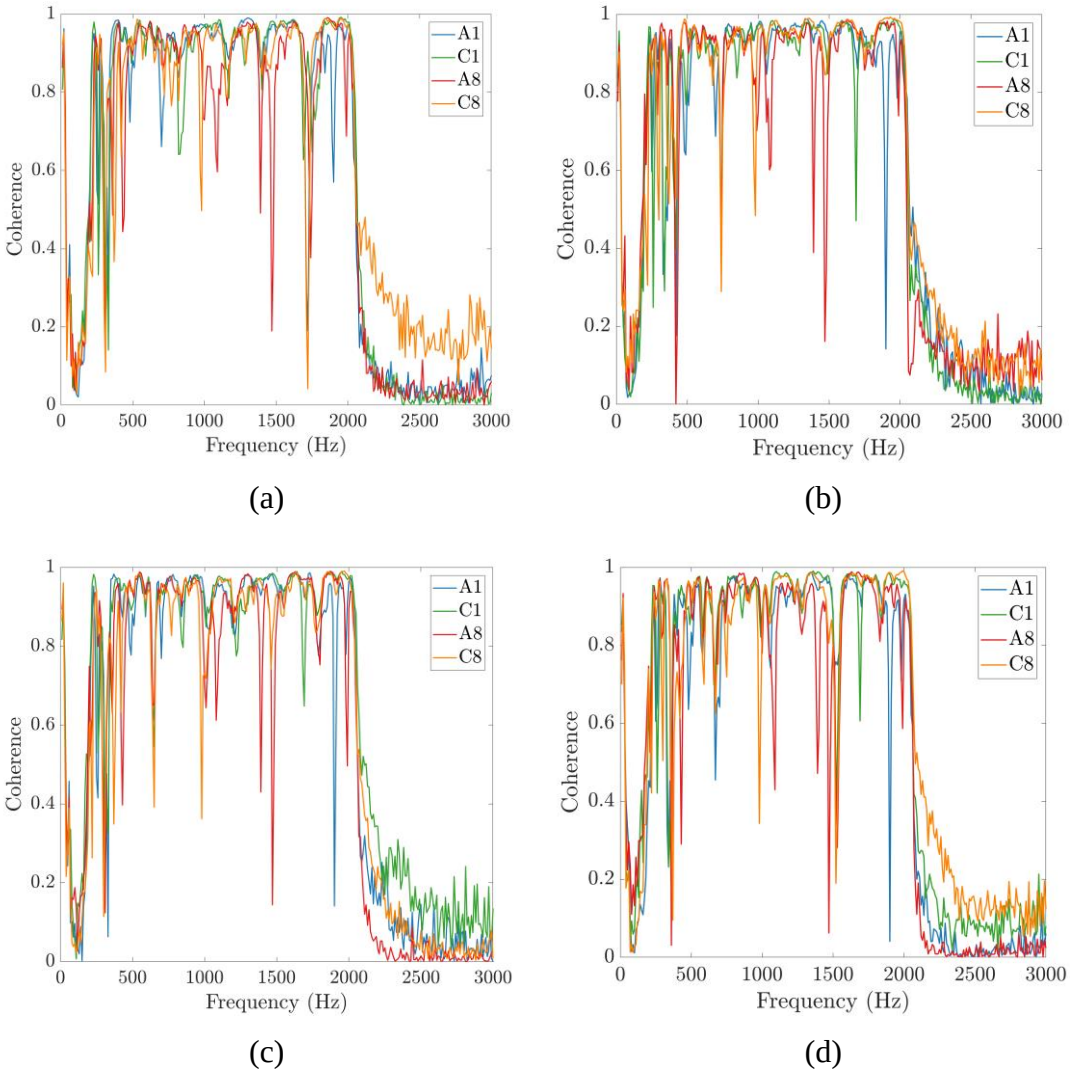

Figure 5.16: Coherence between the reference microphone at the (a) A1, (b) C1, (c) A8 and (d) C8 positions to error microphones at the A1, C1, A8 and C8 positions.

Table 5.4: Coherence and expected attenuation between individual reference and error microphones.

Reference	Error	Attenuation (dB)	Coherence
A1	A1	20.045	0.990104
A1	C1	20.8304	0.99174
A1	A8	20.4019	0.990884
A1	C8	20.1646	0.990372
C1	A1	18.6531	0.986364
C1	C1	19.6973	0.989278
C1	A8	20.0663	0.990151
C1	C8	20.2931	0.990653
A8	A1	19.2638	0.988153
A8	C1	20.0702	0.99016
A8	A8	19.0877	0.987662
A8	C8	21.4099	0.992772
C8	A1	19.0608	0.987586
C8	C1	20.2331	0.990523
C8	A8	19.5045	0.988791
C8	C8	20.3575	0.99079

The level of expected attenuation in Table 5.4 can be achieved is the causality conditions are met. In this application, the causality condition is achieved through the implementation of low-delay analogue to digital converters and parallelised implementation on a FPGA controller. It was also found that the fully-coupled implementation required a longer computation time than that afforded by the 6.4 cm acoustic distance (i.e. 0.186 ms). Hence, the collocated implementation of FXLMS was adopted to meet the causality condition.

5.4. Observation Microphones

To analyse the active noise reduction performance in the entire three-dimensional interior of the test chamber, an array of observation microphones is arranged in two formations: (1) 12 microphones in a plane array monitoring the entire aperture, and (2) 7 microphones distributed in the chamber following ISO 16283-3 guidelines.

5.4.1. Placement of Observation Microphones

A total of 18 free-field microphones (G.R.A.S. 40PH) were distributed within the chamber to determine the passive and active control attenuation performance by the fully glazed window and the active control system, respectively. The analogue microphone data was acquired through five 4-channel data acquisition cards (NI 9234) mounted on a standalone processing chassis (NI cDAQ 9137) via the NI LabVIEW software interface. All the microphones were calibrated with a GRAS 42AB Class 1 calibrator, which uses a 1000 Hz sine tone at 114 dB.

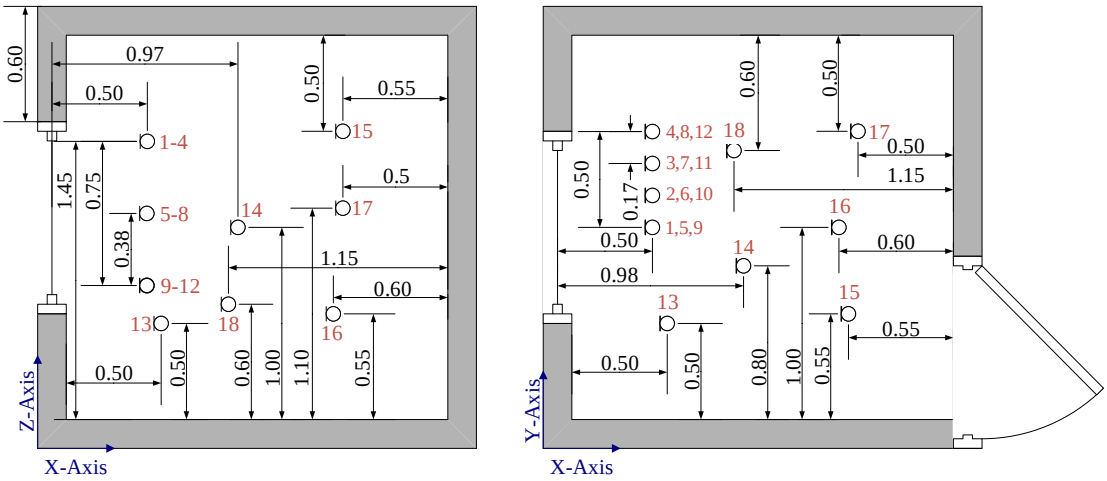

Figure 5.17: Placement of observation microphones in the test chamber in the side view cross-section *xz*-plane (left) and the top view cross-section *xy*-plane (right), where

microphones 1 to 12 represent a plane array of microphones in front of the window aperture, and microphones 1 and 13 to 18 are arranged according to the guidelines in ISO 16283-3.

The physical locations of the microphones (labelled 1 to 18) in the test chamber are depicted in Figure 5.17. Microphones 1 to 12 are arranged in a planar array to cover the entire open aperture of the two-panel sliding window, whereas microphones 1 and 13 to 18 are arranged in accordance to the guidelines stated in ISO 16283-3 [International Organization for Standardization, 2016].

5.4.2. Evaluation Criteria

The time-averaged SPL readings from all O observation microphones, $SPL_{TA,o}$, are used to determine SPL_{EA}, which is the energy-average sound pressure level in the chamber, given by

$$SPL_{EA} = 10\log_{10}\left(\frac{1}{O}\sum_{o=1}^{O}10^{SPL_{TA,o}/10}\right). \tag{5.9}$$

The energy-average SPL, SPL_{EA}, represents the space and time average of the SPL in the chamber as defined in ISO 16283-3 [International Organization for Standardization, 2016]. Hence, SPL_{EA} is calculated using the time-averaged sound pressure level from microphones 1, and 13 to 18 as shown in Figure 5.17.

To evaluate the average sound pressure across the entire open aperture, a planar array of microphones is placed 0.5 m away from the window as depicted in Figure 5.17. The planar average SPL, SPL_{PA}, is calculated using Eq. (5.9) with data from microphones 1 to 12.

5.5. Passive Attenuation Performance of Fully-closed Windows

The passive attenuation of the windows is evaluated by comparing the energy-average sound pressure level reduction, SPL_{EA}, when the windows are tightly shut as compared to the state where the windows fully-opened (L_o = 0.4 m). The average sound pressure level of a planar array of microphones are included to evaluate the sound pressure near the open aperture, as shown in Figure 5.17. The windows are lined with an airtight foam tape for reducing the air (and sound) leakage through the window gaps, a common treatment in a domestic scenario.

5.5.1. Tonal Performance at Normal Incidence

The attenuation performance due to passive insulation of a fully-closed window is analysed with tonal signals from the normally incident primary noise source. The SPL_{EA} of the tonal signals from 100 Hz to 1 kHz in 100 Hz intervals, and from 1200 Hz to 2 kHz in 200 Hz intervals are shown in Figure 5.18(a). The orange and blue bars represent the SPL_{EA} when the windows are opened and fully-closed, respectively.

Aside from the low sound pressure at 100 Hz due to the formation of modes, as shown in Section 5.1.2, there is significant reduction in SPL_{EA} (microphone 1, and 13 to 18) especially above 500 Hz. The planar-average SPL (from microphone 1 to 12), SPL_{PA}, exhibits a similar trend to the SPL_{EA} measurements, as shown in Figure 5.18(b). Since the planar arrangement is only 0.5 m away from the window aperture, the sound pressure levels are proportionally higher than the energy-average. However, the attenuation in the planar arrangement is noticeably higher than the energy-average in the mid frequencies (400 Hz to 800 Hz).

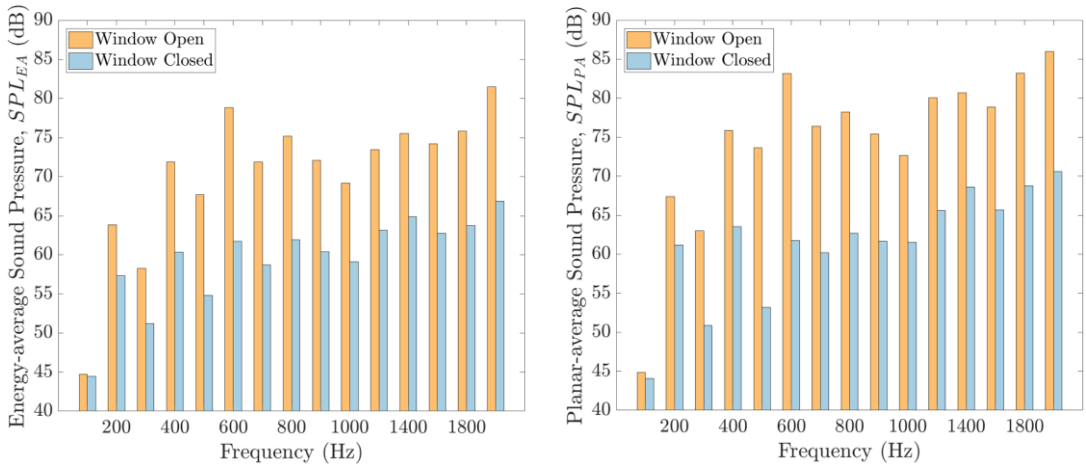

(a) (b)

Figure 5.18: (a) Energy-average SPL of microphones 1, and 13 to 18, and (b) the planar average SPL of microphones 1 to 12, in the test chamber with the windows fully opened (orange) and fully closed (blue) with tonal excitation, at 0° incidence.

5.5.2. Tonal Performance at Oblique Incidences

To understand the attenuation performance of noise impinging from oblique incidences, the primary source is placed at a 30° angle. The same frequencies in section 5.5.1 were measured with all 18 observation microphones with the windows open (orange) and fully-closed (blue), as shown in Figure 5.19.

The attenuation in SPL_{EA} and SPL_{PA} are noticeably reduced as compared to the normal incidence, as shown in Figure 5.19(a) and (b) respectively. Both averages still register low sound pressure at 100 Hz due to the modal effects.

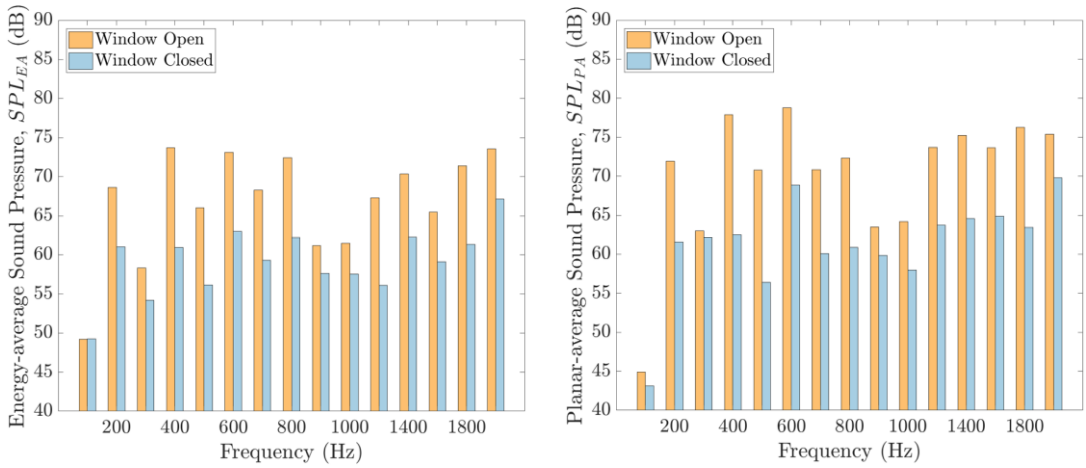

(a) (b)

Figure 5.19: (a) Energy-average SPL of microphones 1, and 13 to 18, and (b) the planar average SPL of microphones 1 to 12, in the test chamber with the windows fully opened (orange) and fully closed (blue) with tonal excitation, at 30° incidence.

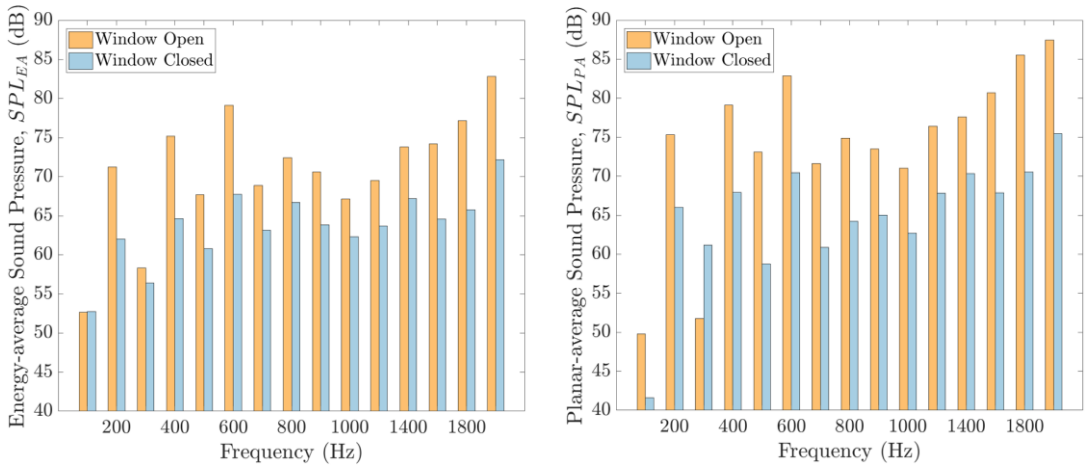

(a) (b)

Figure 5.20: (a) Energy-average SPL of microphones 1, and 13 to 18, and (b) the planar average SPL of microphones 1 to 12, in the test chamber with the windows fully opened (orange) and fully closed (blue) with tonal excitation, at both 0° and 30° incidences.

When both the normal incidence and 30° sources are activated, attenuation levels in SPL_{EA} and SPL_{PA} are similarly lower than the normal incidence case, as shown in Figure 5.20. It is also worth noting that there is an increase in SPL_{PA} at 300 Hz with full-glazing, which could be attributed to mode enhancements at the window opening.

For a clearer comparison, the passive attenuation of the fully-closed window is plotted as a function of frequency in Figure 5.21. The 0°, 30°, and both 0° and 30° angles of incidence are represented by the blue, green and red line plots respectively; the solid lines and the dashed lines representing the attenuation in planar-average and the energy-average SPLs, respectively. Except at 300 Hz when the primary sources are active at both 0° and 30°, the SPL_{EA} attenuation is lower or at least equal to the planar array.

The attenuation at the lower frequencies exhibit a similar trend to the fully-glazed scenario in the FEM simulations, as shown in Figure 4.12, where there is a sharp reduction in attenuation below 500 Hz. Attenuation performance at the higher frequencies deviate from the general increase in attenuation performance from 500 Hz to 2 kHz in the FEM simulations and instead plateaus between 10 to 15 dB after 600 Hz. As the FEM simulations measure the sound power attenuation and the test chamber experiment measures the reduction in average sound pressure level, a direct comparison between the attenuation values is inappropriate. However, attenuation in the test chamber is a closer representation of the actual performance of a fully-closed window in an in-situ environment and will be used as the basis for comparison for the active control system.

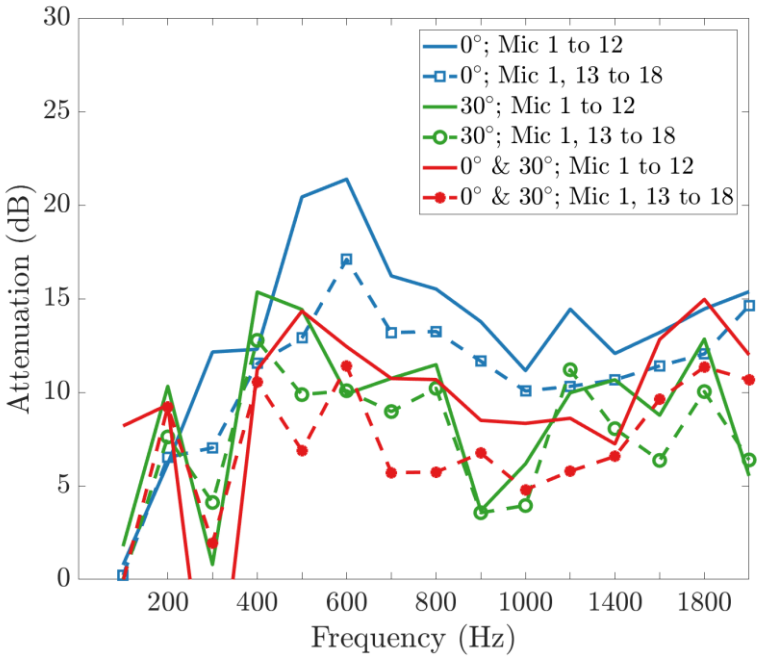

Figure 5.21: Attenuation as a function of frequency when the tonal source is at 0° (blue line), 30° (green line), and both (red line) angles of incidence. The solid line represents the SPL_{PA} attenuation levels (microphones 1 to 12) and the dashed lines represent the SPL_{EA} attenuation (microphones 1, and 13 to 18).

5.5.3. Broadband Performance

As a basis for comparison for active noise control performance, two bandlimited white noise signals are employed to evaluate the passive attenuation performance of the fully-closed window, namely, 200 Hz to 2 kHz and 500 Hz to 2 kHz. The 100 Hz frequency is omitted due to modal issues.

The energy-average and planar-average SPLs when only the normally incident primary source is activated, are depicted in Figure 5.22(a) and (b) respectively. No noticeable difference is observed between the average sound pressure level between both bandlimited white noise signals.

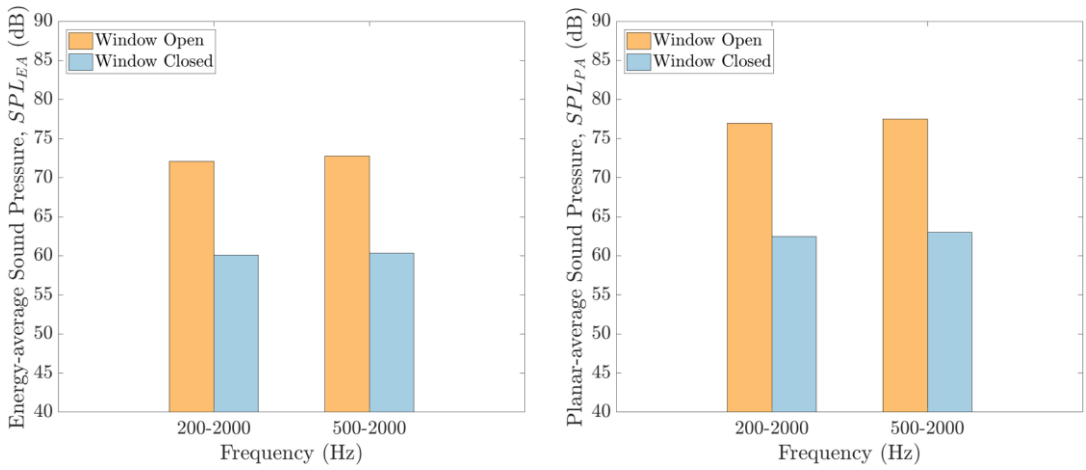

(a) (b)

Figure 5.22: (a) Energy-average SPL of microphones 1, and 13 to 18, and (b) the planar average SPL of microphones 1 to 12, in the test chamber with the windows fully opened (orange) and fully closed (blue) with broadband excitation, at 0° incidence.

The passive attenuation when the primary noise is at 0°, 30°, and both 0° and 30° is summarised in Table 5.5, showing both the energy-average and average sound pressure level across the planar array. In all cases, the attenuation at 30° incidence is about 5 dB lower than when the primary noise is normally incident. This observation is consistent with the tonal measurements in 5.5.2, with the exception at 200 Hz. There is no noticeable difference in attenuation performance between the two bandlimited white noise cases, indicating that the attenuation in the lower frequency region is poor, as shown in the single frequency cases.

Table 5.5: Passive attenuation in dB for bandlimited white noise signal of 200 Hz to 2 kHz and 500 Hz to 2 kHz emitted by noise source at: (1) 0° only, (2) 30° only, and (3) both 0° and 30° angles of incidence.

Frequency	200 Hz to 2 kHz			500 Hz to 2 kHz		
Angle of Incidence	0° only	30° only	0° & 30°	0° only	30° only	0° & 30°
Planar	14.47	9.61	11.25	14.49	10.14	11.51
Energy-average	12.02	7.88	8.49	12.39	8.10	8.74

5.6. Real-time Active Noise Control Performance

The active noise control system described in Section 5.2 is firstly evaluated in terms of its tonal attenuation performance from 100 Hz to 2 kHz, and next by its broadband performance with two bandlimited white noise signals, 200 Hz to 2 kHz and 500 Hz to 2 kHz. Similar to 5.5, both the energy-average and planar-average SPLs were used as the performance measure of the active control system.

5.6.1. Tonal Performance at Normal Incidence

At normal incidence, the active control system has reduced the SPL_{EA} and SPL_{PA} across all frequencies except at 100 Hz, as shown in Figure 5.23(a) and (b) respectively. For a direct comparison, the passive and active attenuation is plotted as a function of frequency in Figure 5.24, as represented by the green and plot lines respectively. The energy-average attenuation and average attenuation across the planar array are represented by the solid and dashed lines respectively.

Although the attenuation levels of the active control system do not exceed the passive attenuation of a fully-closed window even for low frequencies (<500 Hz), the deviations are at most 5 dB for frequencies less than 1 kHz, as shown in Figure 5.28. There is a roll off in attenuation performance in the active control system after 1 kHz as it approaches its physical limits (<2.6 kHz).

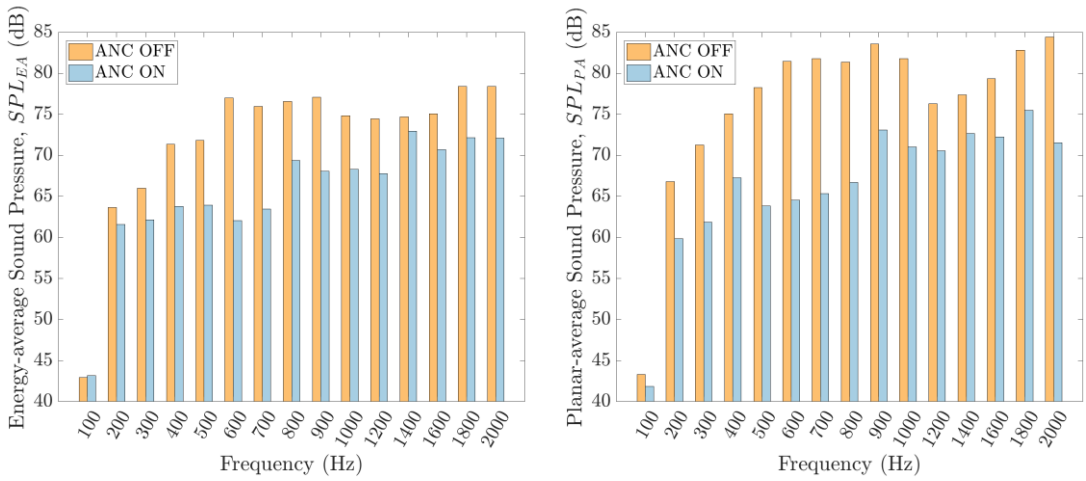

(a) (b)

Figure 5.23: (a) Energy-average SPL of microphones 1, and 13 to 18, and (b) the planar average SPL of microphones 1 to 12, in the test chamber with the windows fully opened and the active control system turned off (orange) and turned on (blue) with tonal excitation, at 0° incidence.

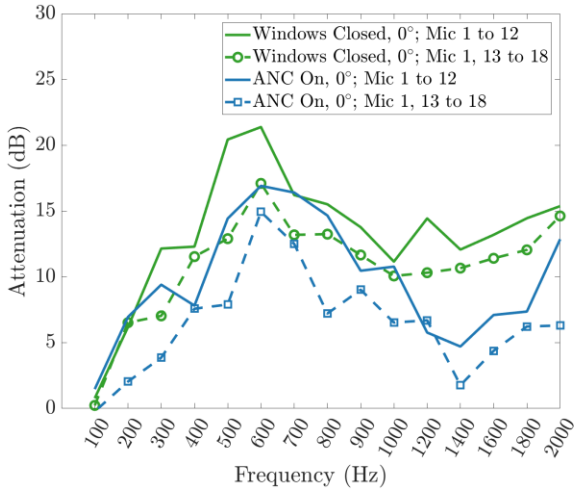

Figure 5.24: Passive (green) and active (blue) attenuation as a function of frequency at normal incidence. The solid line represents the SPL_{PA} attenuation levels (microphones 1 to 12) and the dashed lines represent the SPL_{EA} attenuation (microphones 1, and 13 to 18).

5.6.2. Tonal Performance at Oblique Incidences

At 30° incidence, the active control system successfully reduces the SPL_{EA} and SPL_{PA} for frequencies across all frequencies below 2 kHz, which is up to the physical limits as defined in Section 4.2.2.3 (~1.83 kHz), as shown in Figure 5.25.

For comparison, the passive attenuation performance of the fully-closed window and the active control system is plotted as a function of frequency, as shown in Figure 5.26. In terms of the planar average, the attenuation performance of the active control system closely matches the passive insulation, and even outperforming it at 600 Hz, 800 Hz and 1.4 kHz. On the other hand, the active control energy-average attenuation performance also closely matches the passive insulation up till 1.2 kHz, but deviates beyond that and resulted in a spill over at 1.6 kHz.

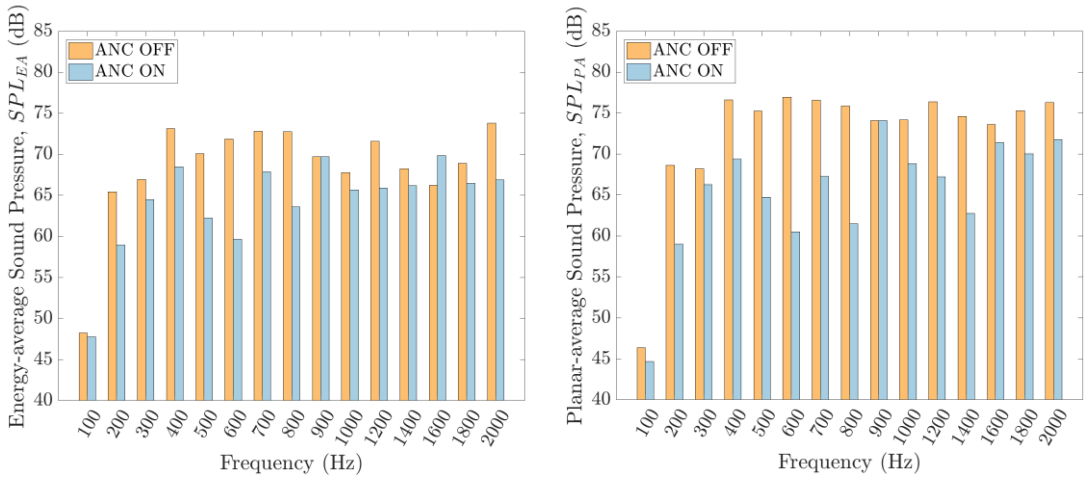

(a) (b)

Figure 5.25: (a) Energy-average SPL of microphones 1, and 13 to 18, and (b) the planar average SPL of microphones 1 to 12, in the test chamber with the windows fully opened and the active control system turned off (orange) and turned on (blue) with tonal excitation, at 30° incidence.

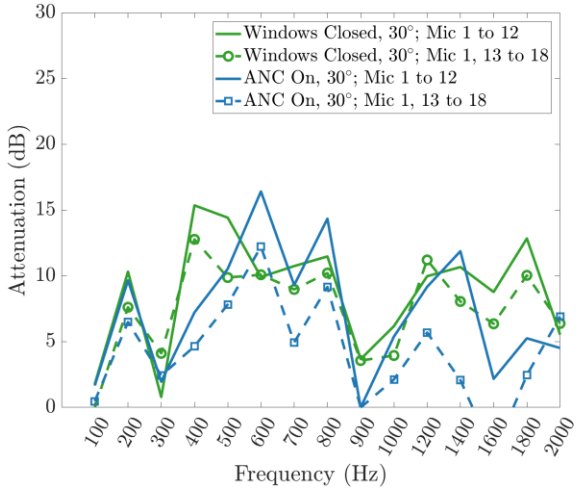

Figure 5.26: Passive (green) and active (blue) attenuation as a function of frequency at normal incidence. The solid line represents the SPL_{PA} attenuation levels (microphones 1 to 12) and the dashed lines represent the SPL_{EA} attenuation (microphones 1, and 13 to 18).

The SPL_{EA} and SPL_{PA} when both the 0° and 30° incidence sources are active is shown in Figure 5.27(a) and (b) respectively. Except at 1.6 kHz for SPL_{EA} and 1.2 kHz for SPL_{PA}, the active control system still achieved significant reduction across the entire frequency range.

In comparison to the passive attenuation performance, the SPL_{EA} and SPL_{PA} attenuation of the active control system closely matches the passive insulation performance for frequencies below 1.2 kHz. Similar to the 30° incidence case, the attenuation performance of the active control system degrades above 1.2 kHz and resulted in a spill over of SPL_{EA} at 1.6 kHz.

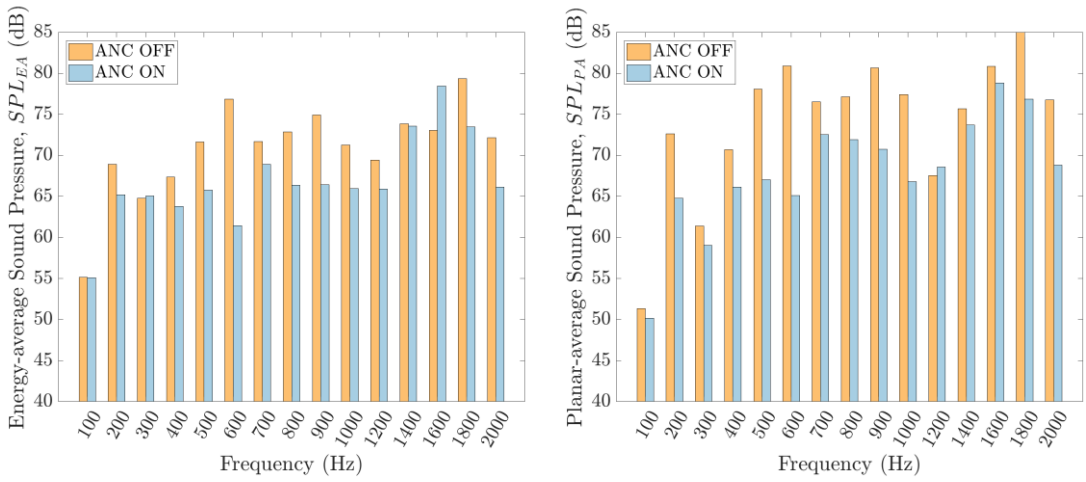

(a) (b)

Figure 5.27: (a) Energy-average SPL of microphones 1, and 13 to 18, and (b) the planar average SPL of microphones 1 to 12, in the test chamber with the windows fully opened and the active control system turned off (orange) and turned on (blue) with tonal excitation, at both 0° and 30° incidence.

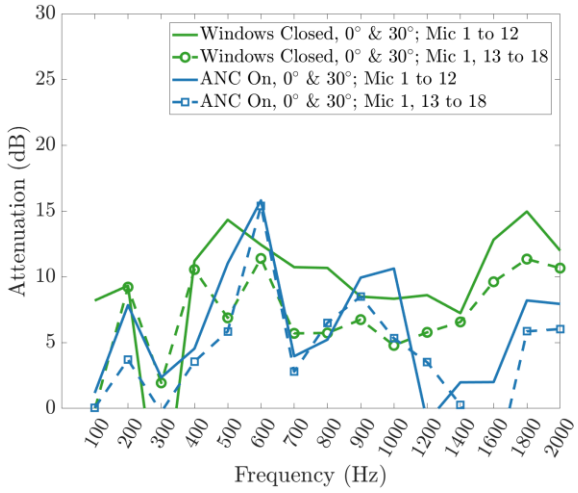

Figure 5.28: Passive (green) and active (blue) attenuation as a function of frequency when sources are at normal and 30° incidence. The solid line represents the SPL_{PA} attenuation levels (microphones 1 to 12) and the dashed lines represent the SPL_{EA} attenuation (microphones 1, and 13 to 18).

5.7. Band-limited White Noise Performance at Different Noise Incidence Angles

The same bandlimited white noise used to determine the passive attenuation of the fully-closed window is employed to evaluate the active control attenuation performance. The SPL_{EA} and SPL_{PA}, before and after active control at all angles of incidence, are shown in Figure 5.29(a) and (b), respectively. Across all cases, the active control system has reduced both the SPL_{EA} and SPL_{PA} of both types of bandlimited white noise.

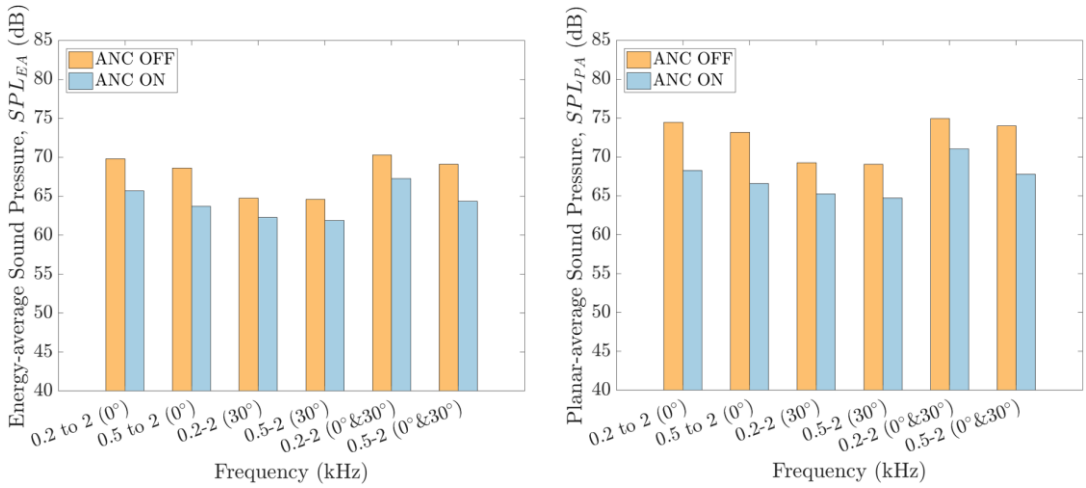

(a) (b)

Figure 5.29: (a) Energy-average SPL of microphones 1, and 13 to 18, and (b) the planar average SPL of microphones 1 to 12, in the test chamber with the windows fully opened and the active control system turned off (orange) and turned on (blue) using band limited white noise at 0° incidence.

The attenuation performance of the active control system is compared with the passive insulation performance of the fully-glazed window with the noise source at normal incidence and at 30° incidence, as shown in Figure 5.30(a) and (b). The active control attenuation performance in both angles of incidence is approximately one-third of the attenuation provided by the passive insulation. The real-time performance of the active control system is only half of the predicted performance of at least 10 dB attenuation from 200 Hz to 2 kHz, as shown in Figure 5.14.

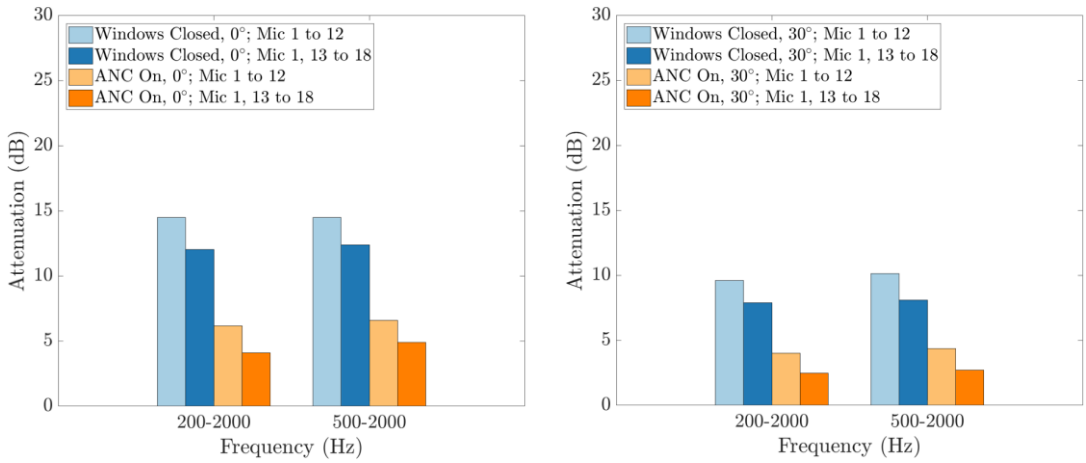

(a) (b)

Figure 5.30: Passive (blue) and active (orange) attenuation as a function of frequency at (a) normal incidence and (b) 30° incidence, in terms of both SPL_{EA} and SPL_{PA}.

5.8. Recorded Environmental Noise Performance

To determine the effectiveness of the 24-channel ANC system in attenuating traffic noise, a bandlimited recording of highway noise in Singapore is used as the primary noise signal. At normal incidence, the attenuation performance of traffic noise closely matches that of the bandlimited white noise for both the energy-average and planar-average SPLs, as shown in Figure 5.31(a) and (b) respectively.

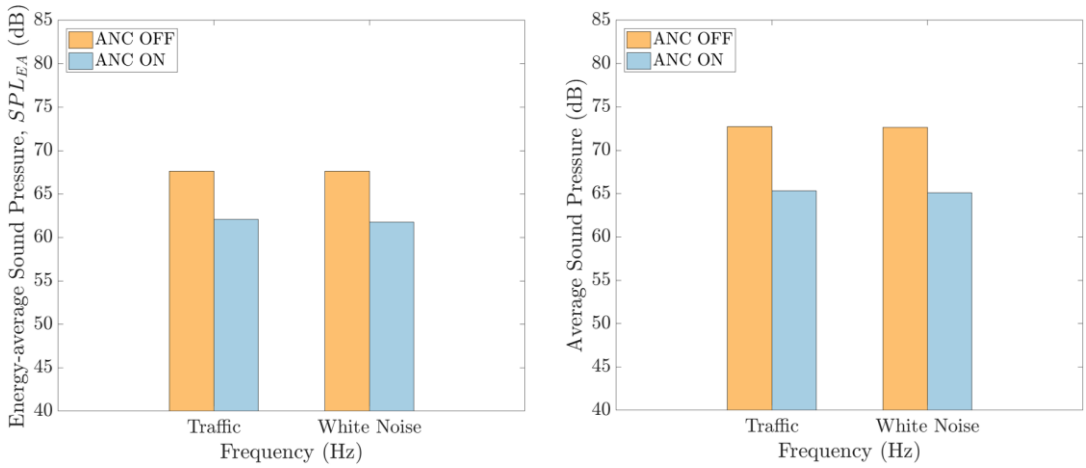

(a) (b)

Figure 5.31: (a) Energy-average SPL of microphones 1, and 13 to 18, and (b) the planar average SPL of microphones 1 to 12, in the test chamber with the windows fully opened and the active control system turned off (orange) and turned on (blue) using band limited traffic and white noise at 0° incidence.

5.9. Summary

A $2\times2\times2$ m^3 test chamber housing a full-sized two-panel sliding window was constructed in a recording studio as a platform to implement an active noise control system. A large loudspeaker that is capable of generating large wavefronts was chosen as the primary noise source. Based on the collocated implementation of Murao and Nishimura, 24 active control units comprising of a single reference microphone and a single electrodynamic loudspeaker was designed and installed onto the window grille. Secondary path responses from the 24 secondary sources to the 24 error microphones were measured for offline predictions of active control performance. Based on the averaging 40 iterations with a bandlimited random noise signal from 100 Hz to 2 kHz, a 10 dB reduction is achieved uniformly across the entire frequency band.

Due to the high computational load and low latency requirements of the collocated implementation, the collocated FXLMS algorithm is implemented on a National Instruments FPGA platform with SAR ADCs and string DACs. The active control performance is evaluated based on the space- and time-average of the SPL in the entire room. The passive insulation of the fully closed sliding window system is measured as a benchmark to the active noise control system. In all noise incidence cases, the performance of the active control system does not exceed that of a fully glazed window. However, in the test of bandlimited white noise and traffic noise, an attenuation of 5 to 7 dB is achieved with the windows almost totally ajar.

The practical implementation issues and preliminary work done to address these issues will be discussed in Chapter 6.

Chapter 6

Considerations for Practical Implementation

Although the fundamental limits of active control have been defined in Chapter 4 and an active control system has been implemented on a full-sized sliding window in Chapter 5, practical deployment of the active control system in a domestic setting poses a different set of challenges. For instance, the placement of error microphones within the vicinity of the domestic living environment is often undesirable due to physical obstruction and poor aesthetics. Investigation into the viability of error microphone omission though the implementation of fixed filters is therefore required. In this chapter, a fixed filter based on the control of noise from multiple incidence angles is designed in the frequency domain and its performance is evaluated.

Additionally, based on design guidelines in Chapter 4, the number of control sources required increases with the desired upper frequency limit of control or with increasing angles of noise incidence. This often results in a dense array of sources that might be visually displeasing. Since it was previously found that having an additional layer of control sources distributed around the boundary aids in the control of certain modes [Wang et al., 2018], a combination of such a dual source arrangement on the boundary with the distributed layout could improve control of scenarios with severe diffraction around the edges of the aperture. Hence, a hybrid layout is designed and evaluated to determine its effectiveness and scenarios in which less sources are distributed in the aperture but with the same attenuation performance as the fully distributed layout.

Lastly, other open issues that are essential to the practicableness of the window ANC system are discussed with reference to some preliminary work conducted.

6.1. Fixed-filter Implementation

The ANC systems introduced in Chapter 2 and proposed in Chapter 5 have been implemented on fully- and partially-opened windows. However, for practical implementations, the requirement of error microphones in the system poses practical placement challenges and privacy concerns. Whilst non-adaptive ANC systems that do not employ error microphones have been realised in a multi-dimensional reverberant room, the optimal filters used in such cases have to be recalculated when the primary or secondary path transfer functions change (e.g. human movement in the room) [Kuo and Morgan, 1996].

However, if the window noise control problem is formulated such that the total acoustic power transmitted through the window is the cost function to be minimised, the ANC performance will be robust to variations in the secondary path for optimal filters that do not employ error microphones [Nelson and Elliott, 1992]. This formulation also assumes that the window opening is the noise source, which is collocated with the reference microphones and secondary sources, yielding a favourable control scenario.

Although global noise attenuation of around 10 dB has been demonstrated experimentally with a fixed set of control filter coefficients in some cases [Kwon and Park, 2013; Murao and Nishimura, 2012], the mechanism behind the formulation of a single filter that is optimal for multiple incidence angles has not been defined. In this section, an optimal filter is formulated in the frequency domain to control noise from multiple incidence angles and validated in FEM simulations. The proposed optimal filter

is focused on the control of noise from multiple incidence angles, which reflects the real-world scenario where the ANC system will be implemented (e.g. control of noise at different storeys of the building).

6.1.1. Global Active Control Formulation

The same global active control formulation in section 4.1 is revisited and reformulated. The complex volume velocity of the control source is firstly decomposed into the convolution between the reference signal and control filter coefficients. The under-determined formulation with infinite solutions is then reformulated to a "full-rank" system to obtain a single optimal solution.

6.1.1.1. Multichannel Control of Tonal Disturbances

The active noise control problem is formulated based on the optimal multichannel control of tonal disturbances [Elliott, 2001]. Acoustic summation of the disturbance signals $\mathbf{d}(e^{j\omega T})$ and secondary source signals (at the error microphone locations) yields a complex vector of residual signals that can be represented in steady-state by

$$\mathbf{e}(e^{j\omega T}) = \mathbf{d}(e^{j\omega T}) + \mathbf{G}(e^{j\omega T})\mathbf{W}(e^{j\omega T})\mathbf{x}(e^{j\omega T}), \tag{6.1}$$

where the normalised frequency $e^{j\omega T}$ will be removed for brevity. The block diagram of the multichannel ANC system is shown in Figure 6.1. J reference microphones are collocated with N secondary sources $(J = N)$, where a vector of $J \times 1$ reference signals $\mathbf{x}$, are filtered by a corresponding set of $N \times J$ control filters $\mathbf{W}$ to yield a vector of $K \times 1$ secondary source input signals (i.e. $\mathbf{q} = \mathbf{W}\mathbf{x}$). The contribution of the

N secondary sources at the M error microphone locations is **Gq**, where **G** is the secondary path transfer function at frequency $f = \omega/2\pi$.

The optimal secondary source input signals $\mathbf{q}_0$ is formulated based on the minimisation of cost function C given by

$$C = \mathbf{e}^{\mathrm{H}}\mathbf{e} = \mathbf{q}^{\mathrm{H}}\mathbf{A}\mathbf{q} + \mathbf{q}^{\mathrm{H}}\mathbf{b} + \mathbf{b}^{\mathrm{H}}\mathbf{q} + \mathbf{d}^{\mathrm{H}}\mathbf{d}, \tag{6.2}$$

where $\mathbf{A} = \mathbf{G}^{\mathrm{H}}\mathbf{G}$, $\mathbf{b} = \mathbf{G}^{\mathrm{H}}\mathbf{d}$, $\mathbf{q} = \mathbf{W}\mathbf{x}$, and superscript $^{\mathrm{H}}$ is the conjugate transpose operator. The optimal $\mathbf{q}_0$ can then be calculated by equating the derivative of (6.2) to zero [Elliott, 2001], which is expressed as

$$\mathbf{q}_0 = -(\mathbf{G}^{\mathrm{H}}\mathbf{G} + \beta\mathbf{I})^{-1}\mathbf{G}^{\mathrm{H}}\mathbf{d}, \tag{6.3}$$

where β is the regularisation parameter [Elliott, 2001; Lam et al., 2015a], and $M > N$.

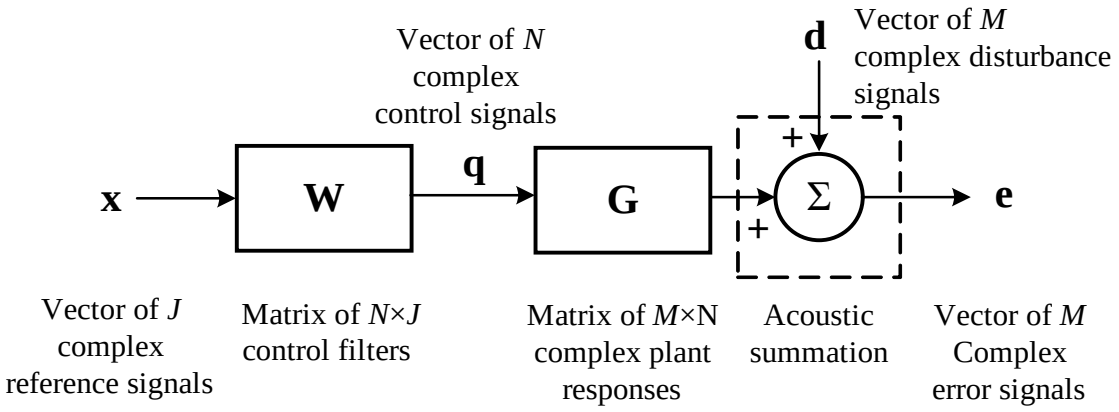

Figure 6.1: Block diagram of the multichannel control system for a specific frequency ω [Elliott, 2001].

6.1.1.2. **Full-rank Fixed Filter Formulation**

The optimal secondary source strength in the tonal case derived in (6.3) is used to derive the optimal fixed filter,

$$\mathbf{q}_0 = \mathbf{W}_0\mathbf{x}, \tag{6.4}$$

where $\mathbf{W}_0$ is the matrix of optimal control filters. However, the optimal filter obtained in (6.4) is an underdetermined problem yielding an infinite number of filter matrices $\mathbf{W}_0$ that can satisfy (6.4).

One solution to realise an optimal fixed filter that can attenuate noise at K noise incidence angles, is to reformulate (6.4) to achieve a full-rank formulation, if $K = N$, by

$$\mathbf{W}_{0,FR} = \mathbf{Q}_{0,\theta_k}\mathbf{X}_{\theta_k}^{-1}, \tag{6.5}$$

where $\mathbf{Q}_{0,\theta_k} = \begin{bmatrix} \mathbf{q}_{0,\theta_1} & \mathbf{q}_{0,\theta_2} & \cdots & \mathbf{q}_{0,\theta_K} \end{bmatrix}$ is the $N \times K$ matrix of optimal source strengths for all K angles of incidence with $k \in \{1,\ 2,\ \ldots,\ K\}$, and calculated with (6.3); and $\mathbf{X}_{\theta_k} = \begin{bmatrix} \mathbf{x}_{\theta_1} & \mathbf{x}_{\theta_2} & \ldots & \mathbf{x}_{\theta_K} \end{bmatrix}$ is the $J \times K$ matrix of corresponding reference signals for K angles of incidence.

6.1.1.3. **Evaluation Parameters**

The sound power attenuation through the aperture is evaluated at the far-field arc in Figure 6.2 as previously defined in section 4.1.1.

6.1.2. Numerical experiments to evaluate the active noise control performance using full-rank fixed filters

The FEM computation plane illustrated in Figure 6.2 is modified from Fig. 4.1 in section 4.1. The eight secondary sources, i.e. $N = 8$, are distributed within the 1 m wide

aperture according to the guidelines in section 4.2.3, i.e. $w < \lambda/(1+\sin\theta)$, where $\theta = 0°$. The entire computation plane is enclosed by a perfectly-matched layer so that all waves are damped to simulate a free-field condition. The acoustic power attenuation is evaluated at 552 points in the far-field arc, with radius of 10 m.

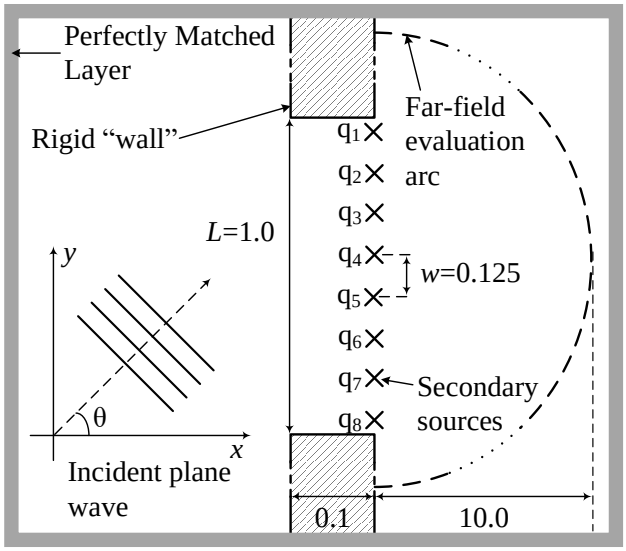

Figure 6.2: 2D FEM simulation model with eight control sources distributed in the aperture according to the recommendations in section 4.2.3.3. All units are in m.

6.1.2.1. **Exact least-squares Solution Performance**

As a benchmark, the exact least-squares solution for each frequency $f \le 2000$ Hz , at each noise incidence angle $\theta_k \in \{0°,\ 5°,\ 15°,\ 30°,\ 45°,\ 60°,\ 75°,\ 90°\}$, i.e. $K = 8,$ is calculated using (6.3). The benchmark far-field sound power attenuation for all θ_k is plotted in Figure 6.3. In general, greater attenuation is achieved at lower frequencies. Attenuation performance (at least 10 dB) is similar across all θ_k when frequency is less than 1300 Hz. The decrease in attenuation performance in the higher frequency range

$(1300 < f < 2000$ Hz$)$ is proportional to the increment in noise incidence angle. For example when $f > 1400$ Hz, attenuation is above 10 dB when noise incidence is at $0°$, whereas a sharp decline is observed for $60°$ angle of incidence.

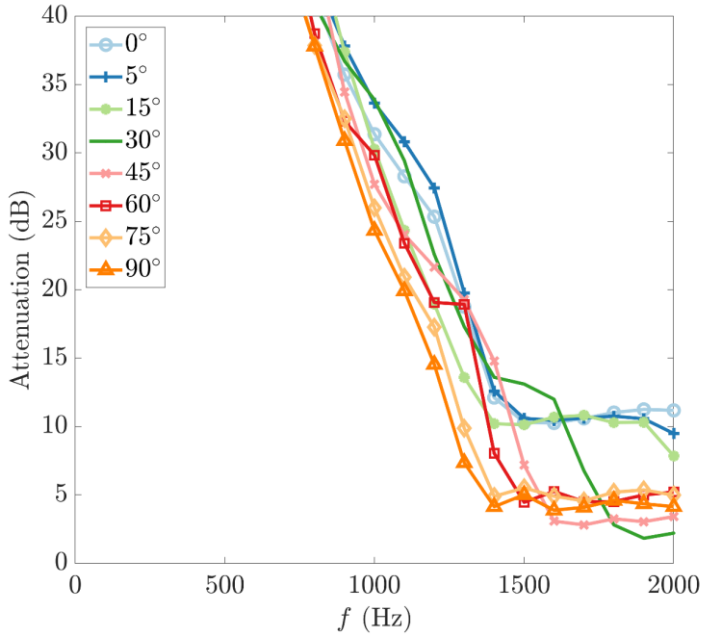

Figure 6.3: Far-field acoustic power attenuation of incidence disturbance at all θ_k, using the optimal least-squares solution in (6.3).

6.1.2.2. **Fixed-filter Performance for Single Incidence**

To quantify the performance reduction due to the introduction of the fixed-filter described in (6.5), the same far-field sound power attenuation performance measure based on (4.6) is used. The fixed filter is calculated in a full-rank manner where $K = N$, with the same angle of incidences θ_k in the exact least-squares method.

The attenuation performance of the full-rank fixed-filter at the same angle of incidences θ_k is shown in Figure 6.4. Comparison of Figure 6.3 and Figure 6.4 indicate

that a single fixed filter is able to obtain the same attenuation performance for a wide range of incidence angles of a specific frequency.

The same full-rank filter is tested at other incidence angles to determine the performance deviation with respect to the optimal exact least-squares method. From the results plotted in Figure 6.5, the full-rank filter attained attenuation performance close to the optimal least-squares method, providing evidence of its feasibility as a practical solution to the open window ANC problem.

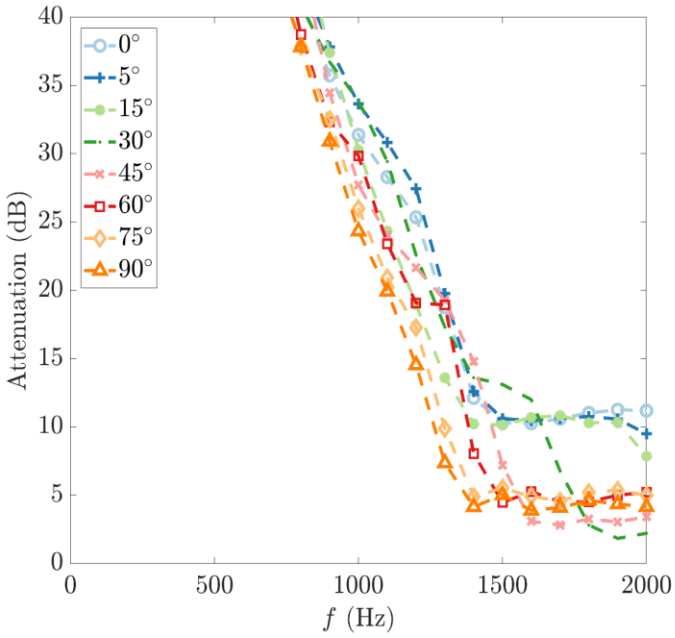

Figure 6.4: Far-field acoustic power attenuation of incidence disturbance at all θ_n, using the fixed-filter calculated in (6.5).

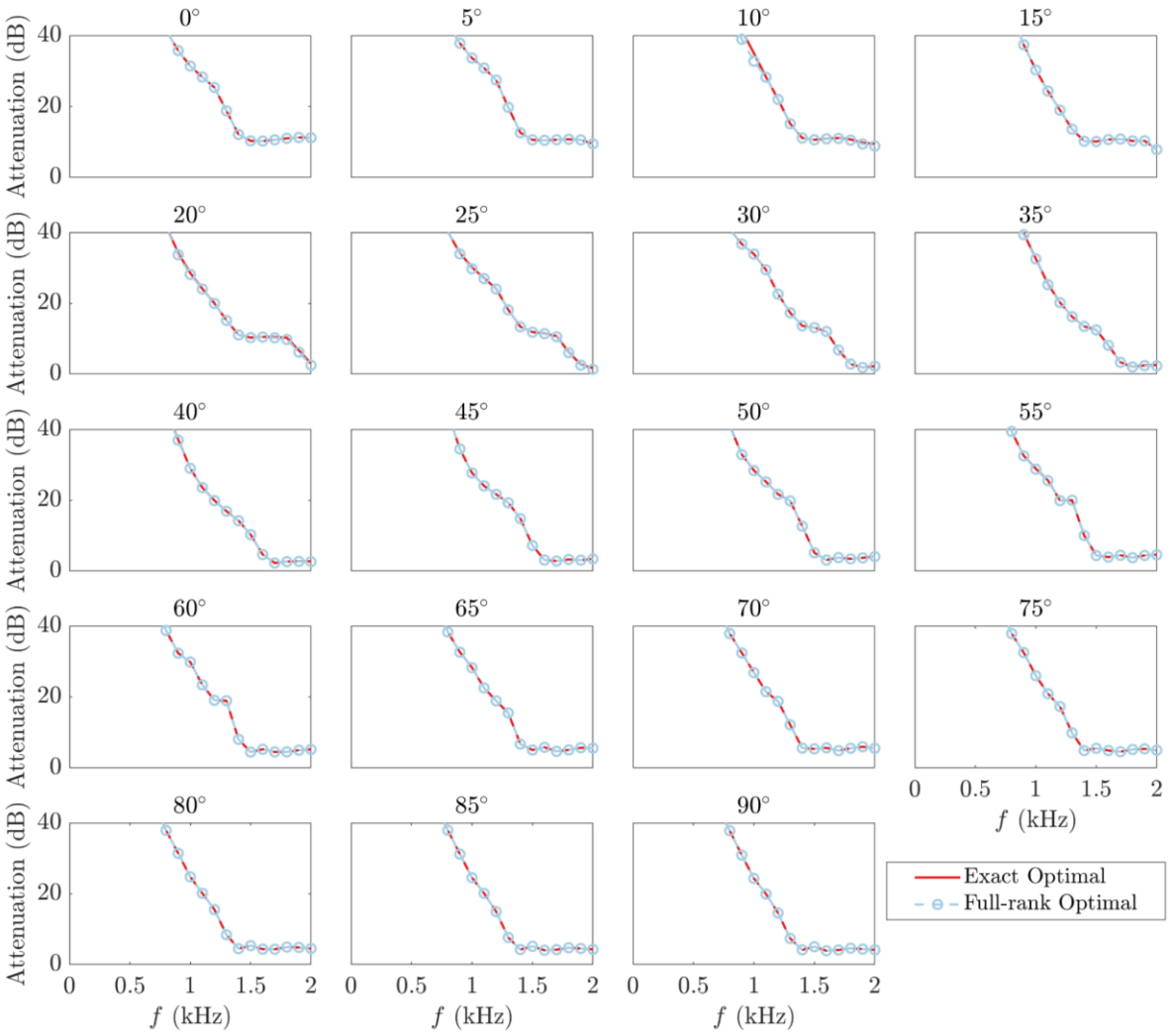

Figure 6.5: Comparison of sound power reduction of the exact least-squares solution with the full-rank optimal solution in a number of incidence angles.

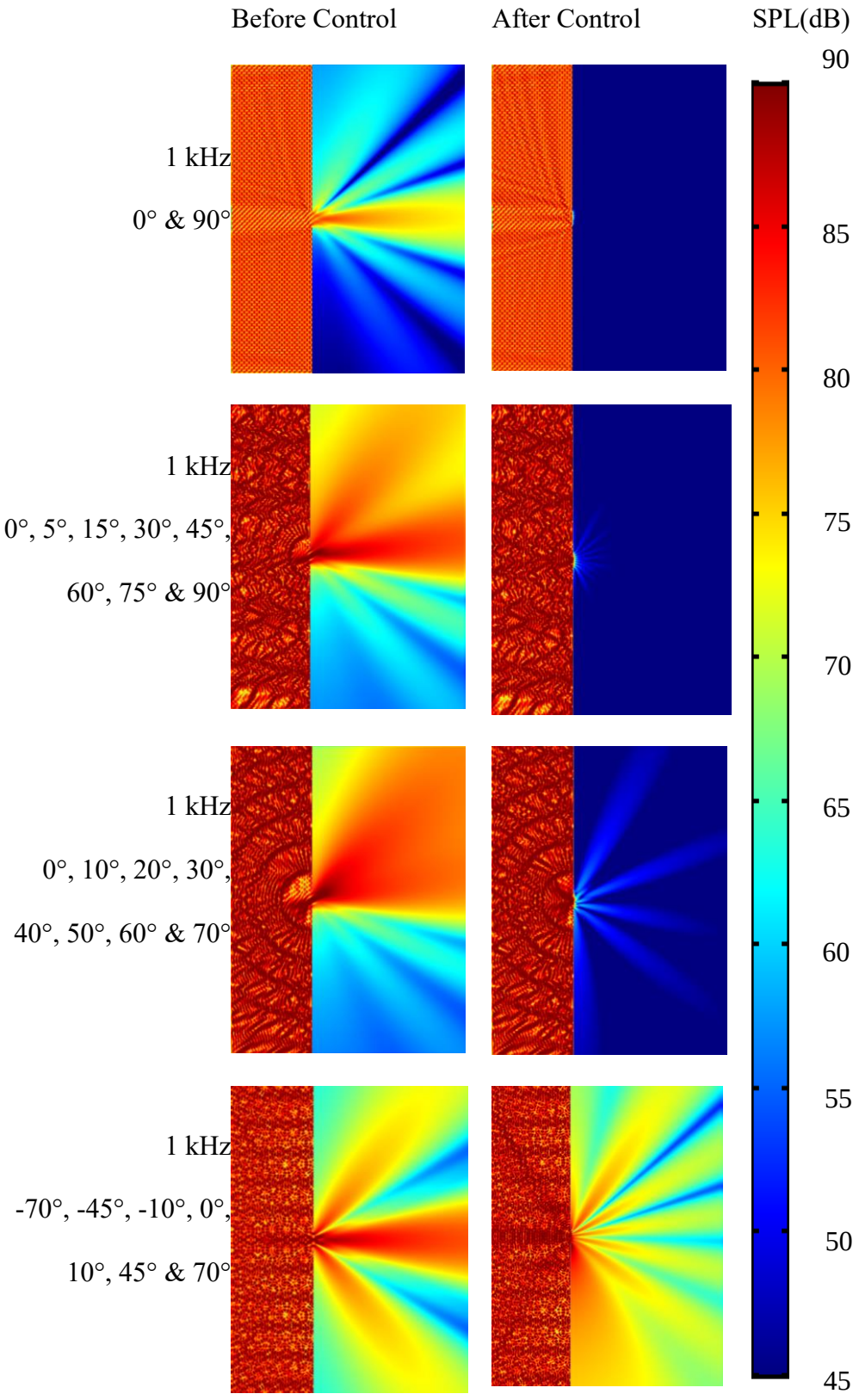

Figure 6.6: Sound pressure distribution of multiple noise plane waves before active noise control (left column) and after active noise control using the same fixed filter in different scenarios (right column).

6.1.2.3. Fixed Filter Performance for Multiple Simultaneous Angles of Incidences

To determine whether the full-rank fixed filter derived using (6.5) could attenuate noise coming from multiple incidence angles at the same time, a scenario with two incident plane waves and two scenarios with 8 incident plane waves are portrayed in this study.

With two incidence plane waves at 0° and 90°, the full-rank filter was able to attenuate the noise 'globally', as shown in the first row of Figure 6.6. A similar global reduction was also achieved when the primary noise field consisted of the same 8 angles of incidence used to formulate the fixed filter, as shown in the second row of Figure 6.6. For a primary noise field with 8 intermediate angles of incidence within the range of angles used to formulate the fixed filter, a slight degradation in attenuation performance is expected and that can be observed in the third row of Figure 6.6.

However, if the primary noise field includes noise coming from angles that deviate greatly from the angles used to formulate the full-rank fixed filter (e.g. negative incidences), the active control system fails to control the noise and even results in spillover in other areas of the interior space. The right figure in the fourth row of Figure 6.6 depicts the said spillover of sound pressure.

6.1.3. Multichannel fixed-filter Formulation for Control of Random Disturbances

To generalise the multichannel active control formulation for multiple angles of incidence with a single set of N control filters, (6.1) is recasted for random disturbance signals [Elliott, 2001] as

$$\mathbf{e} = \mathbf{d} + \mathbf{GWx}, \tag{6.6}$$

where $\mathbf{d}$ and $\mathbf{x}$ are vectors of random disturbances. The cost function to be minimised is thus

$$C_1 = E\left[\mathbf{e}^{\mathrm{H}}\mathbf{e}\right] = \text{trace}\, E\left[\mathbf{e}\mathbf{e}^{\mathrm{H}}\right], \tag{6.7}$$

where $E[\ ]$ denotes the expectation operation taken over ensembles of random data. The cost function C_1 can be written in terms of spectral density matrices through expansion using (6.6) to give

$$C_1 = \text{trace}\left[\mathbf{GWS}_{xx}\mathbf{W}^{\mathrm{H}}\mathbf{G}^{\mathrm{H}} + \mathbf{GWS}_{xd}^{\mathrm{H}} + \mathbf{S}_{xd}\mathbf{W}^{\mathrm{H}}\mathbf{G}^{\mathrm{H}} + \mathbf{S}_{dd}\right], \tag{6.8}$$

where the cross spectral density matrix for the reference signals, and the cross spectral density matrix between the disturbance and reference signals as

$$\mathbf{S}_{xx} = E\left[\mathbf{x}\mathbf{x}^{\mathrm{H}}\right], \tag{6.9}$$

$$\mathbf{S}_{xd} = E\left[\mathbf{d}\mathbf{x}^{\mathrm{H}}\right], \tag{6.10}$$

respectively. The optimum controller response at each frequency is obtained by setting the matrix of complex derivatives of (6.8) to zero, yielding

$$\mathbf{W}_0 = -\left[\mathbf{G}^{\mathrm{H}}\mathbf{G}\right]^{-1}\mathbf{G}^{\mathrm{H}}\mathbf{S}_{xd}\mathbf{S}_{xx}^{-1}, \tag{6.11}$$

where both $\mathbf{G}^{\mathrm{H}}\mathbf{G}$ and $\mathbf{S}_{xx}^{-1}$ are inherently assumed to be positive definite and invertible.

To obtain optimal control of noise from multiple incidences with a set of control filters, the reference vector can be represented by a scalar random process modified by a $K \times 1$ vector of paths [Elliott and Cheer, 2015] to give

$$\mathbf{x} = \mathbf{r}_\theta v, \tag{6.12}$$

where v is a scalar random process with unit variance, and $\mathbf{r}_\theta$ is a $K \times 1$ vector of paths that modify the K angles of incidence of the impinging noise wave. This relationship can be represented in a block diagram by extending Figure 6.1 to give Figure 6.7.

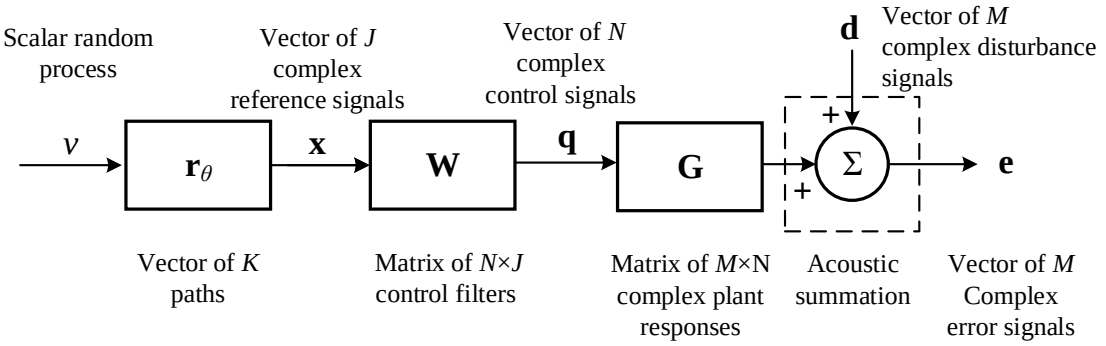

Figure 6.7: Block diagram of the control system illustrating the generation of the reference signals impinging from K angles of incidences.

In the instance of a single noise incidence angle, the cross spectral density $\mathbf{S}_{xx}$ will become

$$\mathbf{S}_{xx} = \mathbf{r}_\theta \mathbf{S}_{vv} \mathbf{r}_\theta^{\mathrm{H}} = \mathbf{r}_\theta \mathbf{r}_\theta^{\mathrm{H}}, \tag{6.13}$$

where $S_{vv} = E\left[v^2\right] = 1,$ and the rank of $\mathbf{S}_{xx}$ will be 1. Hence, the optimal control filter calculated with (6.11) has to be formulated with $K > 1$ to ensure that the assumption of non-singularity of $\mathbf{S}_{xx}$ will not be violated.

6.1.3.1. **Regularised Form**

To draw further connection to the deterministic case, the regularised form of the optimal filter in (6.11) is obtained by introducing an effort weighting parameter into the cost function C_1, similar to (6.2), to give

$$C_2 = E\left[\mathbf{e}^{\mathrm{H}}\mathbf{e} + \beta\mathbf{u}^{\mathrm{H}}\mathbf{u}\right] = \text{trace}\, E\left[\mathbf{e}\mathbf{e}^{\mathrm{H}}\right] + \beta\, \text{trace}\, E\left[\mathbf{u}\mathbf{u}^{\mathrm{H}}\right], \tag{6.14}$$

where **u = Wx** and β is the positive real regularisation parameter. Equation (6.14) is expanded with (6.6), (6.9) and (6.10) to become

$$C_2 = \text{trace}\left[\mathbf{G}\mathbf{W}\mathbf{S}_{xx}\mathbf{W}^{\mathrm{H}}\mathbf{G}^{\mathrm{H}} + \mathbf{G}\mathbf{W}\mathbf{S}_{xd}^{\mathrm{H}} + \mathbf{S}_{xd}\mathbf{W}^{\mathrm{H}}\mathbf{G}^{\mathrm{H}} + \mathbf{S}_{dd}\right] + \beta\, \text{trace}\left[\mathbf{W}\mathbf{S}_{xx}\mathbf{W}\right]. \tag{6.15}$$

The partial differentiation of C_2 with respect to **W** and can be expressed as

$$\begin{aligned}\frac{\partial C_2}{\partial \mathbf{W}} &= 2\left[\mathbf{G}^{\mathrm{H}}\mathbf{G}\mathbf{W}\mathbf{S}_{xx} + \mathbf{G}^{\mathrm{H}}\mathbf{S}_{xd} + \beta\mathbf{W}\mathbf{S}_{xx}\right] \\ &= 2\left[\left(\mathbf{G}^{\mathrm{H}}\mathbf{G} + \beta\mathbf{I}\right)\mathbf{W}\mathbf{S}_{xx} + \mathbf{G}^{\mathrm{H}}\mathbf{S}_{xd}\right].\end{aligned} \tag{6.16}$$

The optimal control filter can be obtained by setting (6.16) to zero, yielding

$$\mathbf{W}_0 = -\left(\mathbf{G}^{\mathrm{H}}\mathbf{G} + \beta\mathbf{I}\right)^{-1}\mathbf{G}^{\mathrm{H}}\mathbf{S}_{xd}\mathbf{S}_{xx}^{-1}, \tag{6.17}$$

where it is bounded by the same assumptions as (6.11).

6.1.3.2. **Simultaneous Control of Noise from Multiple Angles of Incidence**

To control noise simultaneously impinging from K incidences with a single control filter, another cost function can be defined as

$$C_3 = \sum_{k=1}^{K} E\left[\mathbf{e}_{\theta}^{\mathrm{H}}\mathbf{e}_{\theta_k}\right] + \beta\sum_{k=1}^{K} E\left[\mathbf{u}_{\theta_k}^{\mathrm{H}}\mathbf{u}_{\theta_k}\right] = \mathrm{trace}\, E\left[\sum_{k=1}^{K}\mathbf{e}_{\theta_k}\mathbf{e}_{\theta_k}^{\mathrm{H}}\right] + \beta\,\mathrm{trace}\, E\left[\sum_{k=1}^{K}\mathbf{u}_{\theta_k}\mathbf{u}_{\theta_k}^{\mathrm{H}}\right].$$

(6.18)

Equation (6.18) is further expanded with $\mathbf{e}_{\theta_k} = \mathbf{d}_{\theta_k} + \mathbf{GWx}_{\theta_k}$ and $\mathbf{u}_{\theta_k} = \mathbf{Wx}_{\theta_k}$ to

$$C_3 = \mathrm{trace}\left[\mathbf{GW}\bar{\mathbf{S}}_{xx}\mathbf{W}^{\mathrm{H}}\mathbf{G}^{\mathrm{H}} + \mathbf{GW}\bar{\mathbf{S}}_{xd}^{\mathrm{H}} + \bar{\mathbf{S}}_{xd}\mathbf{W}^{\mathrm{H}}\mathbf{G}^{\mathrm{H}} + \bar{\mathbf{S}}_{dd}\right] + \beta\,\mathrm{trace}\left[\mathbf{W}\bar{\mathbf{S}}_{xx}\mathbf{W}^{\mathrm{H}}\right],$$

(6.19)

where

$$\bar{\mathbf{S}}_{xx} = \sum_{k=1}^{K}\mathbf{x}_{\theta_k}\mathbf{x}_{\theta_k}^{\mathrm{H}}, \tag{6.20}$$

$$\bar{\mathbf{S}}_{dd} = \sum_{k=1}^{K}\mathbf{d}_{\theta_k}\mathbf{d}_{\theta_k}^{\mathrm{H}}, \tag{6.21}$$

and

$$\bar{\mathbf{S}}_{xd} = \sum_{k=1}^{K}\mathbf{d}_{\theta_k}\mathbf{x}_{\theta_k}^{\mathrm{H}}. \tag{6.22}$$

Hence, the cost function C_3 is minimised by setting its complex derivatives with respect to $\mathbf{W}$ to zero to give

$$\mathbf{W}_0 = -\left(\mathbf{G}^{\mathrm{H}}\mathbf{G} + \beta\mathbf{I}\right)^{-1}\mathbf{G}^{\mathrm{H}}\bar{\mathbf{S}}_{xd}\bar{\mathbf{S}}_{xx}^{-1}, \tag{6.23}$$

which adopts a similar form as (6.17) above.

At the k-th incidence angle, the reference signal can be characterised by its reference path as

$$\mathbf{x}_{\theta_k} = \mathbf{r}_{\theta_k} v_{\theta}, \tag{6.24}$$

where $\mathbf{r}_{\theta_k}$ is the transfer function that modifies the random process v_θ driving the source at incidence angle θ. Similarly, the disturbance signal can also be characterised by its primary path as

$$\mathbf{d}_{\theta_k} = \mathbf{p}_{\theta_k} v_\theta. \tag{6.25}$$

By substituting (6.24) and (6.25) into (6.20) and (6.22), the cross spectral densities are rewritten as

$$\bar{\mathbf{S}}_{xx} = E\left[\sum_{k=1}^{K} \mathbf{r}_{\theta_k} v_\theta^2 \mathbf{r}_{\theta_k}^{\mathrm{H}}\right] = \sum_{k=1}^{K} \mathbf{r}_{\theta_k} \mathbf{r}_{\theta_k}^{\mathrm{H}}, \tag{6.26}$$

and

$$\bar{\mathbf{S}}_{xd} = E\left[\sum_{k=1}^{K} \mathbf{p}_{\theta_k} v_\theta^2 \mathbf{r}_{\theta_k}^{\mathrm{H}}\right] = \sum_{k=1}^{K} \mathbf{p}_{\theta_k} \mathbf{r}_{\theta_k}^{\mathrm{H}}, \tag{6.27}$$

where $E\left[v_\theta^2\right] = 1$. Therefore, $\bar{\mathbf{S}}_{xx}$ is full rank when there are more incidence angles than reference sensors ($K > J$).

6.1.3.3. **Generalisation of the deterministic formulation**

The deterministic formulation can be reanalysed by revisiting (6.5), where the matrix of optimal solutions for K angles of incidence $\mathbf{Q}_{0,\theta}$ in the equation is expressed as

$$\mathbf{Q}_{0,\theta} = -\left(\mathbf{G}^{\mathrm{H}}\mathbf{G} + \beta\mathbf{I}\right)^{-1} \mathbf{G}^{\mathrm{H}}\mathbf{D}_\theta, \tag{6.28}$$

where $\mathbf{D}_\theta = \left[\mathbf{d}_{\theta_1} \quad \mathbf{d}_{\theta_2} \quad \cdots \quad \mathbf{d}_{\theta_K}\right]$. Hence, by substituting (6.28) into (6.5), the optimal control filter formulation is expanded to

$$\mathbf{W}_{0,FR} = -\left(\mathbf{G}^{\mathrm{H}}\mathbf{G} + \beta\mathbf{I}\right)^{-1} \mathbf{G}^{\mathrm{H}}\mathbf{D}_\theta \mathbf{X}_\theta^{\mathrm{H}} \left(\mathbf{X}_\theta \mathbf{X}_\theta^{\mathrm{H}}\right)^{-1}, \tag{6.29}$$

where $\mathbf{D}_\theta \mathbf{X}_\theta^{\mathrm{H}} = \sum_{k=1}^{K} \mathbf{d}_{\theta_k} \mathbf{x}_{\theta_k}^{\mathrm{H}}$ and $\mathbf{X}_\theta \mathbf{X}_\theta^{\mathrm{H}} = \sum_{k=1}^{K} \mathbf{x}_{\theta_k} \mathbf{x}_{\theta_k}^{\mathrm{H}}$. Since $\mathbf{x}_{\theta_k}$ and $\mathbf{d}_{\theta_k}$ are deterministic vectors, they correspond to $\mathbf{r}_{\theta_k}$ and $\mathbf{p}_{\theta_k}$ in Eqs. (6.26) and (6.27), respectively. Hence, as long as $\bar{\mathbf{S}}_{xx}$ in (6.23) is full rank, the results in section 6.1.2 is valid for general random signals.

6.2. Hybrid Source Arrangement with Double-layered Sources at the Periphery

Although the planar arrangement of sources has a higher frequency upper limit of effective control than boundary control methods, the proposed double-layer boundary control by Wang et al has yielded promising results in controlling acoustic modes in a rectangular duct with a baffled opening [Wang et al., 2017a, 2017c, 2018].

Investigation into the physical mechanisms of the double-layer boundary layout ANC system reveal that addition of another layer of sources at a different height eases the burden on the single-layer system in controlling high-intensity modes [Wang et al., 2018]. Without effort control mechanisms in place [Elliott, 2001], the sources at the nodal lines of the modes will be overdriven (i.e. in the single-layer system) resulting in a control spill-over effect and distortion; and reducing the attenuation performance or even destabilise the adaptive system. This coincides with the observations in section 4.2.2.1, where the attenuation performance degrades as the sources are nearer to the edge of the wall. Moreover, the double-layer boundary layout is still bounded by the size of the aperture and has also not been investigated for application on an open aperture.

For a clearer understanding, this section will firstly investigate the normal particle velocity distribution across the open aperture. Secondly, to understand the degree to

which the physical positioning of the control source affects the attenuation performance of the double-layer configuration, the proximity to the wall edge and its separation distance between layers will be investigated here using 2D numerical simulations. Thirdly, a hybrid approach using both the double-layer configuration coupled with the planar layout is proposed. The hybrid solution aims to reduce the visual obstruction in the open aperture caused by the control sources by requiring less control sources distributed across the open aperture, whilst maintaining attenuation performance. Finally, scenarios which favour the deployment of the hybrid configuration is discussed.

6.2.1. FEM Simulation Model

To account for the effects of scattering around the edges of the aperture, the physical limits of active noise control attenuation is investigated with numerical methods. The study is performed using the 2D finite element method (FEM), with a maximum element size of one-sixth of the wavelength at 4 kHz. Based on the free-field 3D analysis of an infinite plane array of control sources [Elliott et al., 2018], the 2D model is sufficient to provide useful insights in this preliminary investigation.

The 2D FEM computation plane measures 10 m by 10 m and is bounded by a perfectly-matched layer to emulate a free-field condition, as shown in Figure 6.8. Two rigid rectangles form the vertical cross section of a window opening of size $L = 1.0$ m. The total number of secondary sources N are optimised to reduce the sum-of-squared pressures at the far-field evaluation arc. The x and y axis intersect in the middle of the aperture, as depicted by the blue axis lines in Figure 6.8.

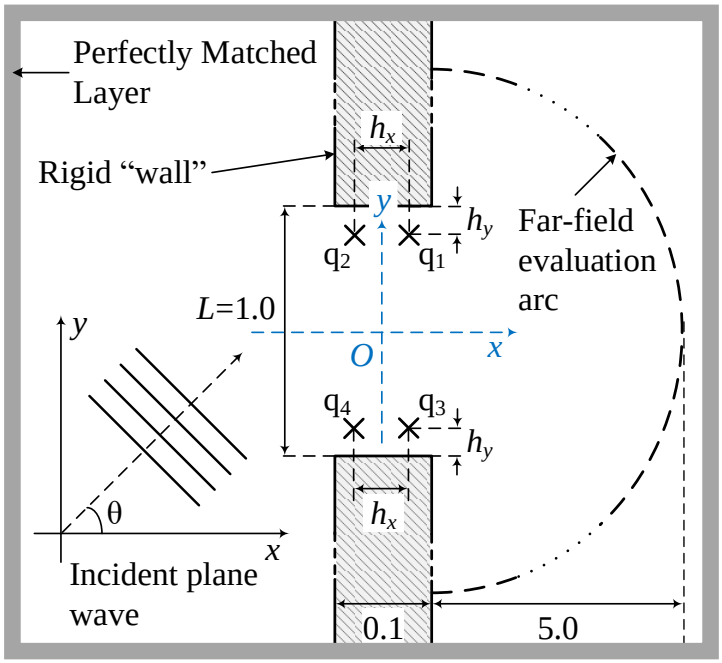

Figure 6.8: Finite element simulation model to evaluate sound power transmission through an open aperture.

6.2.1.1. Active Control Formulation and Evaluation Parameters

The active control system follows the formulation which minimises the total power transmitted through the aperture at the far-field arc that envelopes the entire opening in section 4.1. The optimised secondary source strengths are calculated with (4.3), where regularisation parameter β was set to the minimum value necessary to obtain a well-conditioned inverse of the matrix. Similarly, the evaluation criteria have been defined in section 4.1.1 as shown in (4.6).

6.2.2. Normal Velocity Distribution Across the Aperture

The cost function defined in (4.3) is the far-field estimate of the sound power emitted through the aperture. Sound power through the aperture can also be described by the

acoustic intensity per unit area, whereby the acoustic intensity is defined as the product between the acoustic pressure and the particle velocity normal to the surface [Nelson and Elliott, 1992]. Since the control sources have been tuned to minimise the acoustic power, the acoustic power distribution across the aperture will reveal the spatial distribution of effort required by the respective sources to achieve effective global control.

With reference to Figure 6.8, the normal particle velocity of a plane wave passing through the aperture in the positive x direction is plotted as a function of the y-axis coordinates between −0.5 and 0.5 m in Figure 6.9. The plots describe the distribution within the aperture, which are represented by the particle velocity normal to a vertical 2D line parallel to the y-axis at $x = -0.5$, 0 and 0.5 m. The three x-axis coordinates represent the left most edge, the central point where the sources are located, and the right most edge of the aperture bounded by the rigid walls. For clarity, the frequency range from 100 Hz to 1000 Hz is represented only by the lower and upper limits and the median value, i.e. 100 Hz, 500 Hz, and 1000 Hz, in Figure 6.9.

In the entire frequency range, the magnitude of the normal particle velocity increases sharply nearing the edges of the aperture and reaches the maximum value on the edge. The magnitude distribution of the normal velocity is similar along all three x-axis coordinates. This observation indicates that sources on the edge have to be driven at disproportionately higher levels, which suggests that an additional source at the edge could improve the control of diffraction at the edges and result in better global control.

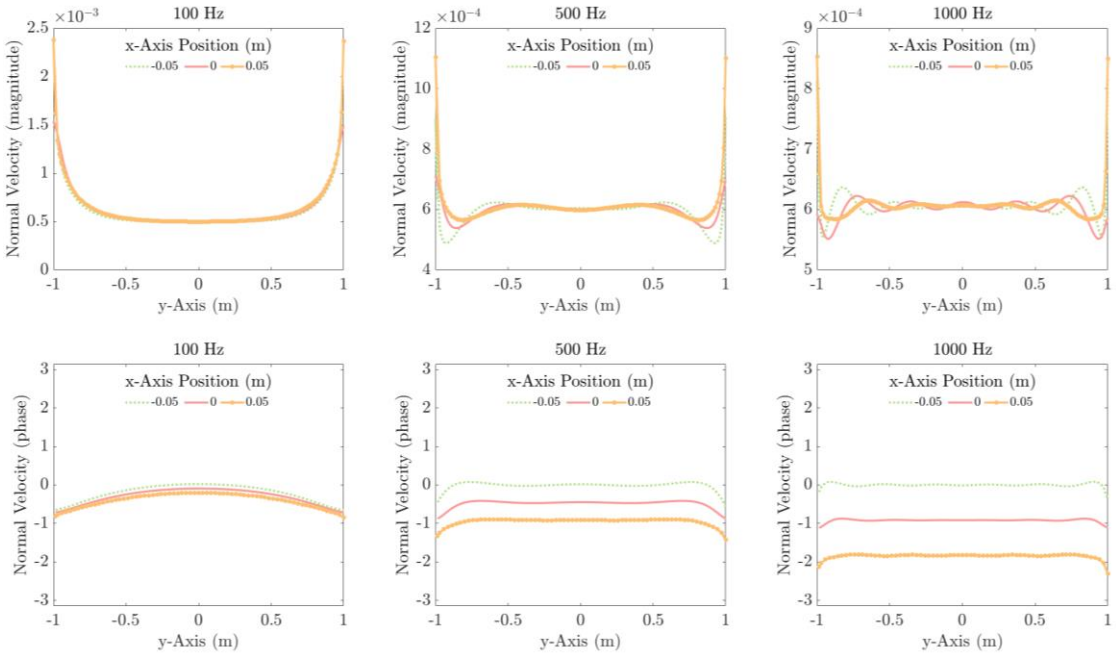

Figure 6.9: Normal velocity magnitude and phase as a function of y-axis coordinates for 100 Hz, 500 Hz, and 1000 Hz, at three x-axis positions (−0.05 m, 0 m, and 0.05 m).

6.2.3. Double-layer Configuration in an Open Aperture

Although the double-layer configuration has been shown to yield more stable attenuation performance than the planar array, albeit up to a lower upper frequency limit [Wang et al., 2017b], it has yet to be implemented in an open aperture scenario. Moreover, the effect of the wall edges on the source placement of the double-layer configuration is still unknown. Therefore, the effect of (1) the separation distance between each pair of sources, h_x, and (2) proximity to the wall edge, h_y, on the attenuation performance is investigated in this section. The separation distance h_x is symmetric about the y-axis, and h_y is anchored to the wall edge such that $h_y = 0$ m indicates that the sources are resting on the wall edge, as depicted in Figure 6.8.

6.2.3.1. **Effect of Source Separation and Proximity to the Edge on Attenuation Performance**

In the 2D scenario, the double-layer configuration can be represented by 2 sources on each edge as depicted in Figure 6.8. The proximity to the edge is anchored at $h_y = 0$ m, and investigated at three distances, namely $h_y = 0$, 0.03, and 0.06 m, i.e. $h_y = 0$ refers to control sources resting on the edge of the wall. With a fixed wall width of 0.1 m as depicted in Figure 6.8, the effect on attenuation is also investigated at three separation distances from a maximum of $h_x = L = 0.1$ m to $h_x = 0.025$ m, at intervals of 0.025 m, symmetric to the y-axis.

Except for a minor deviation in the case where $h_x = 0.1$ and $h_y = 0$ m at 90° incidence, the results of the 9 configurations (3 proximities to the edge and 3 separation distances) are indistinguishable, as shown in Figure 6.10 for (a) normal incidence, (b) 30° incidence, (c) 60° incidence, and (d) 90° incidence. Hence, the double layer configuration appears to be unaffected by the proximity to the edges of the wall unlike in the planar configuration where it is important not to place the sources on the edges of the wall [Lam et al., 2018a]. Although the separation distance does not affect the attenuation performance of the double-layer configuration, it is important not to place the sources too close to each other to prevent overdriving. The separation distance will henceforth be set to $h_x = 0.1$ and $h_y = 0$ m for simulations in the subsequent sections.

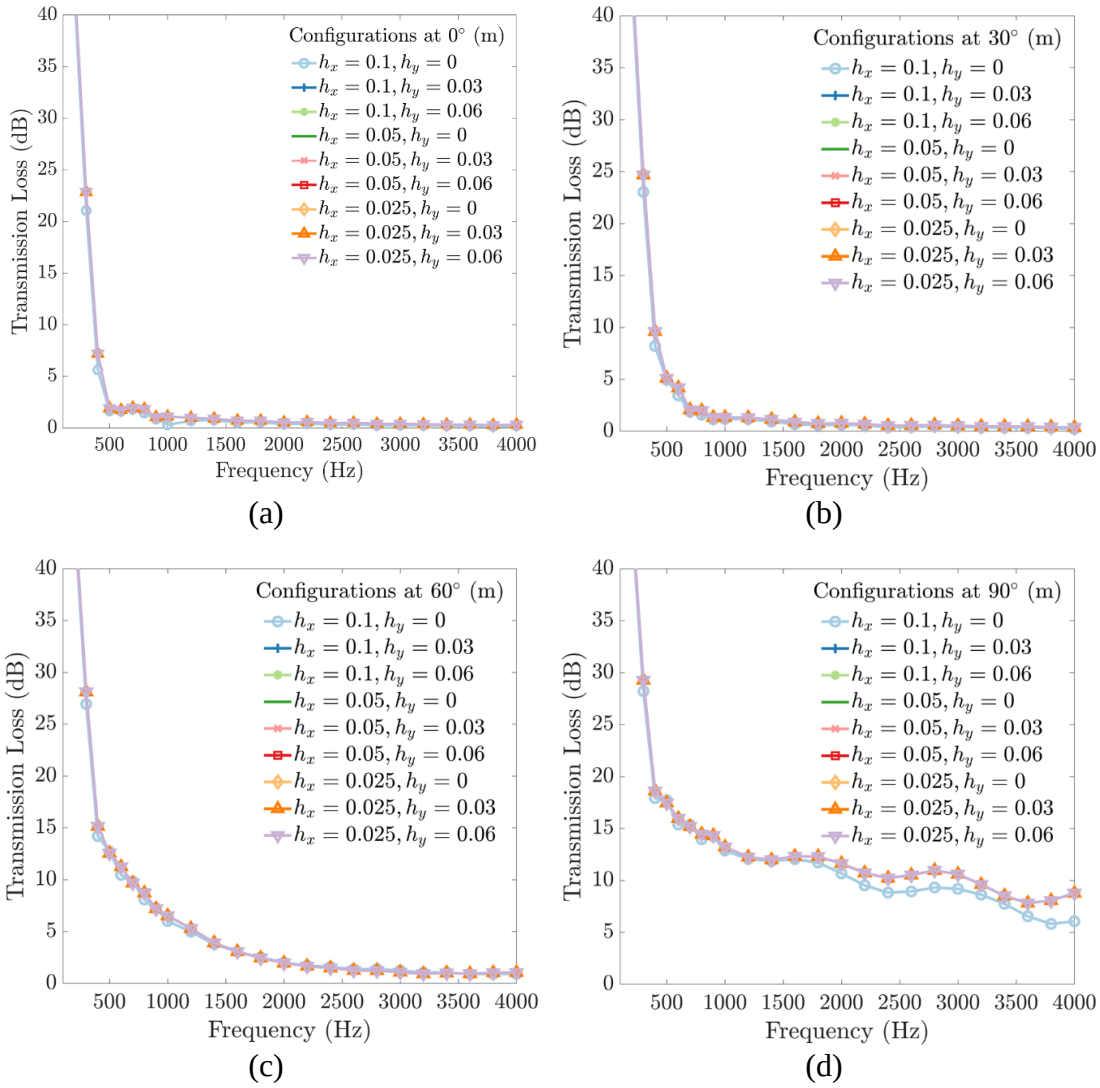

Figure 6.10: Transmission loss of the 4-channel double-layer configuration with different separation distances at angles of incidence at (a) 0°, (b) 30°, (c) 60° and, (d) 90°.

6.2.4. Hybrid Configuration in an Open Aperture

Since the upper frequency limit of attenuation performance of the double-layer configuration is still limited by the size of the open aperture, a hybrid configuration which comprises of both the double-layer and planar layouts is proposed. For practicality, the hybrid configuration should consist of the same number of sources as

the planar configuration. The 4-source double-layer configuration is shown in Figure 6.11(a) as a comparison. The 8-source planar arrangement with a source separation distance of $w_p = L/8$, and the 8-source hybrid arrangement with a separation distance of $w_h = L/4$, is depicted in Figure 6.11(b) and (c) respectively.

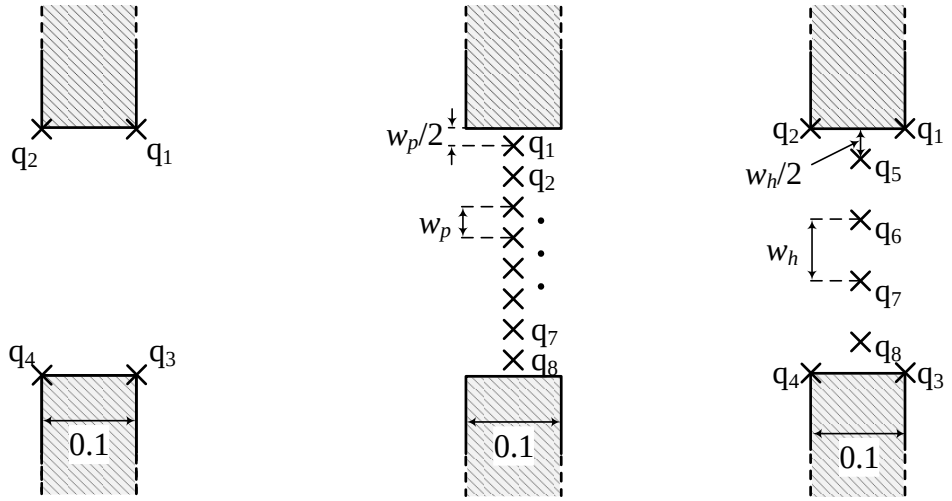

Figure 6.11: Source positioning of the (a) 4 source double-layer boundary array, (b) 8 source planar array, and the (c) 8 source hybrid array.

6.2.4.1. **Performance as a Function of Frequency at all angles of Incidence**

The attenuation performance as a function of frequency for the 8-source planar array and 8-source hybrid configuration are plotted in Figure 6.12(a) and (b), respectively, for angles of incidence from 0° to 90°. At normal incidence, both cases exhibit an upper limit at frequencies where the acoustic wavelength are equals to the separation distances w_p and w_h, where subscripts $_p$ and $_h$ represents planar and hybrid configurations respectively. As the incidence angles increase, the hybrid configuration deviates from the general guidelines showing increased attenuation at steeper angles of incidence, as

emphasised in Figure 6.13. In absolute terms, however, the planar configuration still excels at gentler angles of incidence (<45°). Hence, it is useful to devise scenarios for which a hybrid configuration would be more effective than the planar configuration, such as at glancing angles of incidence.

6.2.4.2. **Conditions for the Effective Deployment of a Hybrid Configuration**

The attenuation performance is evaluated for 0°, 30°, 60°, and 90° angles of incidence as a function of normalised frequency kw_p and kw_h, for the 8-source planar and hybrid configurations respectively. k represents the acoustic wavenumber, which is 2 times π divided by the acoustic wavelength λ.

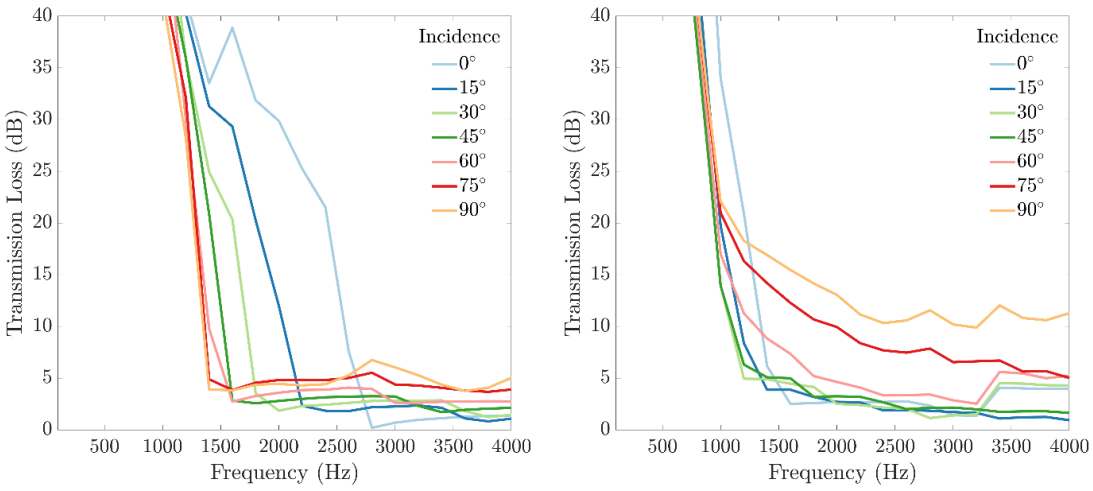

Figure 6.12: Transmission loss as a function of frequency at all angles of incidence using the (a) planar configuration, and with the (2) hybrid configuration.

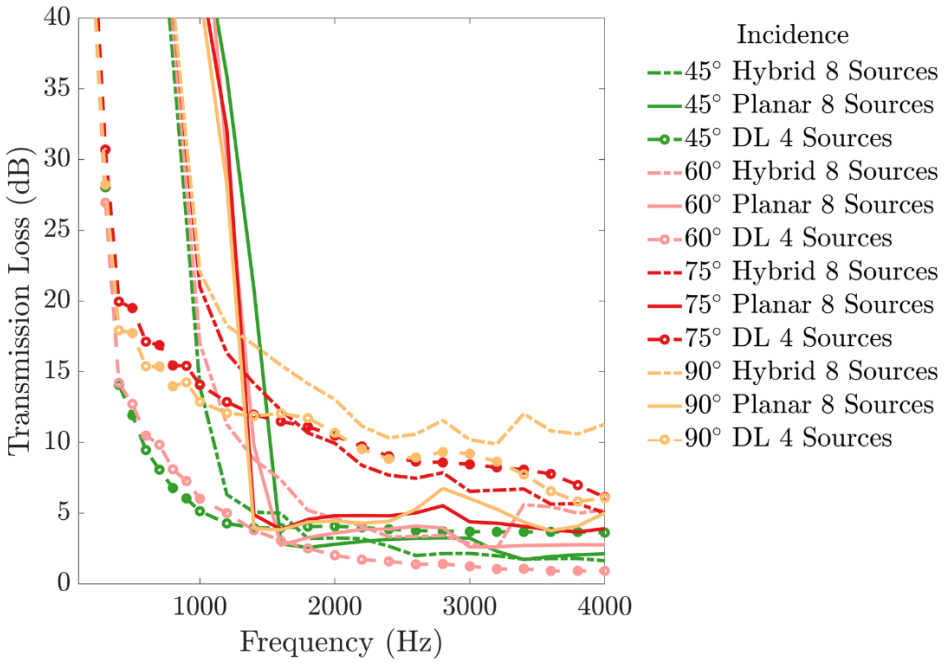

Figure 6.13: Transmission loss as a function of frequency at incidence angles above 45° for the 8 sources planar (solid line), 8 sources hybrid (dashed), and 4 sources double-layer (dashed with circular markers) configurations.

Attenuation performance of the 8-source planar array is consistent with the general guidelines reported by Lam et al. [Lam et al., 2018a], where there is a sharp termination when kw_p is $2\pi/(1+\sin\theta)$, as shown in Figure 6.14(a). As discussed in Chapter 0, the 8-channel hybrid layout only adheres to the guidelines for normal incidence, as indicated by the light blue solid line in Figure 6.14(b). In other words, the planar array is only effective up to the acoustic wavelength as large as the separation between control sources at normal incidence, and up to half the acoustic wavelength at 90° incidence.

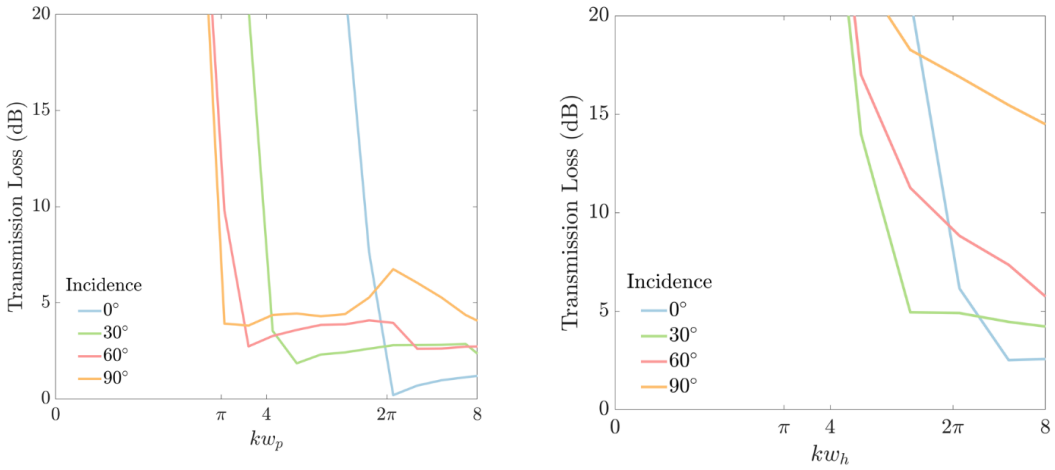

(a) (b)

Figure 6.14: Transmission loss for the (a) 8-source planar array, (b) 8-source hybrid boundary array, as a function of kw.

Attenuation performance of the 8-source hybrid configuration is plotted for the same angles of incidence in Figure 6.14:(b). The augmentation of the double-layer sources on the edge improves the attenuation upper limit of the system up to wavelengths equivalent to the separation distance between the planar arrangement in the hybrid array, for all angles of incidence, i.e. $kw_h \approx 2\pi$, for all $\theta \leq 90°$. This improvement indicates that the double-layer sources are contributing significantly to the attenuation of the primary noise at oblique incidences. It is then essential to generalize the conditions for which the attenuation performance of the hybrid configuration will exceed that of the planar array.

The suggested minimum number of control sources N for the planar array is derived in (4.9) in section 4.2.3.3. [Lam et al., 2018a]. Since the minimum number of sources required for the double-layer configuration is four, and the cut-off frequency seems to converge at $kw = 2\pi$ for all angles of incidence, the minimum number of control sources for the hybrid configuration can be written as

$$N > 4 + \left\lceil \frac{L}{\lambda} \right\rceil, N \in \mathbb{Z}^{+}. \tag{6.30}$$

By inferring from Eqs. (4.9) and (6.30), the conditions for which the hybrid configuration is more effective than a planar array can be generalized to

$$\frac{L \sin\theta}{\lambda} > 4, \tag{6.31}$$

and further generalised in terms of the minimum upper frequency limit to justify the deployment of the hybrid array to

$$f_{lim} > \frac{4c_0}{L \sin\theta}, \text{ for all } 0° < \theta \leq 90°, \tag{6.32}$$

where f_{lim} refers to the required upper frequency limit for effective control and c_0 refers to the speed of sound in air. For instance, if the ANC system is required to be effective up to 90°, the desired upper frequency limit f_{lim} must be greater than 1373.6 Hz ($L = 1$ m) to justify the deployment of the hybrid layout instead of a planar array.

6.3. Summary

In the real-time implementation of any ANC system in the real-world, there are numerous considerations and design choices that can limit the control performance. Two of the main hurdles to the real-world implementation were investigated theoretically and numerically in this section. The first hurdle considers the difficulties in the placement of error microphones within the domestic living quarters on the basis of privacy concerns and physical obstruction. The second hurdle is concerning the visual obstruction of the somewhat dense array of sources distributed in the window aperture.

6.3.1. Fixed-filter Implementation

Error microphones are an essential component to an effective active noise control system. However, physical constraints do not always favour the presence of error microphones during implementation. For the specific problem of ANC through open windows, a fixed-filter formulation is studied to determine the noise attenuation performance degradation for different noise incidence angles.

With the aim to minimise average noise power attenuated across different incidence angles, a full-rank fixed filter formulation was proposed. Our acoustic simulation demonstrated that the full-rank fixed-filter approach is able to attenuate noise with similar performance to the exact least-squares solution, even for incidence angles excluded from the full-rank calculations (from 0° to 90° in increments of 5°).

Despite evidence that the fixed-filter approach could cover a wide range of individual incidence angles, and even multiple noise plane waves from a few incident angles, the performance of the fixed filter is still bounded by acoustical limitations. As shown in this study, the performance of the full-rank fixed filter is dependent on the angles used to formulate the filter. However, the limits of attenuation performance have yet to be investigated in a diffused primary noise field (1) with various combination of angles used in filter formulation; (2) filters designed with overdetermined formulation ($K > N$); (3) and how the number of secondary sources M affects the range of incidence angles that can be controlled with a fixed filter.

6.3.2. Hybrid Source Arrangement with Double-layered Sources at the Periphery

The double-layered active noise control configuration is investigated for application in open apertures. Through 2D FEM simulations, attenuation performance of the double-layer source configuration is mostly unaffected by positioning in terms of proximity to the wall edge and the separation distance between layers. Additionally, through further testing, the attenuation performance is also unaffected by the asymmetrical control source positioning within the depth of the wall.

As an attempt to reduce the visual obstruction caused by distributing the sources across the aperture, a hybrid source configuration of a double-layered control source arrangement at the edge of the wall coupled with a planar array consisting of lesser sources (i.e. separated farther apart) is proposed. Although the attenuation performance of the hybrid configuration pales in comparison with the planar array at normal primary incidence, it exhibits increased attenuation at steep incidences. Hence, the conditions for which the hybrid configuration outperforms the planar array is devised.

In practice, the hybrid method could be the solution for large apertures or extremely steep angles of incidences (e.g. noise at the upper floors of a tall high-rise building, neighbourly noise).

6.3.3. Open Issues

Although fixed filters seem to be an enticing solution, their real-time implementation could be thwarted by the extensive tuning process or the requirement of potentially long filter lengths. Hence, the error microphones have to be included for adaptive control but

shifted away from their desired locations, presenting an avenue for the implementation of virtual sensing approaches [Cheer et al., 2018; Jung et al., 2017].

If the physical error microphones are placed in a manner such that the auxiliary filters are causal, i.e. physical microphones nearer to control sources than the desired virtual locations, current remote/virtual techniques will suffice. Hence, the successful implementation of the virtual microphone technique is still dependent on the careful placement of the error microphones. Moreover, the inclusion of auxiliary filters increases the already high computation complexity of the multichannel ANC system.

To realise the system at a reasonable cost, the computational complexity of the multichannel ANC system has to be further reduced. So far, several preliminary investigations have been conducted to explore potential areas where the computational complexity can be reduced. One straightforward method is to reduce the number of error signals used in the control algorithm, such as grouping neighbouring error microphones [Murao et al., 2013] or mixing the error microphone signals [Murao et al., 2017]. By manipulating the error signals, however, the control performance is unavoidably reduced, especially when the signal arrives from an oblique incidence angle.

If the noise signature can be classified, control filters could be pre-trained and stored in a database. A selective approach could be adopted to first classify the impinging noise and thereafter select the appropriate control filters from the database [Ranjan et al., 2016; Shi et al., 2018].

Finally, for high computational loads that necessitates the implementation on an FPGA, the control algorithm should be optimized for the hardware architecture. For instance, a systolic FXLMS implementation [Shi et al., 2016] or a parallel architecture implementation of the FXLMS algorithm [Shi et al., 2017].

Since these approaches have only been studied preliminarily, their practical usage requires further validations in experimental setups and in operational environments.

Chapter 7

Conclusions and Further Work

7.1. Conclusions

The traction towards active control methods to quieten environmental noise that propagate through window apertures of living quarters has been motivated by four factors: maintenance of natural ventilation function, access to the building façade, allowance of daylight ingress, and the ability to control noise in the lower frequencies. This thesis has investigated the active control of noise through window aperture from the perspective of practical realisation. For clarity, the conclusions are grouped into three sections: physical limits of active noise control, real-time active noise control, and considerations for practical implementation.

7.1.1. Physical Limits of Active Noise Control

Although active control methods for window apertures have been demonstrated in the past, their physical limits of control have not been defined – an important first step in designing a practical active control system. This thesis firstly investigated the fundamental limits of control of noise through apertures using numerical methods.

Since the equivalent source method shared similarities with the active control formulation, a preliminary study was conducted in Chapter 3 to evaluate its suitability and accuracy in modelling the acoustic field of the window problem. Despite its computational similarities to the active control formulation and the introduction of regularisation methods to prevent ill-conditioning during matrix inversions, the

equivalent source method was inherently limited by the physical dimensions of the rigid wall with respect to the wavelength of interest in this study – i.e. thickness of the wall was too thin compared to acoustic wavelength.

A finite-element method based numerical modelling approach was adopted to investigate the fundamental limits of active control through the aperture in Chapter 4. Based on a free-field study on the active control of planar noise with an infinite plane array sources, it was deemed that a 2D model could provide sufficient accuracy. To understand the interaction between the acoustic fields of the array of control sources and the impinging noise plane wave, the positions of the array of sources were systematically iterated across the range of frequencies of interest (100 to 2000 Hz) and angles of incidences (0º to 90º). Contrary to the practice of placing sources on the boundary of the aperture in several past experimental studies, it was found in 4.2.2.1 that the control sources should not be placed at the edge of the aperture for optimal performance and that it should be half the separation distance away from the wall – i.e. $v = w/2$. For the best average performance across all frequencies, the array of sources should be placed in the centre of the depth of the aperture. In an unobstructed aperture, it was found in 4.2.3.3 that the sources should be separated by the shortest wavelength of interest weighted by the sine of the incidence angle added to 1 – i.e. $w < \lambda/(1+\sin\theta)$. The findings agree with the those in the free-field simulation. Based on the fundamental limits of control defined for a number of control source arrangements, a practical guideline was developed to decide on the minimum number of sources required for good control up to the desired frequency and angle of incidence.

Before the real-time active control system was realised in a typical full-sized sliding window, its fundamental limits of control are investigated with an accurate replication of the dimensions in an FEM model. The passive insulation performance of a single-

glaze window in the 1 m wide aperture was first quantified as a benchmark for the active control system performance, which revealed that the passive insulation is reduced drastically even with a slight gap. In the presence of the glass panel, the general rule that the sources should be not placed on the edge was shown to still be true, in an attempt to replicate a past study numerically in section 4.3.3. Using the guidelines source placement and deciding on the number of sources required for good control, it was shown in section 4.3 that the active control implementation in the partially glazed aperture of a typical sliding window system outperforms the passive insulation of a fully-glazed aperture.

7.1.2. Real-time Active Noise Control

To investigate the attenuation performance of a real-time active noise control system in a window, a cubic chamber was constructed and placed in a recording studio. A full-sized sliding window with similar dimensions to the simulation model was fabricated according to the building standards in Singapore and installed onto one of the vertical sides of the chamber. A total of 24 active control units inspired by past studies were custom designed and secured onto the security grille of the window – a typical fixture in Singapore.

An average broadband (100 to 2000 Hz) attenuation of 10 dB was predicted at the error microphones via a fully-coupled multichannel FXLMS simulation using the measured transfer functions between the secondary sources and an array of 24 error microphones. To evaluate the actual real-time ANC performance, an array of 18 class 1 calibrated microphones was distributed inside the test chamber, where 12 microphones formed a planar array stretching across the window aperture, and the rest of the

microphones were distributed in accordance to the ISO 16283-3 to evaluate the energy-average sound pressure levels.

Due to the high computational complexity of a 24 channel system, a collocated-FXLMS control algorithm was adopted and implemented on an FPGA platform. In the tonal experiments at normal incidence, energy-average attenuation performance of the active control system with partial glazing (~55%) was comparable (< 5 dB lower) to the passive performance fully-glazed system from 400 Hz to 1200 Hz. In the attenuation of broadband noise at normal incidence, the energy-average attenuation of the active control system was notably poorer than the fully-glazed window as the ANC system was shown to perform poorly for high frequency tones (> 1200 Hz). At oblique incidences, the ANC system performance closely matches that of the full-glazed passive attenuation up till approximately 1200 Hz, suggesting that passive insulation is less effective for oblique noise sources. When the noise is bandlimited to between 400 Hz and 1300 Hz, the active control system attained an energy-average reduction of 5 to 7 dB for both recorded traffic noise and white noise. The discrepancy between the numerical and the real-time experiments is largely due to the limitation of the electronic components.

7.1.3. Considerations for Practical Implementation

To increase the practicability of active control solutions for window apertures, preliminary studies were carried out to address two specific issues pertaining to the visual and physical obstruction caused by: error microphones, and the dense array of control sources in the aperture.

The concept of employing a fixed filter to omit the need for error microphones was investigated theoretically and numerically. By implementing the designed filter numerically in the 2D FEM model of the window aperture, it was found that a single, carefully-designed filter could attenuate noise from a wide range of incidence angles, up to two sources (theoretically up to the number of sources used in the formulation) impinging simultaneously at the same time. Although the initial theoretical formulation and subsequent numerical implementation was based on deterministic signals, a further theoretical derivation shows that the results could be casted in the framework of random disturbances.

Based on the findings in Chapter 4, the required number of sources increases with the angle of noise incidence – a typical scenario in a high-rise building implementation for the upper levels. Since a dense array of control sources is visually displeasing, an approach adapted from a recent study was proposed to reduce the number of sources required without decreasing the attenuation performance. Results of the numerical study showed that the number of sources distributed in the aperture could be halved by adopting the double-layer source approach at the edge of the aperture without any loss in attenuation performance but only for near glancing angles of incidence. Nevertheless, a guideline based on that defined in section 4.2.2.3 was devised to decide when the proposed hybrid approach is suitable.

7.2. Recommendations for Further Work

The main hurdle to the real-world deployment of the active control system for window aperture lies in the high computational complexity of the multichannel ANC system. Besides extensions proposed in Chapter 6, other feasible directions could be undertaken.

Decentralisation of the control algorithm [Elliott, 2001; Murao et al., 2016; Zhang et al., 2019, 2013] could be the enabling factor for the mass production of individual control units with embedded controllers. However, a large open aperture could prove to be difficult for a decentralised approach to achieve satisfactory performance especially for noise impinging from oblique incidences. An elegant approach is thus required to segregate the aperture into smaller cells for successful implementation of the decentralised control technique.

The long-term stability of an adaptive control system is also vital to the practicability of the any ANC system. One major trade-off with using small speakers or audio amplifiers is their susceptibility in being overdriven as they are operating close to their maximum output capacity. Traditional effort-weighting methods or nonlinear adaptive systems come at an expense of significantly increased computational complexity. Hence, it is desirable to develop solutions that do not increase the computational complexity of the system but still able to constraint the output power and guarantee system stability [Shi et al., 2019].

The human perception of sound is not a only a physical process at the periphery of the hearing system (up to the inner ear) but also a neurological process where signals are interpreted in the brain [Zwicker and Fastl, 2013]. The soundscape approach, where it is the acoustic environment as perceived or experienced by humans in context [International Organization for Standardization, 2014], could be adopted in which ANC is an excellent first step in enhancing the sonic environment. One common approach in soundscape design is to first reduce the unwanted sounds (e.g. environmental noise by ANC), followed by enhancement of wanted sounds (e.g. water stream sounds, birdsongs). It was found that when stream sounds and birdsongs were augmented with traffic noise in an outdoors environment it decreased the perceived loudness and

increase the overall pleasantness [Hong et al., 2017]. Since the subjective evaluations were conducted in the context of an outdoors scenario, a separate study targeted at indoor environments could provide a more accurate insight. If the indoor evaluations arrive at similar conclusions, the residual error signal from the ANC window system could be augmented by wanted sounds for a quieter indoor soundscape.

Author's Publication

Part of the work presented in this thesis has been published in journals as:

- Lam, B., Elliott, S., Cheer, J., and Gan, W.-S. (2018). "Physical limits on the performance of active noise control through open windows," Appl. Acoust., 137, 9–17. doi:10.1016/j.apacoust.2018.02.024
- Lam, B., Shi, C., Shi, D., and Gan, W.-S. (2018). "Active control of sound through full-sized open windows," Build. Environ., 141, 16–27. doi:10.1016/j.buildenv.2018.05.042
- Elliott, S. J., Cheer, J., Lam, B., Shi, C., and Gan, W. (2018). "A wavenumber approach to analysing the active control of plane waves with arrays of secondary sources," J. Sound Vib., 419, 405–419. doi:10.1016/j.jsv.2018.01.028

Part of the work presented in this thesis has also been published in conferences as:

- Lam, B., Elliott, S. J., Cheer, J., and Gan, W.-S. (2015). "The Physical Limits of Active Noise Control of Open Windows," In K. M. Lim (Ed.), Proc. 12th West. Pacific Acoust. Conf., Singapore, 184–189.
- Lam, B., Elliott, S. J., Cheer, J., and Gan, W.-S. (2015). "Regularisation of the equivalent source method for robust numerical modelling of acoustic scattering," INTER-NOISE NOISE-CON Congr. Conf. Proceedings, InterNoise15, Institute of Noise Control Engineering, San Francisco, CA, USA, 976–987.
- Lam, B., and Gan, W.-S. (2016). "Active Acoustic Windows: Towards a Quieter Home," IEEE Potentials, 35, 11–18. doi:10.1109/MPOT.2014.2310776
- Lam, B., He, J., Murao, T., Shi, C., Gan, W.-S., and Elliott, S. J. (2016). "Feasibility of the full-rank fixed-filter approach in the active control of noise through open windows," INTER-NOISE NOISE-CON Congr. Conf. Proceedings, InterNoise16, Hamburg, Germany, 3548–3555.

- Lam, B., Shi, C., and Gan, W. (2017). “Active Noise Control Systems for Open Windows : Current Updates and Future Perspectives,” Proc. 24th Int. Congr. Sound Vib., London, UK, 1–7.
- Lam, B., and Gan, W.-S. (2017). “Effects of acoustic scattering on the active control of noise through apertures,” COMSOL Conf. 2017, Singapore.
- Lam, B., Gan, W., and Elliott, S. (2018). “Hybrid source arrangement for active control of noise through apertures at oblique incidences: A preliminary investigation,” Proc. 25th Int. Congr. Sound Vib. ICSV25, Hiroshima, Japan, 1–8.
- Fasciani, S., He, J., Lam, B., Murao, T., and Gan, W.-S. (2015). “Comparative study of cone-shaped versus flat-panel speakers for active noise control of multi-tonal signals in open windows,” INTER-NOISE NOISE-CON Congr. Conf. Proc., San Francisco, CA, USA, 1109–1120.
- He, J., Lam, B., Murao, T., Ranjan, R., and Gan, W.-S. (2016). “Symmetric design of multiple-channel active noise control systems for open windows,” INTER-NOISE NOISE-CON Congr. Conf. Proceedings, InterNoise16, Institute of Noise Control Engineering, Hamburg, Germany, 613–622.
- Ranjan, R., He, J., Murao, T., Lam, B., and Gan, W.-S. (2016). “Selective Active Noise Control System for Open Windows using Sound Classification,” INTER-NOISE NOISE-CON Congr. Conf. Proceedings, InterNoise16, Hamburg, Germany, 482–492.
- Elliott, S., Cheer, J., Lam, B., Shi, C., and Gan, W. (2017). “Controlling Incident Sound Fields With Source Arrays in Free Space and Through Apertures,” In B. M. Gibbs (Ed.), Proc. 24th Int. Congr. Sound Vib., London, UK, 1–7.

Work carried out during the course of my PhD but not included in this thesis are:

- Lam, B., Shi, C., and Gan, W. (2014). “Feasibility of a length-limited parametric source for active noise control applications,” In M. J. Crocker, M. Pawelczyk, and J. Tian (Eds.), Proc. 21st Int. Congr. Sound Vib. ICSV21, Beijing, China, 1–8.

- Shi, C., Murao, T., Shi, D., Lam, B., and Gan, W.-S. (2016). “Open loop active control of noise through open windows,” J. Acoust. Soc. Am., 140, 3313–3313. doi:10.1121/1.4970553
- Murao, T., Nishimura, M., He, J., Lam, B., Ranjan, R., Shi, C., and Gan, W.-S. (2016). “Feasibility study on decentralized control system for active acoustic shielding,” INTER-NOISE NOISE-CON Congr. Conf. Proceedings, InterNoise16, Hamburg, Germany, 1106–1115.
- Shi, C., Li, H., Shi, D., Lam, B., and Gan, W. (2017). “Understanding Multiple-Input Multiple-Output Active Noise Control from a Perspective of Sampling and Reconstruction,” Asia-Pacific Signal Inf. Process. Assoc. Annu. Summit Conf. (APSIPA ASC), IEEE, 124–129. doi:10.1109/APSIPA.2017.8282013
- Shi, D., Lam, B., and Gan, W.-S. (2018). “A novel selective active noise control algorithm to overcome practical implementation issue,” 2018 IEEE Int. Conf. Acoust. Speech Signal Process., IEEE, Calgary, Canada, 1–5.
- Shi, D., Gan, W.-S., Lam, B., and Shi, C. (2019). “Two-gradient direction FXLMS: An adaptive active noise control algorithm with output constraint,” Mech. Syst. Signal Process., 116, 651–667. doi:10.1016/j.ymssp.2018.06.062

Appendix A

The minimum power output of free field incoherent line sources and the active control of sound

The free field complex pressure of the cylindrical waves radiating from an infinite incoherent line source is defined by

$$p(r) = \frac{k\rho_0 c_0 q}{4} H_0^{(2)}(kr), \tag{A.1}$$

where r denotes the radial distance from the source, ρ_o is the density of air, c_0 is the speed of sound in air, q is the total volume velocity per unit length, $H_0^{(2)}$ is the zeroth-order Hankel function of the 2nd kind [Beranek and Mellow, 2012b].

In the far-field, the Hankel function becomes

$$H_0^{(2)}(kr)\Big|_{r\to\infty} = \sqrt{\frac{2}{\pi kr}} e^{-j\left(kr-\frac{\pi}{4}\right)}, \tag{A.2}$$

so the resulting far-field complex pressure for an incoherent line source is written as

$$p(r) = \frac{\rho_0 c_0 q}{2}\sqrt{\frac{k}{2\pi r}} e^{-j\left(kr-\frac{\pi}{4}\right)}. \tag{A.3}$$

The acoustic power output of the incoherent line source can be derived from the far-field acoustic power definition [Bies and Hansen, 2009] given by

$$W = \frac{|p(r)|^2}{2\rho_0 c_0}\cdot 2\pi r, \tag{A.4}$$

to give

$$W = \frac{\rho_0 c_0 k |q|^2}{8} = \frac{1}{2} Z_o |q|^2 , \tag{A.5}$$

where $Z_o = (\rho_0 c_0 k)/4$.

The complex pressure in (A.1) can also be written as

$$p(r) = q \cdot Z(r), \tag{A.6}$$

where $Z(r)$ is a complex impedance given by

$$Z(r) = Z_o H_0^{(2)}(kr) = Z_o \left[J_0(kr) - jY_0(kr) \right], \tag{A.7}$$

where J_0 and Y_0 are the zeroth-order Bessel function of the first and second kind, respectively. Since the power output of the source [Nelson et al., 1987] is also given by

$$W = \frac{1}{2} |q|^2 \, \mathrm{Re}\{Z(r)\}, \tag{A.8}$$

it arrives at the same expression as (A.5) by directly recognising that $J_0(kr) \to 1$ as $kr \to 0$ [Beranek and Mellow, 2012c].

With the complex pressure and the power output of the incoherent line source defined in free-field conditions, we can formulate the power output of an incoherent line primary source in the presence of a secondary control source in the same fashion as the monopole case given by

$$W = \frac{1}{2} \mathrm{Re} \left\{ \left[p_p(r_p) + p_s(r_p) \right]^* \cdot q_p + \left[p_p(r_s) + p_s(r_s) \right]^* \cdot q_s \right\}, \tag{A.9}$$

where * represents complex conjugate operator; q_p and q_s are the complex strengths of the primary and secondary source respectively; $p_p(r_p)$ and $p_p(r_s)$ respectively

represent the pressure contributions of the primary and secondary sources to the primary source location [Nelson et al., 1987]; it follows that $p_p(r_s)$ and $p_s(r_s)$ respectively represent the pressure contributions of the primary and secondary sources at the secondary source location. By relating to their complex impedances from (A.6), (A.9) can be expanded to

$$W = \frac{1}{2}\mathrm{Re}\left\{|q_s|^2 Z_s^*(r_s) + q_s Z_p^*(r_s) q_p^* + q_p Z_s^*(r_p) q_s + |q_p|^2 Z_p^*(r_p)\right\}. \quad \text{(A.10)}$$

Further simplification is achieved by applying the principle of reciprocity, which equates $Z_p(r_s)$ and $Z_s(r_p)$ in (A.10) to arrive at

$$W = \frac{1}{2}\begin{bmatrix} |q_s|^2 \mathrm{Re}\{Z_s(r_s)\} + q_s^* \mathrm{Re}\{Z_p(r_s)\} q_p + \\ q_p^* \mathrm{Re}\{Z_p(r_s)\} q_s + |q_p|^2 \mathrm{Re}\{Z_p(r_p)\} \end{bmatrix}. \quad \text{(A.11)}$$

From (A.7), it is clear that $\mathrm{Re}\{Z_s(r_s)\} = \mathrm{Re}\{Z_p(r_p)\} = Z_o$ and $\mathrm{Re}\{Z_p(r_s)\} = J_o(kr_s)$. If the separation distance between the sources is represented by *w*, (A.11) can be represented in the complex quadratic form [Nelson and Elliott, 1992] as

$$W = A|q_s|^2 + q_s^* b + b^* q_s + c, \quad \text{(A.12)}$$

where $A = (1/2)Z_0$, $b = -(1/2)Z_0 q_p J_0(kw)$, and $c = (1/2)Z_0|q_p|^2$. The last term represents the power output of the primary source alone and shall be denoted by W_p. As A is greater than zero, the quadratic function in (A.12) has a unique minimum characterised by the optimal secondary source strength given by

$$q_{s,opt} = A^{-1}b = -q_p J_0(kw), \quad \text{(A.13)}$$

and its minimum power output is thus given by

$$W_0 = c - b^* A^{-1} b = W_p \left[1 - J_0^2 \left(kw \right) \right]. \tag{A.14}$$

Unsurprisingly, the derived optimal secondary source power output in terms of incoherent line sources in 2D arrives at the same expression as optimal secondary force input applied to control a point primary force on an infinite thin elastic plate [Fuller et al., 1996].

Appendix B

Equipment details

The equipment utilised for the measurements and experiments in this thesis are detailed in the following subsections.

B.1. Room response measurement

The frequency response and reverberation time of the test chamber described in section 5.1.2 is measured with a logarithmic sine sweep using the following setup:

- Genelec 8320A Smart Active Monitoring (SAM™) Studio Monitor
- Creative Sound Blaster E5 24-bit USB Digital-to-Analog Converter
- miniDSP UMIK-1 USB audio class 1 omni-directional USB measurement microphone
- Windows 10 Notebook running Room EQ Wizard (REW) room acoustics software

B.2. Acoustic camera setup in the test chamber

The sound pressure distribution of the primary source (Genelec 8351A) described in section 5.1.3. was characterized with an acoustic camera calibrated to measure the sound impinging into the window aperture with the following setup:

- Brüel & Kjær BK Connect Acoustic Camera Type 9712-W-FEN
    - Brüel & Kjær WA-1764-W-001 30-channel, sliced wheel array with integral cables and a removable reflective plate

        - Brüel & Kjær Type 4959 0.25 inch prepolarized CCLD microphone with TEDS
    - Brüel & Kjær LAN-XI Data Acquisition Hardware
        - 1 unit of the front-end frame with GPS Type 3660-C-100 (5-module)
        - 2 units of the 12-channel input module Type 3053-B-120 with array connector front panel UA-2112-120
        - 1 unit of the 6-channel input module Type 3050-A-060 with array connector front panel UA-2112-060
        - 1 unit of the battery module Type 2831
- Windows 10 notebook running BK Connect software with Array Analysis Type 8430 module

B.3. Real-time 24-Channel active noise control system

The real-time active noise control system as detailed in section 5.2 can be described in terms of its major components in chronological order: (a) the active control units, comprising of both the reference microphone and control speaker; (b) the controller, which is executing the adaptive algorithm; (c) the primary noise source that is producing the disturbance to be cancelled; and (d) the error microphones at which the disturbance is minimized.

B.3.1. Active control units

- 24 custom enclosures 3D printed using Makerbot Replicator 5th Generation with polylactide (PLA) thermoplastic

- 24 units of Visaton BF 45 full-range loudspeaker drivers secured to the 3D printed enclosure with nylon screws
- 24 reference sensors secured to the 3D printed enclosure with silicone gel and made up of individual breakout boards consisting of a single electret condenser microphone CUI CMA-4544PF-W preamplified with MAXIM MAX4466
- Speaker amplifiers

B.3.2. Controller

- National Instruments cRIO-9039 CompactRIO controller
- National Instruments NI-9220 16-channel C series voltage input module
- National Instruments NI-9264 16-channel C series voltage output module
- Windows 7 desktop PC running LabVIEW 2017 for monitoring and execution of the cRIO-9039 CompactRIO controller

B.3.3. Primary noise source

- Genelec 8351A Smart Active Monitoring (SAM™) Studio Monitor
- ASUS Xonar Essence One USB digital-to-analog converter
- Windows 7 desktop PC running Audacity

B.3.4. Error microphone

- 24 units of individual breakout boards consisting of a single electret condenser microphone CUI CMA-4544PF-W preamplified with MAXIM MAX4466

B.4. Monitoring microphone setup in the test chamber

- 18 units of G.R.A.S. 40PH CCP free-field array microphones as monitoring microphones
- G.R.A.S. 42 AB sound calibrator, Class 1
- 5 units of National Instruments NI-9234, 4-channel, C series sound and vibration input module
- National Instruments cDAQ-9137 CompactDAQ controller
- Windows 10 laptop running LabVIEW 2017 for monitoring and communication with the standalone cDAQ-9137 controller

B.5. Equipment Specifications

The datasheets of the electronic components used in the custom active control units described in B.3.1, and microphone and amplifier breakout boards for the reference microphone described in B.3.1 and error microphones described in B.3.4 are detailed in the following subsections.

B.5.1. Visaton BF 45 S Data Sheet

Breitband-Systeme / Fullrange Systems

VISATON GERMANY

BF 45 - 4 Ohm

Art. No. 2240

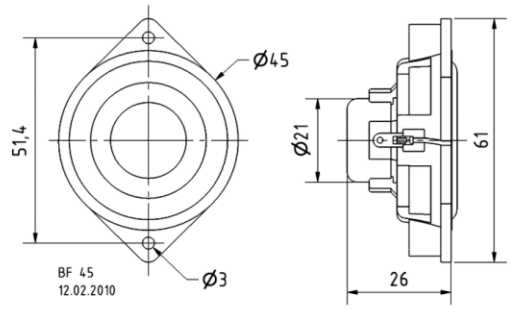

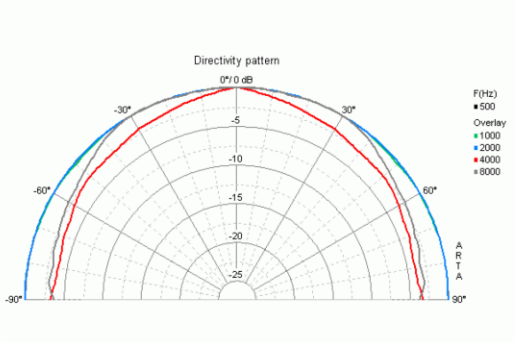

Technische Daten / Technical data

Nennbelastbarkeit Rated power	4 W
Musikbelastbarkeit Maximum power	8 W
Nennimpedanz Z Nominal impedance Z	4 Ohm
Übertragungsbereich Frequency response	90–20000 Hz
Mittlerer Schalldruckpegel Mean sound pressure level	79 dB (1 W/1 m)
Resonanzfrequenz fs Resonance frequency fs	158 Hz
Obere Polplattenhöhe Height of front pole-plate	3 mm
Schwingspulendurchmesser Voice coil diameter	17 mm
Wickelhöhe Height of winding	4 mm
Schallwandöffnung Cutout diameter	45 mm
Gewicht netto Net weight	0,032 kg

01.10.2015

VISATON GmbH • Ohligser Straße 29-31 • D-42781 Haan • Tel.: 02129/552-0 • Fax 02129/552-10 • E-Mail: visaton@visaton.com

B.5.2. CUI CMA-4544PF-W Data Sheet

CUI INC

date 06/2008

PART NUMBER: CMA-4544PF-W **DESCRIPTION:** electret condenser microphone

SPECIFICATIONS

directivity	omnidirectional	
sensitivity (S)	-44 ±2 dB	f = 1KHz, 1Pa 0dB = 1V/Pa
sensitivity reduction (ΔS-Vs)	-3 dB	f = 1KHz, 1Pa Vs = 3.0 ~ 2.0 V dc
operating voltage	3 V dc (standard), 10 V dc (max.)	
output impedance (Zout)	2.2 KΩ	f = 1KHz, 1Pa
operating frequency (f)	20 ~ 20,000 Hz	
current consumption (IDSS)	0.5 mA max.	Vs = 3.0 V dc RL = 2.2KΩ
signal to noise ratio (S/N)	60 dBA	f = 1KHz, 1Pa A-weighted
operating temperature	-20 ~ +70° C	
storage temperature	-20 ~ +70° C	
dimensions	ø9.7 x 4.5 mm	
weight	0.80 g max.	
material	Al	
terminal	pin type (hand soldering only)	
RoHS	yes	

note: We use the "Pascal (Pa)" indication of sensitivity as per the recomendation of I.E.C. (International Electrotechnical Commission). The sensitivity of "Pa" will increase 20dB compared to the "ubar" indication. Example: -60dB (0dB = 1V/ubar) = -40dB (1V/Pa)

APPEARANCE DRAWING

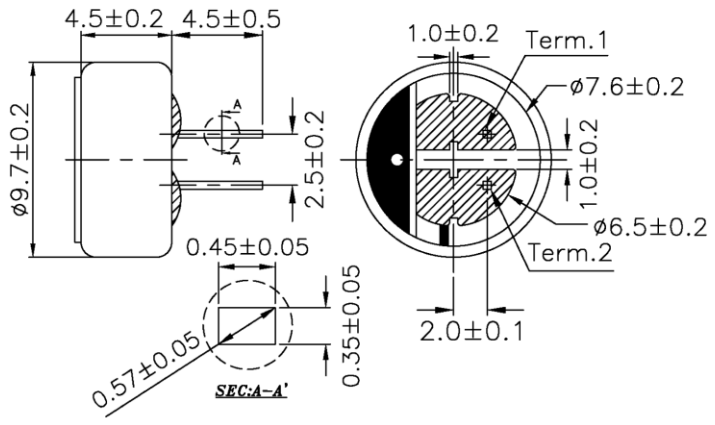

B.5.3. MAXIM MAX4466 Datasheet

Low-Cost, Micropower, SC70/SOT23-8, Microphone Preamplifiers with Complete Shutdown

ABSOLUTE MAXIMUM RATINGS

Supply Voltage (V_{CC} to GND).....+6V
All Other Pins to GND.....-0.3V to (V_{CC} + 0.3V)
Output Short-Circuit Duration
OUT Shorted to GND or V_{CC}.....Continuous
Continuous Power Dissipation (T_A = +70°C)
5-Pin SC70 (derate 2.5mW/°C above +70°C).....200mW
5-Pin SOT23 (derate 7.1mW/°C above +70°C).....571mW
8-Pin SOT23 (derate 5.3mW/°C above +70°C).....421mW
8-Pin SO (derate 5.88mW/°C above +70°C).....471mW
Operating Temperature Range .....-40°C to +85°C
Storage Temperature Range.....-65°C to +150°C
Junction Temperature.....+150°C
Lead Temperature (soldering, 10s).....+300°C

Stresses beyond those listed under "Absolute Maximum Ratings" may cause permanent damage to the device. These are stress ratings only, and functional operation of the device at these or any other conditions beyond those indicated in the operational sections of the specifications is not implied. Exposure to absolute maximum rating conditions for extended periods may affect device reliability.

ELECTRICAL CHARACTERISTICS

(V_{CC} = +5V, V_{CM} = 0, V_{OUT} = V_{CC}/2, R_L = ∞ to V_{CC}/2, SHDN = GND (MAX4467/MAX4468 only). T_A = T_{MIN} to T_{MAX}, unless otherwise noted. Typical values specified at T_A = +25°C.) (Note 1)

PARAMETER	SYMBOL	CONDITIONS		MIN	TYP	MAX	UNITS
Supply Voltage Range	V_{CC}	Inferred from PSRR test		2.4		5.5	V
Supply Current (Per Amplifier)	I_{CC}	T_A = +25°C			24	48	µA
		T_A = T_{MIN} to T_{MAX}				60	
Supply Current in Shutdown	I_{SHDN}	SHDN = V_{CC} (Note 2)			5	50	nA
Input Offset Voltage	V_{OS}				±1	±5	mV
Input Bias Current	I_B	V_{CM} = -0.1V			±2.5	±100	nA
Input Offset Current Range	I_{OS}	V_{CM} = -0.1V			±1	±15	nA
Input Common-Mode Range	V_{CM}	Inferred from CMRR test		-0.1		V_{CC} - 0.1	V
Common-Mode Rejection Ratio	CMRR	-0.1V ≤ V_{CM} ≤ V_{CC} - 1V		80	126		dB
Power-Supply Rejection Ratio	PSRR	2.4V ≤ V_{CC} ≤ 5.5V		80	112		dB
		MAX4465/MAX4467/MAX4469, f = 3.4kHz			75		
		MAX4466/MAX4468, f = 3.4kHz			80		
Open-Loop Gain	A_{VOL}	R_L = 100kΩ to V_{CC}/2, 0.05V ≤ V_{OUT} ≤ V_{CC} - 0.05V			125		dB
		R_L = 10kΩ to V_{CC}/2, 0.1V ≤ V_{OUT} ≤ V_{CC} - 0.1V		80	95		
Output Voltage Swing High	V_{OH}	$\lvert V_{CC} - V_{OH} \rvert$	R_L = 100kΩ		10		mV
			R_L = 10kΩ		16	50	
Output Voltage Swing Low	V_{OL}		R_L = 100kΩ		10		mV
			R_L = 10kΩ		14	50	
Output Short-Circuit Current		To either supply rail			15		mA
Output Leakage Current in Shutdown		SHDN = V_{CC}, 0 ≤ V_{OUT} ≤ V_{CC}; (Notes 2, 3)			±0.5	±100	nA
SHDN Logic Low	V_{IL}	(Note 2)				V_{CC} × 0.3	V
SHDN Logic High	V_{IH}	(Note 2)		V_{CC} × 0.7			V
SHDN Input Current		(Note 2)			2	25	nA
Gain Bandwidth Product	GBWP	MAX4465/MAX4467/MAX4469			200		kHz
		MAX4466/MAX4468			600		

Bibliography

Agha, A., Ranjan, R., and Gan, W.-S. (**2017**). “Noisy vehicle surveillance camera: A system to deter noisy vehicle in smart city,” Appl. Acoust., **117**, 236–245. doi:10.1016/j.apacoust.2016.05.025

Bai, M. R., Chen, C.-C., and Lin, J.-H. (**2011**). “On optimal retreat distance for the equivalent source method-based nearfield acoustical holography,” J. Acoust. Soc. Am., **129**, 1407–1416. doi:10.1121/1.3533734

Basner, M., Babisch, W., Davis, A., Brink, M., Clark, C., Janssen, S., and Stansfeld, S. (**2014**). “Auditory and non-auditory effects of noise on health,” Lancet (London, England), **383**, 1325–32. doi:10.1016/S0140-6736(13)61613-X

Beranek, L. L., and Mellow, T. J. (**2012**). “Chapter 7 - Loudspeaker systems,” In L. L. Beranek and T. J. Mellow (Eds.), Acoust. Sound Fields Transducers, Academic Press, pp. 289–389. doi:http://dx.doi.org/10.1016/B978-0-12-391421-7.00007-5

Beranek, L. L., and Mellow, T. J. (**2012**). “Chapter 12 - Radiation and scattering of sound by the boundary value method,” In L. L. Beranek and T. J. Mellow (Eds.), Acoust. Sound Fields Transducers, Academic Press, pp. 487–533. doi:http://dx.doi.org/10.1016/B978-0-12-391421-7.00012-9

Beranek, L. L., and Mellow, T. J. (**2012**). “Chapter 2 - The wave equation and solutions,” In L. L. Beranek and T. J. Mellow (Eds.), Acoust. Sound Fields Transducers, Academic Press, pp. 21–63. doi:http://dx.doi.org/10.1016/B978-0-12-391421-7.00002-6

Bi, C.-X., Chen, X.-Z., and Chen, J. (**2008**). “Sound field separation technique based on equivalent source method and its application in nearfield acoustic holography,” J.

Acoust. Soc. Am., **123**, 1472–1478. doi:10.1121/1.2837489

Bi, C.-X., and Stuart Bolton, J. (**2012**). "An equivalent source technique for recovering the free sound field in a noisy environment," J. Acoust. Soc. Am., **131**, 1260–1270. doi:10.1121/1.3675004

Bies, D. A., and Hansen, C. H. (**2009**). *Engineering noise control: theory and practice*, CRC press.

Carme, C., Schevin, O., Romerowski, C., and Clavard, J. (**2016**). "Active opening windows," Proc. 23rd Int. Congr. Sound Vib. ICSV23, Athens, Greece.

Carme, C., Schevin, O., Romerowski, C., and Clavard, J. (**2016**). "Active Noise Control Applied to Open Windows," INTER-NOISE NOISE-CON Congr. Conf. Proc., Hamburg, Germany, 3058–3064.

Cheer, J., and Elliott, S. J. (**2015**). "Multichannel control systems for the attenuation of interior road noise in vehicles," Mech. Syst. Signal Process., **60**–**61**, 753–769. doi:http://dx.doi.org/10.1016/j.ymssp.2015.01.008

Cheer, J., Elliott, S. J., Oh, E., and Jeong, J. (**2018**). "Application of the remote microphone method to active noise control in a mobile phone," J. Acoust. Soc. Am., **143**, 2142–2151. doi:10.1121/1.5031009

Cho, Y., Wang, S., Hyun, J., Oh, S., and Goo, S. (**2018**). "Analysis of sound absorption performance of an electroacoustic absorber using a vented enclosure," J. Sound Vib., **417**, 110–131. doi:10.1016/j.jsv.2017.11.051

COMSOL Multiphysics (**2015**). "Acoustics Module User's Guide,."

Crocker, M. J. (**2007**). *Handbook of noise and vibration control*, John Wiley & Sons, Hoboken, N.J., xxiv, 1569 p. pages. Retrieved from

http://dx.doi.org/10.1002/9780470209707 Wiley MIT Access Only

Eder, J., Hanselka, J., and Sachau, D. (**2017**). "Experimental study on the effect of the number of system components of an active noise blocker on the global noise reduction," INTER-NOISE NOISE-CON Congr. Conf. Proc., Hong Kong SAR, China, 5298–5309.

Elliott, S., Cheer, J., Lam, B., Shi, C., and Gan, W. (**2017**). "Controlling Incident Sound Fields With Source Arrays in Free Space and Through Apertures," In B. M. Gibbs (Ed.), Proc. 24th Int. Congr. Sound Vib., London, UK, 1–7.

Elliott, S. J. (**2001**). *Signal Processing for Active Control*, Academic Press, London, UK, 511 pages.

Elliott, S. J., and Cheer, J. (**2015**). "Modeling local active sound control with remote sensors in spatially random pressure fields," J. Acoust. Soc. Am., **137**, 1936–1946. doi:10.1121/1.4916274

Elliott, S. J., Cheer, J., Lam, B., Shi, C., and Gan, W. (**2018**). "A wavenumber approach to analysing the active control of plane waves with arrays of secondary sources," J. Sound Vib., **419**, 405–419. doi:10.1016/j.jsv.2018.01.028

Emms, G. W. (**2000**). *Active sound power absorbers: their effect on sound transmission through wall openings*, The University of Auckland, PhD Thesis.

Emms, G. W., and Fox, C. (**2001**). "Control of sound transmission through an aperture using active sound absorption techniques: a theoretical investigation," Appl. Acoust., **62**, 735–747. doi:10.1016/S0003-682X(00)00063-3

European Environment Agency (**2017**). *Managing exposure to noise in Europe*, Publications Office of the European Union, Luxembourg, 4 pages. doi:10.2800/338580

Fahnline, J. B., and Koopmann, G. H. (**1991**). “A numerical solution for the general radiation problem based on the combined methods of superposition and singular-value decomposition,” J. Acoust. Soc. Am., **90**, 2808–2819. doi:doi:http://dx.doi.org/10.1121/1.401878

Fairweather, G., Karageorghis, A., and Martin, P. A. (**2003**). “The method of fundamental solutions for scattering and radiation problems,” Eng. Anal. Bound. Elem., **27**, 759–769. doi:http://dx.doi.org/10.1016/S0955-7997(03)00017-1

Fan, R., Su, Z., and Cheng, L. (**2013**). “Modeling, analysis, and validation of an active T-shaped noise barrier,” J. Acoust. Soc. Am., **134**, 1990–2003. doi:10.1121/1.4817887

Fasciani, S., He, J., Lam, B., Murao, T., and Gan, W.-S. (**2015**). “Comparative study of cone-shaped versus flat-panel speakers for active noise control of multi-tonal signals in open windows,” INTER-NOISE NOISE-CON Congr. Conf. Proc., San Francisco, CA, USA, 1109–1120.

Field, C. D., and Fricke, F. R. (**1998**). “Theory and applications of quarter-wave resonators: A prelude to their use for attenuating noise entering buildings through ventilation openings,” Appl. Acoust., **53**, 117–132. doi:10.1016/S0003-682X(97)00035-2

Fisk, W. J., and Rosenfeld, A. H. (**1997**). “Estimates of Improved Productivity and Health from Better Indoor Environments,” Indoor Air, **7**, 158–172. doi:10.1111/j.1600-0668.1997.t01-1-00002.x

Ford, R. D., and Kerry, G. (**1973**). “The sound insulation of partially open double glazing,” Appl. Acoust., **6**, 57–72. doi:10.1016/0003-682X(73)90029-7

Fritschi, L., Brown, L., Kim, R., Schwela, D., and Kephalopolous, S. (**2011**). *Burden of*

disease from environmental noise: Quantification of healthy life years lost in Europe, The Regional Office for Europe of the World Health Organization, Copenhagen, Denmark, 106 pages.

Fuller, C. R., Elliott, S. J. (Stephen J. ., and Nelson, P. A. (**1996**). *Active control of vibration*, Academic Press, 332 pages. Retrieved from https://www-sciencedirect-com.ezlibproxy1.ntu.edu.sg/science/book/9780122694400

Gounot, Y. J. R., and Musafir, R. E. (**2007**). "On appropriate equivalent monopole sets for rigid body scattering problems," J. Acoust. Soc. Am., **122**, 3195–3205. doi:10.1121/1.2799504

Gounot, Y. J. R., and Musafir, R. E. (**2011**). "Simulation of scattered fields: some guidelines for the equivalent source method," J. Sound Vib., **330**, 3698–3709.

Gounot, Y., Musafir, R. E., and Slama, J. G. (**2005**). "A comparative study of two variants of the equivalent sources method in scattering problems," Acta Acust. united with Acust., **91**, 860–872.

Guarinoni, M., Ganzleben, C., and Murphy, E. (**2012**). *Towards A Comprehensive Noise Strategy*, The Publications Office of the European Union, Brussels, 81 pages. doi:10.2861/22191

Hanselka, J., Jukkert, S., and Sachau, D. (**2016**). "Experimental Study on the Influence of the Sensor and Actuator Arrangement on the Performance of an Active Noise Blocker for a Tilted Window," INTER-NOISE NOISE-CON Congr. Conf. Proc., Hamburg, Germany, 3046–3057.

Hansen, C., Snyder, S., Qiu, X., Brooks, L., and Moreau, D. (**2012**). *Active Control of Noise and Vibration, Second Edition*, CRC Press.

Hart, C. R., and Lau, S.-K. (**2012**). "Active noise control with linear control source and

sensor arrays for a noise barrier," J. Sound Vib., **331**, 15–26. doi:10.1016/j.jsv.2011.08.016

Holste, F. (**1997**). "An equivalent source method for calculation of the sound radiated from aircraft engines," J. Sound Vib., **203**, 667–695.

Hong, J. Y., Lam, B., Ong, Z.-T., Gupta, R., and Gan, W.-S. (**2017**). "Suitability of natural sounds to enhance soundscape quality in urban residential areas," Proc. 24th Int. Congr. Sound Vib.,.

Huang, X., Zou, H., and Qiu, X. (**2015**). "A preliminary study on the performance of indoor active noise barriers based on 2D simulations," Build. Environ., **94**, 891–899. doi:10.1016/j.buildenv.2015.06.034

International Organization for Standardization (**2008**). *Acoustics - Measurement of room acoustic parameters, Part 2: Reverberation time in ordinary rooms*, ISO 3382-22008, Geneva, Switzerland.

International Organization for Standardization (**2014**). *Acoustics — Soundscape — Part 1 : Definition and conceptual framework*, ISO 12913-1, International Organization for Standardization, Geneva, Switzerland, 4 pages.

International Organization for Standardization (**2016**). *Field measurement of sound insulation in buildings and of building elements - Part 3: Façade sound insulation*, 1st ed., 37 pages.

Ise, S. (**2005**). "The Boundary Surface Control Principle and Its Applications," IEICE Trans. Fundam. Electron. Commun. Comput. Sci., **E88**–**A**, 1656–1664.

Jagniatinskis, A., and Fiks, B. (**2014**). "Assessment of environmental noise from long-term window microphone measurements," Appl. Acoust., **76**, 377–385. doi:http://dx.doi.org/10.1016/j.apacoust.2013.09.007

Jakob, A., and Möser, M. (**2003**). “Active control of double-glazed windows Part I: Feedforward control,” Appl. Acoust., **64**, 163–182.

Jakob, A., and Möser, M. (**2003**). “Active control of double-glazed windows Part II: Feedback control,” Appl. Acoust., **64**, 183–196. doi:10.1016/S0003-682X(02)00071-3

Jeans, R., and Mathews, I. C. (**1992**). “The wave superposition method as a robust technique for computing acoustic fields,” J. Acoust. Soc. Am., **92**, 1156–1166. doi:doi:http://dx.doi.org/10.1121/1.404042

Johnson, M. E., Elliott, S. J., Baek, K.-H., and Garcia-Bonito, J. (**1998**). “An equivalent source technique for calculating the sound field inside an enclosure containing scattering objects,” J. Acoust. Soc. Am., **104**, 1221–1231. doi:10.1121/1.424330

Jung, W., Elliott, S. J., and Cheer, J. (**2017**). “Combining the remote microphone technique with head-tracking for local active sound control,” J. Acoust. Soc. Am., **142**, 298–307. doi:10.1121/1.4994292

Kajikawa, Y., Gan, W.-S., and Kuo, S. M. (**2012**). “Recent advances on active noise control: open issues and innovative applications,” APSIPA Trans. Signal Inf. Process., **1**, e3. doi:10.1017/ATSIP.2012.4

Kang, J. (**2009**). “An acoustic window system with optimum ventilation and daylighting performance,” Noise Vib. Worldw., **37**, 9–17. doi:10.1260/095745606779385108

Kim, S., and Lee, S. (**2014**). “Air transparent soundproof window,” AIP Adv., **4**, 117123. doi:10.1063/1.4902155

Koopmann, G. H., Song, L., and Fahnline, J. B. (**1989**). “A method for computing acoustic fields based on the principle of wave superposition,” J. Acoust. Soc. Am., **86**, 2433–2438. doi:doi:http://dx.doi.org/10.1121/1.398450

Kuo, S. M., and Morgan, D. R. (**1996**). *Active noise control systems: algorithms and DSP implementations*, Wiley.

Kwon, B., and Park, Y. (**2013**). "Interior noise control with an active window system," Appl. Acoust., **74**, 647–652. doi:10.1016/j.apacoust.2012.11.005

Lam, B., Elliott, S., Cheer, J., and Gan, W.-S. (**2018**). "Physical limits on the performance of active noise control through open windows," Appl. Acoust., **137**, 9–17. doi:10.1016/j.apacoust.2018.02.024

Lam, B., Elliott, S. J., Cheer, J., and Gan, W.-S. (**2015**). "Regularisation of the equivalent source method for robust numerical modelling of acoustic scattering," INTER-NOISE NOISE-CON Congr. Conf. Proceedings, InterNoise15, Institute of Noise Control Engineering, San Francisco, CA, USA, 976–987.

Lam, B., Elliott, S. J., Cheer, J., and Gan, W.-S. (**2015**). "The Physical Limits of Active Noise Control of Open Windows," In K. M. Lim (Ed.), Proc. 12th West. Pacific Acoust. Conf., Singapore, 184–189.

Lam, B., and Gan, W.-S. (**2016**). "Active Acoustic Windows: Towards a Quieter Home," IEEE Potentials, **35**, 11–18. doi:10.1109/MPOT.2014.2310776

Lam, B., Gan, W., and Elliott, S. (**2018**). "Hybrid source arrangement for active control of noise through apertures at oblique incidences: A preliminary investigation," Proc. 25th Int. Congr. Sound Vib. ICSV25, Hiroshima, Japan, 1–8.

Lam, B., He, J., Murao, T., Shi, C., Gan, W.-S., and Elliott, S. J. (**2016**). "Feasibility of the full-rank fixed-filter approach in the active control of noise through open windows," INTER-NOISE NOISE-CON Congr. Conf. Proceedings, InterNoise16, Hamburg, Germany, 3548–3555.

Lam, B., Shi, C., Shi, D., and Gan, W.-S. (**2018**). "Active control of sound through full-

sized open windows," Build. Environ., **141**, 16–27. doi:10.1016/j.buildenv.2018.05.042

Leblanc, A., Ing, R. K., and Lavie, A. (**2010**). "A Wave Superposition Method Based on Monopole Sources with Unique Solution for All Wave Numbers," Acta Acust. united with Acust., **96**, 125–130. doi:10.3813/AAA.918263

Lee, H. M., Tan, L. B., Lim, K. M., and Lee, H. P. (**2016**). "Experimental study of the acoustical performance of a sonic crystal window in a reverberant sound field," Build. Acoust., , doi: 10.1177/1351010X16681015. doi:10.1177/1351010X16681015

Lee, H. M., Tan, L. B., Lim, K. M., and Lee, H. P. (**2017**). "Acoustical performance of a sonic crystal window," Int. J. Mech. Eng. Robot. Res., **6**, 6–10. doi:10.18178/ijmerr.6.1.6-10

Lee, S. (**2017**). "Review: The Use of Equivalent Source Method in Computational Acoustics," J. Comput. Acoust., **25**, 1630001. doi:10.1142/S0218396X16300012

Lee, S., Brentner, K. S., and Morris, P. J. (**2010**). "Acoustic scattering in the time domain using an equivalent source method," AIAA J., **48**, 2772–2780.

Lee, S., Brentner, K. S., and Morris, P. J. (**2011**). "Assessment of time-domain equivalent source method for acoustic scattering," AIAA J., **49**, 1897–1906.

Lim, K.-M., Lee, H. M., Tan, L. B., and Lee, H. P. (**2017**). "Incorporating sonic crystals in windows for noise attenuation," Proc. 24th Int. Congr. Sound Vib. ICSV24,.

Magnusson, I., Pàmies, T., and Romeu, J. (**2014**). "Active control of sound transmission through an aperture in a thin wall," INTER-NOISE NOISE-CON Congr. Conf. Proceedings, NoiseCon14, Institute of Noise Control Engineering, Florida, 1037–1044.

Murao, T., and Nishimura, M. (**2012**). “Basic Study on Active Acoustic Shielding,” J. Environ. Eng., **7**, 76–91.

Murao, T., Nishimura, M., He, J., Lam, B., Ranjan, R., Shi, C., and Gan, W.-S. (**2016**). “Feasibility study on decentralized control system for active acoustic shielding,” INTER-NOISE NOISE-CON Congr. Conf. Proceedings, InterNoise16, Hamburg, Germany, 1106–1115.

Murao, T., Nishimura, M., and Sakurama, K. (**2013**). “Basic study on active acoustic shielding: Phase 5 improving decentralized control algorithm to enlarge AAS window,” INTER-NOISE NOISE-CON Congr. Conf. Proc., Institute of Noise Control Engineering, Innsbruck, Austria, 2956–2965.

Murao, T., Nishimura, M., Sakurama, K., and Nishida, S. (**2014**). “Basic study on active acoustic shielding (Improving noise-reducing performance in low-frequency range),” Mech. Eng. J., **1**, EPS0065-EPS0065. doi:10.1299/mej.2014eps0065

Murao, T., Shi, C., Gan, W.-S., and Nishimura, M. (**2017**). “Mixed-error approach for multi-channel active noise control of open windows,” Appl. Acoust., **127**, 305–315. doi:10.1016/j.apacoust.2017.06.024

Murphy, E., and King, E. A. (**2014**). *Environmental Noise Pollution*, Elsevier. doi:10.1016/C2012-0-13587-0

Nathalie, R. (**2011**). *Health co-benefits of climate change mitigation: Housing sector*, (Elaine Ruth Fletcher, Ed.) WHO Press, World Health Organization, Geneva, Switzerland, 120 pages.

Nelson, P. A., Curtis, A. R. D., Elliott, S. J., and Bullmore, A. J. (**1987**). “The minimum power output of free field point sources and the active control of sound,” J. Sound Vib., **116**, 397–414. doi:10.1016/S0022-460X(87)81373-1

Nelson, P. A., and Elliott, S. J. (**1992**). *Active control of sound*, Academic Press. Retrieved from http://books.google.com.sg/books?id=6csYAQAAIAAJ

Nilsson, M., Bengtsson, J., and Klaeboe, R. (**2014**). *Environmental Methods for Transport Noise Reduction*, (M. Nilsson, J. Bengtsson, and R. Klaeboe, Eds.) CRC Press, 294 pages. doi:10.1201/b17606

Nishimura, M., Ohnishi, K., Kanamori, N., and Ito, K. (**2008**). "Basic study on active acoustic shielding," INTER-NOISE NOISE-CON Congr. Conf. Proc., Institute of Noise Control Engineering, 440–455.

Nugent, C., Blanes, N., Fons, J., Maza, M. S. de la, Ramos, M. J., Domingues, F., Beek, A. van, et al. (**2014**). *Noise in Europe 2014*, Publications Office of the European Union, Luxembourg, 62 pages. doi:10.2800/763331

Pàmies, T., Romeu, J., Arcos, R., and Martin, S. (**2014**). "Analytical Simulations on Active Control of Sound Transmission Through an Aperture in a Rectangular Enclosure," Acta Acust. united with Acust., **100**, 277–284. doi:10.3813/AAA.918707

Pàmies, T., Romeu, J., Genescà, M., and Arcos, R. (**2014**). "Active control of aircraft fly-over sound transmission through an open window," Appl. Acoust., **84**, 116–121. doi:10.1016/j.apacoust.2014.02.018

Pàmies, T., Romeu, J., Genescà, M., and Balastegui, A. (**2011**). "Sound radiation from an aperture in a rectangular enclosure under low modal conditions," J. Acoust. Soc. Am., **130**, 239–248. doi:10.1121/1.3596465

Piscoya, R., Brick, H., Ochmann, M., and Költzsch, P. (**2008**). "Equivalent source method and boundary element method for calculating combustion noise," Acta Acust. united with Acust., **94**, 514–527.

Qiu, X. (**2017**). “Recent advances on active control of sound transmission through ventilation windows,” Proc. 24th Int. Congr. Sound Vib.,.

Quirt, J. D. (**1982**). “Sound transmission through windows I Single and double glazing,” J. Acoust. Soc. Am., **72**, 834–844. doi:doi:http://dx.doi.org/10.1121/1.388263

Ranjan, R., He, J., Murao, T., Lam, B., and Gan, W.-S. (**2016**). “Selective Active Noise Control System for Open Windows using Sound Classification,” INTER-NOISE NOISE-CON Congr. Conf. Proceedings, InterNoise16, Hamburg, Germany, 482–492.

Rdzanek, W. P. (**2018**). “Sound scattering and transmission through a circular cylindrical aperture revisited using the radial polynomials,” J. Acoust. Soc. Am., **143**, 1259–1282. doi:10.1121/1.5025159

Van Renterghem, T., and Botteldooren, D. (**2012**). “On the choice between walls and berms for road traffic noise shielding including wind effects,” Landsc. Urban Plan., **105**, 199–210. doi:10.1016/J.LANDURBPLAN.2011.12.017

De Salis, M. H. F., Oldham, D. J., and Sharples, S. (**2002**). “Noise control strategies for naturally ventilated buildings,” Build. Environ., **37**, 471–484. doi:10.1016/S0360-1323(01)00047-6

Samarasinghe, P. N., Zhang, W., and Abhayapala, T. D. (**2016**). “Recent Advances in Active Noise Control Inside Automobile Cabins: Toward quieter cars,” IEEE Signal Process. Mag., **33**, 61–73. doi:10.1109/MSP.2016.2601942

Schwela, D. H., Finegold, L. S., and Gjestland, T. (**2014**). “Progress on environmental noise policies from 2008-2013 in Asia and the world,” INTER-NOISE NOISE-CON Congr. Conf. Proc., Melbourne, Australia, 6042–6053.

Science Communication Unit, U. of the W. of E. (UWE) (**2017**). *Science for*

Environment Policy (2017) Noise abatement approaches. Future Brief 17, Produced for the European Commission DG Environment, Bristol, UK, 25 pages. doi:10.2779/016648

Shi, D., Gan, W.-S., Lam, B., and Shi, C. (**2019**). "Two-gradient direction FXLMS: An adaptive active noise control algorithm with output constraint," Mech. Syst. Signal Process., **116**, 651–667. doi:10.1016/j.ymssp.2018.06.062

Shi, D., He, J., Shi, C., Murao, T., and Gan, W.-S. (**2017**). "Multiple parallel branch with folding architecture for multichannel filtered-x least mean square algorithm," 2017 IEEE Int. Conf. Acoust. Speech Signal Process.,.

Shi, D., Lam, B., and Gan, W.-S. (**2018**). "A novel selective active noise control algorithm to overcome practical implementation issue," 2018 IEEE Int. Conf. Acoust. Speech Signal Process., IEEE, Calgary, Canada, 1–5.

Shi, D., Shi, C., and Gan, W.-S. (**2016**). "A systolic FxLMS structure for implementation of feedforward active noise control on FPGA," 2016 Asia-Pacific Signal Inf. Process. Assoc. Annu. Summit Conf., IEEE, 1–6. doi:10.1109/APSIPA.2016.7820755

Sieck, C. F. (**2013**). *Investigation of sound transmission through an open window into a room* University of Nebraska-Lincoln, 63 pages.

Song, L., Koopmann, G. H., and Fahnline, J. B. (**1991**). "Numerical errors associated with the method of superposition for computing acoustic fields," J. Acoust. Soc. Am., **89**, 2625–2633. doi:doi:http://dx.doi.org/10.1121/1.400701

SPRING (Standards Productivity and Innovation Board) Singapore (**2007**). *Specification for aluminium alloy windows*, SS 212.2 (ICS 91.060.50), SPRING (Standards Productivity and Innovation Board) Singapore, Singapore, 4th Rev., 57

pages.

Stansfeld, S. A., and Matheson, M. P. (**2003**). “Noise pollution: non-auditory effects on health,” Br. Med. Bull., **68**, 243–257. doi:10.1093/bmb/ldg033

Stephenson, R. J., and Vulkan, G. H. (**1968**). “Traffic noise,” J. Sound Vib., **7**, 247–262. doi:10.1016/0022-460X(68)90271-X

Tadeu, A. J. B., and Mateus, D. M. R. (**2001**). “Sound transmission through single, double and triple glazing Experimental evaluation,” Appl. Acoust., **62**, 307–325. doi:http://dx.doi.org/10.1016/S0003-682X(00)00032-3

Tadeu, A., Pereira, A., Godinho, L., and António, J. (**2007**). “Prediction of airborne sound and impact sound insulation provided by single and multilayer systems using analytical expressions,” Appl. Acoust., **68**, 17–42. doi:http://dx.doi.org/10.1016/j.apacoust.2006.05.012

Tang, S.-K. (**2017**). “A Review on Natural Ventilation-enabling Façade Noise Control Devices for Congested High-Rise Cities,” Appl. Sci., **7**, 175. doi:10.3390/app7020175

Tao, J., Wang, S., Qiu, X., and Pan, J. (**2016**). “Performance of an independent planar virtual sound barrier at the opening of a rectangular enclosure,” Appl. Acoust., **105**, 215–223. doi:10.1016/j.apacoust.2015.12.019

Tong, Y. G., Tang, S. K., Kang, J., Fung, A., and Yeung, M. K. L. (**2015**). “Full scale field study of sound transmission across plenum windows,” Appl. Acoust., **89**, 244–253. doi:10.1016/j.apacoust.2014.10.003

Utley, W. A., Buller, I. B., Keighley, E. C., and Sargent, J. W. (**1986**). “The effectiveness and acceptability of measures for insulating dwellings against traffic noise,” J. Sound Vib., **109**, 1–18. doi:10.1016/S0022-460X(86)80018-9

Valdivia, N. P., and Williams, E. G. (**2006**). “Study of the comparison of the methods of equivalent sources and boundary element methods for near-field acoustic holography,” J. Acoust. Soc. Am., **120**, 3694–3705.

Wang, S., Tao, J., and Qiu, X. (**2015**). “Performance of a planar virtual sound barrier at the baffled opening of a rectangular cavity,” J. Acoust. Soc. Am., **138**, 2836–2847. doi:10.1121/1.4934267

Wang, S., Tao, J., and Qiu, X. (**2017**). “Controlling sound radiation through an opening with secondary loudspeakers along its boundaries,” Sci. Rep., **7**, 13385. doi:10.1038/s41598-017-13546-2

Wang, S., Tao, J., Qiu, X., and Pan, J. (**2017**). “A boundary secondary source arrangement for a virtual sound barrier system at a cavity opening,” INTER-NOISE NOISE-CON Congr. Conf. Proc., Hong Kong SAR, China, 1733–1740.

Wang, S., Tao, J., Qiu, X., and Pan, J. (**2018**). “Mechanisms of active control of sound radiation from an opening with boundary installed secondary sources,” J. Acoust. Soc. Am., **143**, 3345–3351. doi:10.1121/1.5040139

Wang, S., Yu, J., Qiu, X., Pawelczyk, M., Shaid, A., and Wang, L. (**2017**). “Active sound radiation control with secondary sources at the edge of the opening,” Appl. Acoust., **117**, 173–179. doi:10.1016/j.apacoust.2016.10.027

Wang, Z. H., Hui, C. K., and Ng, C. F. (**2014**). “The acoustic performance of ventilated window with quarter-wave resonators and membrane absorber,” Appl. Acoust., **78**, 1–6. doi:10.1016/j.apacoust.2013.09.015

Warnaka, G. E. (**1982**). “Active Attenuation of Noise: The State of the Art,” Noise Control Eng., **18**, 100. doi:10.3397/1.2832205

World Health Organization Regional Office for Europe (**2009**). *Night noise guidelines*

for Europe, World Heal. Organ., The Regional Office for Europe of the World Health Organization, Copenhagen, Denmark, 154 pages.

Yu, X., Lau, S.-K., Cheng, L., and Cui, F. (**2017**). "A numerical investigation on the sound insulation of ventilation windows," Appl. Acoust., **117**, 113–121. doi:10.1016/j.apacoust.2016.11.006

Yu, X., Rajamani, R., Stelson, K. A., and Cui, T. (**2007**). "Active control of sound transmission through windows with carbon nanotube-based transparent actuators," Control Syst. Technol. IEEE Trans., **15**, 704–714.

Yuya, N. (**2010**). "The Acoustic Design of Soundproofing Doors and Windows," Open Acoust. J., **3**, 30–37. doi:10.2174/1874837601003010030

Yuya, N., Sohei, N., Tsuyoshi, N., and Takashi, Y. (**2009**). "Sound propagation in soundproofing casement windows," Appl. Acoust., **70**, 1160–1167. doi:10.1016/j.apacoust.2009.04.006

Zhang, G., Tao, J., Qiu, X., and Burnett, I. (**2019**). "Decentralized Two-Channel Active Noise Control for Single Frequency by Shaping Matrix Eigenvalues," IEEE/ACM Trans. Audio, Speech, Lang. Process., **27**, 44–52. doi:10.1109/TASLP.2018.2869686

Zhang, L., Tao, J., and Qiu, X. (**2013**). "Performance analysis of decentralized multi-channel feedback systems for active noise control in free space," Appl. Acoust., **74**, 181–188. doi:http://dx.doi.org/10.1016/j.apacoust.2012.07.008

Zwicker, E., and Fastl, H. (**2013**). *Psychoacoustics: Facts and models*, Springer Science & Business Media, Vol. 22.